# Maximising Utilisation of the DC-Link Voltage in the Field Weakening Region for AC Motor Drives


**Hamidreza Gashtil**

**B.Sc., M.Sc.**


A thesis submitted for the degree of Doctor of Philosophy

December 2019


School of Electrical and Electronic Engineering

Newcastle University

United Kingdom

# ABSTRACT

Most standard electric drives have two operational regions: the constant torque region and field-weakening region. In order to increase the power level at the field-weakening region, the phase voltage must be increased. The phase voltage, however, is a function of the inverter input voltage and the control scheme that is applied to the inverter. Several methods have been applied to optimise the stator voltage modulation to maximise the power level at the field-weakening region. These methods suffer from fake voltage extension, which produce high current ripples, and a step reduction of motor currents in the transient area from the constant torque region to the field-weakening region. Adding extra regulators for these methods was proposed, but this still would not show any significant improvement in electric-drive performance and increase the additional complexity of the closed-loop control system.

During the course of this research, several control schemes based on mathematical modelling and voltage feedback mechanism are proposed to tackle the aforementioned issues. In the proposed novel methods, flux-producing current is designed based on the position of the stator voltage vector to push the stator voltage to the hexagonal voltage boundary. This consequently causes a smooth transition from the constant torque region to the field-weakening region, and it also increases the output torque and power of the electric machine without applying extra controllers or producing a step reduction on the d-axis current. The capabilities of the proposed schemes have been evaluated and compared to conventional model-based and closed-loop voltage algorithms by using MATLAB simulation and an experimental test set-up. This research also developed and proposed two parameter estimation techniques based on EKF and combined MRAS-KF to improve the accuracy of online estimation techniques. The performance of developed estimation schemes was investigated by using MATLAB simulation and a plant emulator-based setup.

# ACKNOWLEDGMENT

I would like to express my gratitude to my supervisory team, Professor Volker Pickert, Dr David Atkinson, Dr Mohamed Dahidah and Dr Damian Giouris, for their invaluable knowledge and guidance through the process of this work. I would like to mention that designing and analysing different parts of software and hardware would not have been achievable without spending many hours a week with Dr Dave Atkinson.

I would also like to thank my family for being supportive over the course of this research, especially as I spent most of my time at university rather than home.

# TABLE OF CONTENTS

# List of Figures

# List of Tables

# PRINCIPAL NOMENCLATURE

| | |
|---|---|
| $L_m$ | Magnetizing Inductance |
| $\psi_m$ | Magnetizing Curve |
| $i_m$ | Magnetizing Current |
| $L_s$ | Stator Inductance |
| $L_r$ | Rotor Inductance |
| $L_{ls}$ | Stator Leakage Inductance |
| $L_{lr}$ | Rotor Leakage Inductance |
| $\lambda_{qr}^e$ | Quadrant axis of Rotor Flux in Flux Reference Frame |
| $v_{dr}^{e}$ | Direct axis of Rotor Voltage in Flux Reference Frame |
| $i_{ds}^e$ | Direct axis of Stator current |
| $i_{qs}^e$ | Quadrant axis of Stator current in Flux Reference Frame |
| $\tau_r$ | Rotor Time Constance in Induction Machine |
| $w_e$ | Speed of Synchronous Frame |
| $w_r$ | Rotor Speed |
| $w_{sl}$ | Slip Speed |
| $e_d$ | Flux Tracking Error in d-axis |
| $e_q$ | Flux Tracking Error in q-axis |
| $T_e^*$ | Reference Torque |
| $e_T$ | Torque Tracking Error |
| $\overline{\iota_{qs}^e}$ | Steady State value of quadrant axis of Stator current in Flux Reference Frame |
| $\overline{\iota_{ds}^e}$ | Steady State value of direct axis of Stator current in Flux Reference Frame |
| $P$ | Number of machines poles |
| $V_{sd}^{e*}$ | Direct axis of Stator voltage in Flux Reference Frame |
| $V_{sq}^{e*}$ | Quadrant axis of Stator voltage in Flux Reference Frame |
| $\mu_{pm}$ | Permeability of the PM |

| | |
|---|---|
| $\mu_0$ | Permeability of the air |
| $l_{core}$ | Total Length of flux paths |
| $\mu_{Fe}$ | Permeability of the Iron |
| $V_{dq}^s$ | Stator voltage in stationary frame |
| $\lambda_{dq}^s$ | Stator Flux in stationary frame |
| $L_\delta$ | Reluctance Component |
| $i_{dq}^{s*}$ | Complex conjugate of stator current |
| $\theta_e$ | Position of rotor flux in IPM (Flux angle) |
| $w_r$ | Mechanical Rotor speed in IPM |
| $w_e$ | Electrical Rotor Speed which is same with rotating speed of synchronous frame in IPM |
| $\psi_m$ | Rotor Flux |
| $L_d$ | D-axis stator Inductance |
| $L_q$ | Q-axis stator Inductance |
| $J$ | Rotor Inertia |
| B | Friction Coefficient |
| $T_L$ | Torque Load |
| $T_e$ | Electrical Torque |
| P | Number of machine poles |
| $i_f$ | Virtual Current Source |
| $L_{ms}$ | Stator mutual inductance in three phase ($\frac{2}{3}L_{ms} = L_m$ in complex plane) |
| $L_{ls}$ | Leankage Inductances |
| $\lambda_{\mathrm{as}}$ | a-Phase flux |
| $L_s$ | Stator inductance ( $L_s = \frac{3}{2}L_{ms} + L_{ls}$) |
| $w_{sl}$ | Slip speed |
| $\tau_r$ | Rotor time constant in induction machine |
| $\sigma$ | Leakage coefficient |
| $V_{Dc}$ | DC link voltage |
| $V_{max,s}$ | Maximum available voltage of inverter |
| $I_{max,s}$ | Rated machine current |
| $\theta_s$ | Stator Flux angle |

| | |
|---|---|
| $\widehat{\theta_s}$ | Estimated stator flux |
| $\widehat{\lambda_{dqs}^{s}}$ | Estimated stator flux |
| $f_e$ | Electrical frequency |
| $mi_{max}$ | Maximum modulation index in digital controller |

# List of Acronyms

| | |
|---|---|
| DC | Direct Current |
| AC | Alternating Current |
| PMSM | Permanent Magnet Synchronous Machine |
| BLDM | Brushless DC motor |
| IPM | Interior permanent magnet |
| SPM | Surface permanent magnet |
| RDC | Resolver to digital Converter |
| DTC | Direct Torque Control |
| FOC | Field oriented control |
| MRAS | Model Reference Adaptive System |
| EKF | Extended Kalman Filter |
| ICE | Internal Combustion Engine |
| IM | Induction machine |
| PI | Proportional and Integral |
| PI | Pulse Width Modulation |
| SVM | Space vector Modulation |
| GCB | General Control board |
| GD | Gate drive |
| mi | Modulation index |
| MTPA | Maximum torque per ampere |
| MPC | Maximum power control |
| FI | Flux increases |
| FD | Flux decreases |

| | |
|---|---|
| TD | Torque decreases |
| LPC | Low Pass Filter |
| TI | Torque increases |
| EV | Electric Vehicle |

# CHAPTER 1

# Introduction and Scope of the Thesis

## 1.1 Introduction

The invention of the internal combustion engine (ICE) in the 19$^{th}$ century increased the productivity of the manufacturing. However, its low efficiency, large size and audible noise led to electric machines becoming an alternative solution [1]. Of all the electric machines that were available, direct current (DC) machines were used in the early 20$^{th}$ century as the first generation of electric machines due to simple control arrangements. Development in power electronics and signal processing meant that alternating current (AC) machines, which require less maintenance and low cost, were eventually considered as a replacement for DC machines for many applications. Recently, even in the field of transportation, induction and permanent magnet machines, which were introduced as two common AC motors, were used as the main source of traction force for electric vehicle (EV) applications [2]. In traction applications, extracting more torque from electrical machines at certain operational speeds has long been a trend. This could be achieved by applying special control methods to extract more DC-link voltage across machine windings. This maximises the inverter output voltage which enables higher current levels at certain speeds.

In this chapter, a brief explanation of performance of traction motors and ICEs in different speed regions is provided. It also covers the reason why maximising inverter output voltage method is being used in traction applications. It then describes different pulse-width modulation (PWM) techniques and explains how the inverter output voltage is impacted when different modulation methods are applied. The chapter also explains which factors have more impact on selecting the modulation type in designing electric machine drive at engineering system-level. The overall scope and novelty of the thesis, followed by the thesis layout, are provided at the end of this chapter.

### 1.2 Performance of traction motors and ICEs in different speed regions

As shown in Fig. 1.1, the middle speed range is the optimum fuel efficiency performance area for ICEs. In this region, the consumed fuel (defined by unit of gram/kWh in Fig. 1.1) is approximately a quarter of low torque/low speed region where ICEs efficiency is minimal and they have relatively inferior performance. Therefore, selecting ICEs for automotive applications, with their stop and go driving profile, cannot be a preferred option. On the other hand, electric motors, which are able to produce high torque in a low-speed region (as shown in Fig. 1.1) and also capable of achieving high efficiency in middle and high-speed areas, is considered as an affordable and much better solution for automotive applications [3]. Furthermore, electric motors have been coupled with ICEs in hybrid electric vehicles (HEVs) in order to improve the overall efficiency of the power drive train system. In HEVs, the ICE is forced to operate in optimal conditions where the electric motor will cover the remaining operational points. Also the electric motor enables regenerative braking where the vehicle is operating in decelerating mode[4]. The reason for keeping ICEs in the system-loop in HEVs is that they could deliver sustainable power over long a period and also they require a short refuelling time [3].

As shown in Fig. 1.1, the low efficiency regions of ICE are marked by a shaded area. In these regions, an electric motor can be controlled in an efficient way to achieve maximum torque and power.

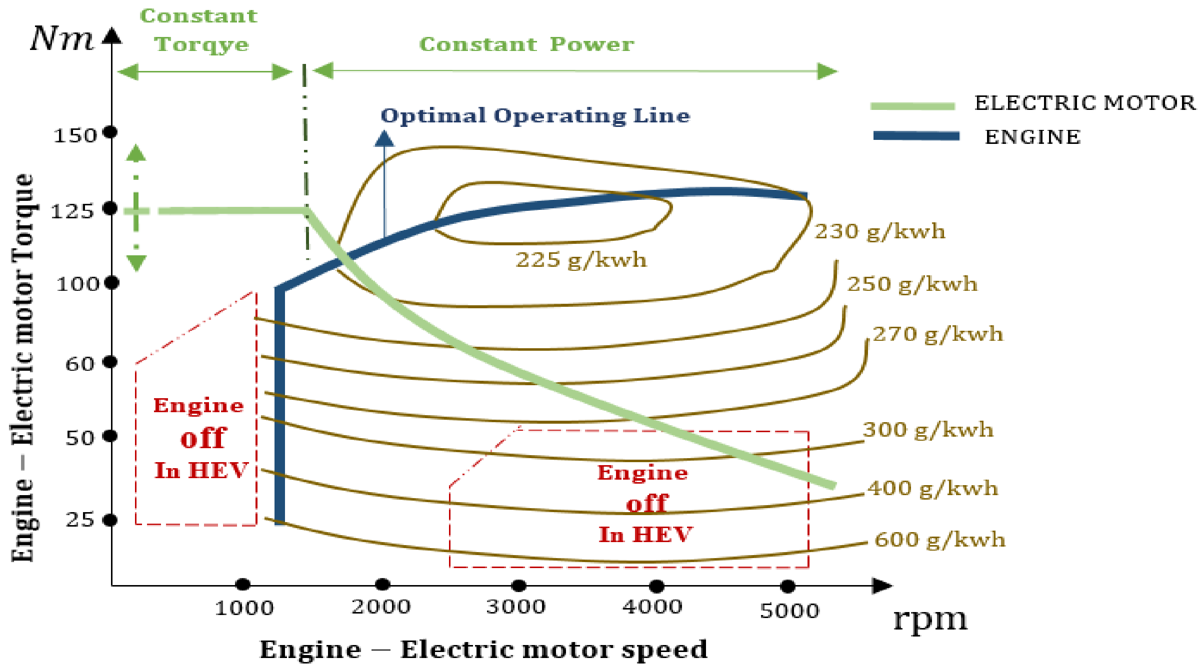


Fig. 1.1Operation of an ICE and an electric motor in low and middle speed range

In the low-speed region, the motor operates in the constant torque mode where utilised DC-link voltage is enough for the motor to compensate back-EMF terms. Therefore, the electric motor is able to produce the maximum torque even in a low-speed region. As speed increases further the required back-EMF voltage could not be satisfied by limited inverter output voltage. Therefore, the motor needs to be controlled in a constant power region by reducing flux where the maximum power can still be extracted [5].

Fig. 1.2 shows the key waveforms for the constant power region. Applying a larger inverter output voltage will increase torque and consequently the output power. Increasing the inverter output voltage can be achieved by applying several control techniques that allow more voltage to be extracted from DC-link voltage. Maximizing the DC-link voltage utilisation allows higher back-EMF to be achieved at each individual speed point [6]. This means that higher currents can be applied to the motor and consequently more torque could be produced. Having more torque and power allows the electric motor to accelerate more quickly. Furthermore, high-speed motors tend to smaller in build, offering cost, weight and size savings. Section 1.3 briefly explains how the output of inverter voltage could be modified by using different PWM techniques. This section also graphically illustrates the maximum achievable voltage for individual methods, and it compares the voltage modulation waveforms.

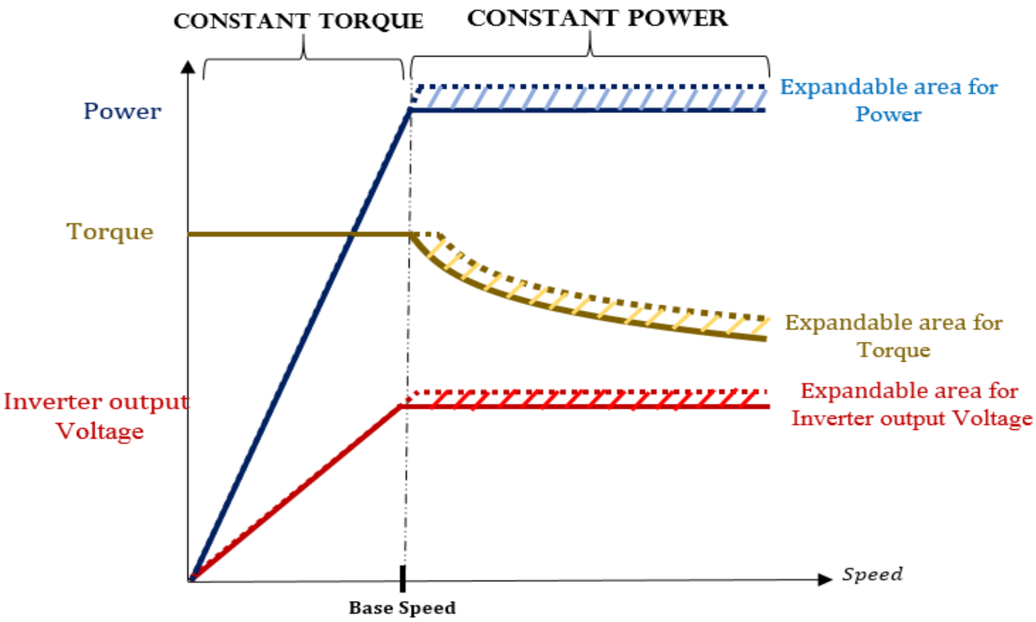


Fig. 1.2 Maximising the utilisation of inverter voltage impacts on output torque and the power of the electric motor

## 1.3 Inverter output voltage at different PWM techniques

The conventional three-phase voltage source inverter consists of six power switches. The two most widely used switching devices are IGBTs and power MOSFETs, which are suitable for high- and low-power applications respectively. The ratio of on and off duties for these switches can be adjusted by different PWM techniques, which will shape the required inverter output voltage. Different modulation techniques were explained in [7] and [8]; however, sinusoidal PWM, space vector modulation (SVM) and six-step modulation are considered to be the most common techniques in motor drives applications [9].

In sinusoidal PWM, three sinusoidal waveforms, which have a 120-degree phase shift between any two phases, are compared with triangular carrier wave in order to determine the turn-on signal of the high-side switches. Two common approaches for implementing sinusoidal modulation are bipolar and unipolar PWM methods, which exhibit different performance in terms of voltage harmonic distortion [10]. In both sinusoidal PWM techniques, the voltage utilisation is low and the rms-phase voltage can only achieve nearly 35% of the DC-link voltage. To increase the voltage utilisation, the space vector PWM technique is used where the third-order harmonic of fundamental signal is added into the control signal in order to reduce the peak of the control signal [11]. Therefore, more room is consequently

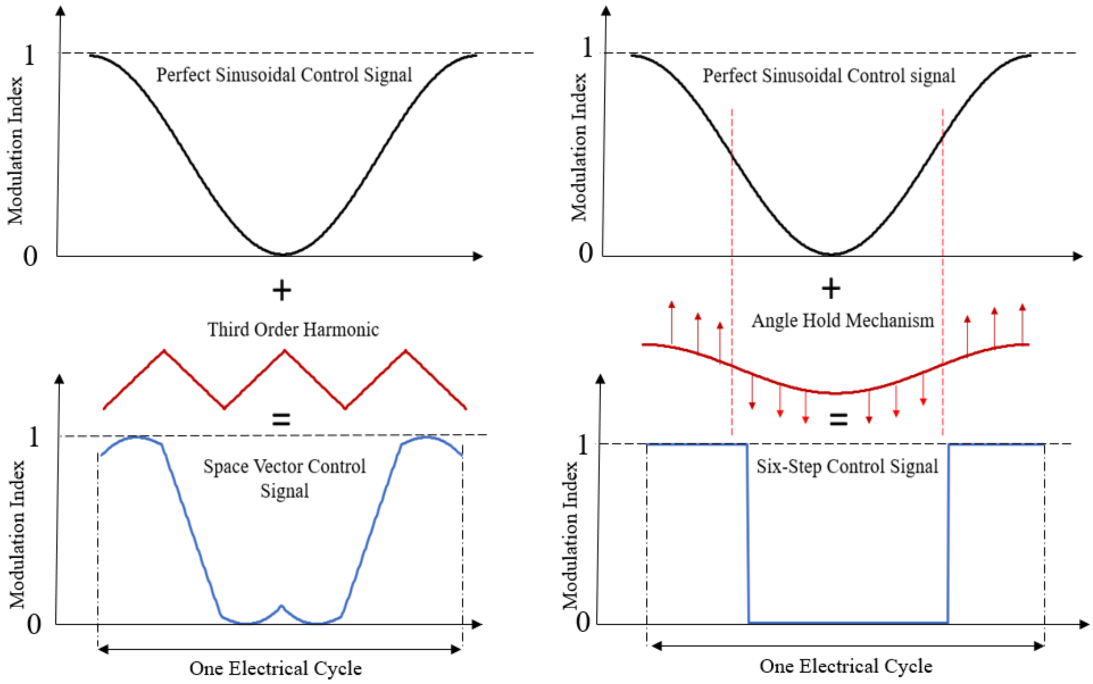


Fig. 1.3 Control signal waveforms in different PWM modulation techniques

provided for the control signal, which causes it to have a higher fundamental component. This has been demonstrated in Fig. 1.3 where the third order harmonic of the sinusoidal signal is added to control signal to produce the ‘’w’’ shape modulation index signal in SVM technique. The produced space vector control signal has higher average comparing with purely sinusoidal control signal. Therefore, more voltage can be extracted from DC-link voltage in SVM technique.

In a star-point connected motor, third-order line-to-line voltage harmonics are cancelled out due to having identical three phase currents shifted by 120 degrees. Therefore, the utilised voltage is increased to 41% of DC-link voltage without applying additional distortion. In this method, the stator voltage vector is created based on eight-inverter switching statues which are mapped into vertices of a hexagon as shown in Fig. 1.4. The time duration required by each vector to produce the desires stator voltage is then considered to calculate the duty ratio of each power switch. As can be seen in Fig. 1.4, the maximum voltage that can be utilised from DC-link voltage could be achieved if the stator voltage is kept in the corners of the hexagon. As demonstrated in Fig. 1.3, in order to keep the stator voltage vector in corner of the hexagonal voltage boundary, the maximum modulation signal is required. This is achieved by pushing the modulation signal from purely sinusoidal or SVM to one or zero depending on the stator voltage angle. Therefore, the modulation index signals can be purely square waveform which maximises the utilisation of DC-link voltage. This could be achieved by applying six-step modulation where the stator angle is held on these corners. This discontinued modulation method does not allow the voltage vector to move continuously around the hexagonal voltage boundary. [12] and [13] presented two most popular six-step modulation techniques and proposed a different angle hold mechanism. In six-step modulation method, the rms-phase voltage can reach to the maximum level of 47% of the DC-link voltage.

Section 1.3.1 explains how the modulation technique can impact on the whole electric machine drive system and highlights the consequences of having maximum voltage utilisation for the system-level engineering design.

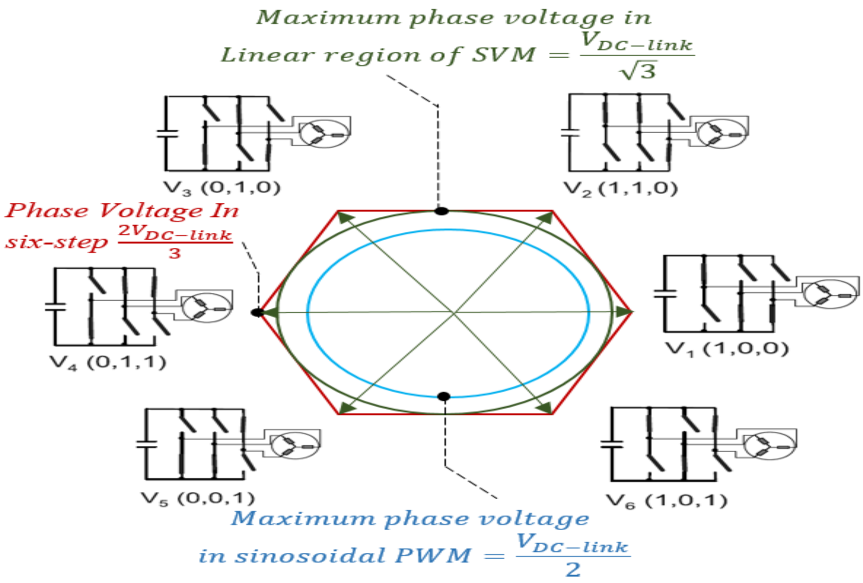


Fig. 1.4 Provided phase voltage in different PWM techniques

### 1.3.1 Electric machine drive system

Before deciding on the type of modulation technique needed for controlling power switches in the inverter, other parts of the electric drive system such as mechanical system, electric power converter and electrical machine, need to be carefully considered [2]. For instance, the produced voltage harmonics as a result of the type of the modulation method used can impact on all drive system parts. As an example in six-step modulation, the square waveform of phase voltage consists of third-, fifth- and seventh-order harmonics which consequently produce fifth- and seventh-order harmonics on the phase current [14]. The current harmonics' components then produce torque ripple in the electric machine which consequently leads to vibration and noise in the entire mechanical system [15, 16]. Furthermore, on the power electronics side, a higher value of bus-bar capacitors is required to deal with the introduced current harmonics. Despite capacitors current distortions also travel into the battery of an electric vehicle which will heat up battery cells and reduces their life-time. [17]. A shorter durability of battery and DC-link capacitors introduce economic and environmental issues which are the two main topics relating to engineering design of an electric drive system. Therefore, the modulation of the control signal needs to be controlled to make a trade-off between having an acceptable level of voltage utilisation and producing fewer voltage harmonic components It should be noticed that having more harmonic components in DC-link voltage and phase currents cause to have more torque ripples in power drive system. Therefore, maximising the voltage extraction from DC-link voltage without adding extra voltage or current harmonics is still an open challenge in electric machine drive system.

## 1.4 Scope and novelty of the thesis

The presented research proposes two novel control methods which push the stator voltage to reach the hexagonal voltage boundary in a field-weakening region increasing output torque and power of an electric machine. This is achieved by designing the d-axis of the stator current by using a mathematical model of the electric machine and implementing a closed-loop stator voltage mechanism. Particular attention is given to a smooth transition between the constant torque region and field-weakening region. This research also proposes a novel on-line estimation technique for both rotor resistance and mutual inductance of the induction machine. Accuracy of their values is required to have reliable control for high-power rate induction machines which have significant variation on magnetising current in field-weakening region. The important scientific contributions from the research in this thesis can be briefly summarised as:

1- A novel model-based control method calculating the flux-producing current based on hexagonal voltage boundary in field-weakening region is developed. Unlike the conventional model-based control technique, the new scheme proposes a novel voltage constraint trajectory in model-based control of electric drives, which consequently expands the torque-speed envelope of induction motors (IM). The proposed method not only realises the starting of a field-weakening region without calculating the base speed, but also matches the staring currents of the field-weakening region with the constant torque region. This provides the smooth transition of current in the different operational regions.

2- A novel closed loop stator voltage scheme is proposed which, unlike existing closed loop voltage methods, increases the voltage utilisation of DC-link voltage from the inscribed circle voltage to the hexagonal voltage limitation in the field-weakening region. The proposed method generates an accurate voltage reference based on the stator voltage angle and aims to reduce the fake voltage extension and q-axis current ripple seen when using other voltage control approaches. In addition, a mathematical model of the closed-loop voltage control scheme is developed, which reduces the step reduction in the d-axis current without the need for additional regulators.

3- A novel motor parameters estimation method is developed for online estimation of rotor resistance and magnetising inductance. In this proposed method, the Kalman Filter (KF) estimator is combined with a model reference adaptive system (MRAS) to improve the flux estimation mechanism. The accurate estimated flux uses a mathematical model to calculate the two main aforementioned IM parameters at the same time. A developed version of Extended KF based on new augmented states is also addressed in this research. This version produces the accurate Jacobean matrix which consequently improves the accuracy of estimation results in IM parameters estimation.

## 1.5 List of Publications

The research findings proposed in this thesis have been published and submitted to the following international conferences and journal:

- H. Gashtil, M. Kimabeigi, J. Goss, and S. Roggia, “Modelling an Interior Permanent Magnet Traction Motor Based on Current Signals Produced in a Space Vector Modulation, ” in *2018 XIII International Conference on Electrical Machines (ICEM)*, 2018, pp. 833-839, [18].
- H. Gashtil, V. Pickert, D. Atkinson, D. Giaouris, and M. Dahidah, “A Case Study of Real Time Implementation of Extended Kalman Filter in Dual Core DSP for The On-line Estimation of Induction Machine Parameters, ” in *2019 IEEE 13th International Conference on Compatibility, Power Electronics and Power Engineering (CPE-POWERENG)*, 2019, pp. 1-7, [19].
- H. Gashtil, V. Pickert, D. Atkinson, D. Giaouris, and M. Dahidah, "Comparative Evaluation of Field Oriented Control and Direct Torque Control Methodologies in Field Weakening Regions for Interior Permanent Magnet Machines ," in *2019 IEEE 13th International Conference on Compatibility, Power Electronics and Power Engineering (CPE-POWERENG)*, 2019, pp. 1-6, [20].
- H. Gashtil, V. Pickert, D. Atkinson, D. Giaouris, and M. Dahidah, " On-line Estimation of Magnetizing Inductance and Rotor Resistance in Extended Kalman-Filter for Induction Machines," in *2019 IEEE 2nd International Conference on Electrical Engineering and Computer Science (EECS)*, 2018, pp.282-588 [21].
- H. Gashtil, M. Dahidah, V. Pickert, D. Atkinson and D. Giaouris, " Improved Voltage Boundary with Model-Based Control Algorithm for Increased Torque in Field Weakening Region of Induction Machines," Accepted in IEEE Transaction on Transportation Electrification.

- H. Gashtil, D. Atkinson, V. Pickert, M. Dahidah and D. Giaouris, " Closed-Loop Voltage Control for Maximizing Inverter Output Voltage in the Field Weakening Region of Induction Machines," In review process for IEEE Transactions on Power Electronics.

- H. Gashtil, D. Atkinson, V. Pickert, M. Dahidah and D. Giaouris, " On-line Estimation of Rotor Resistance and Magnetizing Inductance with Combining Kalman Filter Algorithm and Model Reference Adaptive System for Induction Motor Drives ," Submitted to IET Control Theory & Applications.

**1.6 Overview of thesis**

The eight chapters of this thesis are organised as follow:

Chapter 1 gives a brief explanation about performance of electrical motors and ICEs in different speed regions. This chapter covers the importance of enlarging torque speed curve in electric machines by applying proper modulation techniques. The list of scientific contributions and publications during the course of this research is also included in this chapter.

Chapter 2 provides a comprehensive literature review for controlling electrical machines in the field-weakening region based on current control algorithms. For these methods, the desired flux and torque producing currents are developed by having closed loop stator voltage mechanism, mathematical modelling of an electric motor, speed loop configuration and look-up tables. Following on from the literature review, attention is focused on closed-loop stator voltage and mathematical modelling algorithms. In this chapter, different motor parameters determination methods are also reviewed, and attention is given to online estimation algorithm where the estimated motor parameters can be used in up-coming control cycles.

Chapter 3 describes the mathematical modelling of an induction and permanent magnet machine. This chapter also explains mathematically the principle of different control algorithms such as variable voltage variable frequency (VVVF), direct torque control (DTC) and field-oriented control (FOC). The mathematical derivation of Kalman-filter and model reference adaptive system as the two main estimation techniques are also provided in this chapter.

Chapter 4 gives the detailed explanation about different test set-ups used to validate the performance of proposed control methods. The main test rig set-up has a 2.2 KW induction machine which is controlled by four-leg IGBT-based inverter. This test set-up is used to verify the voltage control algorithms in the field weakening region. To validate the performance of the online estimation method, a dual core experimenter kit, which performs as a real-time plant emulator, is then utilised.

Chapter 5 describes the new model-based voltage scheme used for controlling an IM in the field-weakening region. In this method, the novel voltage trajectory is defined to calculated flux and torque producing currents. This allows the electric motor to produce higher torque and power in the field-weakening region. The smooth transition from constant torque to field weakening region without applying extra regulators or base speed calculation is also addressed in this chapter. The performance of the proposed method is compared against the conventional model-based control in Simulink and an experimental test rig.

Chapter 6 presents the new closed loop voltage control scheme for the field-weakening region of IM. In this method, the reference stator voltage based on hexagonal voltage boundary and stator voltage angle is developed for creating flux-producing current. This chapter also provides the comprehensive analysis of stator voltage vector performance in field-weakening regions when inverter voltage is maximised. The proposed scheme is then validated and tested by using Simulink and test bench set-up. Furthermore, the proposed method is compared with conventional and active timing voltage control methods in the field-weakening region.

Chapter 7 gives a full description of a novel parameter estimation algorithm where a Kalman-filter algorithm is combined with a model reference adaptive system to improve the accuracy of estimated parameters. This chapter also develops an extended Kalman-filter algorithm, which is based on a new Jacobian matrix, to estimate magnetising inductance and rotor resistance of IM. The performance of the developed estimation algorithm is then verified and tested in an experimenter control kit and simulation.

Chapter 8 provides the overall conclusions of the thesis and it recommends future works.

# CHAPTER 2

# Motor Control Schemes for Field Weakening - A Literature Review

## 2.1 Introduction

Extracting the maximum torque from an induction machine (IM) over the entire speed range is of prime importance for many applications such as traction drives [22]. This is particularly true when operating in the field-weakening (FW) region where a high flux within a high-speed region is important to produce the optimum torque. However, high flux levels in the high speed region produce a large back electromagnetic force (EMF) which cannot be supported by the inverter output voltage [23]. Therefore, the design of a suitable reference flux signal, which produces the maximum torque in accordance with the available DC-link voltage $V_{DC}$, has become a research trend in traction drive applications. A suitable control of reference flux in an IM can be achieved by designing an optimum flux producing current $i_{ds}^{e*}$. The desired $i_{ds}^{e*}$needs to be produced within the control system, which must fulfil the following merits: low computation process, simple implementation, robustness to parameter variation and adaptiveness for IMs with different power rates. In this chapter, a review of the different control methods for producing $i_{ds}^{e*}$ in IM electric drives is provided. The main focus is given to model-based control methods and voltage regulation methods, the problems associated with these control strategies and the suggested solutions, which are proposed on Chapter 5 and Chapter 6.

In this chapter, a review of the different motor parameter estimation techniques is also provided. The main focus is given to the estimation of rotor resistance and magnetising inductance as they need to be accurate to guarantee the alignment of the field-oriented method.

## 2.2 Closed loop current-based control

All current-based control methods share a common feature, which is that the desired flux and torque are produced by controlling the d and q axes of stator currents. Generating the flux-producing current is always challenging, especially during high-speed operations where the voltage is limited by the inverter [24]. Fig. 2.1 shows four control methods that generate the reference flux in the field-weakening region of a conventional IM drive (Method A to Method D). All four methods produce the command for the flux-producing current ($i_{ds}^{e*}$), which determines the reference flux, and each method establishes $i_{ds}^{e*}$ analytically differently based on the considered control parameter.

### *2.2.1 $\frac{1}{\omega_r}$ based control method*

In Method A, the d-axis rotor flux ($\lambda_{dr}^{e}$) in the rotor-flux-oriented (RFO) frame is used as the control parameter. Often, the command d-axis flux ( $\lambda_{dr}^{e*}$) is based on the inverse value of the rotor speed ($\omega_r$) in the field-weakening region for conventional IM drives [25]. However, the maximum torque capability of the machine cannot be attained because the accessible inverter voltage is not utilised. On the other hand, an improvement of torque in the FW region can be achieved by employing the stator-field-oriented (SFO) scheme, where the stator flux is changing proportionally to the inverse of $\omega_r$ [26]. However, the derived desired current in SFO cannot be delivered at higher-speed operation again due to the limited inverter voltage. Therefore, the stator current is forced to drop to ensure that the reference voltage does not exceed the normal space vector modulation (SVM) voltage region. This reduction in current leads to a corresponding reduction in motor torque.

### *2.2.2 Closed-loop stator voltage control*

To compensate for the voltage limitation, a voltage detection method is proposed in Method B. In this method, $i_{ds}^{e*}$ is generated by comparing the maximum available voltage in SVM and the magnitude of the synchronous voltage vector. As shown in Fig. 2.2, this method can be categorised in four main groups called Group A, B, C and D. The key difference between Group A to D is the maximum voltage available from the inverter for a given voltage modulation level. In Group A, the inscribed voltage circle is within the hexagonal voltage boundary (black hexagons in Fig. 2.2), which is considered as maximum

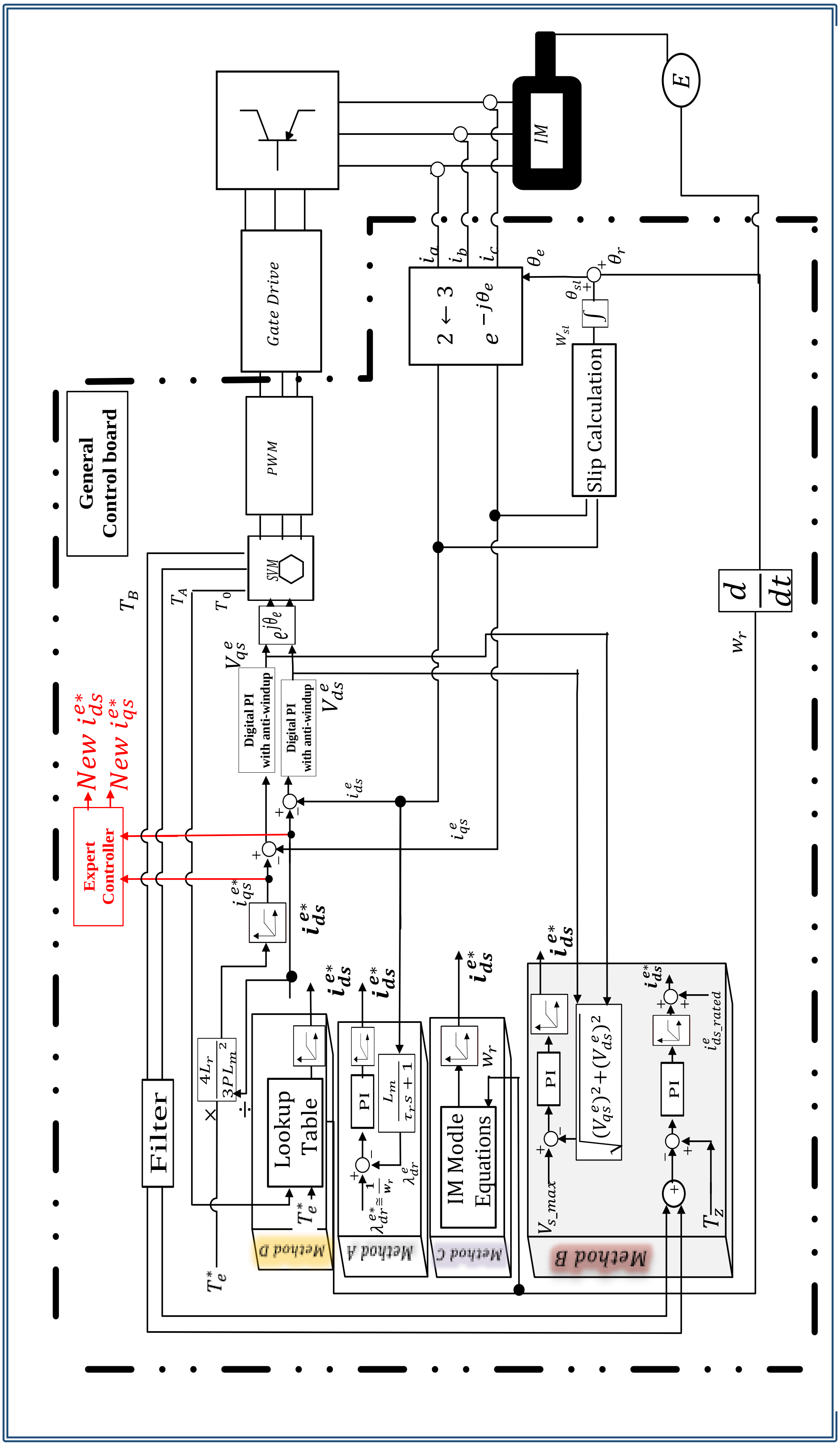


Fig. 2. 1Block diagram for producing $i_{ds}^{e*}$ in the field-weakening region by applying $\frac{1}{w_r}$ algorithm (Method A), voltage detection algorithm (Method B), model-based algorithm (Method C) and look-up table (Method D)

reference voltage [27]. Using a base voltage of $V_{DC}$, the p.u. value of the inscribed circle (red line in Group A of Fig. 2.2) is 0.5774. The available inverter voltage based on the Group A method is relatively low; however, there is no torque ripple as the modulations signals remain sinusoidal.

### *2.2.2.1 Closed-loop stator voltage control based on extended reference voltage*

To extract more inverter voltage at the cost of higher low-order harmonics, a nonlinear modulation is used in Group B allowing the reference vector to extend beyond the inscribed circle [28, 29]. In this group, the radius of the reference voltage circle can be increased beyond 0.5774 to 0.6665 p.u. As shown in Group B in Fig. 2.2, the parts of the extended circle which are inside the hexagonal boundary improve the inverter voltage utilisation. However, the parts that are outside the hexagonal voltage boundary are a fake extension, which increases the torque ripples. This is because the difference between the circular reference voltage and stator voltage amplitude ($\sqrt{V_{ds}^{s\,2} + V_{qs}^{s\,2}}$) is larger than zero. This means that the d-axis of the stator voltage becomes higher in the limited inverter voltage region which causes a natural

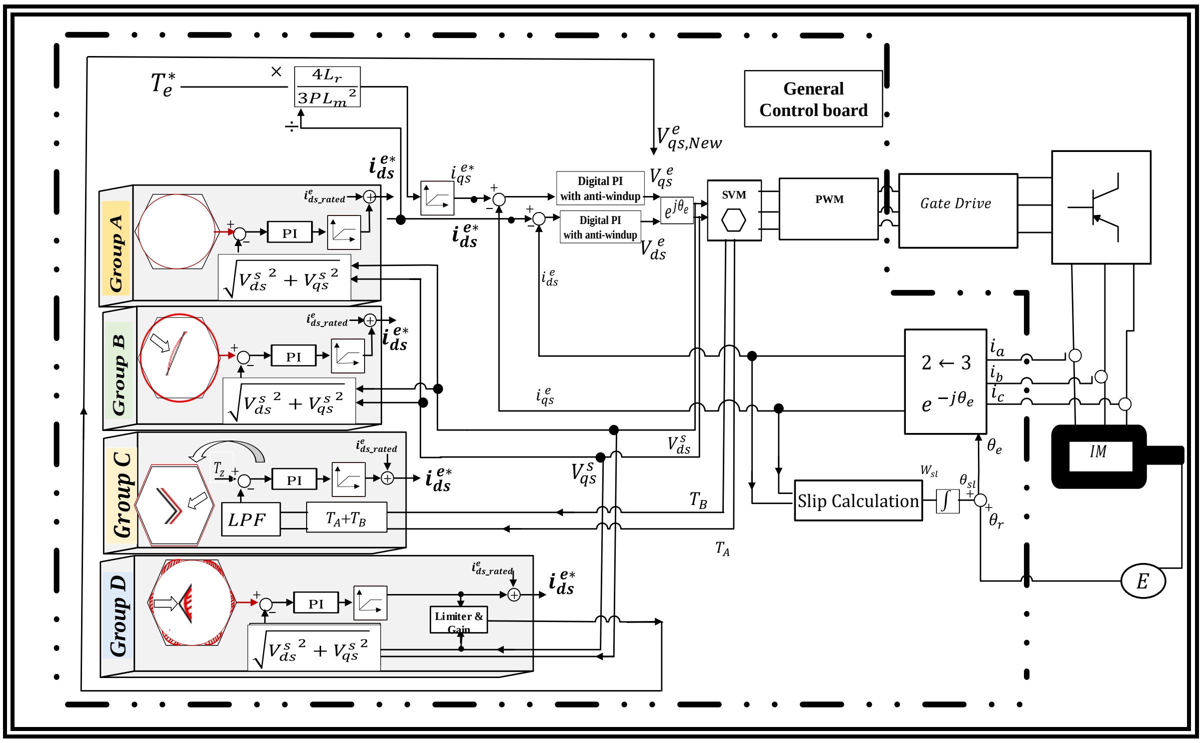


Fig. 2.2 Block diagram for producing $i_{ds}^{e*}$ based on Method B. (Group A) inscribed voltage circle as the reference signal, (Group B) extended voltage circle placed in the outside of the inscribed voltage circle as the reference signal, (Group C) switching time period as the refference signal, (Group D) optimum incribed voltage circle as the refference signal.

drop in the q-axis stator current. In addition the current starts oscillating and the oscillation in the q-axis of the stator current increases the torque ripples.

#### *2.2.2.2 Closed-loop stator voltage control based on controlling the active timing*

The fake voltage extension regions [30, 31], explained in the section above (Group B), are reduced by the method proposed in Group C, where the active switching times $T_A, T_B$ and the switching period $T_z$ are considered as the control parameters [30, 31]. As the null switching time $T_0$ is inversely proportional to the reference vector amplitude, the reference vector that follows a hexagonal trajectory is guaranteed to produce $T_0$ equal to zero. Therefore, the inverter output voltage is increased to 0.6311 p.u. when it is normalised by the base voltage $V_{DC}$. As shown in Fig. 2.2, Group C uses a low-pass filter (LPF) after summation of $T_A, T_B$ resulting in a magnitude reduction. So, flux weakening occurs when the hexagonal voltage boundary is exceeded. This causes the fake hexagonal stator voltage to be achieved (the red hexagon in Group C of Fig. 2.2), which results in passing the d-q axis of stator voltage margins and consequently forces the stator currents to drop resulting in increased torque ripple [32]. This also causes $i_{ds}^{e*}$ to be poorly controlled in the transition period from the constant torque (CT) region to the field-weakening (FW) region as it sees a large step reduction in the current. It should be noticed that the use of LPFs limits the bandwidth of the system's dynamic response, which is not desirable for very high-speed operation. Furthermore, the determination of the PI controller gains for the outer closed loop is based on trial and error, which will not guarantee the stability and high performance of the system. In this method, the transition from the field-weakening regions is also sensitive to motor parameters, which degrade the reliability of the control system. Therefore, the proposed method in chapter 6 is developed to address the mathematical based calculation of closed loop PI gains and provide smooth transition between different operational regions.

#### *2.2.2.3 Closed-loop stator voltage control based on modified stator voltage*

To improve the transient performance and minimize the torque ripple in the FW region, a method which modifies the q-axis of stator voltage is described by [32]. As shown in Group D of Fig. 2.2, the adjusted q-axis of stator voltage $v_{qs,New}^{e}$ is developed to satisfy and limit the adjustable circular reference voltage (red circles in Group D) within the hexagonal voltage boundary. By keeping the reference voltage inside the voltage boundary, the dynamic performance of the current controller improves and consequently the torque ripple is reduced [33, 34]. However, the maximum hexagonal inverter voltage cannot be extracted in this method.

### *2.2.3 Model-based control*

In Method C, voltage and current equations of the IM are derived in the synchronous frame to define $i_{ds}^{e*}$ [35, 36]. The model requires voltage and current limitations to satisfy the constraints at any specific speed [33, 37]. In addition, the model reflects acceleration and deceleration performance. Consequently, a flux controller based on the machine model is required in order to produce the desired $i_{ds}^{e*}$ during fast acceleration and deceleration of the motor [38, 39]. Furthermore, as a result of calculating $i_{ds}^{e*}$ based on the machine model, this method is sensitive to the magnetising inductance ($L_m$) [36, 40]. This however is true as long as the variation of the magnetising current ($i_m$) is high in the FW region [41]. Therefore, a lookup table of $L_m$ based on $i_m$ must be used, otherwise variations of $L_m$ can be neglected in Method C. A limitation of Method C is that the stator voltage vector is constrained to lie inside the inscribed voltage circle within the hexagonal voltage boundary and therefore the maximum output voltage is not available [5, 42].

### *2.2.4 Look-up table-based method*

Method D acquires $i_{ds}^{e*}$ from a look-up table. The reference torque signal $T_e^*$, which is based on the $w_r$, and the null switching time $T_0$ of SVM are the key indexes for determining the reference current value [43]. Using this method retains the maximum torque regardless of variation of $V_{DC}$ [31]. However, developing the efficient look-up table requires the use of high-precision measurement devices. In addition, a long time period of experimental tests is required to generate the data for the table.

## 2.3 Improving current controllers' performance and reducing torque ripples in closed-loop current based control methods

Fig. 2.1 also shows expert controllers which have recently been researched. These expert controllers

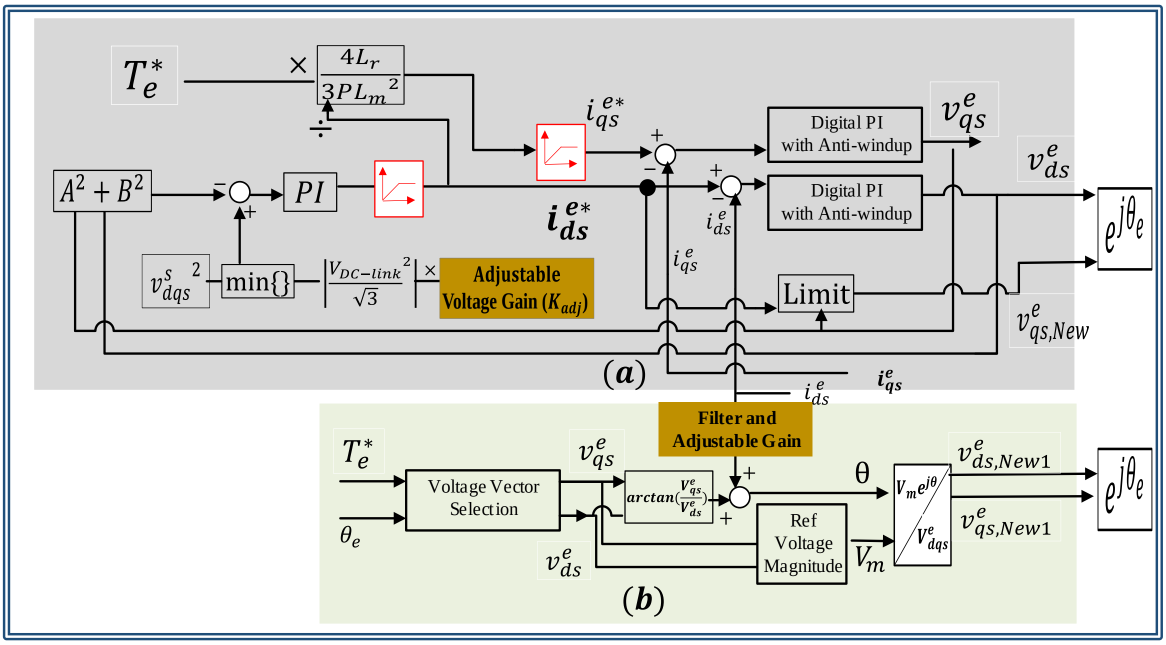


Fig. 2.1 Reducing the torque ripple in the maximum torque region (a) modification of voltage vector in current-based controller and (b) designing the voltage reference without current controllers

can be added to all four methods and are placed before the current regulators to avoid the fast tuning of reference current, especially for high fundamental frequency performance [5]. Furthermore, conventional expert controllers are enhanced by implementing the fuzzy interface in the case of tuning failure [44]. These expert controllers expand the stability of the responses for PI current controllers but do not improve the utilisation of $V_{DC}$. All four methods described above try to extend the voltage in the field-weakening region by applying the optimum command for $i_{ds}^{e*}$ so that higher output torques can be achieved. However, operating drives in voltage extension regions causes increased torque ripple [45]. Consequently despite improving PI-controller performance due to expert controllers, research in minimising torque ripple in the field-weakening region has also been conducted and the two most common techniques are shown in Fig. 2.3. In [32], alterations in q-axis of stator voltage $v_{qs}^e$ help to improve the dynamic performance of the current controller, which in turn reduces the torque ripple. An adjusted q-axis of stator voltage $v_{qs,New}^e$ is limited to satisfy the adjustable reference voltage, $K_{adj}\frac{V_{DC}}{\sqrt{3}}$. In this way, the ordinary, $v_{qs}^e$ , which is generated by the torque controller, is not directly used in SVM (Fig. 2.3a). In [33], the torque control is based on the voltage angle method which, improves the torque ripple. As shown in Fig. 2.3b, the $v_{dqs}^e$ is obtained from the intersection of the hexagon boundary and torque equation, derived in terms of d-q axis voltage. The placement of the hexagonal voltage boundary depends on the electrical rotor position $\theta_e$ as the voltage boundary rotates in a synchronous frame. In this method, the voltage angle $arctan\frac{v_{qs}^e}{v_{ds}^e}$ is determined from the intersection of the voltage limitation contour and the command torque curve $T_e^*$. The reason for adding the adjusted $i_{ds}^e$ term to determine $arctan\frac{v_{qs}^e}{v_{ds}^e}$ is improve the stability of the control structure which results in reduced torque ripple. Therefore, the desired voltage signals $v_{dqs,New1}^e$ are produced without using the current controllers. The dark yellow boxes in Fig. 2.3a and b are the additional adjustable regulators, which are defined as part of the control method.

## 2.4 Summary of overview

From all of the aforementioned publications, it can be realised that the IM can be controlled by the d-axis current in the FW region. As shown in Fig. 2.1 and Fig. 2.2, the inverter voltage utilisation in field weakening region can be controlled by d-axis current. By comparing all of the listed control algorithms, the model-based control method and closed-loop stator voltage control (Method B and C in Fig. 2.1) can be considered as efficient techniques for controlling IM in the FW region. Method B is seen as efficient in terms of having less parameters sensitivity, greater ease of implementation and good performance in the entire speed operation. Method C shows fewer regulators compared to Method A, Method B and torque-ripple-reducing methods, as shown in Fig. 2.3, where all require at least one extra regulator. A smaller number of regulators for developing $i_{ds}^{e*}$ makes tuning IM drives much easier and more user-friendly, especially in practical tests. Although the required number of regulators is the same in both Method C and Method D, however, Method D requires additional experimental tests for extracting an accurate look-up table. These tests are time-consuming and they require sensors with high accuracy.

So far the control algorithm in Method C relies on the description of the inscribed voltage circle constraint that lies within the hexagonal voltage boundary. As the full hexagonal voltage boundary is never reached, the torque in the field-weakening region is limited. In Chapter 5, a proposed model-based control algorithm is introduced to maximise the voltage utilisation of the inverter resulting in

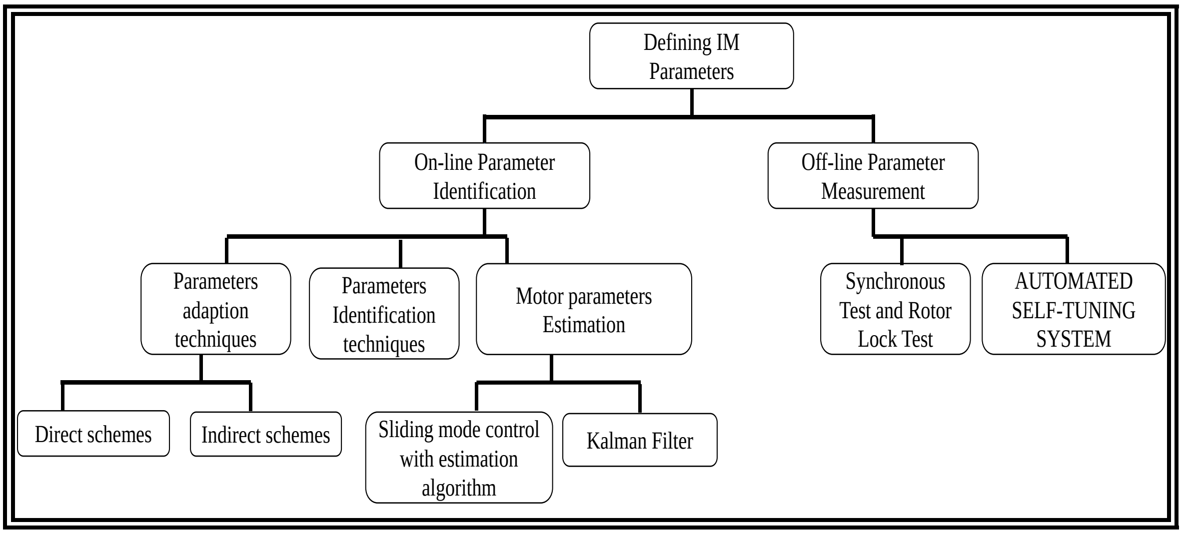


Fig. 2.4 Defining IM Parameters

higher torque and power in the field-weakening region. In addition, a proposed closed-loop stator voltage control is introduced in Chapter 6 to extract the whole hexagonal voltage boundary in the field-weakening region without producing a fake voltage extension the in d-axis current.

Although aforementioned sections explain current-based control methods for IM drives in the FW region, an accurate slip calculation still needs to be addressed in order to improve the controlled system performance. The accurate slip calculation could not be achieved without accessing an accurate value of rotor resistance and magnetising inductances, which change widely with frequency, temperature and applied current amplitude [46, 47]. In addition to slip calculation, the accurate value of magnetising inductance is also required in EV applications where the torque-producing current is calculated from torque demand [48, 49].

### 2.5 Motor parameters estimation

As shown in Fig. 2.4, the online parameter identification and offline parameter measurement are the two main solutions used to extract the motor parameters [50]. During offline measurement, the stator and rotor parameters are calculated by using power analyser both when the IM operates at synchronous speed and when the rotor is locked [51]. Locking the rotor requires the shaft of the motor to be to mechanically fixed either by using a bespoke fixture or by controlling the load dynamometer [52]. An automated self-tuning system is an alternative solution which has less dependency on equipment such as a power analyser and mechanical load [50]. Also, synchronous testing is unable to determine the motor parameters prior to start-up of the motor drive. In an automated self-tuning system, the accuracy of the measured rotor time constant depends on the voltage sensor which measures voltage transients. As such automated self-tuning relies on high-bandwidth voltage transducers. Rotor and stator parameters cannot be dynamically compensated during motor operation.

Therefore, online parameters identification methods are proposed to overcome the weakness of the offline estimation methods, especially during the dynamic performance of the motor [41]. As shown in Fig. 2.4, online parameter identification can be divided into parameter adaption, parameter identification and motor parameter estimation. Parameter adaptions techniques can be further divided into direct and indirect schemes [53]. Direct adaption methods use signal injection, which suffers from parameter dependency and requires additional transducers [54]. In the indirect scheme, the parameters such as reactive power or airgap power are measured and tracked and the difference with its command value is used to compensate the adapted motor parameters. The most important adapted parameter in indirect identification techniques for IM is the rotor time constant where the adapted rotor time constant varies until the flux achieves the wanted orientation [46]. It should be noticed that the algorithms based on model reference adaptive system (MRAS) are also placed within the indirect techniques [55, 56]. It is well known that the different functional candidate such as stator voltage or rotor flux are utilised in various MRAS algorithms to guarantee the orientation. However, the accurate orientation in MRAS-based methods is achieved when the actual magnetising inductances are applied [57].

Motor parameter identification is the other online parameter determination method. In this method, the separate identifiers are utilised for motor inductances and resistances. These identifies consist of analysing the harmonics vectors in stator voltage and current to calculate the reactive power. The selection of reactive power is due to its robustness against the variation of the stator and rotor resistance. This extraction of harmonic components from voltage and current signal requires a digital filter, which degrades the dynamic performance of the system's high-speed operation [58].

To eliminate degradation of the system performance as a result of identification techniques, the online estimation of motor parameters is used. One of the well-known techniques in this sub-group is the

Kalman filter (KF), where the stochastic state space model is solved by applying the Gaussian distribution to estimate the states of IM. In [59], the extended Kalman filter (EKF) presents the online estimation of rotor resistance. However, the derivation of magnetising inductance has not been considered, which causes inaccurate estimation in rotor resistance. Therefore, EKF which considers the estimation of magnetising inductance and rotor resistance, has been developed in [60], [61]and [62]. The minimal selected sample, instead of single-point linearisation of the nonlinear system, applied in EKF, is also used to improve the processing time in the unscented Kalman filter (UKF) [63]. Designing the state observers by helping the high-order-sliding-mode control (HOSM) and applying the parameter estimation techniques is an alternative estimation method [64].

Although motor parameters identification based on the estimation methods provide more precise dynamic results in term of motor parameters estimation, so far there are few papers that address the online estimation of both magnetising inductances and rotor resistance at the same time [57]. In [65] a so-called passive design is implemented to estimate motor parameters; however, its performance depends on the current controllers. This means that the proposed scheme is not considered an effective method for parameter estimation.

From all of the aforementioned publications in Section 2.4, it can be concluded that the accuracy of motor parameter estimation impacts on the dynamic performance of IM drives. Moreover, the EKF and MRAS are considered as two main identification techniques that can improve the drive system performance and increase system robustness. However, the EKF method was only applied to correctly estimate one of the motor parameters, and MRAS method was mostly used as a speed estimator. Therefore, a new EFK and combined KF and MRAS estimators are introduced in Chapter 7 to provide a more accurate and robust estimation of rotor resistance and magnetising inductance.

## 2.6 Summary

In this chapter a review of different control algorithms used for creating the flux-producing current in IM for FW region has been provided. This review focuses on the closed-loop current-based methods and provides a description of the weaknesses of each individual scheme. It appears that, despite all attempts to improve the IM performance in the FW region, finding a control algorithm that can utilise the whole hexagonal voltage without applying additional regulators or extending the fake voltage is still challenging and needs more investigation. The proposed method described later operates in such a way that it will overcome the drawbacks listed.

Also, this chapter presents various parameter identification methods, which play an important role in IM drives application. It appears that, despite all the IM parameter identification improvements, finding an estimation method that can accurately estimate the rotor resistance and magnetising inductance in different operating conditions and a limited processing time environment is still challenging. Therefore, a novel proposed estimation method that makes it more suitable for IM drives is proposed in this research work.

# CHAPTER 3

# Dynamic Model and Control of Induction Motor for Traction Applications

### 3.1 Introduction

IMs are affordable alternating current (AC) machines that do not need to have any permanent magnets, brushes or commutators [66]. Thus, IMs are applicable for high-temperature applications and are robust to mechanical shock and vibration [67]. Therefore, IMs are widely used in high-performance applications such as traction drives and elevators [68]. The high dynamic operation in torque or speed drives can be achieved by employing proper control methods operating on fast microcontrollers. Designing such control methods requires an accurate model of IM [6].

In this chapter, the background research on a number of topics relating to the project is presented. The given context in this chapter provides the initial materials for the novel concepts presented later. The starting point of the chapter explains the mathematical modelling of IM. Then, the machine model is used to develop the control principle of different motor control techniques such as variable voltage variable frequency (VVVF), indirect field-oriented control (IFOC) and direct torque control (DTC). Finally, the model reference adaptive system (MRAS) and Kalman filter (KF) are described as the two main methods for estimating the motor states and parameters.

### 3.2 Mathematical modelling of the induction machine

The performance of the IM can be analysed by developing the equivalent circuit of the IM as shown in Fig 3.1. Based on the equivalent circuit of the IM, which contains the stator and rotor circuits, two equations can be derived as follows:

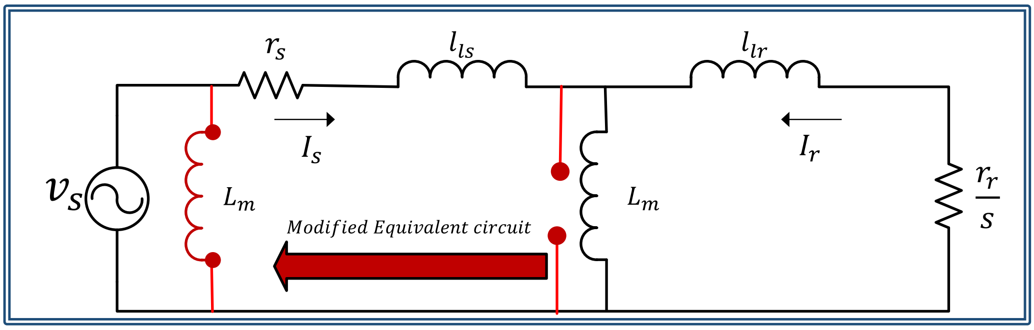


Fig. 3.1 Steady-state per-phase equivalent circuit of an IM

$$\boldsymbol{v_s} = (r_s + j\omega_e L_{ls})\boldsymbol{I}_s + j\omega_e L_m(\boldsymbol{I}_s + \boldsymbol{I}_r) \tag{3.1}$$

$$0 = (\frac{r_r}{s} + j\omega_e L_{lr})\boldsymbol{I}_r + j\omega_e L_m(\boldsymbol{I}_s + \boldsymbol{I}_r) \tag{3.2}$$

where $\boldsymbol{v}_s$, $\boldsymbol{I}_s$ and $\boldsymbol{I}_r$ are stator voltage phasor, stator and rotor current phasors, respectively. In (3.2), the normalised speed difference between the rotor shaft $\omega_r$ and electrical speed $\omega_e$ for the $P$-pole machine is defined by the slip:

$$s = \frac{\omega_e - (P/2)\omega_r}{\omega_e} \tag{3.3}$$

By substituting (3.3) in (3.2), the rotor equation can be rewritten as:

$$0 = (r_r + j(\omega_e - (P/2)\omega_r)L_{lr})\boldsymbol{I_r} + j(\omega_e - (P/2)\omega_r)L_m(\boldsymbol{I_s} + \boldsymbol{I_r}) \tag{3.4}$$

As can be realised from (3.4), the slip speed $\omega_e - (P/2)\omega_r$ governs the rotor circuit. It also plays the key role of producing the power transferred from the stator circuit to the rotor circuit through the airgap. The airgap power $P_{ag}$ can be calculated with:

$$P_{ag} = 3\boldsymbol{I}_r{}^2 r_r \frac{1}{s} = 3\boldsymbol{I}_r{}^2 r_r + 3\boldsymbol{I}_r{}^2 r_r \frac{1-s}{s} \tag{3.5}$$

In (3.5), $3\boldsymbol{I}_r{}^2 r_r$ and $3\boldsymbol{I}_r{}^2 r_r \frac{1-s}{s}$ are defined as rotor copper loss $P_{copper\_loss}$ and mechanical power $P_m$ respectively. Therefore, the mechanical power loss can be used to derive the electrical torque in IM as follows:

$$T_e = \frac{P_m}{\omega_r} = 3\boldsymbol{I}_r{}^2 r_r \frac{1-s}{s\omega_r} \tag{3.6}$$

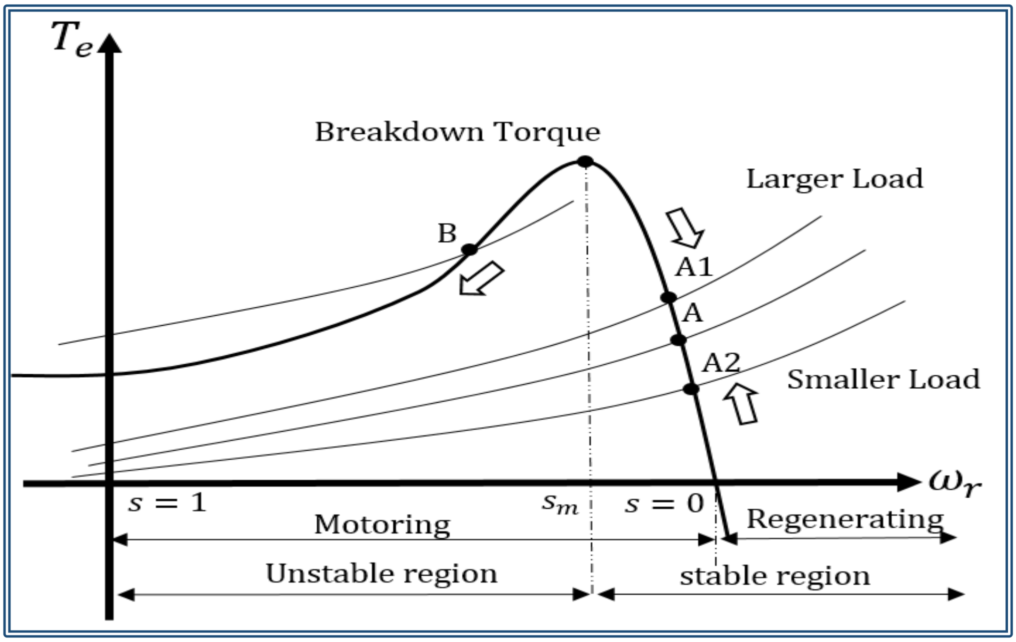


Fig. 3.2 Torque-speed curve of an induction machine

As can be realised from (3.6), the rotor current $\boldsymbol{I}_r$ plays an important role in determining the electrical torque in IM. To simplify the calculation of $\boldsymbol{I}_r$ in the rotor circuit in Fig. 3.1, the magnetizing inductance is moved to the source. This simplification is acceptable due to low voltage drop over the stator resistance $r_s$ and stator leakage inductance $L_{ls}$. Therefore, the modified rotor current $\boldsymbol{I}_r^*$ in the simplified equivalent circuit can be calculated as:

$$\boldsymbol{I}_r^* = \frac{\boldsymbol{v}_s}{\sqrt{(r_s + \frac{r_r}{s})^2 + \omega_e{}^2(L_{ls} + L_{lr})^2}} \tag{3.7}$$

By substituting (3.7) in (3.6), the electromagnetic torque is calculated by:

$$T_e = \frac{3r_r\boldsymbol{v}_s{}^2(1-s)}{(s\omega_r)(r_s + \frac{r_r}{s})^2 + \omega_e{}^2(L_{ls} + L_{lr})^2} \tag{3.8}$$

Equation (3.8) is used to draw the torque-speed curve of IM as a function of $s$. These expression of torque as a function of slip is a key role in Section 3.3.1 where the variable voltage variable frequency is explained.

As can be realised from Fig. 3.2, the IM operates in motoring $s > 0$ or regenerating $s < 0$ modes with respect to field speed. In general, IMs have the higher field speed comprising rotor speed in motoring mode and vice versa for regenerating mode [1]. As shown in Fig. 3.2, the torque is a linear function of

$s$ in the neighbourhood of $s = 0$. This can be proved by using $\frac{P}{2\omega_e} = \frac{1-s}{\omega_r}$ from (3.3) and rewriting (3.8) for small slip values:

$$T_e \approx \frac{3P{v_s}^2}{2\omega_e r_r} s \tag{3.9}$$

As shown in Fig. 3.2, IMs can operate in stable or unstable regions depending on the intersection point of load curve and torque speed curve. In the stable region, the load increment causes the reduction of motor speed which impacts on raising the slip and consequently torque. The graphical demonstration of this situation is shown in Fig. 3.2 where point $A$ moves to $A1$. In a load reduction situation, the speed increases and point $A$ moves to $A2$. This happens as a result of reduction in slip and torque. Therefore in the stable operations region, the motor operating points tend to revert to original point $A$ if the load is returned to the original point. However, in an unstable region, the load increment at point $B$ reduces the speed which drops slip and torque. Reaping of load increment causes the speed to reach zero. As shown in Fig. 3.2, the boundary between the stable and unstable region is distinguished by the breakdown torque which is the maximum torque of IM. The required torque maximising slip $s_m$ for producing the breakdown torque could be derived by taking the derivative of (3.8) in respect of $s$.

To control the field and torque of the IMs at same time, more rigorous IM model derivation is required based on the flux linkage equations. The expression for flux leakage in IM is started by calculating the first component of produced leakage flux $\boldsymbol{\lambda}_{\mathrm{as}(1)}$ resulting from $a$ −phase stator current $\boldsymbol{i}_{as}$ as follows:

$$\boldsymbol{\lambda}_{\mathrm{as}(1)} = (L_{ms}+L_{ls})\, \boldsymbol{i}_{as} \tag{3.10}$$

where $L_{ms}$ is the stator mutual inductance. The second component of leakage flux in the $a$ −phase $\boldsymbol{\lambda}_{\mathrm{as}(2)}$ is created by the $b$ −phase stator current $\boldsymbol{i}_{bs}$ as follows:

$$\boldsymbol{\lambda}_{\mathrm{as}(2)} = -0.5L_{ms}\, \boldsymbol{i}_{bs} \tag{3.11}$$

The reason of having the coefficient $-0.5$ in (3.11) is because the $a$ −phase coil and $b$ −phase coil are separated by $120^{\circ}$. The third contribution for $a$ −phase flux leakage is the result of $c$ −phase stator current $\boldsymbol{i}_{cs}$ and it can be calculated by:

$$\boldsymbol{\lambda}_{\mathrm{as}(3)} = -0.5L_{ms}\,\boldsymbol{i}_{cs} \tag{3.12}$$

As a result of symmetric configuration for phases, the first part of stator flux $\vec{\boldsymbol{\lambda}}_{\mathrm{abcs}(1)}$ produced by the stator currents can be presented as:

$$\vec{\boldsymbol{\lambda}}_{abcs(1)} = \begin{bmatrix} L_{ms}+L_{ls} & -0.5L_{ms} & -0.5L_{ms} \\ -0.5L_{ms} & L_{ms}+L_{ls} & -0.5L_{ms} \\ -0.5L_{ms} & -0.5L_{ms} & L_{ms}+L_{ls} \end{bmatrix} \begin{bmatrix} \boldsymbol{i}_{as} \\ \boldsymbol{i}_{bs} \\ \boldsymbol{i}_{cs} \end{bmatrix} \tag{3.13}$$

The second flux term, which affects the stator flux, is generated by rotor currents $\vec{\boldsymbol{i}}_{abcr}$. This rotor flux term $\vec{\boldsymbol{\lambda}}_{\mathrm{abcr}(2)}$ depends on the rotor position $\theta_r$ and $\vec{\boldsymbol{i}}_{abcr}$. Using the same procedure, the first term of stator flux is used to find the effect of rotor current on the stator flux:

$$\vec{\boldsymbol{\lambda}}_{\mathrm{abcr}(2)} = L_{ms} \begin{bmatrix} \cos\theta_r & \cos(\theta_r + 2\pi/3\,) & \cos(\theta_r - 2\pi/3\,) \\ \cos(\theta_r - 2\pi/3\,) & \cos\theta_r & \cos(\theta_r + 2\pi/3\,) \\ \cos(\theta_r + 2\pi/3\,) & \cos(\theta_r - 2\pi/3\,) & \cos\theta_r \end{bmatrix} \begin{bmatrix} \boldsymbol{i}_{ar} \\ \boldsymbol{i}_{br} \\ \boldsymbol{i}_{cr} \end{bmatrix} \tag{3.14}$$

Therefore, the stator flux vector $\boldsymbol{\lambda}_{\mathrm{abcs}}$ seen from the stator frame can be defined by:

$$\vec{\boldsymbol{\lambda}}_{abcs} = \vec{\boldsymbol{\lambda}}_{abcs(1)} + \vec{\boldsymbol{\lambda}}_{abcr(2)} \tag{3.15}$$

To map $\vec{\lambda}_{\mathrm{abcs}}$ into the complex plane, the following computation procedure needs to be applied:

$$\vec{\boldsymbol{\lambda}}_{dqs}^{s} = \frac{2}{3}\vec{\boldsymbol{\lambda}}_{\mathrm{abcs}} = \frac{2}{3}\left(\frac{3}{2}L_{ms} + L_{ls}\right)\vec{\boldsymbol{i}}_{abcs} + \frac{2}{3}\left(\frac{3}{2}L_{ms}\right)\vec{\boldsymbol{i}}_{abcr} \tag{3.16}$$

$$\vec{\boldsymbol{i}}_{dqs}^{s} = i_{ds} + j i_{qs} = \frac{2}{3}\vec{\boldsymbol{i}}_{abcs} \tag{3.17}$$

$$\vec{\boldsymbol{i}}_{dqr}^{s} = i_{dr} + j i_{qr} = \frac{2}{3}\vec{\boldsymbol{i}}_{abcr} \tag{3.18}$$

$$\vec{\boldsymbol{\lambda}}_{dqs}^{s} = L_s\,\vec{\boldsymbol{i}}_{dqs}^{s} + L_m\,\vec{\boldsymbol{i}}_{dqr}^{s} \tag{3.19}$$

where the stator inductance $L_s$ and magnetising inductance $L_m$ are defined as $\frac{3}{2}L_{ms} + L_{ls}$ and $\frac{3}{2}L_{ms}$ respectively. A similar procedure can be applied to find out the rotor flux in a stationary frame:

$$\vec{\boldsymbol{\lambda}}_{dqr}^{s} = L_r\,\vec{\boldsymbol{i}}_{dqr}^{s} + L_m\,\vec{\boldsymbol{i}}_{dqs}^{s} \tag{3.20}$$

where rotor inductance $L_r$ is defined by $\frac{3}{2}L_{ms} + L_{lr}$. It should be clarified that the subscripts $r$ and $s$ stand for rotor and stator quantities.

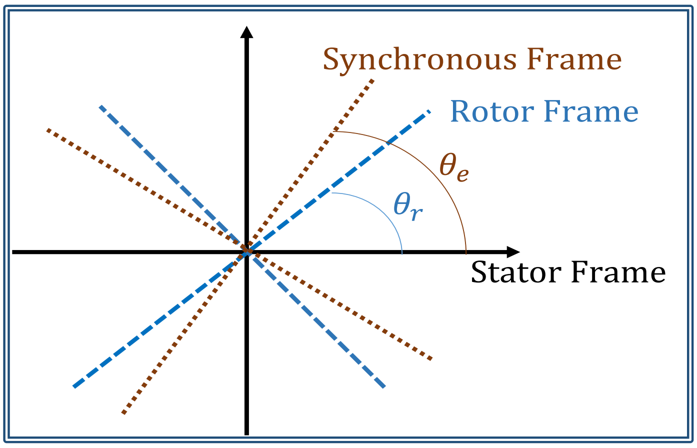


Fig. 3.3 Stator, rotor and synchronous frames

Therefore, the stator and rotor voltage equations can be obtained by:

$$\vec{\boldsymbol{v}}_{dqs}^{s} = r_s \vec{\boldsymbol{i}}_{dqs}^{s} + \frac{d}{dt} \vec{\boldsymbol{\lambda}}_{dqs}^{s} \tag{3.21}$$

$$\vec{\boldsymbol{v}}_{dqr}^{s} = r_r \vec{\boldsymbol{i}}_{dqr}^{s} + \frac{d}{dt} \vec{\boldsymbol{\lambda}}_{dqr}^{s} \tag{3.22}$$

The new presentation of stator voltage and rotor voltage in a synchronise frame, which rotates at the same speed of electrical angular velocity $\omega_e$, can be achieved by:

$$\vec{\boldsymbol{v}}_{dqs}^{e} = e^{-j\theta_e} \vec{\boldsymbol{v}}_{dqs}^{s} \tag{3.23}$$

$$\begin{aligned}
\vec{\boldsymbol{v}}_{dqs}^{e} &= r_s \vec{\boldsymbol{i}}_{dqs}^{e} + e^{-j\theta_e} p \vec{\boldsymbol{\lambda}}_{dqs}^{s} \\
&= r_s \vec{\boldsymbol{i}}_{dqs}^{e} + e^{-j\theta_e} p e^{-j\theta_e} e^{j\theta_e} \vec{\boldsymbol{\lambda}}_{dqs}^{s} \\
&= r_s \vec{\boldsymbol{i}}_{dqs}^{e} + e^{-j\theta_e} (j\omega_e e^{j\theta_e} e^{-j\theta_e} \vec{\boldsymbol{\lambda}}_{dqs}^{s} + e^{j\theta_e} p \vec{\boldsymbol{\lambda}}_{dqs}^{e}) \\
&= r_s \vec{\boldsymbol{i}}_{dqs}^{e} + p \vec{\boldsymbol{\lambda}}_{dqs}^{e} + j\omega_e \vec{\boldsymbol{\lambda}}_{dqs}^{e}
\end{aligned}$$

$$\vec{\boldsymbol{v}}_{dqr}^{e} = e^{-j(\theta_e - \theta_r)} \vec{\boldsymbol{v}}_{dqr}^{s} \tag{3.24}$$

$$0 = r_s \vec{\boldsymbol{i}}_{dqr}^{e} + p \vec{\boldsymbol{\lambda}}_{dqr}^{e} + j(\omega_e - \omega_r) \vec{\boldsymbol{\lambda}}_{dqr}^{e}$$

As can be realised from Fig. 3.3, (3.23) and (3.24), the used transferring angle in stator voltage and rotor voltage are $\theta_e$ and $\theta_e - \theta_r$ respectively. Furthermore, it is obvious that the rotor is shorted in IM and therefore $\boldsymbol{v}_{dqr}^{e} = 0$ in (3.24). Note that the differential operator, $p$, is used in (3.23) and (3.24) instead of $\frac{d}{dt}$ in (3.21) and (3.22).

Utilising (3.23) and (3.24), the IM model can be developed based on the stator and rotor currents variables in a synchronous frame as follows:

$$\begin{bmatrix} v_{ds}^e \\ v_{qs}^e \\ 0 \\ 0 \end{bmatrix} = \begin{bmatrix} r_s + pL_s & -\omega_e L_s & pL_\mathrm{m} & -\omega_e L_\mathrm{m} \\ w_e L_s & r_\mathrm{s} + pL_\mathrm{s} & \omega_e L_\mathrm{m} & pL_\mathrm{m} \\ pL_\mathrm{m} & -\omega_{sl} L_\mathrm{m} & r_\mathrm{r} + pL_\mathrm{r} & -\omega_{sl} L_\mathrm{r} \\ \omega_{sl} L_\mathrm{m} & pL_\mathrm{m} & \omega_{sl} L_\mathrm{r} & r_\mathrm{r} + pL_\mathrm{r} \end{bmatrix} \begin{bmatrix} i_{ds}^e \\ i_{qs}^e \\ i_{dr}^e \\ i_{qr}^e \end{bmatrix}, \omega_{sl} = \omega_e - \omega_r \tag{3.25}$$

To derive the electromagnetic torque $T_e$ equation based on the stator and rotor current components, the electrical power $P_e$ applied to the motor needs to be developed as follows:

$$P_e = \frac{3}{2}\left(v_{ds}^e i_{ds}^e + v_{qs}^e i_{qs}^e\right) = \tag{3.26}$$

$$= \frac{3}{2}\, i_{ds}^e \left((r_s + pL_\mathrm{s}) i_{ds}^e - \omega_e L_s\, i_{qs}^e + pL_\mathrm{m} i_{dr}^e - \omega_e L_m i_{qr}^e\right)$$

$$+ \frac{3}{2}\, i_{qs}^e \left((r_s + pL_\mathrm{s}) i_{qs}^e \omega_e L_m\, i_{dr}^e + pL_\mathrm{m} i_{qr}^e + \omega_e L_s i_{ds}^e\right)$$

Equation (3.26) is achieved by substituting (3.19) and (3.20) within (3.23) and (3.24). Finally, the gradient of $P_e$ with respect to $\omega_r$ is developed to define $T_e$, which is:

$$T_e = \frac{dP_e}{d\omega_r} = \frac{P}{2}\frac{dP_e}{d\omega_e} = \frac{3}{2}\frac{P}{2} L_m (i_{qs}^e i_{dr}^e - i_{ds}^e i_{qr}^e) \tag{3.27}$$

### 3.3 Principle of induction motor control methods

The three-phase voltage source inverter (VSI) is the most commonly used inverter in EV applications. With access to this type of inverter, different motor control algorithms can be developed to control the IMs [69]. The control on speed or torque, either directly or through the current controllers, are the targets of these control algorithms. The complexity and performance of the control algorithms vary depending on the selected control scheme and the need to satisfy restrictions on software and hardware set-up. Determination of air-gap flux is a key parameter in analysing performance of the control method. The position of the air-gap flux can be determined by using sensor, which adds extra cost and maintenance in the closed-loop system, or estimation methods based on using the voltage model. This method is not reliable on low speed region as the result of having integration drift. Therefore, the rotor-field oriented control explained in section 3.3.2, is considered as common technique for controlling IMs.

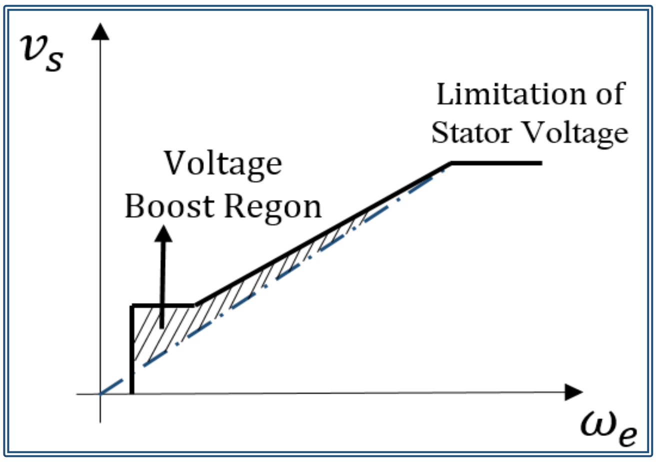


Fig. 3.4 Control pattern for VVVF scheme

### 3.3.1 Slip-based variable voltage variable frequency control (VVVFC)

The VVVFC is the most basic form of speed control [70]. In this method, the stator flux $\lambda_s$ is kept constant by keeping the applied stator voltage in proportion to the electrical frequency as shown in Fig. 3.4. The constant voltage to frequency $v_s/F_e$ ratio means that the electromagnetic torque just depends on slip. This can be proved by using (3.3) and rewriting (3.8) to:

$$T_e = \frac{3P}{2}\frac{(v_s{}^2)}{(\omega_e{}^2)}\frac{r_r\omega_{sl}}{r_r{}^2 + \omega_{sl}{}^2 L_{lr}{}^2} = \frac{3P}{2}\boldsymbol{\lambda}_s^2 \frac{r_r\omega_{sl}}{r_r{}^2 + \omega_{sl}{}^2 L_{lr}{}^2} \tag{3.28}$$

As shown in Fig. 3.5, the output of the speed regulator defines the demand torque. Equation (3.28) is then used to construct the required slip in proportion to the reference torque. The calculated slip is added to the speed of the rotor to shape the electrical speed which is the input of VVVF. The pattern shown in Fig. 3.4 is then applied to determine the desired voltage level. This closed loop control system and controlled signals are shown by yellow region in Fig. 3.5 as control elements. It should be noted that the stator voltage needs to be boosted in the low-speed region as shown in Fig. 3.4. The boosted voltage is required to compensate the voltage drop over the stator resistance. It can also be realised from Fig. 3.4 that the stator voltage is restricted in certain points due to limited inverter voltage. The table used for determining the voltage level in VVVF control shows that this method is suitable for many applications such as subway trains and locomotives where the precision is not as essential. However, high-performance control algorithms, such as field-oriented control or direct-torque control, need to be used in electric vehicle drives where accurate control of flux and torque is required.

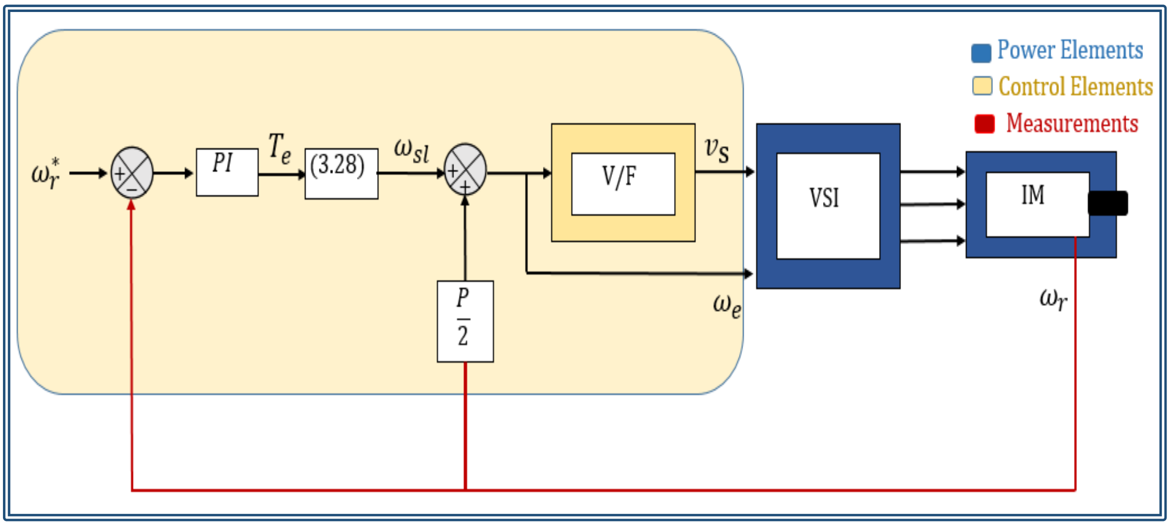


Fig. 3.5 Slip based variable voltage variable frequency controller

### 3.3.2 Rotor field-oriented control (RFOC)

As explained in Section (3.2), the description of IM in a synchronous frame provides two degrees of freedom for flux regulation and torque control. Aligning the d-axis of the synchronous frame with rotor flux or air-gap field presents a type of field-oriented method. The position of the air-gap flux can be directly obtained by using sensors. However, this is an undesirable technique as a result of adding extra cost and maintenance to the closed-loop system [71]. Therefore, the alternative method based on RFOC is used to obtain the position of the air-gap flux. In this method, the d-axis of the synchronous frame is aligned with the rotor flux which consequently results in $\lambda_{qr}^e = 0$. The flux alignment is achieved by calculating the speed difference between electric field and mechanical rotor speed from (3.25) and (3.20) as follows:

$$\lambda_{qr}^e = 0 = L_r\, i_{qr}^e + L_m\, i_{qs}^e \rightarrow i_{qr}^e = \frac{-L_m\, i_{qs}^e}{L_r} \tag{3.29}$$

$$v_{qr}^e = r_r\, i_{qr}^s + p\lambda_{qr}^s + \omega_{sl}\, \lambda_{dr}^s \rightarrow 0 = r_r\, i_{qr}^s + \omega_{sl}\, \lambda_{dr}^s \rightarrow \omega_{sl} = \frac{r_r\, L_m\, i_{qs}^e}{L_r\, \lambda_{dr}^s} \tag{3.30}$$

By adding the calculated slip in (3.30) to the rotor speed, the d-axis of the rotor flux could be aligned with the d-axis of the synchronous frame and it can be calculated by:

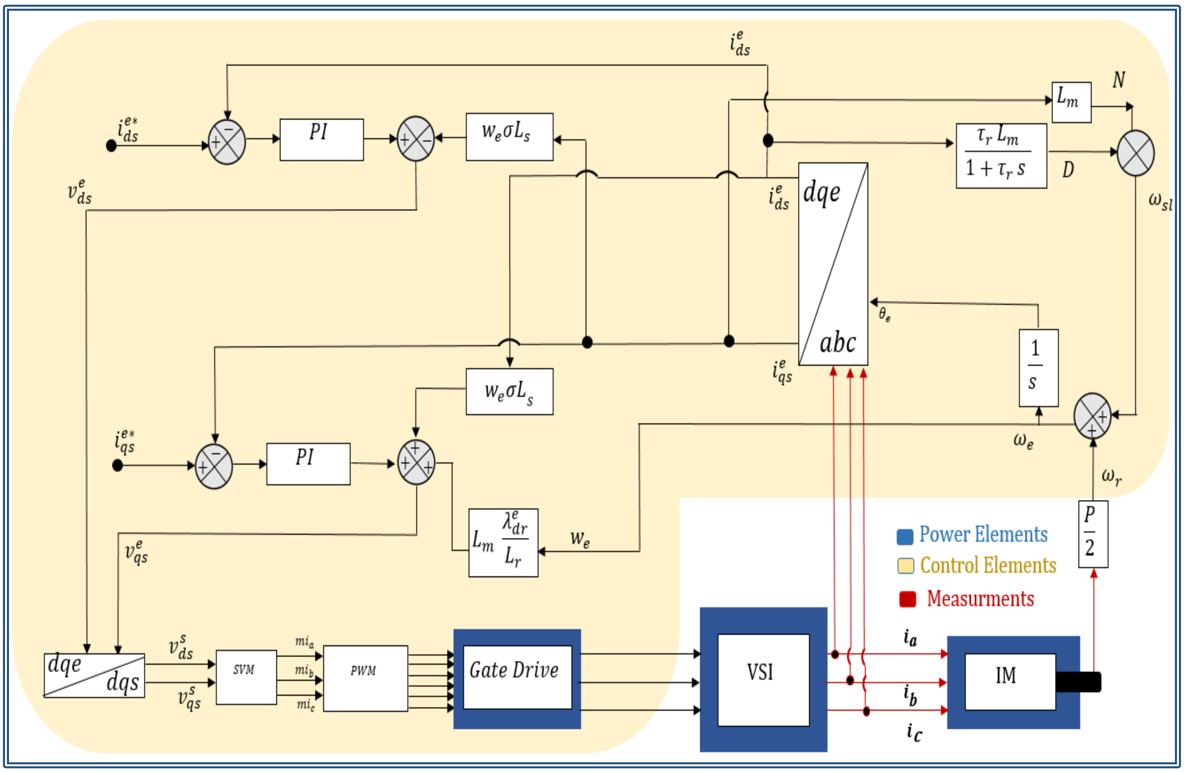


Fig. 3.6 Rotor field-oriented control block diagram

$$v_{dr}^{e} = r_r\, i_{dr}^{s} + p\lambda_{dr}^{s} - \omega_{sl}\, \lambda_{qr}^{s} \rightarrow 0 = r_r\, i_{dr}^{s} + p(L_r\, i_{dr}^{e} + L_m\, i_{ds}^{e}) \qquad (3.31)$$

$$\rightarrow i_{dr}^{e} = \frac{-L_m\, p i_{ds}^{e}}{r_r + pL_r}, \lambda_{dr}^{e} = L_m\, i_{ds}^{e} + L_r \left( \frac{-L_m\, p i_{ds}^{e}}{r_r + pL_r} \right) = \frac{L_m}{1 + p\tau_r} i_{ds}^{e}$$

As can be realised from (3.30) and (3.31), the rotor flux and stator currents play the main role of implementing RFOC. Therefore, the simplified handling of rotor field-oriented control could be achieved by considering stator currents and rotor flux as the state variables in the modelling of IM. The modified model of IM based on flux and current is derived in (3.32) by using (3.19) and (3.20) as follows:

$$\begin{bmatrix} v_{ds}^{e} \\ v_{qs}^{e} \\ 0 \\ 0 \end{bmatrix} = \begin{bmatrix} r_s + pL_s & -\omega_e L_s & pL_m & -\omega_e L_m \\ w_e L_s & r_s + pL_s & \omega_e L_m & pL_m \\ pL_m & -\omega_{sl} L_m & r_r + pL_r & -\omega_{sl} L_r \\ \omega_{sl} L_m & pL_m & \omega_{sl} L_r & r_r + pL_r \end{bmatrix} \begin{bmatrix} i_{ds}^{e} \\ i_{qs}^{e} \\ i_{dr}^{e} \\ i_{qr}^{e} \end{bmatrix} \qquad (3.32)$$

$$= \begin{bmatrix} r_s + pL_s & -\omega_e L_s & pL_m & -\omega_e L_m \\ w_e L_s & r_s + pL_s & \omega_e L_m & pL_m \\ pL_m & -\omega_{sl} L_m & r_r + pL_r & -\omega_{sl} L_r \\ \omega_{sl} L_m & pL_m & \omega_{sl} L_r & r_r + pL_r \end{bmatrix} \begin{bmatrix} 1 & 0 & 0 & 0 \\ 0 & 1 & 0 & 0 \\ -L_m/L_r & 0 & 1/L_r & 0 \\ 0 & -L_m/L_r & 0 & 1/L_r \end{bmatrix} \begin{bmatrix} i_{ds}^{e} \\ i_{qs}^{e} \\ \lambda_{dr}^{e} \\ \lambda_{qr}^{e} \end{bmatrix}$$

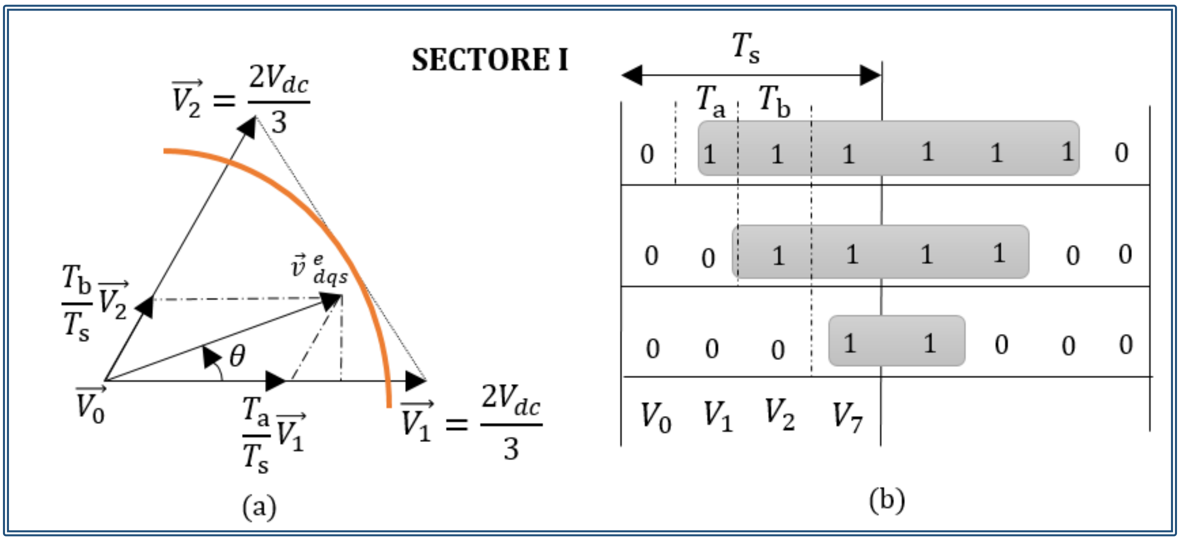


Fig. 3.7 SVM scheme in sector one (a) Synchronised stator voltage by active vectors (b) Gating signals

For IMs controlled by FOC, the electromagnetic torque can be calculated just by having the d-axis of rotor flux and q-axis stator. This can be achieved by using the developed torque equation in (3.27) as follows:

$$T_e = \frac{3}{2}\frac{P}{2}L_m\left(i^e_{qs}i^e_{dr} - i^e_{ds}i^e_{qr}\right) = \frac{3}{2}\frac{P}{2}L_m Im \tag{3.33}$$

$$= \frac{3}{2}\frac{P}{2}\frac{L_m}{L_r}Im\{\vec{\boldsymbol{\iota}}^{\,e}_{dqs}\vec{\boldsymbol{\lambda}}^{e*}_{dqr}\} = \frac{3}{2}\frac{P}{2}\frac{L_m}{L_r}\left(\boldsymbol{\lambda}^e_{dr}\boldsymbol{i}^e_{qs}\right)$$

In (3.33), the complex part of $xy$ is implied with $Im\ \{xy\}$.

Fig. 3.6 shows the block diagram of rotor field oriented control where the slip is calculated by using the components of the stator current vector. The measurement of three phase currents are used to construct the current vector. Two current regulators are applied to help the stator currents to follow the reference d-q axis currents, which are responsible for producing the required flux and electromagnetic torque within the IMs. Decoupling feedback terms are also added to the output of the PI controllers to create the reference stator voltage vector. The combination of eight active vectors for six available sectors in space vector modulation (SVM) is the key to produce the reference stator voltage. In SVM, the dwell times for active vectors are calculated and passed to the power switches to extract the required stator voltage from DC-link voltage $V_{DC}$. Figure 3.7a shows the first sector of SVM where the active times $T_a$ and $T_b$ can be calculated by:

$$\vec{v}\,^{e}_{dqs}T_s = \vec{V}\,_1 T_a + \vec{V}\,_2 T_b + \vec{V}\,_0 T_0 \tag{3.34}$$

$$v\,^{e}_{dqs}T_s\cos\theta + jv\,^{e}_{dqs}T_s\sin\theta = \frac{2}{3}V_{DC}T_a + \frac{1}{3}V_{DC}T_b + j\frac{1}{\sqrt{3}}V_{DC}T_b \rightarrow$$

$$v\,^{e}_{dqs}\cos\theta\,(T_a + T_b + T_0) + jv\,^{e}_{dqs}\sin\theta\,(T_a + T_b + T_c) = \frac{2}{3}V_{DC}T_a + \frac{1}{3}V_{DC}T_b + j\frac{1}{\sqrt{3}}V_{DC}T_b \rightarrow$$

$$T_a = T_s\frac{\sqrt{3}v\,^{e}_{dqs}}{V_{DC}}\sin\left(\frac{\pi}{3} - \theta\right)$$

$$T_b = T_s\frac{\sqrt{3}v\,^{e}_{dqs}}{V_{DC}}\sin(\theta)$$

$$T_c = T_s - T_a - T_b$$

where $T_0$ is the null time for vector $\vec{V}\,_0, \vec{V}\,_7$ and $T_s$ denotes the switching time period. The defined $T_a, T_b$, $T_0$ and structured gate signals $s_a, s_b$, $s_0$ shown in Fig. 3.7b are then used to calculate the modulation index $m_a, m_b, m_s$ as follow:

$$m_a = \frac{s_a}{T_s} = \frac{T_a/2 + T_b/2 + T_s/2}{T_s} \tag{3.35}$$

$$m_b = \frac{s_b}{T_s} = \frac{-T_a/2 + T_b/2 + T_s/2}{T_s}$$

$$m_c = \frac{s_c}{T_s} = \frac{-T_a/2 - T_b/2 + T_s/2}{T_s}$$

The modulation indexes are calculated from required active timings which are produced based on the position of stator voltage vector in individual sectors. The calculated modulation signals are compared with the carrier signals to produce pulse width modulations controlling the power electronic switches.

### 3.3.3 Direct Torque Control (DTC)

The control on the stator flux and electromagnetic torque could also be achieved by DTC method where the intermediate current controllers are not required [72]. In this method, the stator flux and torque are estimated based on the measured stator currents and voltages. Therefore, the flux and torque estimations could be achieved by using (3.21) and stationary based representation of (3.33) respectively. It needs to

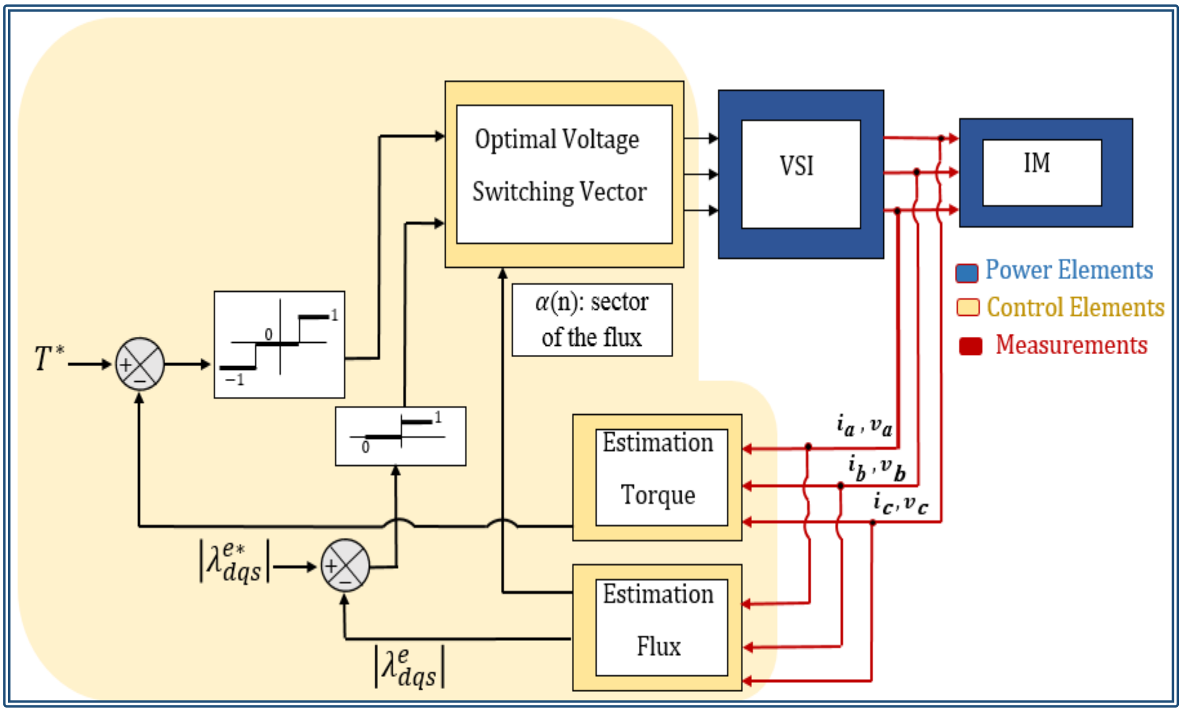


Fig. 3.8 Direct torque control block diagram

be noted that the integration of stator flux in (3.21) is replaced with the filter to reduce the drift problems associated with the open-loop integrator [73]. As shown in Fig 3.8, the estimated flux and torque are then compared with the desired values to energise the hysteresis controllers. The output of the controllers determines the voltage vector, which needs to be applied to the IM, according to the voltage look-up table.

The three and two-level hysteresis controllers are designed for the torque control and flux control sections respectively. In torque loop control, if the estimated torque was lower than the desired value, then the electromagnetic torque needs to be raised by applying the suitable voltage vector which increases the flux level in the same direction of the machine speed and vice versa. It should be pointed that the forward acceleration and backward de-acceleration of stator flux in flux control loop produces a positive and negative output torque. Therefore, the level of flux needs to be adjusted to satisfy the demand signals. Figure 3.9 illustrates the impact of applied voltage vectors on flux vector placed on the first sector. As Fig. 3.9 illustrates, the flux and torque are both increased by applying $\overrightarrow{v_2^s}$. The optimum vector table based on output of the hysteresis controllers is presented in Table 3.1 where all sectors are included. As can be seen from the performance of the hysteresis regulators, DTC scheme operates in

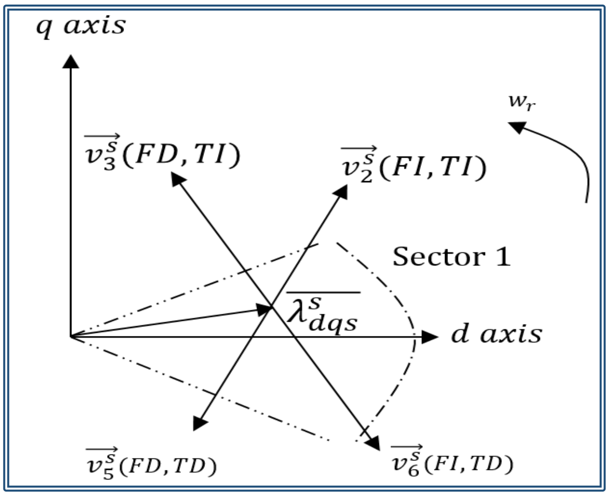


Fig. 3.9 Selected voltage to satisfy torque and flux requirements

variable switching frequency [74]. Therefore, an additional modulation scheme can be applied to keep the switching frequency at a certain value. It needs to be noted that DTC exhibits torque and current ripples in steady-state operation and it also suffers from accuracy issues of flux estimation in the low speed-region [74]. The weakness of the DTC scheme in the steady-state region causes FOC scheme is to be selected as a better solution for controlling electric motors in EV applications [75].

Table 3. 1 Optimum switching vector DTC

| $\boldsymbol{d\,\lambda_{dqs}^s}$ | $\boldsymbol{d}\,T_e^s$ | $sector\ 1$ | $sector\ 2$ | $sector\ 3$ | $sector\ 4$ | $sector\ 5$ | $sector\ 6$ |
|---|---|---|---|---|---|---|---|
| 1 | 1 | $u_2^s$ | $u_3^s$ | $u_4^s$ | $u_5^s$ | $u_6^s$ | $u_1^s$ |
| 1 | 0 | $u_7^s$ | $u_0^s$ | $u_7^s$ | $u_7^s$ | $u_0^s$ | $u_7^s$ |
| 1 | -1 | $u_6^s$ | $u_1^s$ | $u_2^s$ | $u_3^s$ | $u_4^s$ | $u_5^s$ |
| 0 | 1 | $u_3^s$ | $u_4^s$ | $u_5^s$ | $u_6^s$ | $u_1^s$ | $u_2^s$ |
| 0 | 0 | $u_0^s$ | $u_7^s$ | $u_0^s$ | $u_7^s$ | $u_0^s$ | $u_7^s$ |
| 0 | -1 | $u_5^s$ | $u_6^s$ | $u_1^s$ | $u_2^s$ | $u_3^s$ | $u_4^s$ |

### 3.4 Principle of induction motor states and parameters estimation

The proper performance of the FOC scheme is achieved by accurate calculation of the slip angle in (3.30) [76]. This happens if both $L_m$ and $r_r$ are estimated precisely [77]. This section deals with the techniques to estimate the states or parameters of IM based on the Kaltman filter algorithm and model reference adaptive system.

#### 3.4.1 Kalman filter (KF) algorithm

To estimate the states of the IM based on estimation algorithms, the state space model is required. In this part, the stationary frame model of IM is presented by using 3.32 as follows:

$$\frac{\partial \boldsymbol{x}(t)}{\partial t} = \boldsymbol{A}\boldsymbol{x}(t) + \boldsymbol{B}\boldsymbol{u}(t) \rightarrow \tag{3.36}$$

$$\frac{\partial}{\partial t}\begin{bmatrix} i_{ds}^{s}(t) \\ i_{qs}^{s}(t) \\ \lambda_{dr}^{s}(t) \\ \lambda_{qr}^{s}(t) \end{bmatrix} = \begin{bmatrix} a & 0 & c & b \\ 0 & a & -b & c \\ \frac{L_m}{\tau_r} & 0 & \frac{-1}{\tau_r} & -\omega_r \\ 0 & \frac{L_m}{\tau_r} & \omega_r & \frac{-1}{\tau_r} \end{bmatrix} \begin{bmatrix} i_{ds}^{s}(t) \\ i_{qs}^{s}(t) \\ \lambda_{dr}^{s}(t) \\ \lambda_{qr}^{s}(t) \end{bmatrix} + \begin{bmatrix} \frac{1}{\sigma L_s} & 0 \\ 0 & \frac{1}{\sigma L_s} \\ 0 & 0 \\ 0 & 0 \end{bmatrix} \begin{bmatrix} v_{ds}^{s}(t) \\ v_{qs}^{s}(t) \end{bmatrix}$$

Where the parameters of state matrix are defined as:

$$\alpha = \frac{-r_s}{\sigma L_s} - \frac{1-\sigma}{\sigma \tau_r}, \quad b = \frac{L_m}{\sigma L_s L_r}\omega_r, \quad c = \frac{L_m}{\sigma L_s L_r \tau_r}, \qquad \sigma = 1 - \frac{{L_m}^2}{L_s L_r}$$

As can be seen from (3.36), the only accessible signals that could be measured by sensors are the three phase currents. Therefore, $i_{dqs}^{s}$is considered as the output signal in the state space model as follows:

$$\boldsymbol{y}(t) = \boldsymbol{H}\boldsymbol{x}(t) \rightarrow \begin{bmatrix} 1 & 0 & 0 & 0 \\ 0 & 1 & 0 & 0 \end{bmatrix} \begin{bmatrix} i_{ds}^{s}(t) \\ i_{qs}^{s}(t) \\ \lambda_{dr}^{s}(t) \\ \lambda_{qr}^{s}(t) \end{bmatrix} \tag{3.37}$$

To present the linear discrete time-varying description of the IM model, the discrete sampling interval $t_s$ is considered and the model can be described as follows:

$$\boldsymbol{x}(k+1) = \boldsymbol{F}(k)\boldsymbol{x}(k) + \boldsymbol{G}(k)\boldsymbol{u}(k) \tag{3.38}$$

$$\boldsymbol{y}(k) = \boldsymbol{H}\boldsymbol{x}(k)$$

where,

$$\boldsymbol{F}(k) = t_s \begin{bmatrix} a & 0 & c & b \\ 0 & a & -b & c \\ \frac{L_m}{\tau_r} & 0 & \frac{-1}{\tau_r} & -\omega_r \\ 0 & \frac{L_m}{\tau_r} & \omega_r & \frac{-1}{\tau_r} \end{bmatrix} + [\boldsymbol{I}]_{4\times4}$$

$\boldsymbol{F}(k), \boldsymbol{G}(k)$ and $\boldsymbol{H}(k)$ are the plant model matrices which are not necessarily constant and could be varied at each time step $k$. The presented discrete model in (3.38) is not a perfect description of the IM model due to ignoring the disturbances and core modelling [78]. Therefore, the stochastic state space model, which contains of process noise $\boldsymbol{w}(k)$ and measurement noise $\boldsymbol{v}(k)$, needs to be modelled and added to discrete model in (3.38). To solve the stochastic state space model, Gaussian distribution needs to be applied [80]. The answers for Gaussian distribution could be achieved by applying the KF method which is the appropriate estimation solution to estimate the unmeasurable states of the IM. Fig. 3.10 shows the block diagram of the KF algorithm which needs the state predictor and state corrector mechanisms to estimate the state in discrete sequence of $k+1$. This is required to calculate state error covariance matrix ($\boldsymbol{P}(k)$) and Kalman gain ($\boldsymbol{K}(k)$) which are explained in Chapter 7. Furthermore, the mathematical development of extended Kalman Filter for estimating the rotor resistance and magnetizing inductance are included in that Chapter.

To improve the accuracy of the estimated state in KF algorithm, the MRAS scheme is used later in novel presented concept. Therefore, the principle of MRAS performance is explained in next section.

### 3.4.2 Model reference adaptive systems (MRAS)

The basic MRAS configuration for parameter identification is shown in Fig. 3.11 [81]. In the reference model, the desired IM states $\boldsymbol{X}$ can be defined based on measurable input signals. These input signals are also used in an adaptive model which identifies the value of the same IM state $\widehat{\boldsymbol{X}}$. The corresponding error ε between reference and adaptive model is utilised in the adaption mechanism which produces the estimation of the required parameter [73]. Afterwards, the estimated parameter is applied in the adaptive model to adjust the identified state value [82]. The proper design of the adaption mechanism guarantees the convergence of error signal to zero after reaping the process several times. The stable design of the

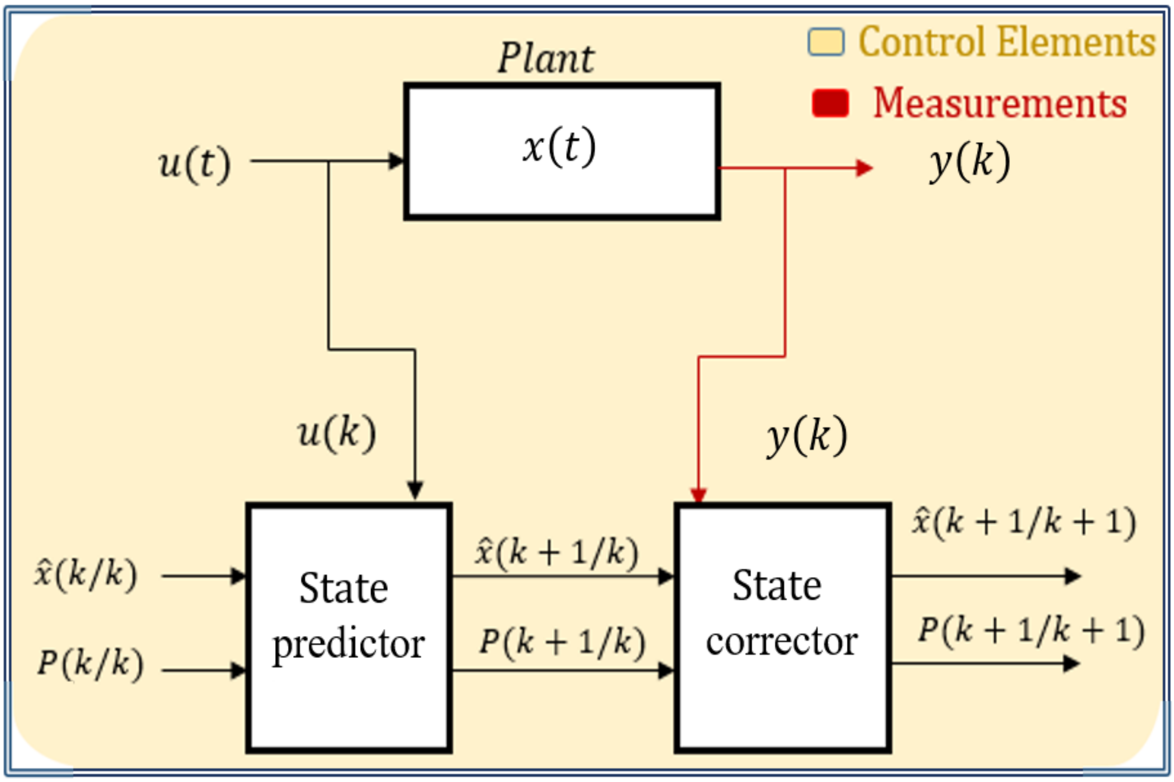


Fig. 3.10 Block diagram of internal structure for Kalman-filter state estimator

adaption mechanism can be guarantee based on Popov's hyperstability theory where the system needs to be presented as combination of a linear feedforward subsystem and a nonlinear feedback subsystem (shown in Fig. 3.11b) [83]. The system's stability can be confirmed if the transfer function of the linear feedforward subsystem is strictly real and positive and also the nonlinear feedforward could be satisfied if [84, 85]:

$$\int_0^t \varepsilon^T W dt \geq -\gamma_0^2 \tag{3.43}$$

where $-W, \varepsilon$ are the input and output of the linear subsystem respectively and $\gamma_0$ is also an arbitrary positive constant. The detailed explanation of designing the reference and adaptive models are described in Chapter 7. In that Chapter, the proposed combination of MRAS and KF based on estimation of rotor flux is explained.

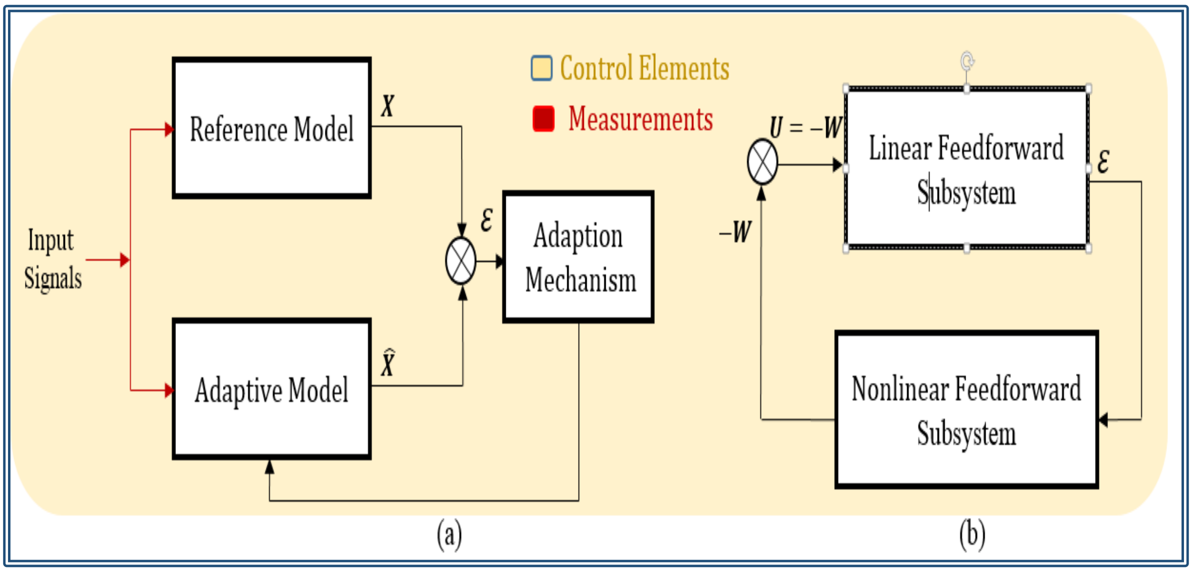


Fig. 3.11 Block diagram (a) A basic MRAS system (b) Hyper-stability theory equivalent system

### 3.5 Summary

This chapter has presented the required modelling of IMs for developing different motor control algorithms. The principal performances for the VVFF, RFOC and DTC methods are then provided in detail. The key dependency of each control schemes is summarised in Table 3.2.

Table 3.2 Summary of key dependency for motor control schemes

| Control Scheme | Dependencies |
|---|---|
| VVVF | Control pattern of voltage vs frequency |
| RFOC | Alignment of rotor flux on d-axis of synchronised frame |
| DTC | Estimation of stator flux and torque in low-speed and high-speed regions |

The KF algorithm and MRAS method have also been presented as two estimation techniques which are employed in Chapter 7 for estimating magnetising inductance and rotor resistance. It should be stated the mathematical model of permanent magnet machines (PMs) and the concepts of RFOC and DTC are also developed and simulated in Appendix A. The results are compared to show the performance of both control algorithm.

# CHAPTER 4

# Plant Emulator in Real-time Microcontroller and Experimental Set-up

## 4.1 Introduction

This chapter describes the implementation of the platforms for validating the proposed control techniques in this work. The first platform is based on a 2.2 KW squirrel cage IM which is controlled by a TMS320F28377D controller board through a four-leg voltage source inverter. This experimental hardware (Fig. 4.1) is used to demonstrate the feasibility and efficiency of the proposed method, which is developed in Chapters 5 and 6, thorough the testing processes. The second test platform consists of Delfino Experimenter Kit F28379D where the real-time plant (2.2 KW induction machine) is emulated on CPU2 of the controller. This platform is used to verify the performance of the extended Kalman filter, which is developed for estimating magnetizing inductance and rotor resistance of IM at the same time.

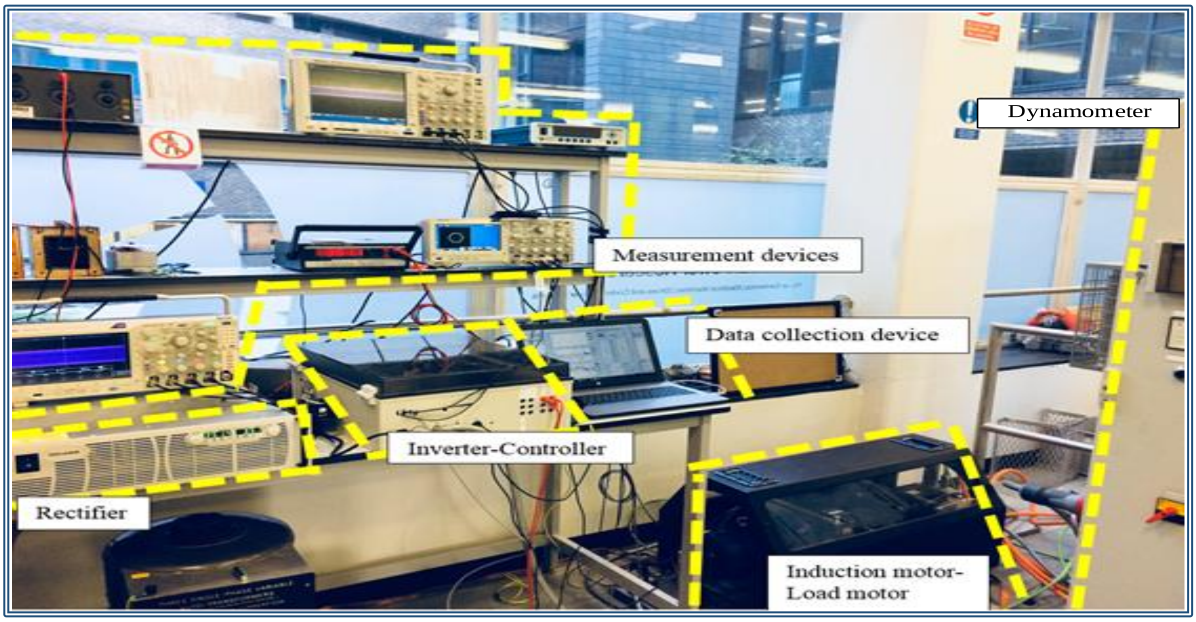


Fig. 4.1 Experimental set-up

### 4.2 Dual-core Experimenter Kit F28379D

F28379D is a microcontroller unit that includes two processing cores (CPU1 and CPU2) and two control law accelerators (CPU1.CLA and CPU2.CLA). Therefore, four 32-bit floating point processing elements are available in this controller board. In a real-time plant emulated test, the CPU1 core is used mainly for communications with the host PC where the graphical user interface (GUI) is used to monitor the internal control variables. These variables could also be monitored on an oscilloscope using the Digital to Analogue Converter (DAC) outputs on the F28379D. The CPU1.CLA implements the RFOC and SVM techniques to calculate the required modulation index signals. This leaves both CPU2 and CPU2.CLA elements available for emulating the IM. The next section explains how the IM emulator is implemented for the experimenter kit.

#### 4.2.1 IM emulator

The IM emulator is the model of IM hardware to be controlled by the microcontroller. The real-time emulation is useful for testing the proposed control schemes when the microcontroller is running in real-time. Therefore, precise monitoring of execution times and memory allocation are important. The IM emulator model is formulated as a first-order differential equation which is developed in (3.20) and (3.21). The fourth-order Runge-Kutta (RK4) as the fixed time step numerical method is implemented in CPU2 to solve the differential equations. Depending on the required accuracy of solutions and the complexity of the IM model, the RK4 can be run multiple times in one PWM cycle. This could be achieved by reducing the fixed time step in RK4 explained in Appendix B.

As shown in Fig. 4.2, the d-q axis of stator voltage is required to solve the differential equations derived in (3.20) and (3.21). Therefore, the stator voltage in the IM emulator algorithm needs to be achieved by calculating the average level of inverter leg voltages over one PWM cycle as follows:

$$v_a = \frac{m_a}{mi_{max}} V_{dc} \tag{4.1}$$

$$v_b = \frac{m_b}{mi_{max}} V_{dc}$$

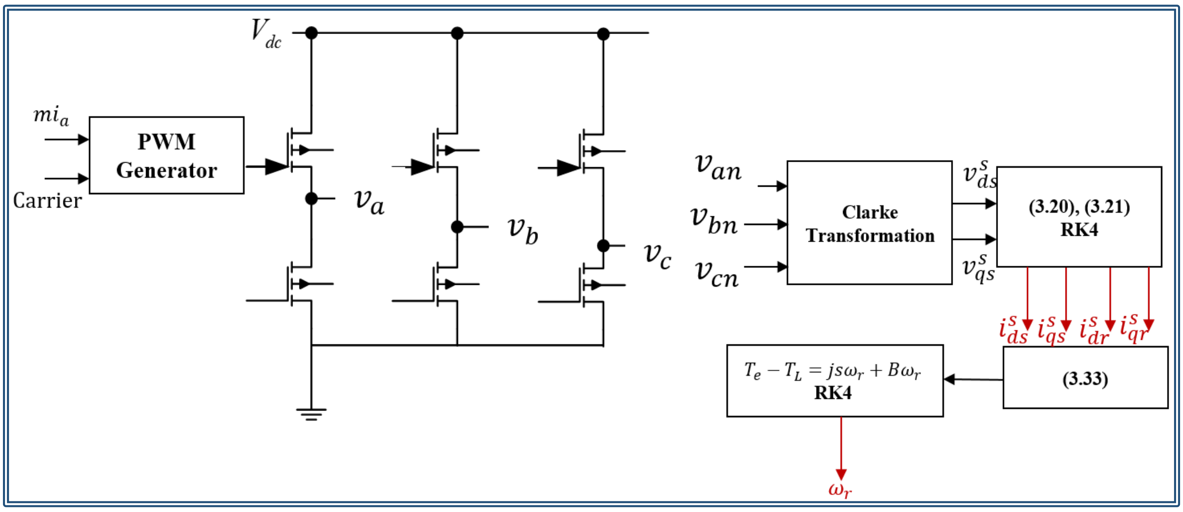


Fig. 4.2 IM emulator model

$$v_c = \frac{m_c}{mi_{max}} V_{dc}$$

where, $m_a$, $m_b$ and $m_c$ are the modulation indexes for $a$-phase, $b$-phase and $c$-phase respectively. These modulation indexes are calculated based on the SVM implemented in CPU1.CLA. The average level of inverter leg voltages and average star-point voltage $v_n$ are then used to calculate average winding phase voltages $v_{an}$, $v_{bn}$ and $v_{cn}$ as follows:

$$v_n = \frac{\boldsymbol{v}_a + \boldsymbol{v}_b + \boldsymbol{v}_c}{3} \tag{4.2}$$

$$v_{an} = \boldsymbol{v}_a - \boldsymbol{v}_n$$

$$v_{bn} = \boldsymbol{v}_b - \boldsymbol{v}_n$$

$$v_{cn} = \boldsymbol{v}_c - \boldsymbol{v}_n$$

As can be seen in Fig. 4.2, the average phase voltages are then used in Clarke transformation to produce $v_{ds}^s$ and $v_{qs}^s$. These stator voltages form the differential equations in (3.20) and (3.21) which are solved by RK4. The execution of the RK4 solver is produced one step ahead of the motor states $i_{ds}^s, i_{qs}^s, i_{dr}^s, i_{qr}^s$ after it is run twice. It needs to be noticed that having $\omega_r$ is essential to solve these differential equations. Therefore, the fifth differential equation, which is based on the electromagnetic torque and inertia, is developed and numerically solved to calculate $\omega_r$ .

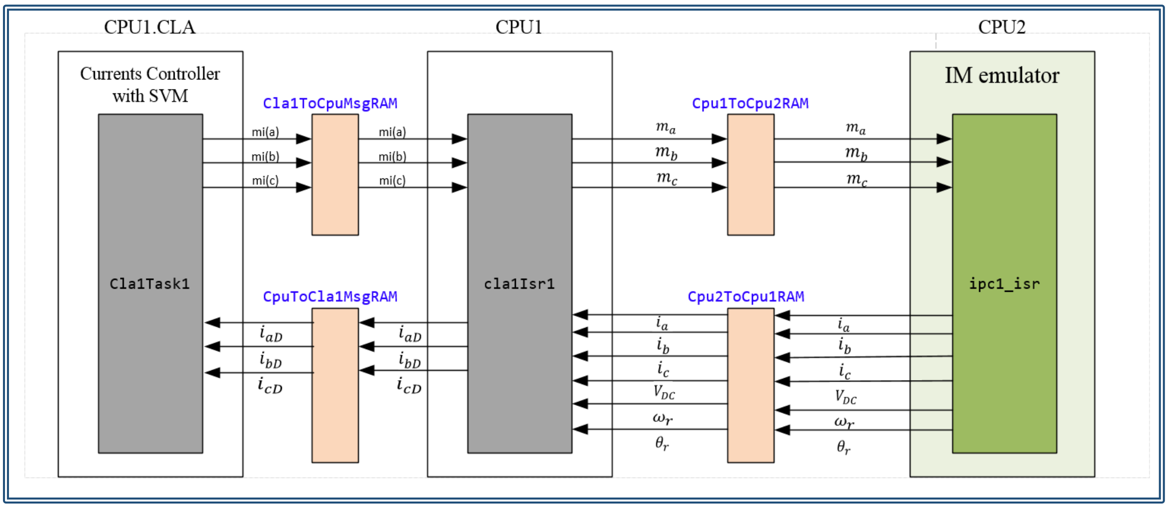


Fig. 4.3 Communication arrangements between the processors in F28379D experimental kit

The calculated $i_{ds}^{s}$ and $i_{qs}^{s}$ are used to estimate the phase currents $i_a$, $i_b$ and $i_c$, which need to be further processed by a model of current sensors, sensor interface circuitry and Analogue to Digital Converters (ADCs). This procedure happens before the digital phase currents $i_{aD}, i_{bD}$ and $i_{cD}$ are passed to the controller's interrupt service routine (ISR) running on CPU1.CLA. The process of phase current digitalisation can be developed by applying the proper scaling factor $sf_x$ and voltage offset $of_x$. The $Sf_x$ is an amalgamation of the current sensors' gains, sensor interface circuitry and ADC. The $Of_x$ is also used in order to create the bipolar signal. Therefore, the digital representation of phase currents can be defined by:

$$i_{aD} = Sf_a i_a + Of_a \tag{4.3}$$

$$i_{bD} = Sf_b i_b + Of_b$$

$$i_{cD} = Sf_c i_c + Of_c$$

### 4.2.2 Interference between CPU1 and CPU2

As shown in Fig. 4.3, there are three ISRs which are executed on the different processing elements. The ipc1-isr, cla1Isr1 and ClaTask1 are executed on CPU2, CPU1 and CPU1.CLA respectively. Each of these ISRs is used to show the completion of the computation tasks. The data flow paths between these ISRs indicate how these interrupts are triggered. As shown in Fig. 4.3, the produced modulation signals in CPU1.CLA are transferred to CPU2 within cla1Isr1. Then, these modulation are used in the plant

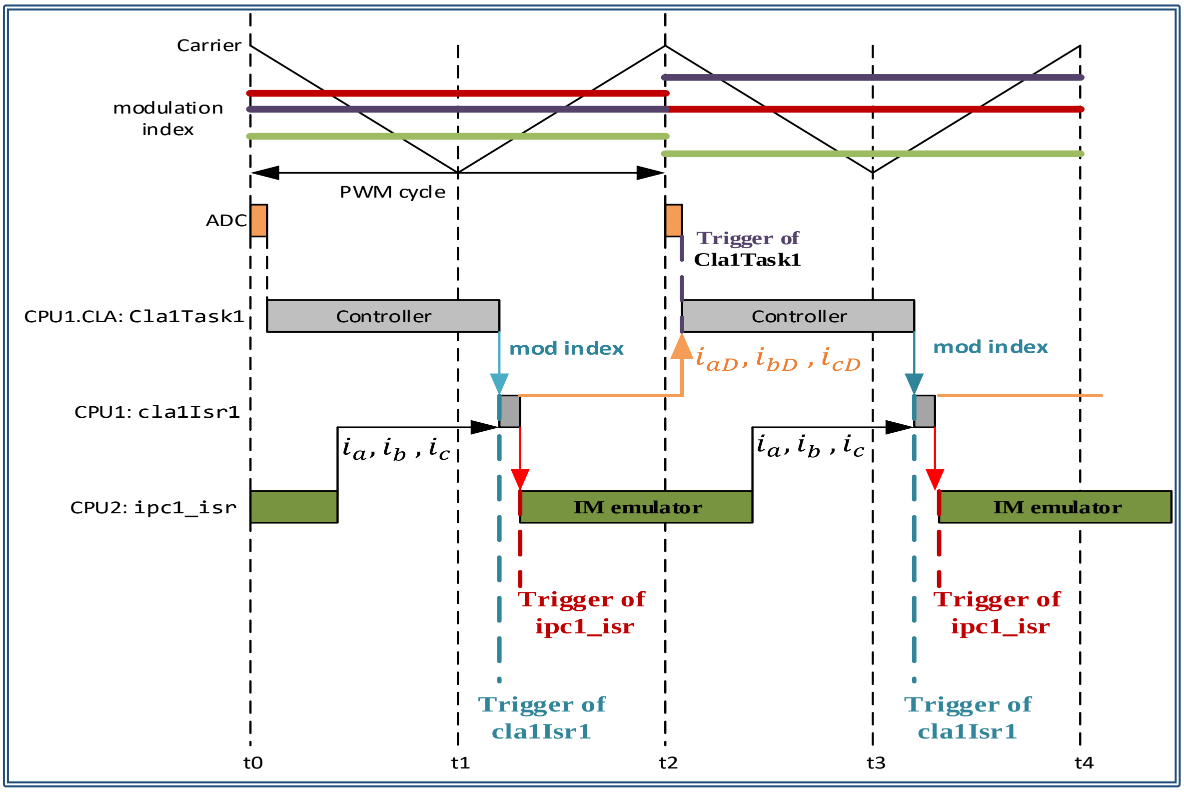


Fig. 4.4 Timing arrangement for the control system including IM emulator

emulator process to determine the motor currents. The calculated motor currents are consequently transferred to CPU1.CLA and this is used for triggering ClaTask1. It needs to be noted that the data of different variables defined in Fig. 4.3 are saved on the various internal processor message RAMs, which are indicated with blue fonts.

### 4.2.3 Timing arrangement for the control system including IM emulator

The timing arrangement for the digital current control system used in motor control schemes is shown in Fig. 4.4. The top of the figures illustrates the triangle PWM carrier signal and the modulation indexes which have a constant level over the whole PWM cycle. These modulation indexes are calculated by controller from previous PWM cycle. This could be realised by looking at $t_1$ when the modulations are calculated and loaded in PWM register which determine the pulse width of the PWM cycle between $t_2$ and $t_4$. The pulse width determines the applied per phase voltage to the IM emulator. The corresponding motor current for this particular pulse width is samples in next PWM cycle happening after $t_4$. The real measurement of the execution timing for the closed loop current control system, including the IM emulator is presented in Fig. 4.5. It needs to be noted that the fixed switching frequency of 20 KHz is considered for this test. Trace 1 of Fig. 4.5 shows the duration of main ISR running in CPU1 which is

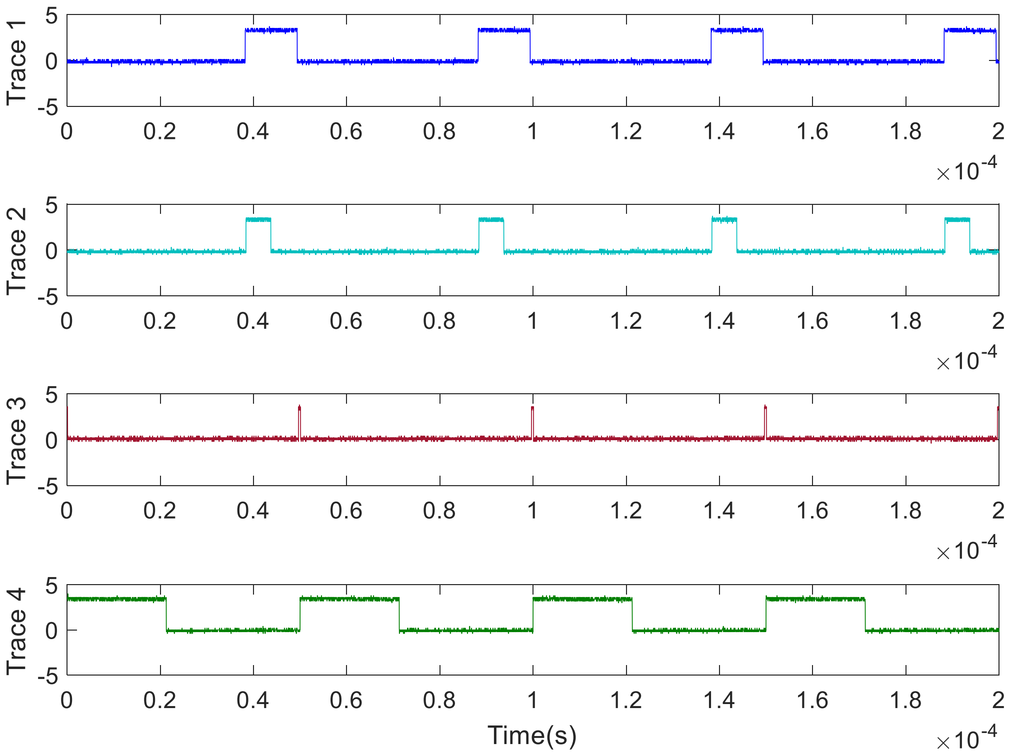


Fig. 4.5 TMS320f28377d timing: Trace 1: CPU1: MainCPU1_ISR, Trace 2: CPU1.CLA: Cla1Task1, Trace 3: CPU1: cla1Isr1 and Trace 4: CPU2: ipc1_isr

11.18 microseconds. Trace 2 shows the duration time (5.32 microsecond) for running the d-q axis current controllers and SVM on CPU1.CLA. Then, the duration of 440 nanoseconds is the time period when the small numbers of variables are transferred between CPU1.CLA and the IM emulator. Consequently, the time duration for running the interrupt service routine (ISR) on CPU2 is 21.30 microseconds. This is the result of executing the RK4 solver twice in CPU2.

The second experimental system, which is based on the real IM, has been designed and built as follow to verify the performance of the concept proposed in Chapter 5 and 6.

## 4.3 Test rig set-up

The schematic diagram of the experimental set-up is shown in Fig. 4. 6. The conventional voltage based inverter utilises the DC-link of 350V provided by the three-phase voltage rectifier. The DC-link voltage is measured by voltage transducer LV25_P which is passing its measurement to one ADCs channel. The other ADCs of the controller are occupied by three current sensors CAS 15_NP. Comparison of the measured motor currents and desired currents determines the required voltage which needs to be

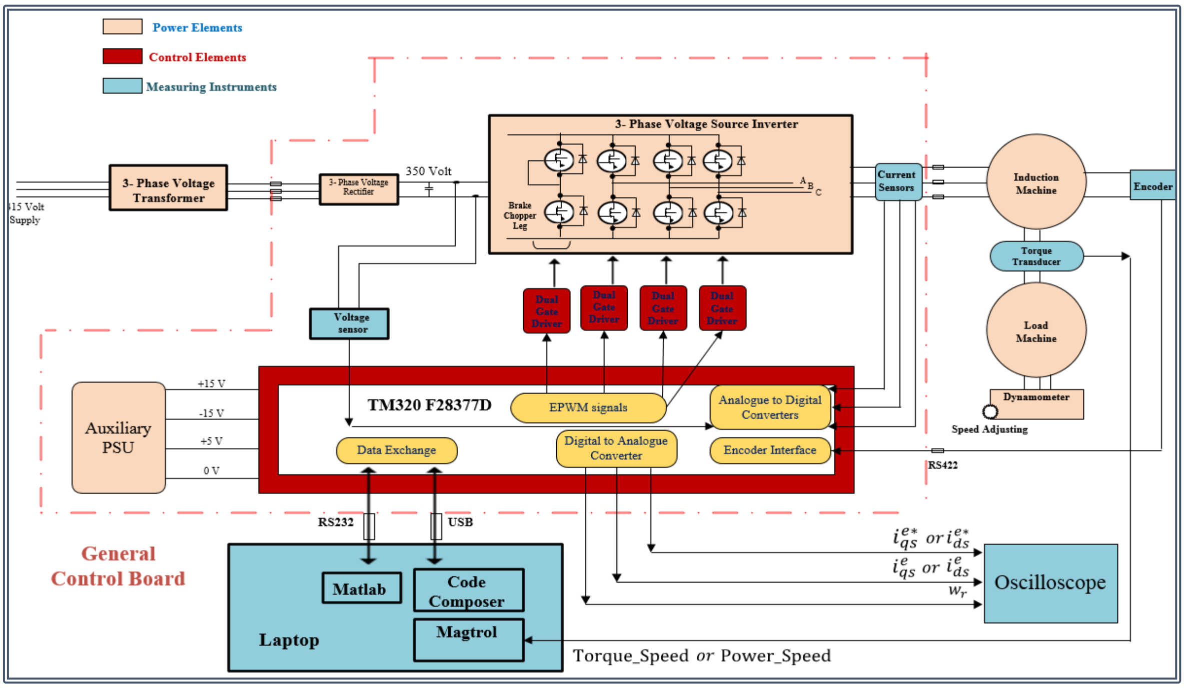


Fig. 4.6 Schematic diagram of exprimental setup

provided by the inverter. The required voltage is achieved by proper controlling of the gate signals of the IGBTs through enhanced pulse width modulation (EPWM) signals. These signals are then boosted by using dual gate drives to provide sufficient gate voltage for each power switch. The utilised gate drivers are equipped with the $V_{CE}$ saturation to prevent the short circuit condition. As shown Fig. 4.6, control the variables inside the controller could also be measured by oscilloscope through available DAC’s outputs. As shown in Fig. 4.6, the load motor operates in speed control mode. The next section explains how the configured test set-up has been initially used to measure the motor parameters.

## 4.3.1 Motor parametrisation

### 4.3.1.1 Locked-rotor test

To determine the value of the rotor resistance and leakage inductances, the locked-rotor test is carried out at rated stator current. In this test, the rotor of induction machine is locked using the dynamometer. The dynamometer is set in speed mode with a demanded speed of zero. This situation maintains the rotor of induction machine in a stationary state while the applied stator voltage is increased using an auto-transformer (Variac). The three-phase auto-transformer voltage is increased until the rated current flows in the stator windings. In this situation ($\omega_r = 0$), the slip has a value of 1, which could be calculated by (3.3). Therefore, the per-phase equivalent circuit of IM can be modelled as follows:

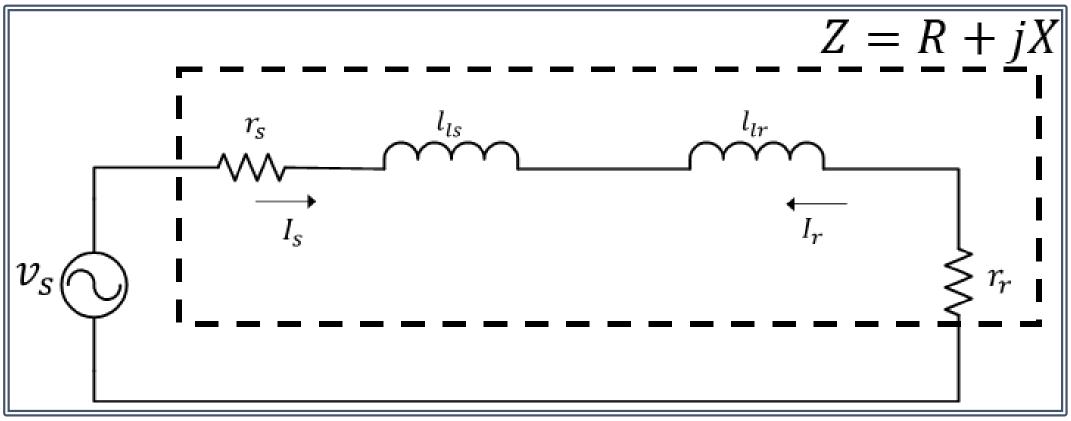


Fig. 4.7 Simplified equivalent circuit for the locked-rotor test

As Fig. 4.7 shows, the middle part of equivalent circuit, which includes the core-loss resistance and magnetising reactance, is ignored. This is a reasonable assumption because the rotor resistance is much less than the parallel combination of core–loss resistance and magnetising reactance. The measured voltage, current and power of each phase in Table 4.1 are then used to calculate the rotor leakage inductance and resistance based on Fig. 4.7. The values of measured currents are based on the range and scale settings of the power analyser. The scale setting of the power analyser depends on the current clamp ratio, which is chosen as 10 mV/A for this experiment. Also, the range of voltage and current are set to 600V and 1A respectively.

Therefore, the rotor resistance and leakage inductances are calculated as follow:

$$Z = \frac{V_s}{I_s} = 9.6383\ \Omega \tag{4.4}$$

$$r_r = Z \cos \emptyset - r_s = 2.5067\ \Omega$$

$$X = Z \sin \emptyset = 8.3584\ \Omega$$

Table 4. 1 Measured parameters in locked-rotor test

| | |
|---|---|
| measured phase voltage (V rms) | 44.24 |
| rated phase current (A rms) | 4.6 |
| measured phase current (A rms) | 4.59 |
| supply frequency (Hz) | 50 |
| measured phase power (KW) | 0.101 |
| measured phase difference (degree) | 60.14 |

The $r_s$ used in (4.4) is the average value of the stator resistances for three phases as explained in the following section.

#### 4.3.1.2 Stator resistance test

To calculate stator resistance for each phase of the induction machine, a DC power supply is used. The power supply is put in constant current mode with a current setting of 0.5 A. After measuring phase to phase voltage, the D.C resistance is calculated by:

$$r_{s,UN} + r_{s,WN} = \frac{V_{UW}}{I_s} \rightarrow r_{s,UN} = r_{s,WN} = 2.292\ \Omega \tag{4.5}$$

$$r_{s,VN} + r_{s,WN} = \frac{V_{WV}}{I_s} \rightarrow r_{s,VN} = r_{s,WN} = 2.291\ \Omega$$

$$r_{s,UN} + r_{s,VN} = \frac{V_{UV}}{I_s} \rightarrow r_{s,UN} = r_{s,VN} = 2.298\ \Omega$$

To validate the measured stator resistances, phase to natural voltage measurement is taken as well (Fig. 4.8b).

$$V_{UN} = 1.153\ (V) \rightarrow r_{s,UN} = 2.3060\ \Omega \tag{4.6}$$

$$V_{VN} = 1.153\ (\mathrm{V}) \rightarrow r_{s,VN} = 2.3060\ \Omega$$

$$V_{WN} = 1.145\ (V) \rightarrow r_{s,WN} = 2.290\ \Omega$$

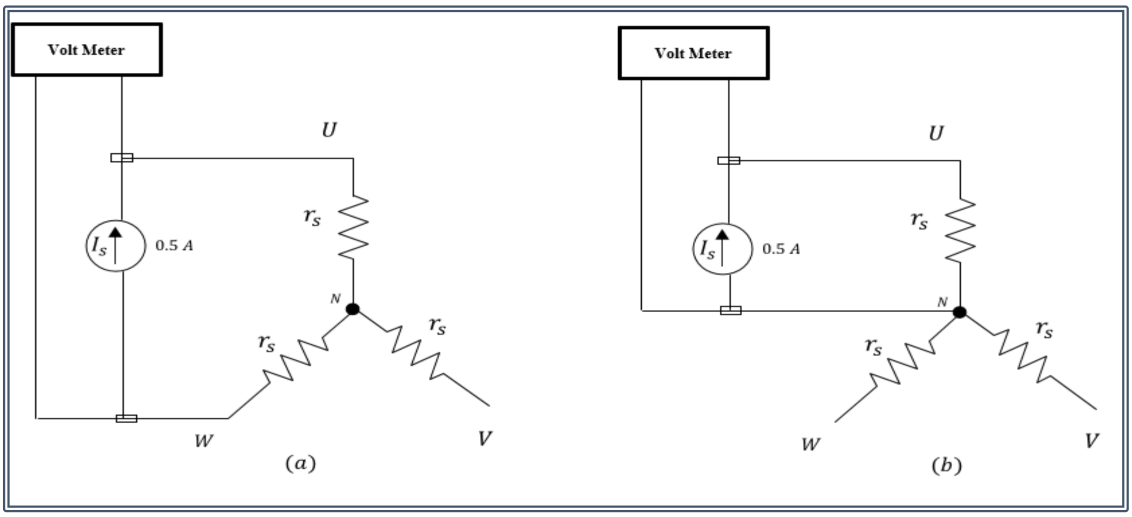


Fig. 4.8 Configuration of D.C. resistance tests for three phase induction machine (a) phase to phase measurement (b) phase to neutral measurement

There are two different tests that can be used to calculate the core-loss resistance and the magnetising inductance. The no-load test is easier to perform, but the synchronous speed test is more accurate.

#### 4.3.1.3 No-load test

In the no-load test, the adjustable AC power supply is used to apply a balanced rated voltage with rated frequency to induction machine stator windings (Table 4.2).

Table 4. 2 Applied parameters for no-load motor test

| | |
|---|---|
| Applied Phase voltage (V rms) | 240 |
| Phase current (A rms) | 2.87 |
| Applied  power (W) | 109 |
| Supply frequency (Hz) | 50 |

In this test the slip is very close to zero as the induction motor rotates at almost synchronous speed. Therefore, the equivalent circuit of the induction machine for the no-load test can be shown by Fig. 4.9. The core loss of the induction machine is much larger than the stator resistance and stator leakage reactance $X_{ls}$. So, the magnetising inductance $L_m$ and core resistance $R_c$ are calculated as follows:

$$cos\,\emptyset = \frac{P_{ph}}{V_{ph}I_{ph}} = 0.158 \rightarrow \emptyset = 80.9092° \tag{4.7}$$

$$I_m = I_s \sin\emptyset = 2.8340\ A$$

$$I_c = I_s \cos\emptyset = 0.4535\ A$$

$$L_m = \frac{V_{ph}}{2\pi f_s I_m} = 0.2696\ H$$

$$R_c = \frac{V_{ph}}{I_c} = 529.2172\ \Omega$$

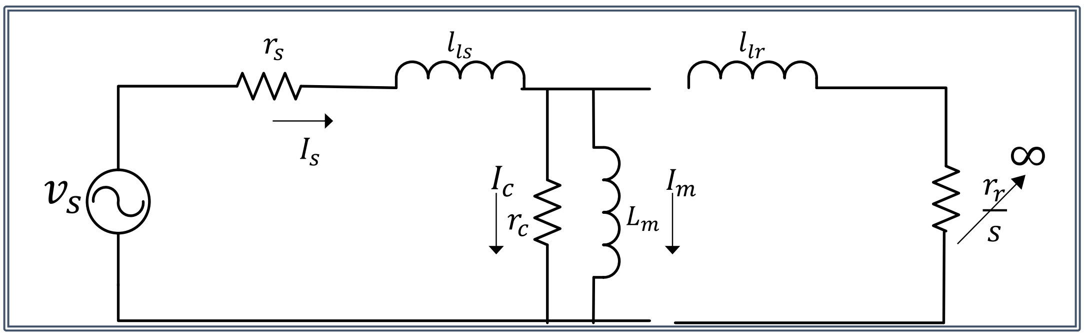


Fig. 4.9 Equivalent circuit for the No-Load Test

To validate the calculated magnetising inductance, the synchronous speed test is considered. In this test, the induction machine is rotated at synchronous speed. Therefore, the slip can be kept at a value of exactly zero and the rotor part of the per phase equivalent circuit can be neglected.

#### 4.3.1.4 Synchronous speed test

To cause the induction motor to rotate at synchronous speed, the dynamometer is required to supply the friction and windage torque. The dynamometer should be set in torque control mode with a demanded torque of zero. The AC supply voltage is then connected to the induction machine in order to accelerate it to no load speed. After the machine has settled at synchronous speed, the dynamometer torque is adjusted to increase the induction machine speed to synchronous speed (1500 rpm). When the induction machine reaches synchronous speed, the following measurements are made:

Table 4. 3 Measured parameters of induction machine in synchronous test

| | |
|---|---|
| Measured phase voltage (V rms) | 239.42 |
| Measured phase current (A rms) | 2.85 |
| Measured phase power (KW) | 109 |
| Measured phase difference (degree) | 80.80 |

By using the measured parameters, the magnetising inductance can be calculated and it has a value of $0.2709H$. The magnetising inductance calculated in the no load test and the synchronous speed test are very close. So, based on locked-rotor and no-load tests, the equivalent parameters of the 2.2 KW induction machine can be defined as follows:

Table 4. 4 Calculated parameters of 2.2 KW induction machine

| | |
|---|---|
| $r_r$ | 2.5067 Ω |
| $r_s$ | 2.291 Ω |
| $L_m$ | 0.2709 $H$ |
| $L_r$ | 0.2842 $H$ |
| $L_s$ | 0.2842 $H$ |

It should be explained that the synchronous speed test is more accurate than the no-load test as it corresponds exactly to the equivalent circuit with the rotor branch removed.

The measured parameters of the IM are then used for simulation modelling and developing the proposed concepts. Several protection configurations are required before testing the performance of the IM based on different control schemes. Therefore, the section 3 and 4 in Appendix C are developed to protect the power inverter and IM in the over-current and voltage situation.

### 4.3.2 Encoder interface

The speed and position information are achieved by helping the rotatory incremental encoder in experimental set-up. The enhanced quadrotor encoder pulse (eQEP) module in F28377d is then used as a direct interface with the implemented encoder. As shown in Fig. 4.10, two quadrature signals (QEPA and QEPB), which are shifted 90° from each other, are generated by two photo elements as the shaft rotates. It should be pointed out that the positive pulse of QEPB before QEPA in Fig. 4.10 shows the anti-clockwise direction of encoder. The quadrature-clock (QCLK) is also generated based on rising or falling edges of QEPA and QEPB. The capture clock rate, which is used to calculate the time period between up-events, can be determined by setting the proper level of capture timer clock pre-scaler bit CCPS in capture control register of the encoder interface module. The capture clock is proportional to the CPU clock (200 MHz) and it needs to be selected high enough to measure accurate speed rate. However, very high capture clock frequency causes inaccurate results in the capturing position for a low-speed condition.

In this experimental set-up, the time period of one UPEVENT is defined as 1.562MHz by setting CCPS at 7. The time period of each QCLK pulse can then be calculated in one UPEVENT period. The one-

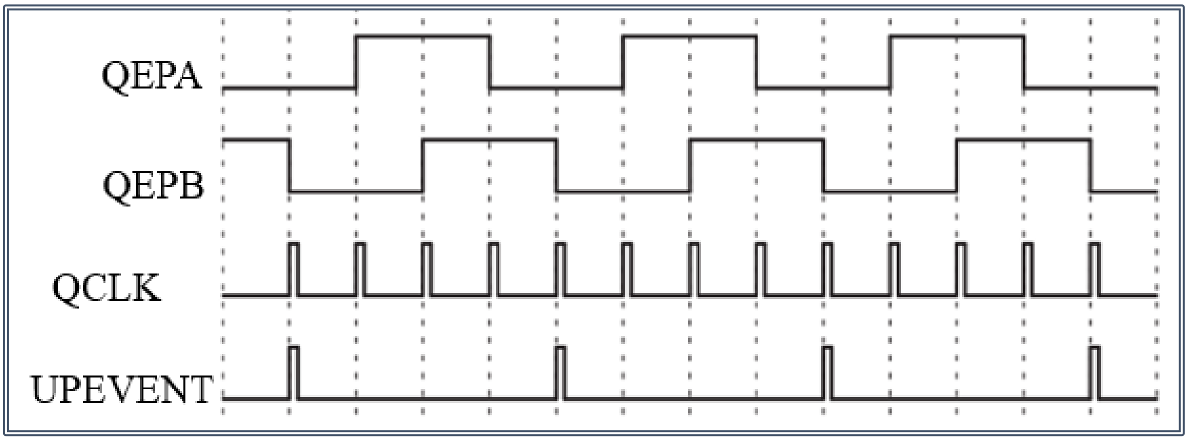


Fig. 4.10 Encoder signals

fourth of calculated time period determines the time period of one pulse in QEPA or QEPB. Therefore, the rotor speed can be calculated for 1024 lines encoder as follows:

$$\omega_r(\mathrm{rad/s}) = \frac{2\pi}{\frac{1024}{2} \times \text{time period of one pulse in QEPA or QEPB}} \tag{4.7}$$

### 4.3.3 No-load and R_L load test for open-loop variable voltage variable frequency VVVF control

In this part of the experimental set-up, the open-loop VVVF control algorithm is implemented as shown in Fig. 4.11. The goal of this test is to monitor the output voltage of the inverter in an open-loop system where currents and speeds are not controlled. This part validates the performance of the SVM in CPU1.CLA in real experimental hardware.

By directly applying the desired $V_{ds}^e$ and $V_{qs}^e$, which are normally produced from current controllers in SVM, the modulation index signals are calculated in CPU1.CLA. The value of $V_{dqs}^e$ is produced by the slider in the GUI control panel. The approved range of slider for determining $V_{dqs}^e$ can be defined as:

$$0 \leq V_{dqs}^e \leq \frac{\sqrt{3}}{2} 2500 \tag{4.8}$$

The value of 2500 is sourced from the ratio of switching frequency (20KHz) and the PWM clock (100MHz). This value also stands for maximum modulation index as the output of SVM. To retain the stator voltage inside the inscribed voltage circle of hexagonal voltage boundary, $\frac{\sqrt{3}}{2}$ needs to be multiplied by the maximum modulation index as demonstrated in (4.8). As derived in (4.9), the frequency of the stator voltage also could also be defined based on the encoder unit (degree).

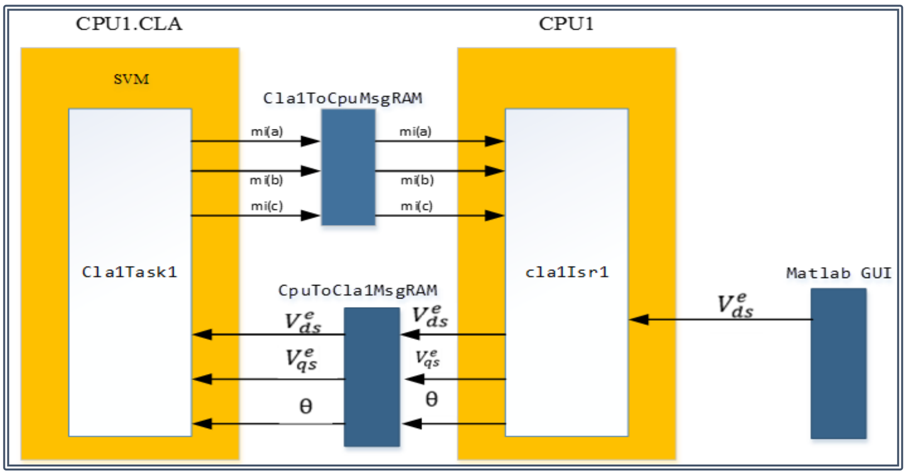
CPU1.CLA
CPU1
SVM
Cla1ToCpuMsgRAM
mi(a)
mi(b)
mi(c)
Cla1Task1
cla1Isr1
CpuToCla1MsgRAM
Matlab GUI
$V_{ds}^{e}$
$V_{qs}^{e}$
θ

(a)

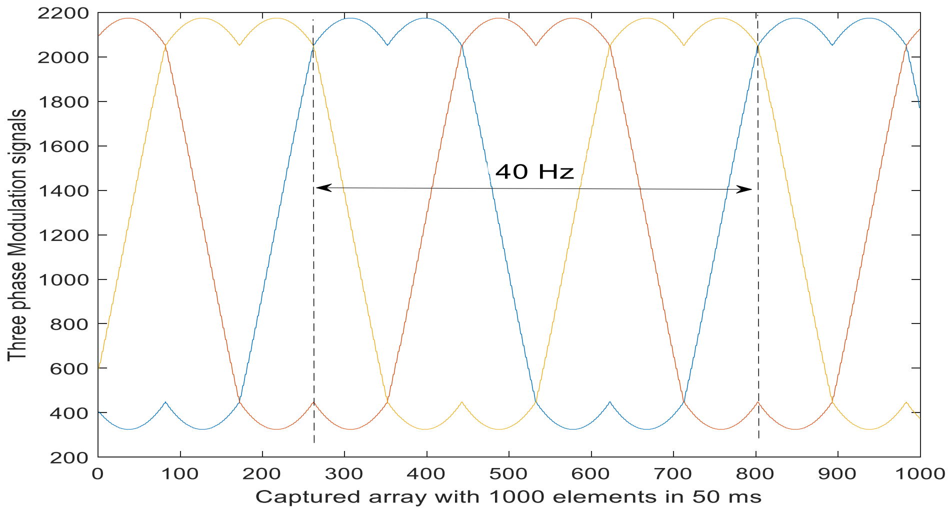
Three phase Modulation signals
40 Hz
Captured array with 1000 elements in 50 ms

(b)

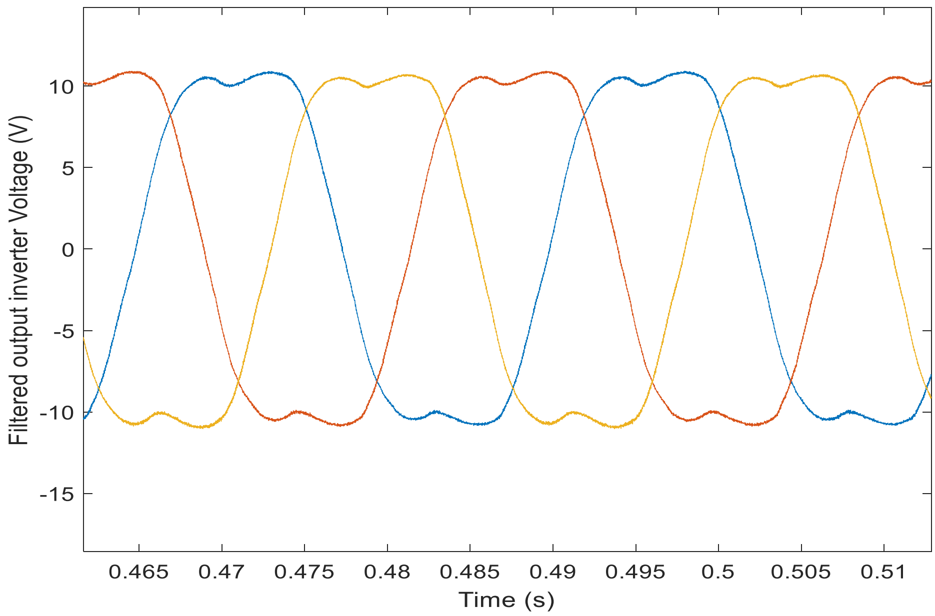
Filtered output inverter Voltage (V)
Time (s)

(c)

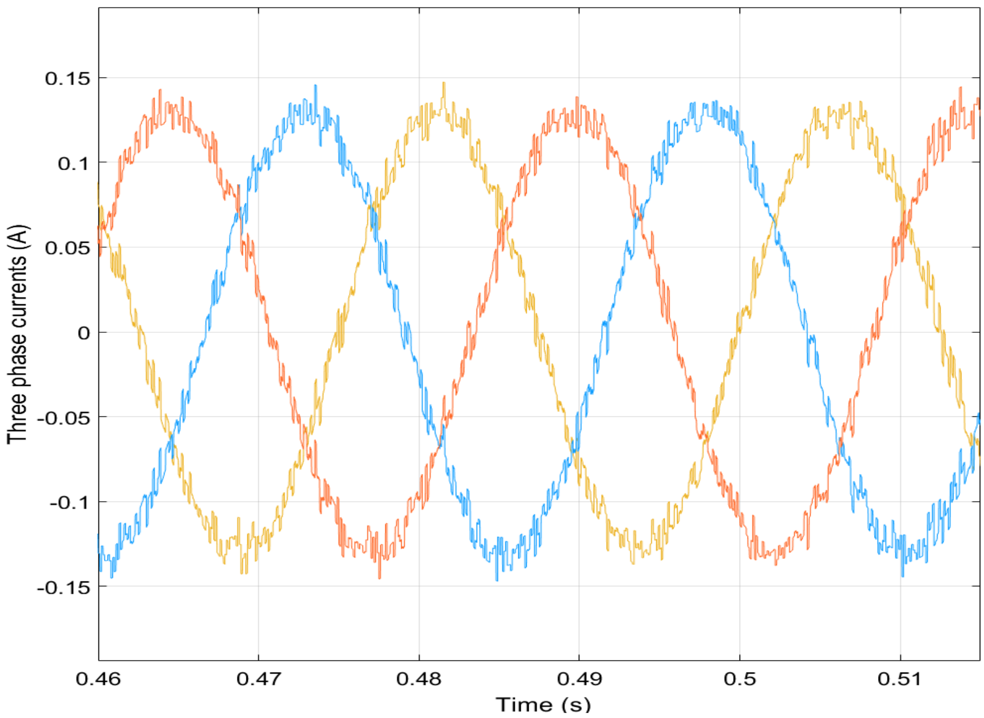


(d)

Fig. 4.11 (a) Open-loop VVVF test (b) Modulation indexes (c) Filtered output inverter voltage with 15V DC-link voltage (d) Three phase currents

$$\omega_r(\mathrm{deg}) = \left(2\pi \times \text{desired Frequency}\frac{\mathrm{rad}}{\mathrm{s}}\right) \times \left(\frac{360\,\mathrm{deg}}{2\pi\ \ \mathrm{rad}}\right) \times \left(\frac{1}{20\ \mathrm{KHz}}\right) \tag{4.9}$$

In this test, the $V_{qs}^{e}$ is kept at zero and $V_{ds}^{e}$ is defined based on (4.8). The electrical frequency of 40Hz is also selected as the desired frequency of stator voltage (4.9). Figure 4.11b and c shows the corresponding modulation index and filtered inverter output voltages. The output of inverter voltage is then applied to the R-L load, which has 100 Ω resistor and 20 mH inductance, to analyse three phase currents (Fig. 4.11d).

As can be seen in Fig. 4.11, the measured output voltage and currents verify the proper performance of SVM and PWMs. Therefore, the current loop can now be added to the system as described in the following section.

### 4.3.4 Tuning current controllers

To tune the gains of the proportional-integral (PI) controller, the 5ms pulse of reference q-axis current with duty cycle of 20% needs to be applied as the desired current. Initially, the integration gain is kept at zero and the proportional gain is raised. This procedure needs to be continued until the measured currents reach to 70% of the reference current. Then, the integration gain needs to be tuned to reduce

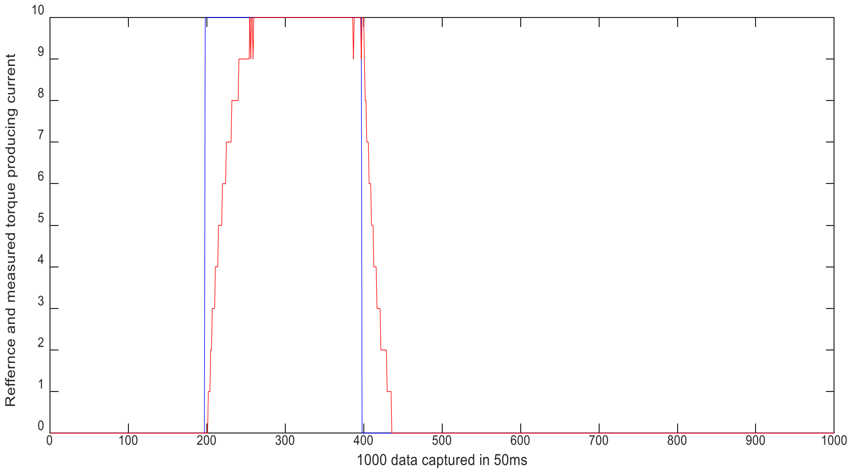


Fig. 4. 12 Performance of digital current controller

the steady-state error. The trade-off between the fast performance of the current controller and the acceptable level of overshoot should be considered for tuning the integration gain. The 5–10 % overshoot is an acceptable rate that prevents current-trip activation. It should also be considered that the tuning PI gains are achieved by defining the electrical speed at zero level. Fig. 4.12 shows the performance of the PI current controller when $i_{qs}^{e*} = 10A$.

### 4.4 Summary

This chapter has presented the test setups which have been used to validate the proposed control schemes in this project. Initially, the dual-core experimenter kit has been explained in detail for emulating IM and making the interface between the control scheme and IM model. Finally, the test rig set-up is explained by dividing it into three different parts, the parameterisation of 2.2 KW squirrel cage IM, the analyses for interfacing different modules and motor control units and the requirement for protecting circuits and calibration of sensors.

# CHAPTER 5

# Model-Based Voltage Control with Maximized Utilization of the DC-Link Voltage in the Field-weakening Region of Induction Machines

### 5.1 Introduction

This chapter proposes a bespoke model-based voltage control method that enables the full hexagonal voltage reference trajectory for the field-weakening region to be reached. So far, all model-based control methods are constrained by the inscribed voltage circle which lies within the hexagonal voltage boundary. This restriction limits the available inverter output voltage across the motor windings, which in turns restricts the output torque of the drive. In order to achieve the full hexagonal voltage trajectory, this chapter introduces a new calculation of the d-axis current for the entire speed range in the field-weakening region. This calculation is based on the hexagonal voltage boundary equations and the stator voltage vector position. This generates a new reference d-axis current that minimises the difference between the hexagonal voltage boundary and its inscribed voltage circle. As a result, the proposed d-axis current maximises the output torque and output power in the field weakening region.

### 5.2 Flux weakening based on the currents control

#### 5.2.1 Mathematical development of the steady-state model

Fig. 5.1 shows the steady-state equivalent circuit model of an IM, where all leakage inductances are referred to the stator side. This is achieved by using (3.25) and letting $p = 0$ and subtituding $\omega_{sl} = \omega_e - \omega_r$. To develop the voltage model of IM in terms of rotor flux, the stator flux $\lambda_{dqs}^e$ should be defined with respect to the rotor flux $\lambda_{dqr}^e$ as shown below:

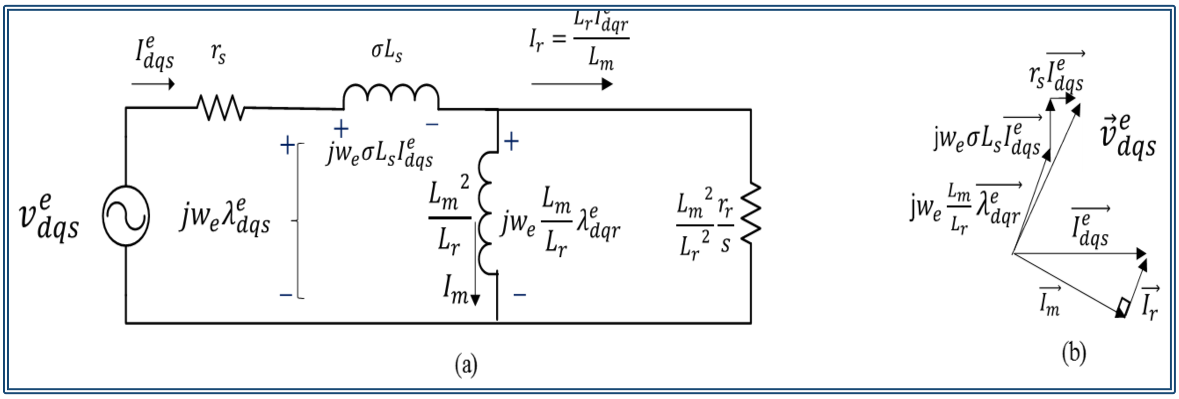


Fig. 5.1 (a) Equivalent circuit of IM with all leakage inductances referred to the stator side (b) Voltage vector diagram for RFOC

$$\lambda^e_{dqs} = \sigma L_s\, I^e_{dqs} + \frac{L_m\, \lambda^e_{dqr}}{L_r} \tag{5.1}$$

Now, the stator voltage model of IM can be defined as follows:

$$v^e_{ds} = r_s\, i^e_{ds} + \sigma L_s\, \frac{d}{dt} i^e_{ds} + \frac{L_m}{L_r}\frac{d}{dt}\lambda^e_{dr} - \omega_e\, \frac{L_m\, \lambda^e_{qr}}{L_r} - \omega_e\, \sigma L_s\, i^e_{qs} \tag{5.2}$$

$$v^e_{qs} = r_s\, i^e_{qs} + \sigma L_s\, \frac{d}{dt} i^e_{qs} + \frac{L_m}{L_r}\frac{d}{dt}\lambda^e_{qr} + \omega_e\, \frac{L_m\, \lambda^e_{dr}}{L_r} + \omega_e\, \sigma L_s\, i^e_{ds} \tag{5.3}$$

Then, the simplified model of IM in steady state condition can be derived as follows:

$$v^e_{ds} = r_s\, i^e_{ds} - \omega_e\, \sigma L_s\, i^e_{qs} \tag{5.4}$$

$$v^e_{qs} = r_s\, i^e_{qs} + \omega_{\mathrm{e}}\, \frac{L_m\, \lambda^e_{dr}}{L_r} + \omega_{\mathrm{e}}\, \sigma L_s\, i^e_{ds} \tag{5.5}$$

Based on the IM model defined by (5.4) and (5.5), the phasor diagram shown in Fig. 5.1b can be produced. As illustrated in Fig.5.1b, the stator voltage $\vec{v}^e_{dqs}$ is compensating the resistance voltage, $r_s\vec{I}^e_{dqs}$, the leakage inductance voltage, $j\omega_{\mathrm{e}}\, \sigma L_s\vec{I}^e_{dqs}$ and the rotor flux voltage, $\mathrm{j}\omega_{\mathrm{e}}\, \frac{L_m}{L_r}\vec{\lambda}^e_{dqr}$. Therefore, all these voltage terms need to be compensated by the stator voltage in order to increase the motor speed. However, the amplitude of $\vec{v}^e_{dqs}$ is restricted by the inverter output voltage $\frac{V_{DC}}{\sqrt{3}}$, in conventional model based control [88]. It is also worth noting that power electronics inverters and electric motors are also limited by the maximum current $I_{s,max}$ rating [2]. Therefore, voltage and current limitations need to be satisfied in all speed operational regions for motor control applications.

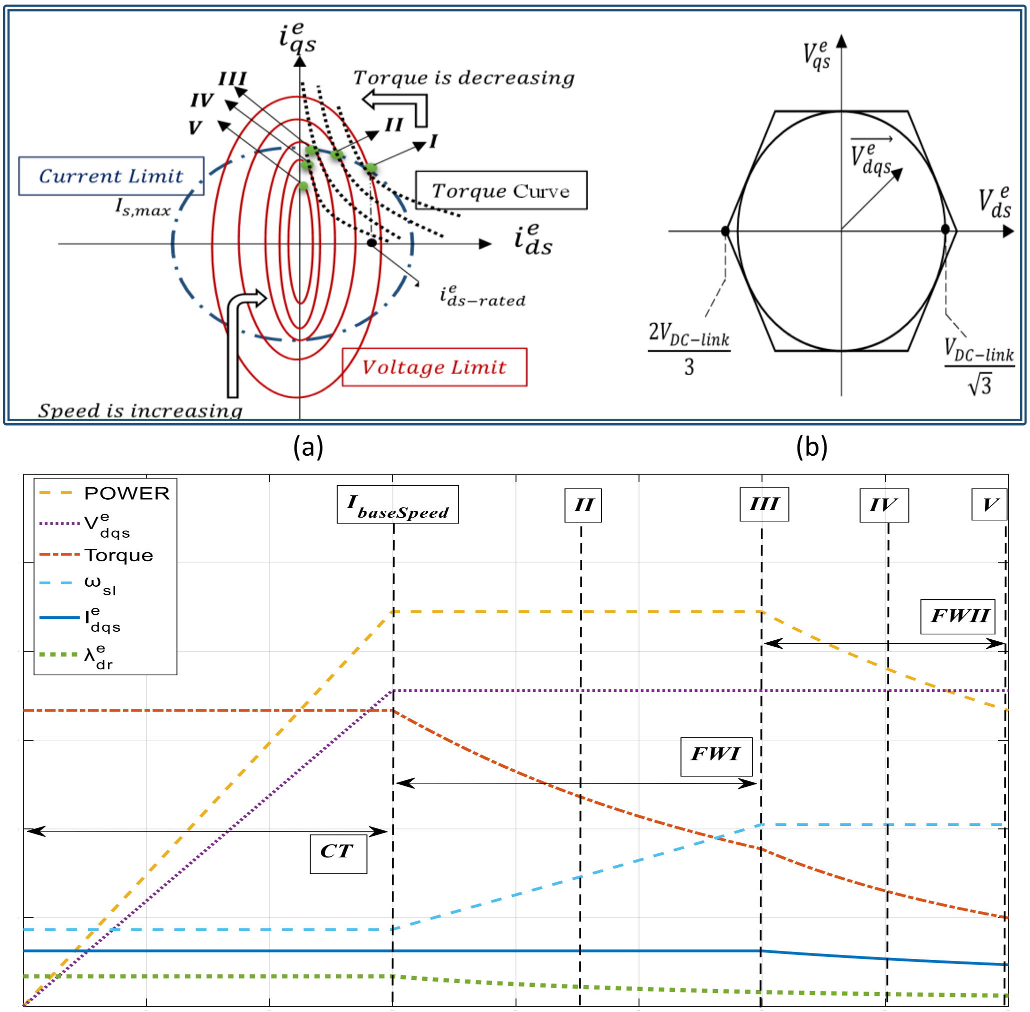


(c)

Fig. 5.2 (a) Current and voltage limits for IM (b) Voltage trajectory in SVM (c) Characterisation of IM in different operational regions

### 5.2.2 Voltage and current constraints as function of current components

In the model-based control method, the reference flux needs to be calculated by using the IM model where the stator current and stator voltage are limited as explained in the Section 5.2.1 above. Therefore, to address the reference flux at each rotor speed, the voltage and current constraints equation must be defined as:

$$\begin{cases} (i_{ds}^e)^2 + (i_{qs}^e)^2 \leq (I_{s,max})^2 \\ (v_{ds}^e)^2 + \left(v_{qs}^e\right)^2 \leq \left(V_{s,max}\right)^2 \end{cases} \tag{5.6}$$

As can be seen from (5.6), the amplitude of stator current, which consists of $i_{ds}^e$ and $i_{qs}^e$, has to be lower than the maximum current rating $I_{s,max}$ of the IM and the inverter. The current constraint equation is illustrated in Fig. 5.2a as a circle. This current limit is satisfied as long as the stator current terms are within the circle. In model-based methods, the voltage constraint equation also needs to be defined in terms of current components. This is because the reference currents are designed based on these two constraints. Therefore, the description of voltage limitation could be expressed in terms of current with the reasonable assumption of neglecting the inductance saturation and resistance loss as shown in (5.4) and (5.5). Hence, the voltage constraint can be achieved by substituting (5.4) and (5.5) into (5.6), yielding (5.7) as follows:

$$\frac{{i_{ds}^{e}}^{2}}{(V_{max,s})^2/(\omega_{\mathrm{e}}\,L_s)^2}+\frac{{i_{qs}^{e}}^{2}}{(V_{max,s})^2/(\omega_{\mathrm{e}}\,\sigma L_s)^2}\leq 1 \tag{5.7}$$

This equation is presented by an ellipse graph on the Cartesian plane of the d-q axis current portrayed in Fig. 5.2a. The major axis of this ellipse is vertical because the value of the denominator $i_{qs}^{e}$ in (5.7) is higher than that of the denominator$i_{ds}^{e}$. This is because the existence of the leakage coefficient in the $i_{qs}^{e}$ denominator has a value of less than one. Furthermore, it should be noted that the extra slope in the voltage ellipse along the $i_{qs}^{e}$ axis needs to be considered in case of high stator resistance and low leakage coefficient $\sigma$ [89]. Likewise, the voltage limitation could be satisfied if the current terms are placed within the voltage ellipse, depicted in Fig. 5.2a. It should also be noted that voltage ellipse shrinks towards its centre as speed increases [90].

Additionally, the maximum available voltage, $V_{s,max}$ in SVM, plays an important role in satisfying the voltage constraint as can be seen from (5.7). This inverter voltage is utilised by the stator voltage, $\vec{v}_{dqs}^{e}$ of the IM to compensate the motor voltage terms depicted in Fig. 5.1a. Figure 5.3 shows that $\vec{v}_{dqs}^{e}$is compensating the two main voltage terms of the motor, $jw_e\frac{L_m}{L_r}\vec{\lambda}_{dqr}^{e}$ and $j\omega_{\mathrm{e}}\,\sigma L_s I_s$ in the constant torque region. The amplitudes of $j\omega_{\mathrm{e}}\,\sigma L_s I_s$ and $j\omega_{\mathrm{e}}\,\frac{L_m}{L_r}\vec{\lambda}_{dqr}^{e}$ are increasing with the speed, which requires higher voltage to be extracted from the inverter. As shown in Fig.5a, the rotor flux voltage, $j\omega_{\mathrm{e}}\,\frac{L_m}{L_r}\vec{\lambda}_{dqr}^{e}$ is the dominant term of the stator voltage at the starting point of the first stage of field weakening (FWI). Therefore, to operate in the first stage of field weakening, reducing the magnetizing current $I_m$ (i.e. hence $\vec{\lambda}_{dqr}^{e}$ ) is considered as an effective way to satisfy the voltage constraint. On the

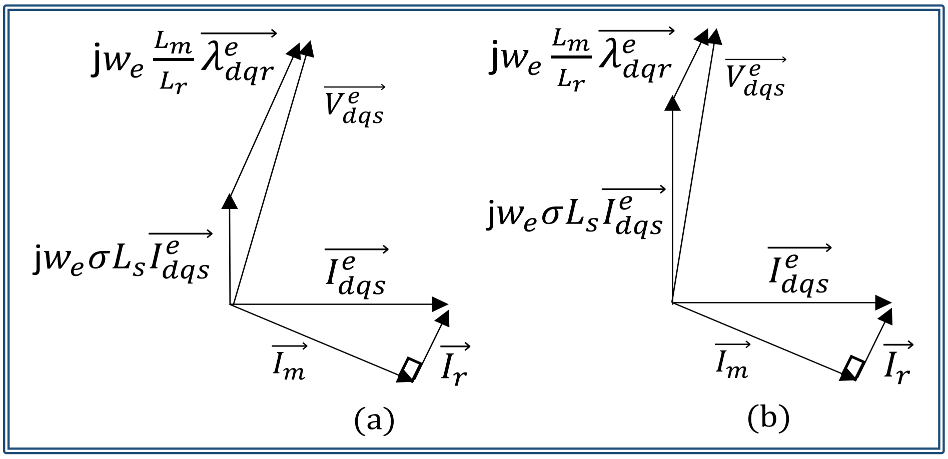


Fig. 5.3 Phasor diagram for stator voltage in (a) First stage of field weakening (b) Second stage of field weakening

other hand, further reduction of $I_m$in FWI results in a voltage drop across $\omega_e \frac{L_m}{L_r}\vec{\lambda}_{dqr}^e$ . Consequently, this makes $\omega_e \sigma L_s I_s$ the dominating element of the absorbed voltage in the second stage of field weakening (FWII) as shown in Fig. 5.3b. To satisfy both, voltage and current constraints in motor control applications, the different operational regions need to be considered when designing the reference currents as explained in the next section.

**5.2.3 Constant torque (CT), first Stage of Field Weakening (FWI) and second Stage of field weakening (FWII)**

Due to the current and voltage constraints, operation of IM is split into three different speed regions (Fig. 5.2c). As shown at Point I in Fig. 5.2a, c, the maximum torque is generated based on the rated flux level and the inverter/machine current limitation in the low speed region (below the base speed) [91, 92]. The region below the base speed is called constant torque (CT). Therefore, the maximum available $i_{qs}^e$ is calculated as follows:

$$\frac{{i_{ds}^e}^2}{(V_{max,s})^2/(\omega_e L_s)^2} + \frac{{i_{qs}^e}^2}{(V_{max,s})^2/(\omega_e \sigma L_s)^2} \leq 1 \tag{5.8}$$

The calculated base speed has to be adjusted based on the flux level at the rated condition which is varied according to rated current. In general, a high current rating, which produces large flux value, causes the lower base speed. The base speed is the starting point of FWI where the maximum power is delivered to the machine by reducing the flux level (Fig. 4c). This flux reduction maintains the back electromagnetic force component ($\omega_{\mathrm{e}} \frac{L_m \lambda_{dr}^e}{L_r}$) at nearly constant level. As shown in Fig. 5.2a, c, the rotor flux is reduced from point I to III by decreasing $i_{ds}^e$ . In model-based voltage control, the reference d-axis and q-axis current signals are calculated using (5.6) and (5.7), which can be expressed as:

$$\begin{cases} i_{qs}^{e*} = \dfrac{4T_e^* L_r}{3PL_m^2 i_{ds}^e} \\ i_{ds}^{e*} = \sqrt{\dfrac{\left(V_{s,max}\right)^2}{2(\omega_{\mathrm{e}}\, L_s)^2} + \dfrac{1}{2}\sqrt{\left(\dfrac{\left(V_{s,max}\right)^2}{(\omega_{\mathrm{e}}\, L_s)^2}\right)^2 - 4\left(\dfrac{4\sigma T_e^* L_r}{\omega_{\mathrm{e}}\, 3PL_m^2}\right)^2}} \end{cases} \tag{5.9}$$

In case the maximum torque is required at any speed, then the maximum q-axis current is used and therefore, (9) becomes:

$$\begin{cases} i_{qs}^{e*} = \sqrt{(I_{s,max})^2 - (i_{ds}^{e*})^2} \\ i_{ds}^{e*} = \sqrt{\dfrac{\left(V_{s,max}\right)^2 - (\omega_{\mathrm{e}}\, \sigma L_s)^2 (I_{s,max})^2}{(\omega_{\mathrm{e}}\, L_s)^2 - (\omega_{\mathrm{e}}\, \sigma L_s)^2}} \end{cases} \tag{5.10}$$

As the speed is increasing in region FWI, the slip speed becomes close to its maximum value (Fig. 5.2c). This is because the available applied q-axis current reaches the limit and the slip speed cannot be further increased. Hence, this is the point where the FWII region begins. The maximum torque in this high speed stage is achieved by keeping the angle between stator and rotor flux at 45°. In this case, the torque-producing-current is reduced as shown in Point III to V in Fig. 5.2a, which leads to a reduction in output power of IM. The current reduction continues until the voltage vector with an amplitude of $V_{s,max}$ is placed at $90° \mp 45°$ in the synchronous frame. This condition can be achieved by:

$$i_{ds}^{e*} = \sqrt{\frac{(V_{s,max})^2}{2(\omega_{\mathrm{e}}\, L_s)^2}} \tag{5.11}$$

$$i_{ds}^{e*} = \sqrt{\frac{(V_{s,max})^2}{2(\omega_{\mathrm{e}}\, L_s)^2}} \tag{5.12}$$

$$\omega_{sl\_max} = \frac{i_{qs}^{e*}}{\tau_r i_{ds}^{e*}} = \frac{1}{\tau_r \sigma} \tag{5.13}$$

So in this speed region, the value of torque-producing-current can be presented as proportional to flux-producing-current ($i_{qs}^{e*} = \frac{\lambda_{ds}^{e}}{\sigma L_s} = \frac{i_{ds}^{e*}}{\sigma}$). In conventional model based control, the calculated $i_{ds}^{e*}$ in (5.8) to (5.12) is based on the inscribed voltage circle within the hexagonal voltage boundary (Fig. 5.2b).

### 5.3 Proposed model based scheme

The proposed voltage control algorithm for field weakening regions is portrayed in Fig. 5.4, where the output torque of the IM is increased as a result of maximum utilization of $V_{DC}$ in SVM.

The maximum inverter voltage is exploited by substituting the equation of each side of the hexagon voltage limitation (5.14) to (5.19) for corresponding angle of stator voltage vector $\theta_v$ into (5.9) to (5.12). So in this case, the stator voltage vector reaches the hexagon boundary, which means maximum $V_{DC}$is extracted. The equations for each side of the hexagon in terms of d-q axis of voltage components are derived based on $\theta_v$ as follows:

$$0 \le \theta_v < \frac{\pi}{3} \quad {V_{s,max}}^2 = (\frac{2}{3}V_{DC}(1 - \frac{\frac{\sqrt{3}}{3}\tan\theta_v}{\frac{\sqrt{3}}{3}\tan\theta_v + 1}))^2 + (\frac{2}{3}V_{DC}(\frac{\tan\theta_v}{\frac{\sqrt{3}}{3}\tan\theta_v + 1}))^2 \tag{5.14}$$

$$\frac{\pi}{3} \le \theta_v < \frac{2\pi}{3} \quad {V_{s,max}}^2 = (\frac{2}{3}V_{DC}(\frac{\sqrt{3}}{2}\tan(\frac{\pi}{2} - \theta_v)))^2 + (\frac{2}{3}V_{DC}\frac{\sqrt{3}}{2})^2 \tag{5.15}$$

$$\frac{2\pi}{3} \le \theta_v < \pi \quad {V_{s,max}}^2 = (\frac{2}{3}V_{DC}(\frac{\frac{\sqrt{3}}{3}\tan(\pi - \theta_v)}{\frac{\sqrt{3}}{3}\tan(\pi - \theta_v) + 1} - 1))^2 + (\frac{2}{3}V_{DC}(\frac{\tan(\pi - \theta_v)}{\frac{\sqrt{3}}{3}\tan(\pi - \theta_v) + 1}))^2 \tag{5.16}$$

$$\pi \le \theta_v < \frac{4\pi}{3} \quad {V_{s,max}}^2 = (\frac{2}{3}V_{DC}(-1 - \frac{\frac{\sqrt{3}}{3}(-\tan(\theta_v - \pi))}{\frac{\sqrt{3}}{3}\tan(\theta_v - \pi) + 1}))^2 + (\frac{2}{3}V_{DC}(\frac{-\tan\theta_v}{\frac{\sqrt{3}}{3}\tan(\theta_v - \pi) + 1}))^2 \tag{5.17}$$

$$\frac{4\pi}{3} \le \theta_v < \frac{5\pi}{3} \quad {V_{s,max}}^2 = (\frac{2}{3}V_{DC}(\frac{\sqrt{3}}{2}\tan(\frac{3\pi}{2} - \theta_v)))^2 + (\frac{2}{3}V_{DC}\frac{\sqrt{3}}{2})^2 \tag{5.18}$$

$$\frac{5\pi}{3} \le \theta_v < 2\pi \quad {V_{s,max}}^2 = (\frac{2}{3}V_{DC}(+1 - \frac{\frac{\sqrt{3}}{3}(-\tan(2\pi - \theta_v))}{\frac{\sqrt{3}}{3}\tan(2\pi - \theta_v) + 1}))^2 + (\frac{2}{3}V_{DC}(\frac{-\tan\theta_v}{\frac{\sqrt{3}}{3}\tan(2\pi - \theta_v) + 1}))^2 \tag{5.19}$$

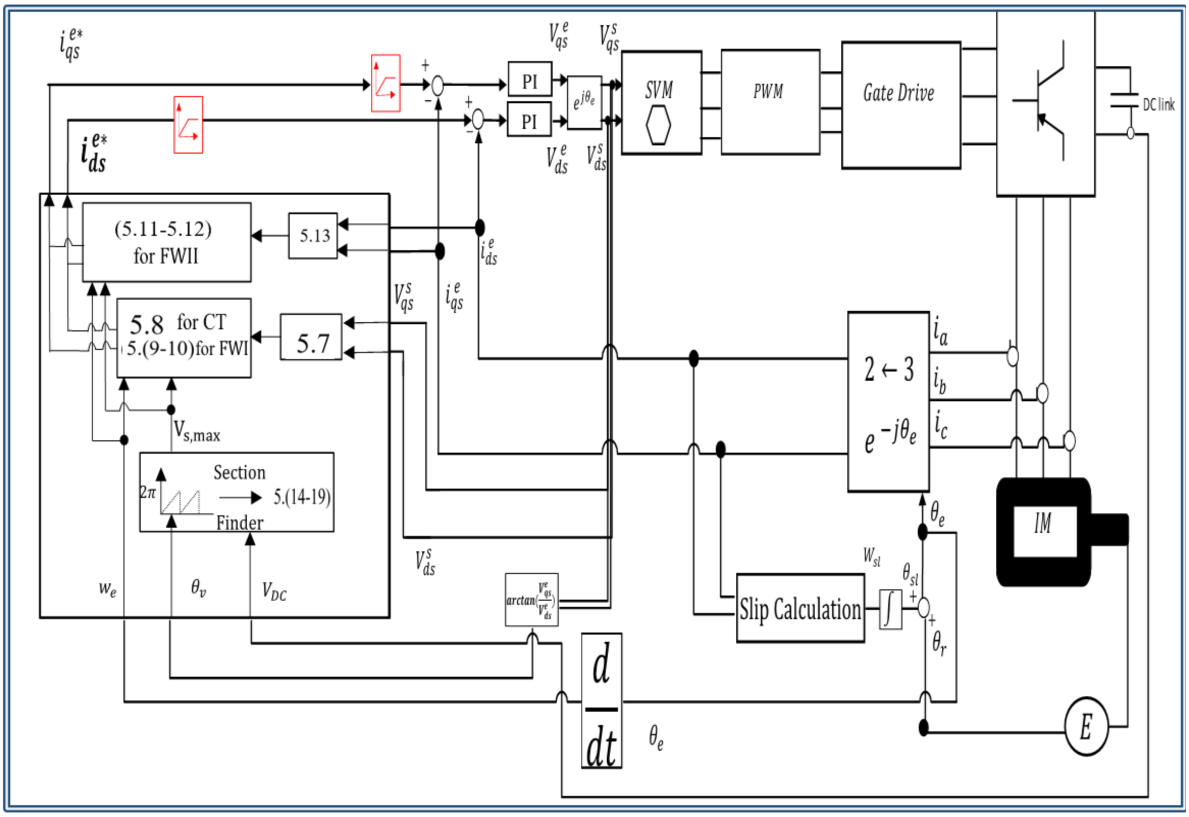


(a)

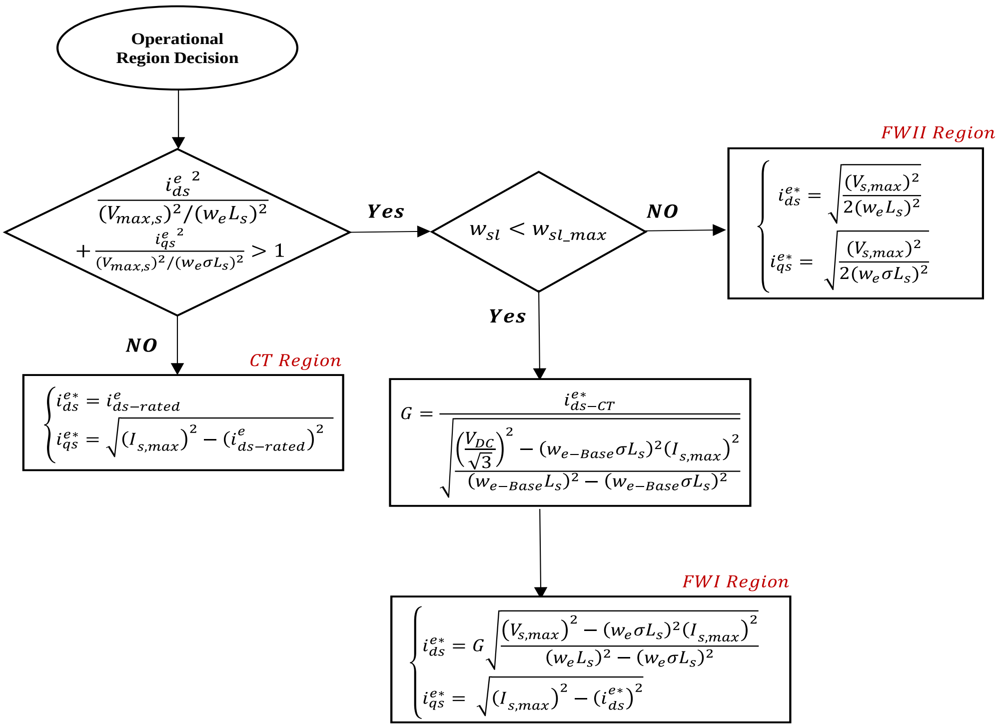


(b)

Fig. 5.4 Proposed model-based control to maximise the utilisation of inverter voltage (a) Block diagram of induction motor drive (b) Proposed algorithm flowchart

As shown in Fig. 5.4a and Fig. 5.4b, $V_{dqs}^{e}$and $i_{dqs}^{e}$ are used in (5.7) and (5.13) to detect the operation regions that facilitate the smooth and automatic transition of the proposed algorithm between CT and FWI and between FWI and FWII. However, it should be considered that if the appropriate flux reduction is not provided by the control scheme, then the drive system loses its controllability. That means that the current controllers lose track of the reference current signals.

To evaluate the performance of the proposed control method, the maximum calculated $i_{qs}^{e*}$ in (5.10) is directly applied to the machine instead of using its value from the torque controller. As shown in Fig. 5.5a, the maximum voltage magnitude, which is moving along the hexagon trajectory, is changing according to $\theta_v$ in any electrical cycle.

The proposed method exploits the maximum DC-link voltage range to increase the output torque and power of the IM. It is worth clarifying that the work presented in this chapter aimed at achieving the hexagonal voltage, which is the full accessible voltage in SVM and not utilising the full inverter voltage achieved by the six-step operational that holds the stator voltage angle and amplitude in the corner of the hexagonal boundary [12].

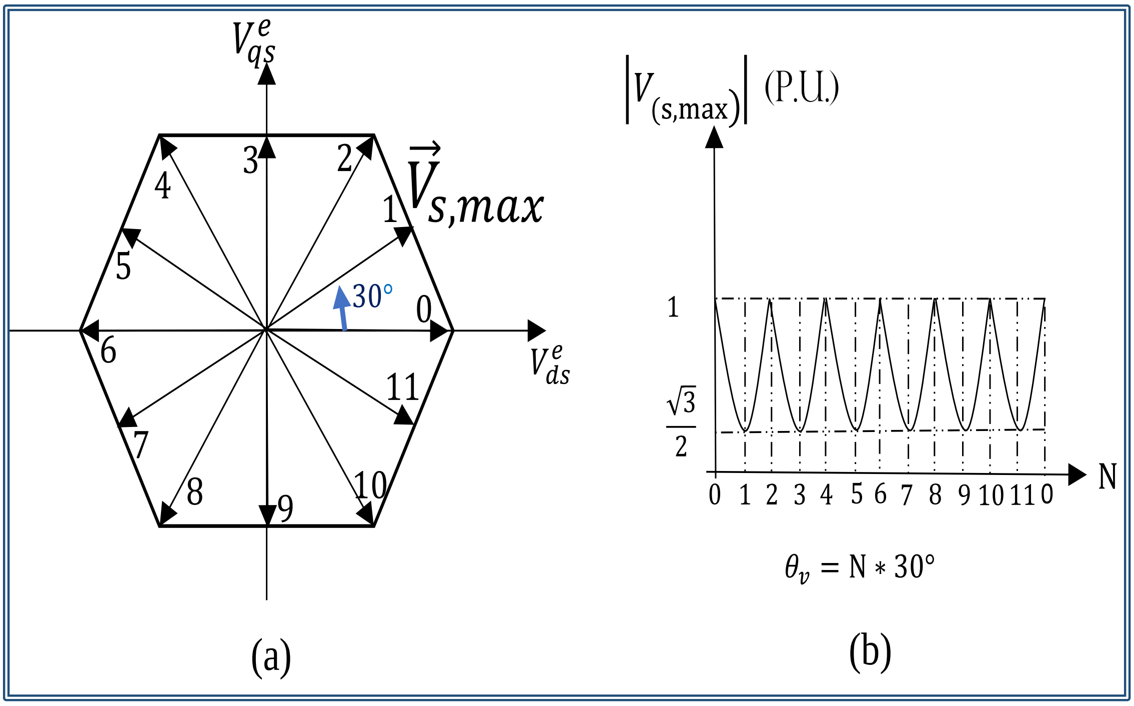


Fig. 5.5 (a)Trajectory of maximum available voltage vector (b) Amplitude of the maximum voltage vector

As shown in Fig. 5.6, the area of voltage constraint is extended in the proposed method. Comparing points A and B in Fig. 5.6 reveals that the voltage extension results in the IM being able to operate at a higher speed for the same $V_{DC}$. This is because more voltage is available to compensate for the back EMF at higher speed. This is the reason that the voltage limitation of point C (placed in the proposed voltage trajectory) at 1,700 rpm is close to point B (placed in the conventional voltage trajectory) at 1,500 rpm. Similarly, by taking a closer look at points C and D in Fig. 5.6, one can see that higher voltage at point C results in a higher torque as demonstrated in Fig. 5.2a. Furthermore, the maximum torque possible from the proposed method which satisfies the voltage and current constraint, is shown in Fig. 5.7 for different speeds. It is worth mentioning that these maximum torque values at different speed operations were achieved in an experimental test. In addition, the calculated optimum value of d-axis current reduces the required number of regulators in this method, which simplifies the control system. As depicted in Fig. 5.4, the reference d-axis current is produced based on mathematical equations without applying any regulators such as one used in Methods A, B and D shown in Fig. 2.1.

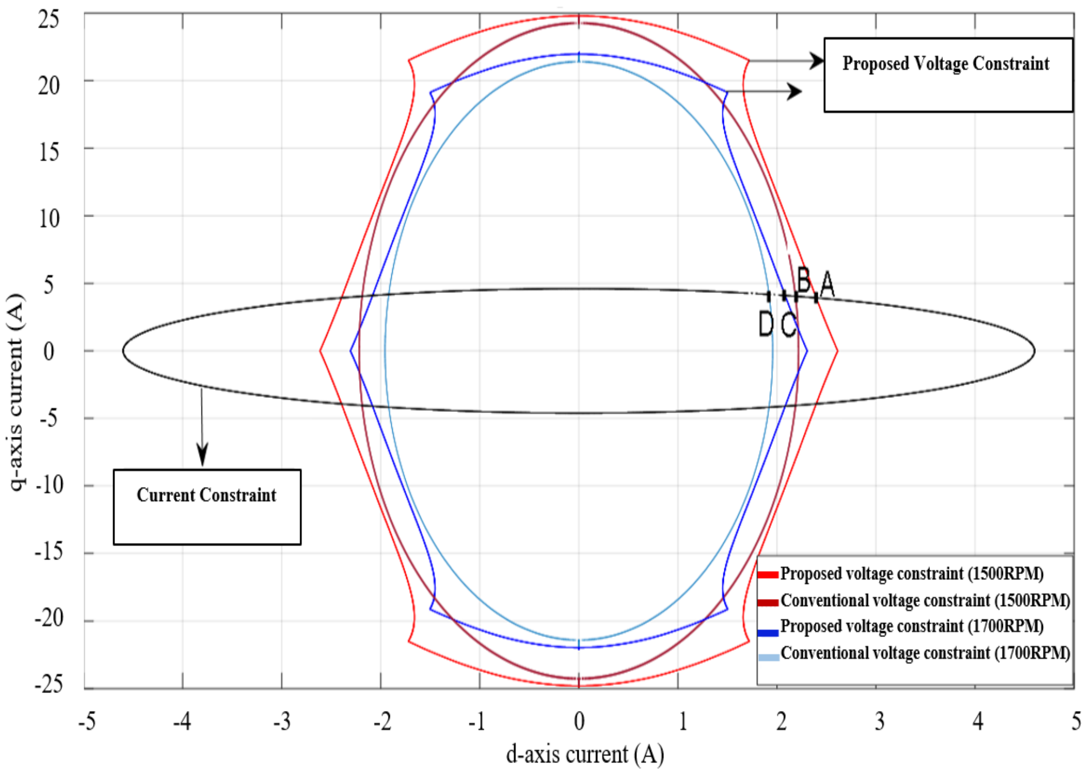


Fig. 5.6 Comparison of voltage constraint in proposed method and conventional model-based method

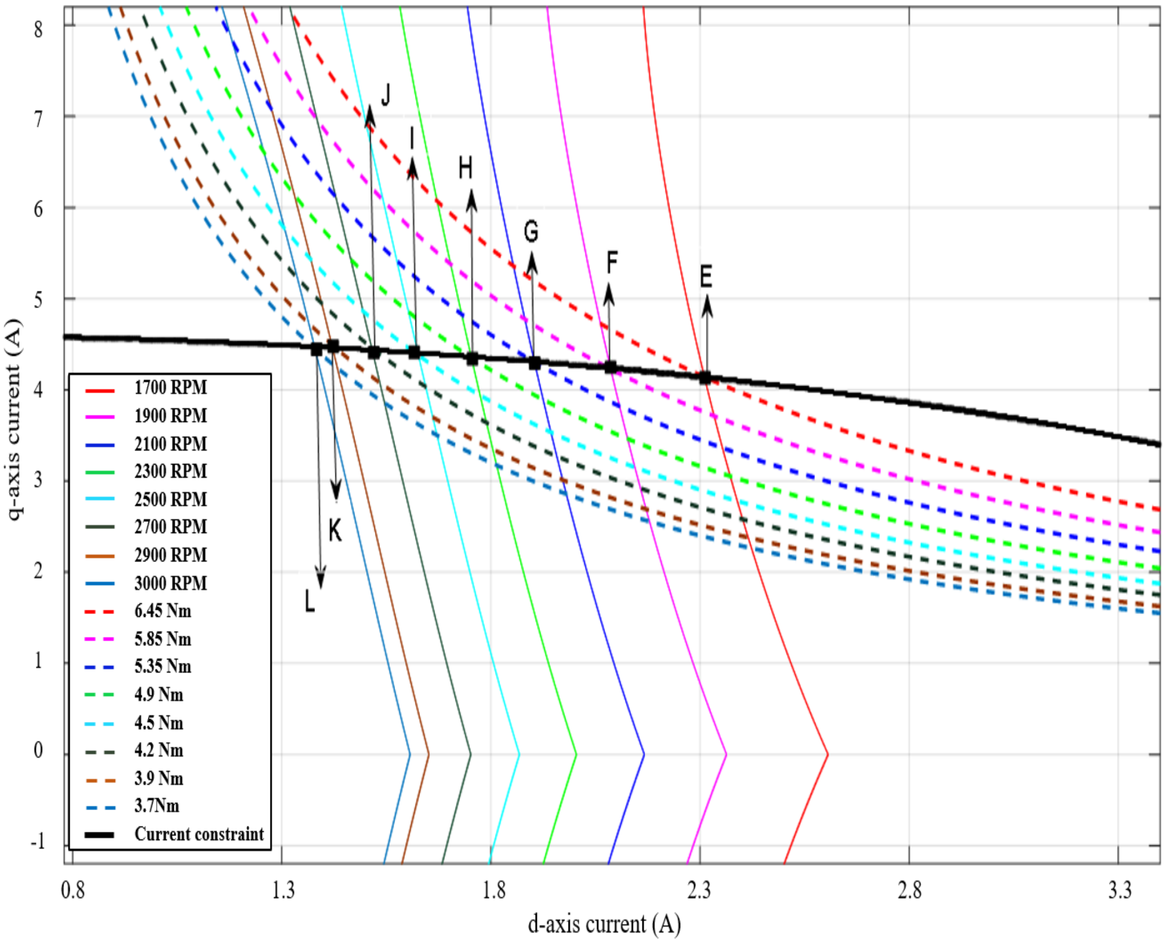


Fig. 5.7 Maximum torque produced by the proposed method at different operational speed for the IM characterised in Table 4.4 (Black solid line: current constraint; other solid line: voltage constraint at different speeds; dashed lines: torque)

In those methods, the reference d-axis current is produced based on a flux regulator, voltage regulator and look-up table, respectively. In practice, tuning these regulators is usually based on the trial and error, which requires a lot of efforts and time and more importantly, optimum performance is not guaranteed. Using the proposed algorithm means that the closed loop controlled system retains its stability even in maximum voltage utilisation condition. This is a result of the parabolic waveform changes in d-axis reference current, which applies the minimum current to satisfy the voltage boundary (as demonstrated in Fig. 5.5). This allows the measured current to closely track the desired current in spite of the lag in rotor flux and error in measured motor currents. This results in sufficient d-axis voltage margin to allow good dynamic performance for the current controller with a consequent reduction in torque ripple. As shown in (5.2), if there is insufficient d-axis of voltage, which happens in cases of high error in the d-axis current controller, then the q-axis current will be decreased. Under this condition the q-axis current fails to follow its reference current resulting in increased torque ripple.

The automatic transition from the CT region to FWI and from FWI to FW2 can also be achieved due to the algorithm recognising the transition points using (7) and (13). The automatic transition also provides starting points for the $i_{ds}^{e*}$ in the FWI region to be matched with the reference d-axis current in the CT region. This is due to the use of a Gain *G* which is multiplied by the d-axis current in (9) or (10) to ensure the correct starting value for $i_{ds}^{e*}$ when moving between regions (as demonstrated in Fig. 5.4b). Moreover, it should also be noted that the Gain *G* is only calculated in the first PWM cycle at the start of field weakening. To calculate this gain, d-axis part of equation (5.10) is used where the $\omega_{\mathrm{e}}$ and $V_{s,max}$ are replaced by $\omega_{\mathrm{e\_base}}$ and $\frac{1}{\sqrt{3}}V_{\mathrm{DC}}$. The replaced values of speed and DC-link voltage guarantee the starting of the field weakening region. This ensures that the minimum value of the parabolic d-axis current will be equal to the reference value of the d-axis current in the constant torque region, $i_{ds-CT}^{e*}$, as illustrated in Fig.5.8. This results in a very smooth torque transient without the need to calculate the base speed.

**5.4 Results**

The proposed control approach is implemented using a dual-core TMS320F28377D microcontroller. CPU1 of the controller is used to realise the control model presented in Fig. 5.4, whereas the d-q axis current controllers and SVM are implemented on CPU1.CLA. The execution time of the main interrupt service routine running in CPU1 is 11.18us for 20 kHz switching frequency. The current controllers and SVM running on CPU1.CLA execute in 5.32us. The experimental setup is based on a test IM coupled with a dynamometer based on a permanent magnet machine as depicted in Fig. 4.6. Sensing is provided by three CAS 15-NP current sensors, an AD215 ISO_AMP and a Gurley 2048 line optical encoder. To test the IM with the proposed torque based controller, the speed is adjusted with the dynamometer. The corresponding reference d-axis current is calculated based on operating speed to utilise the maximum of $V_{DC}$ and therefore provides the maximum torque. As the maximum speed of the load machine is restricted to 3,000 rpm, the field-weakening region of test IM is started at a lower base speed by applying 350V inverter input voltage instead of 700V. Thus tests were conducted at 1.1kW instead of 2.2kW, which is the rated power of the test motor.

### 5.4.1 Simulation and experimental results

#### 5.4.1.1 Reference and measured d-q axis current in CT and FW region

Fig. 5.8 shows the simulation results of the proposed controller from the CT region to the FW region. The theoretical analysis in Part C of Section II and the graph shown in Fig. 5.2 are confirmed by decreasing the d-axis current in the FW region as can be noticed in Fig. 5.8a1. It shows that the command for the flux-producing current $i_{ds}^{e*}$ has a sequence of parabolic shape that varies with $\theta_v$ and it is closely followed by measuring the d-axis current. This is because the parabolic variation of $i_{ds}^{e*}$ in the proposed method ensures that the produced back EMF is always compensated by the maximum available inverter voltage. Furthermore, the proposed method reduces $i_{ds}^{e*}$ at the bottom points of the parabolic shape, where the hexagonal voltage boundary has the lowest amplitude. As a result, motor currents follow the current references without any natural drop. The steady state results for d-q axis currents are demonstrated in Fig. 5a2, a3, b2, b3 for constant speed of 1,800 rpm and 2,500 rpm.

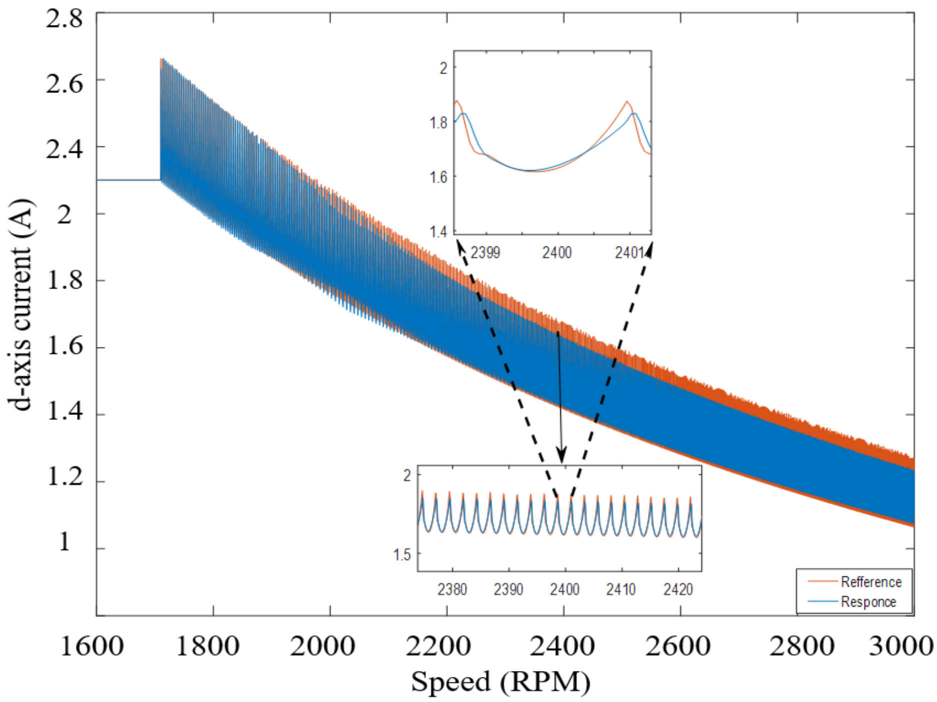


(a1)

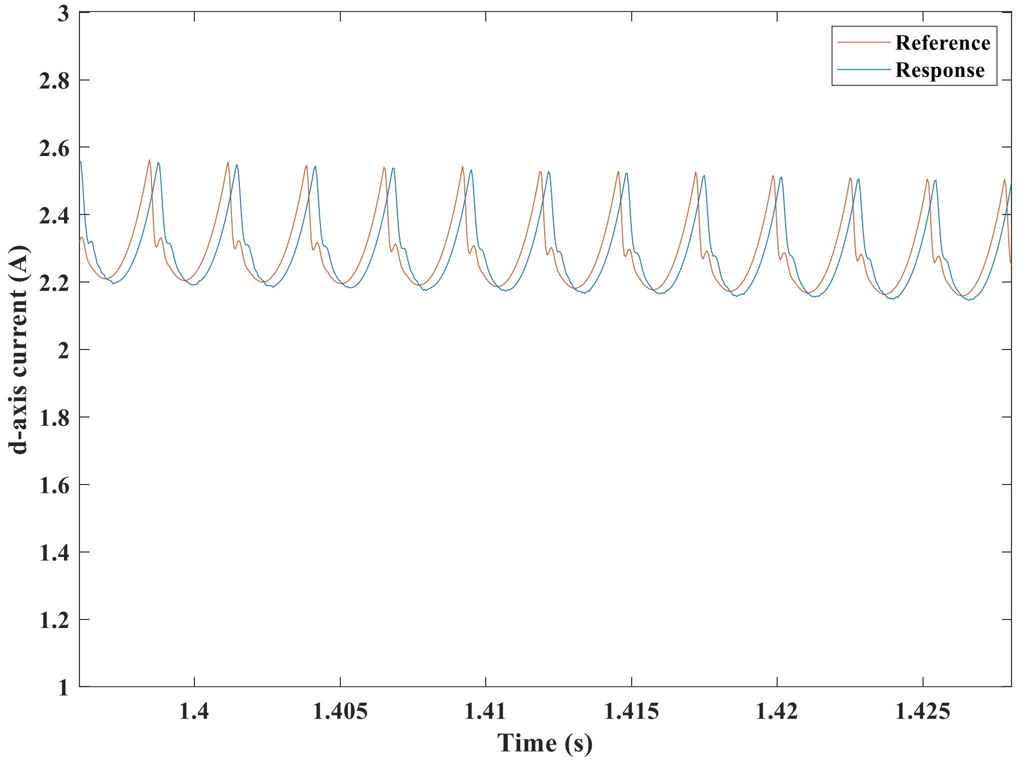
Reference
Response
d-axis current (A)
Time (s)
3
2.8
2.6
2.4
2.2
2
1.8
1.6
1.4
1.2
1
1.4
1.405
1.41
1.415
1.42
1.425

(a2)

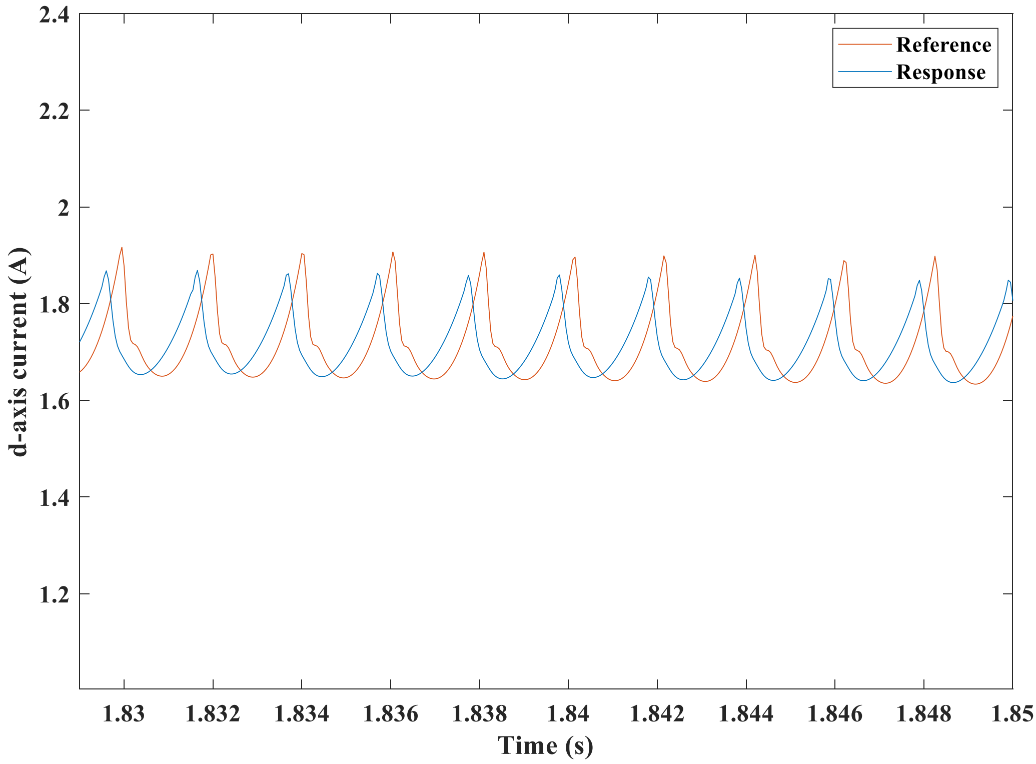
Reference
Response
d-axis current (A)
Time (s)
2.4
2.2
2
1.8
1.6
1.4
1.2
1.83
1.832
1.834
1.836
1.838
1.84
1.842
1.844
1.846
1.848
1.85

(a3)

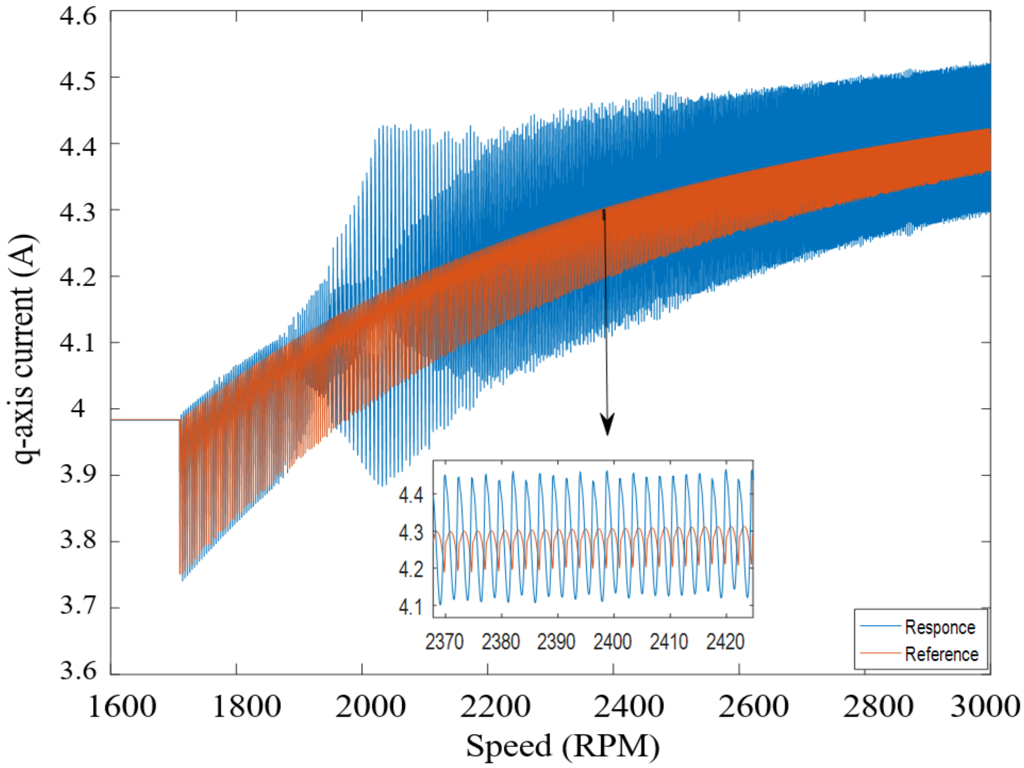

q-axis current (A)
Speed (RPM)
Responce
Reference


(b1)

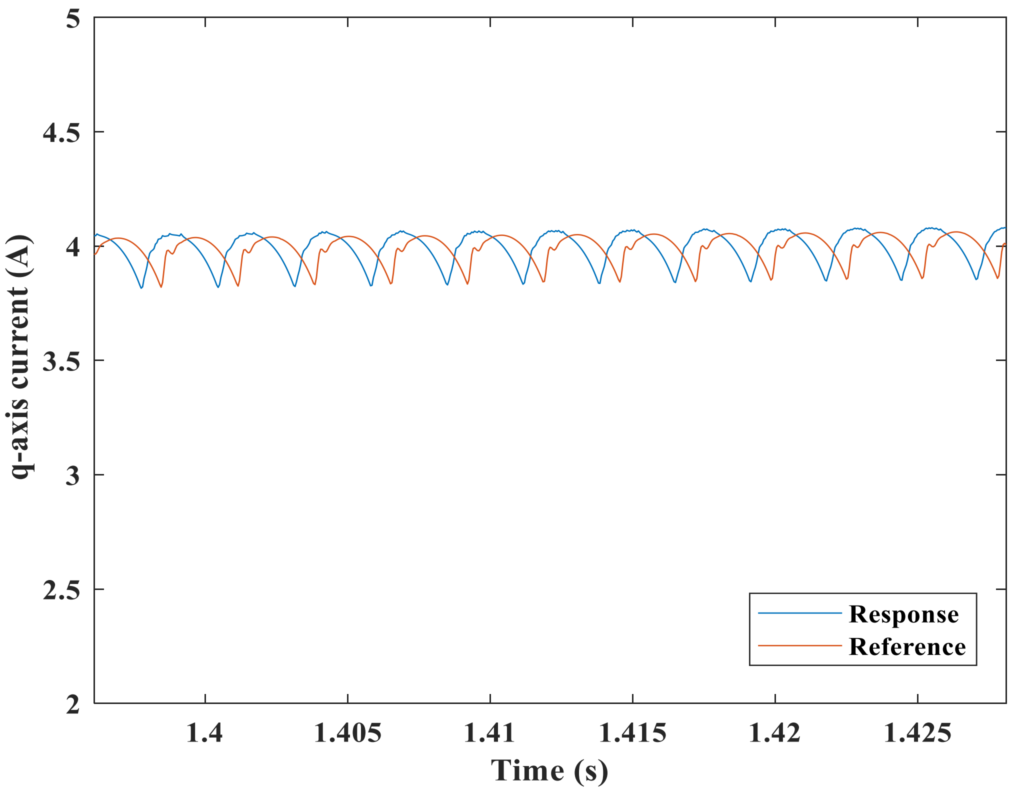

q-axis current (A)
Time (s)
Response
Reference


(b2)

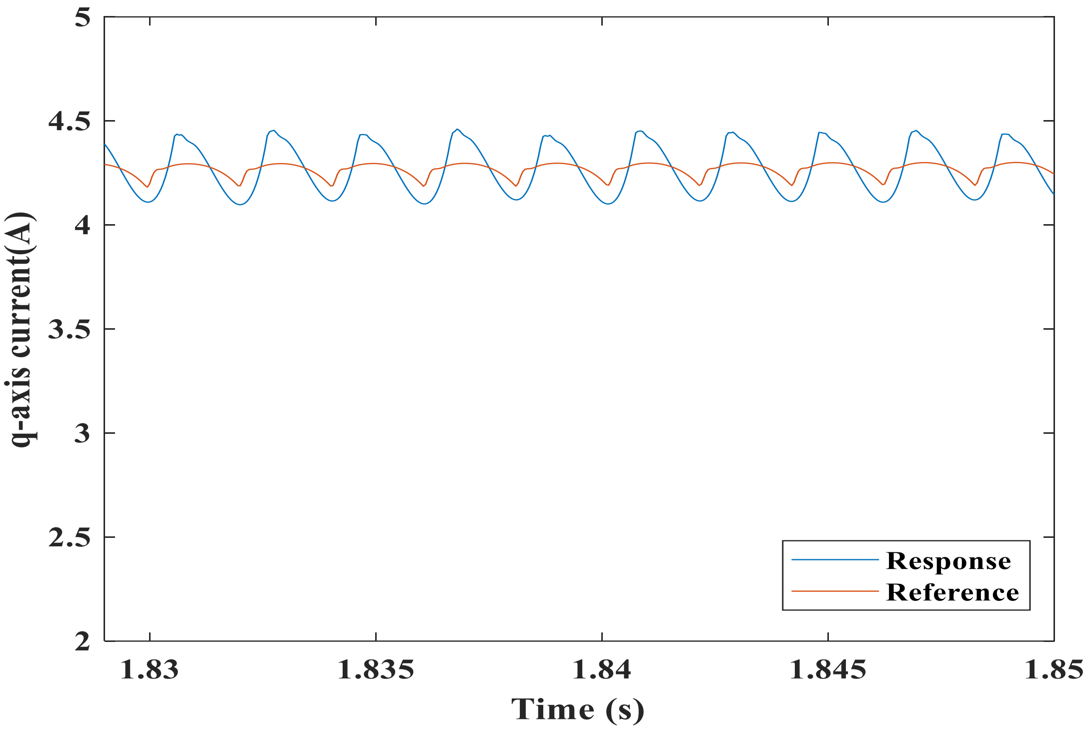


(b3)

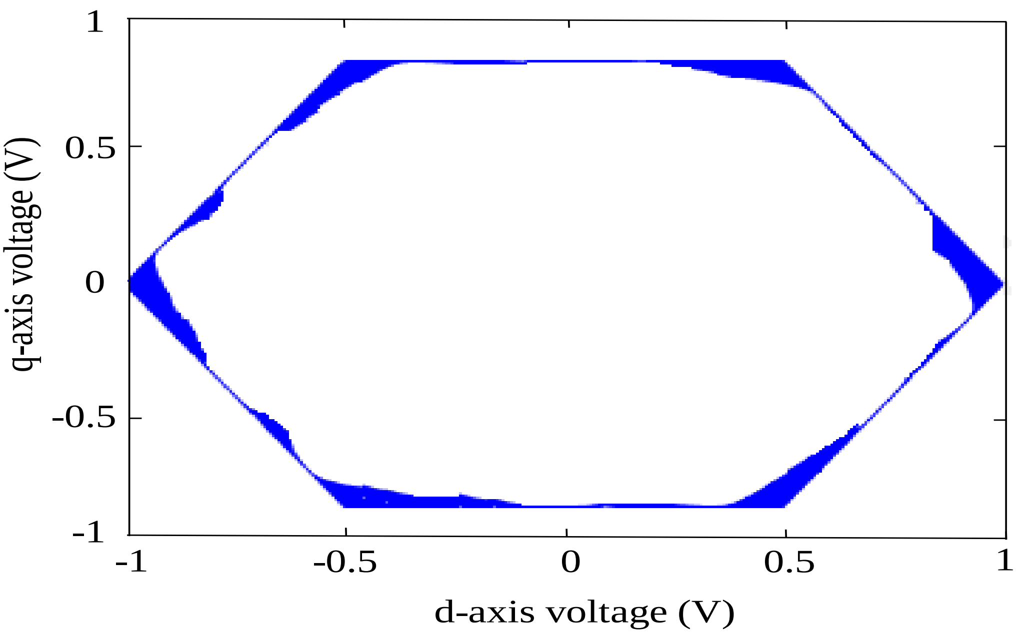


(C)

Fig. 5.8 Simulation results: (a) d-axis current (a1) in speed range of 1,600 rpm to 3,000 rpm, (a2) in steady-state condition for speed of 1,800rpm and torque of 5.8N.m and (a3) in steady-state condition for speed of 2,500rpm and torque of 4N.m (b) q-axis current (b1) in speed range of 1,600 rpm to 3,000 rpm (b2) ) in steady-state condition for speed of 1,800rpm and torque of 5.8N.m and (b3) in steady-state condition for speed of 2,400rpm and torque of 4N.m (c) voltage trajectory (P.U.) in rotor speed of 2,400 rpm.

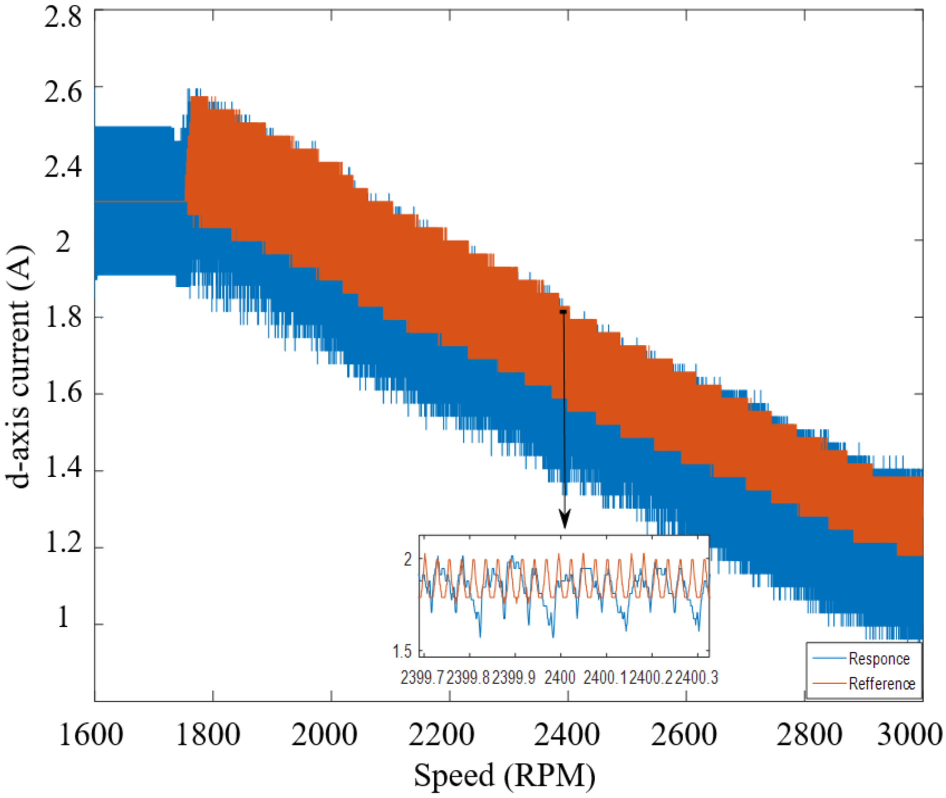
2.8
2.6
2.4
2
1.8
1.6
1.4
1.2
1
d-axis current (A)
2
1.5
2399.7 2399.8 2399.9 2400 2400.1 2400.2 2400.3
Responce
Refference
1600
1800
2000
2200
2400
2600
2800
3000
Speed (RPM)

(a)

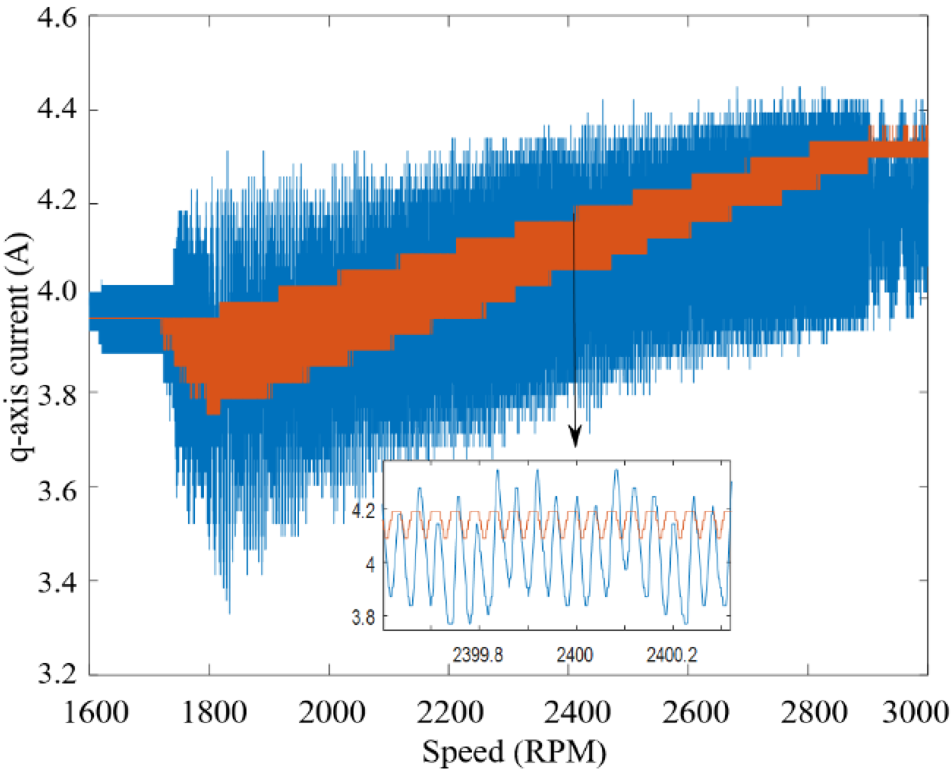
4.6
4.4
4.2
4.0
3.8
3.6
3.4
3.2
q-axis current (A)
4.2
4
3.8
2399.8
2400
2400.2
1600
1800
2000
2200
2400
2600
2800
3000
Speed (RPM)

(b)

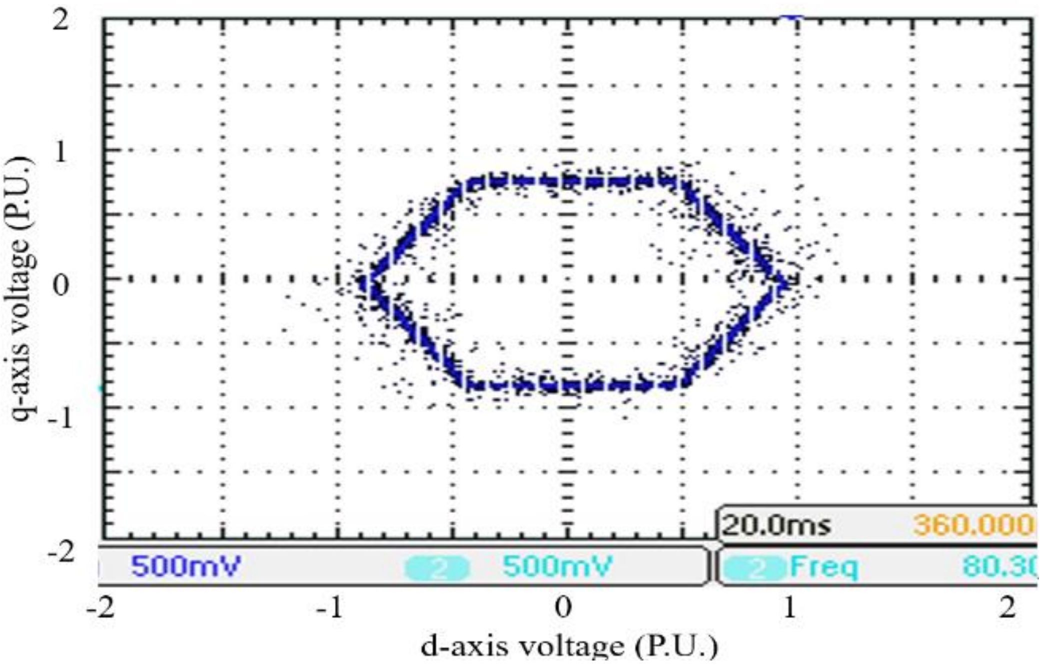


(c)

Fig. 5.9 Experimental results. (a) d-axis current. (b) q-axis current (c) voltage trajectory in rotor speed of 2,400rpm.

#### 5.4.1.2 Satisfied voltage and current constraint

The increment of q-axis current in Fig. 5.9b is the result of satisfying the current constraint explained in (11) and confirmed in Fig. 5.10a. As shown in Fig. 5.9c, the voltage vector trajectory is contained within the hexagon boundary corresponding to that explained in Fig. 5.2b. In addition, Fig. 5.10b, shows the d-q axis of voltages at 2,400 rpm, which guarantees the extraction of hexagonal voltage in terms of d-q axis voltage components as derived in (14) to (19). As shown in Fig. 5.8a1, the automatic and smooth transition from CT to FW is achieved in proposed algorithm as the starting point of $i_{ds}^{e*}$ in FWI is matched with the value in the CT region. Therefore, the electromagnetic torque starts the FWI from the last torque point in CT region. The experimental results in Fig. 5.9 and 5.11 show good agreement with the corresponding simulation results. The speed and reference and measured d-q axis currents are captured by oscilloscope via digital to analogue converters (DACs). Since there are only three DACs available in the microcontroller used in the experiment, separate tests have been conducted: conducted: $i_{ds}^{e*}, i_{ds}^{e}$ vs. speed (Fig. 5.9a) and $i_{qs}^{e*}, i_{qs}^{e}$ vs. speed (Fig. 5.9b). It is worth mentioning that the small difference between measured $i_{ds}^{e}$and $i_{qs}^{e}$ in MATLAB simulation and the experimental results is due to the existing error in current sensors and the offset in the analogue-to-digital converter (ADC). Also, the noise sensitivity of the DAC signals, which are in the low voltage range of 0 to 3V, causes some ripples in measured current signals even in the CT region.

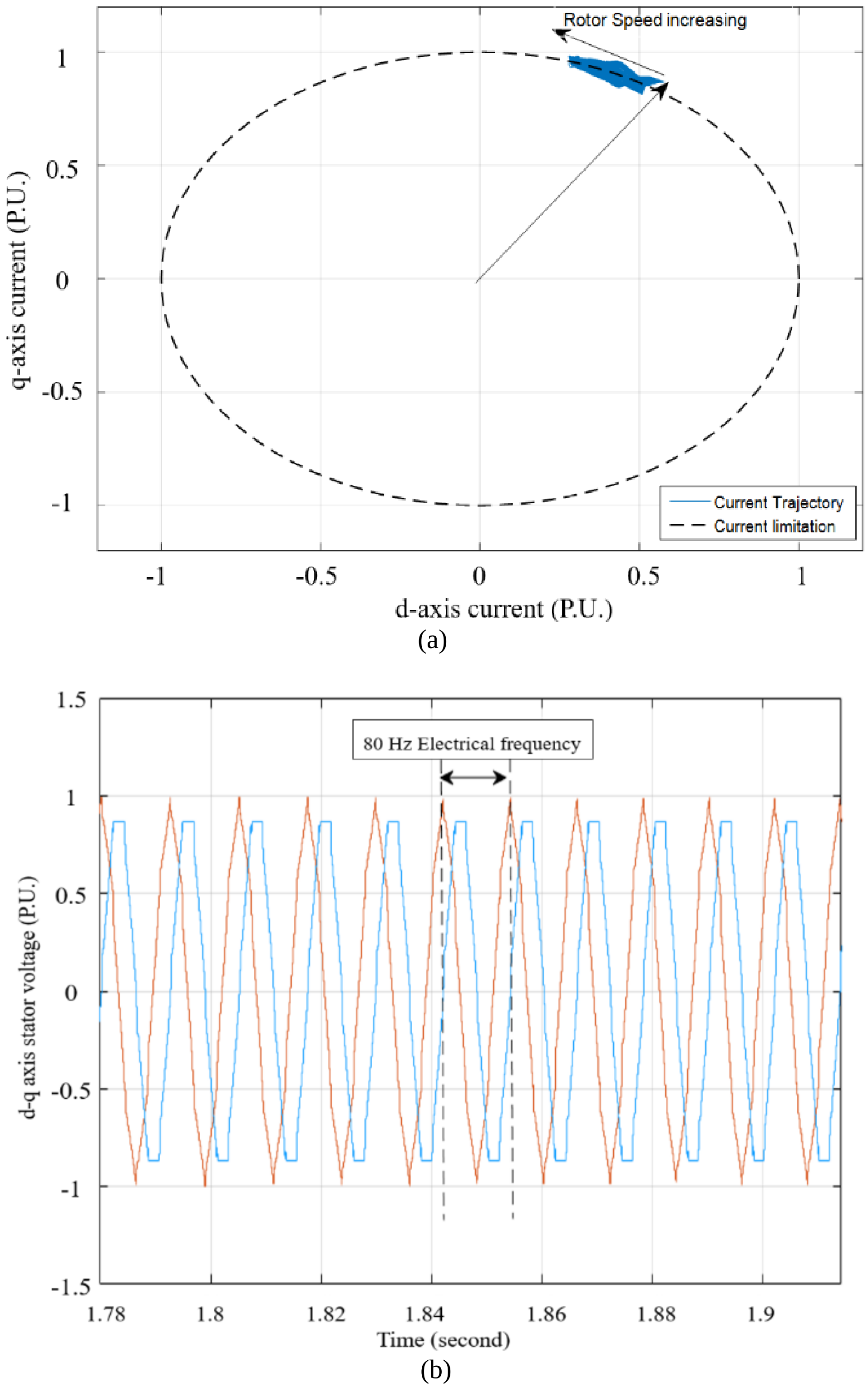


Fig. 5.10 Simulation results: (a) Current trajectory from standstill to 3,000 rpm. (b) d-q-axis of voltage (P.U.) in stationary frame at 2,400 rpm

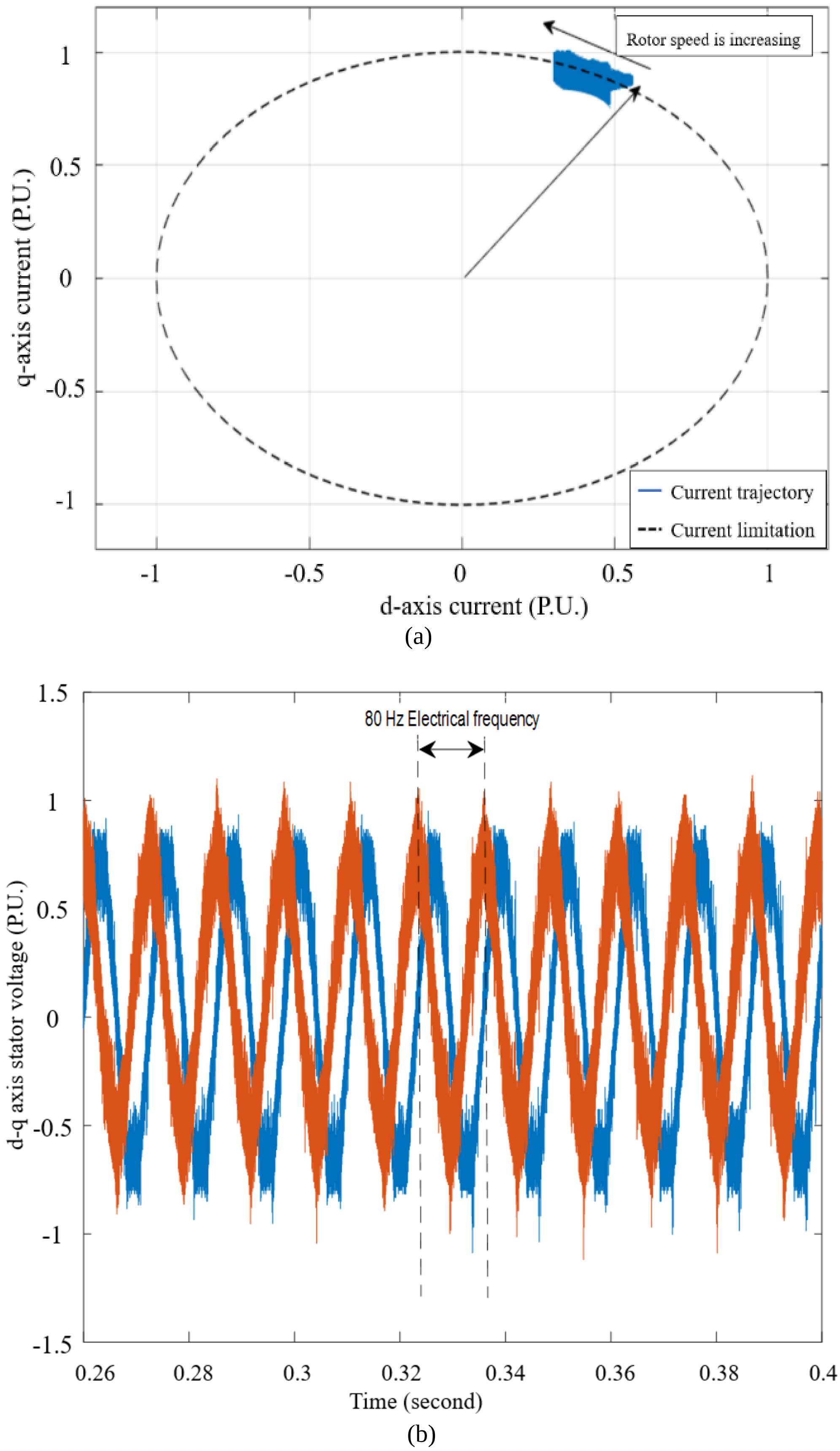


Fig. 5. 11 Experimental results: (a) Current trajectory from standstill to 3,000 rpm (b) d-q-axis of voltage (P.U.) in stationary frame at 2,400 rpm

### 5.4.1.3 Output torque and power in CT and FW region

In Fig. 5.12, the degradation of the dynamic performance of PI controllers and $i_{qs}^{e}$ ripples is illustrated based on a situation where $i_{ds}^{e*}$ is kept constant at the maximum value instead of parabolic variation. In this situation, the back EMF will not be compensated by the inverter, which naturally causes $i_{qs}^{e}$ to be dropped in the field weakening region as shown by (4) and (5). This eventually produces high current ripples causing PI controllers to saturate, resulting in high torque ripples. Furthermore, by continuing to apply inferior $i_{ds}^{e*}$, the current controllers will lose their stability and eventually fail.

As the improved utilisation of DC link voltage is attained by applying the proposed method, the maximum torque and power are achieved for a given speed in comparison with conventional model-based control (i.e. Fig. 5.13), as explained as in Method C in Section I. As shown in Fig. 5.13, the output torque and power as a function of speed are captured by Magtrol software, which is connected to torque transducer. The experimental result in Fig. 5.13a clearly shows the improvement in the maximum torque capability at a particular speed. The small difference between experimental and calculated torque (Fig. 5.13a and Fig. 5.7) is due to windage and friction losses.

It should also be noted that the effect of the small variation of $i_{ds}^{e*}$ will be cancelled out in high speed operation and will not be experienced in power train systems. This can be clearly observed from Fig. 5.13a, where the torque ripple is exactly the same in both cases, i.e. the proposed method and the conventional one, which further confirms that the ripple of the $i_{ds}^{e*}$ is not reflected in the output torque.

As explained before in this chapter, the model-based algorithm is a parameter dependent control method. The calculated reference currents presented in (5.8) to (5.12) are a function of $\sigma L_s$ and $L_s$. The on-line estimation method explained in Chapter 7 is required for controlling the high power/speed IMs where the inductance saturation is an important concept. However, for low-power rate IM, the accuracy of the parameter measurement methods explained in Chapter 4 impact on the performance of the model-based control algorithm. The accurate measurement of motor parameter is confirmed in this chapter as the result of achieving the hexagonal voltage boundary without causing the natural drop in motor currents. Therefore, the reference current are calculated correctly by using the accurate measurement of the motor parameters.

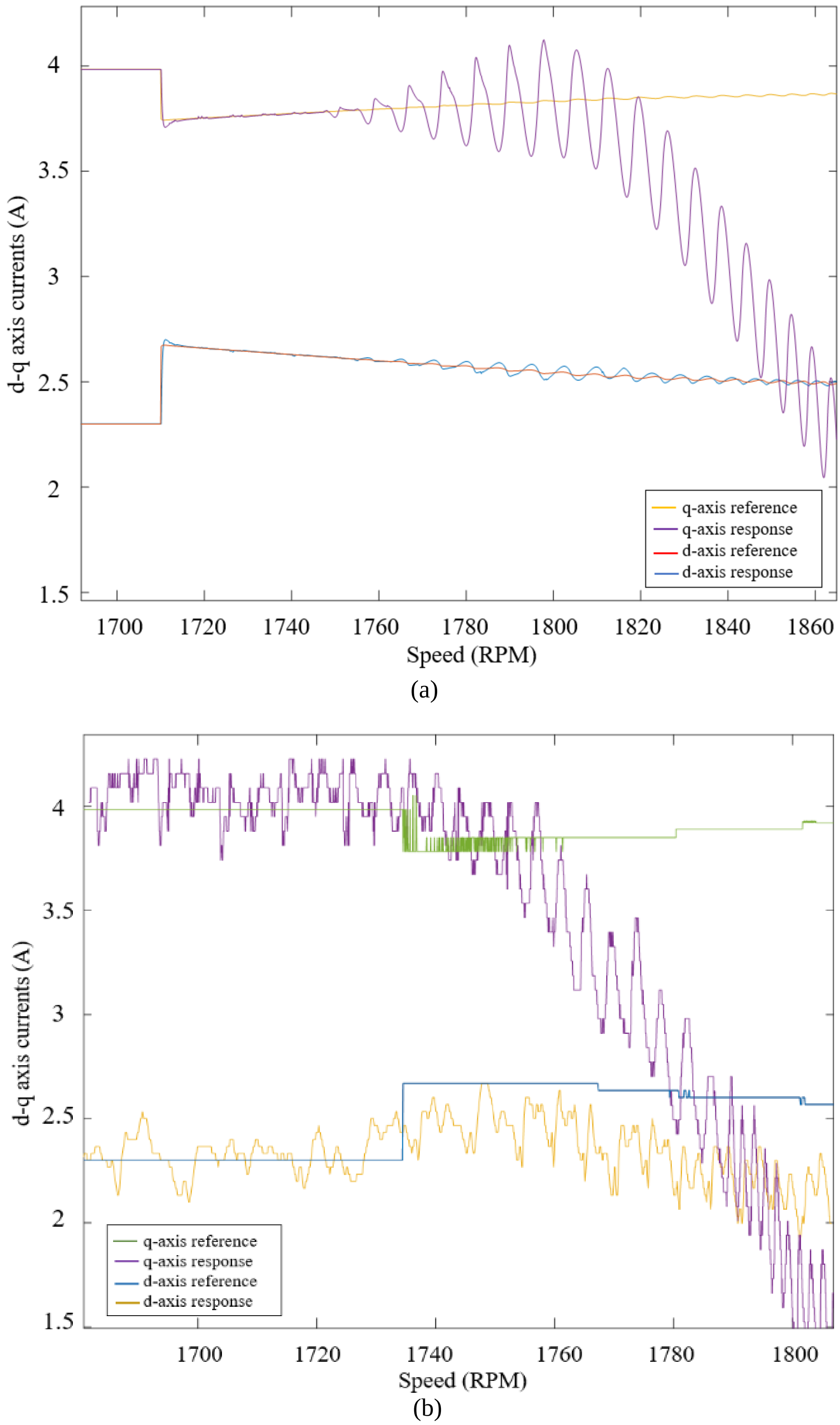


Fig. 5. 12 The performance of the current controllers with a constant d-axis current in each electrical cycle (a) Simulation result (b) Experimental result

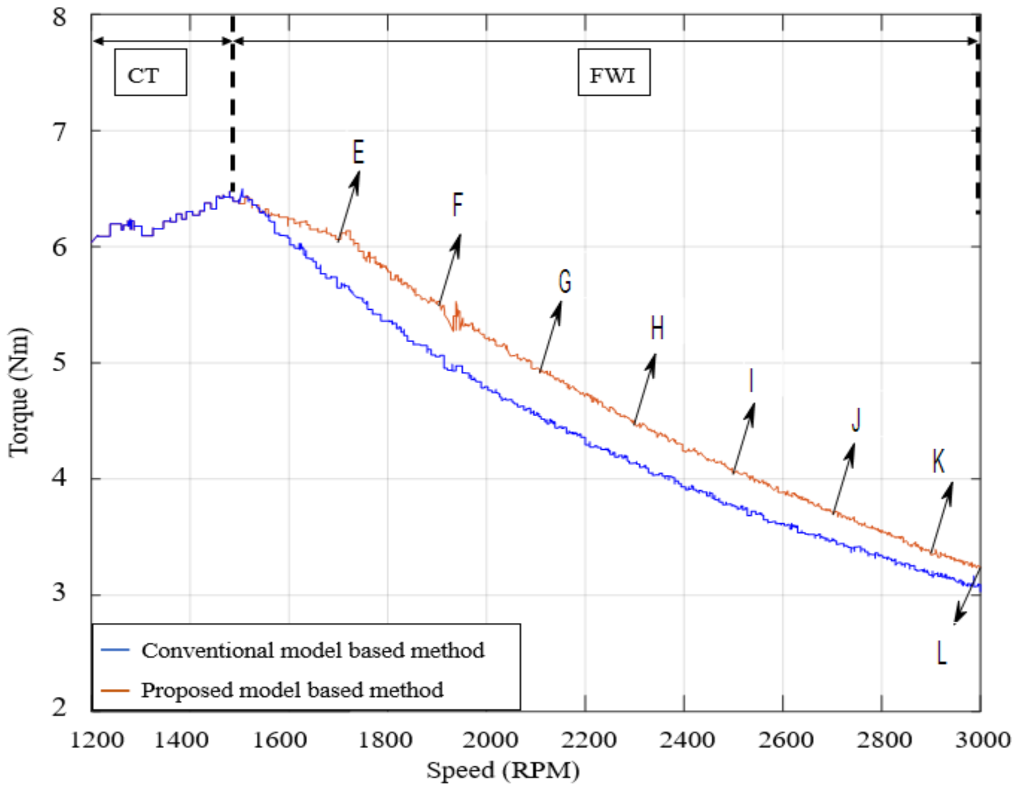


(a)

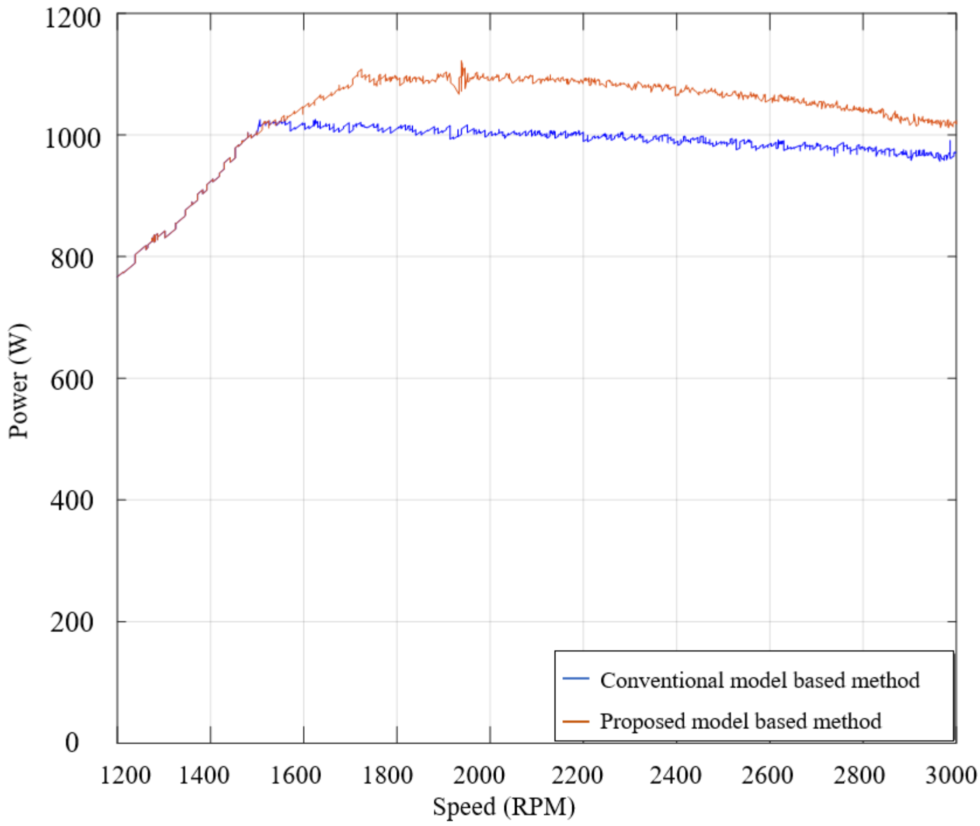


(b)

Fig. 5. 13 Experimental results (a) Output torque (b) Output power

### 5.5 Summary

In this chapter, a new model-based voltage control method is presented to improve the utilisation of DC-link voltage in the field weakening region. The reference d-axis current signals are calculated based on the hexagonal voltage boundary and the stator voltage vector position. With the new proposed reference current waveform, the output torque and power of the IM are increased. The calculated optimum value of the d-axis current reduces the required number of regulators or voltage feedback signals, simplifying the overall control system. This proposed method also allows the stability of the current controllers as a result of the parabolic variation in amplitude of the d-axis current. This means that sufficient d-axis voltage is available, avoiding the natural drop of motor currents, and consequently reducing the torque ripples. Furthermore, the algorithm recognises the beginning of the field weakening and matches the starting values of reference currents in this region with the desired currents in the constant torque area. As a result, the calculation of the base speed is not required and smooth transition from the constant torque region to the constant power region is achieved. The feasibility of the proposed method is confirmed, analytically, by simulation and experiment.

# CHAPTER 6

# Closed-Loop Voltage Control for Maximising Inverter Output Voltage in the Field-weakening Region of Induction Machines

## 6.1 Introduction

As explained before, it is desirable in AC motor drives to maximise the utilisation of DC link voltage to increase the output torque and power in the field weakening region. This chapter focuses on maximising the voltage utilisation of DC-link voltage by proposing the closed-loop voltage control method. In this method, the extracted voltage is maximised without reflecting the fake extended voltage in d-axis current explained in Methods B to D (Fig. 2.2). This is achieved by applying $i_{ds}^{e*}$ based on the closed loop stator voltage control where the proposed reference voltage amplitude is defined with respect to the electrical rotor position $\theta_e$. This reference voltage is able to compensate the difference between the inscribed circle voltage and hexagonal voltage limitation and therefore maximises the output torque and power in the field-weakening region. The closed-loop voltage control method based on the proposed reference voltage configuration gives rise to a closed loop transfer function, which is used for optimising the design of the outer PI controller. This helps the proposed method to have a smooth transition between constant torque and the field-weakening regions. The corresponding smooth transition of d-axis current also prevents a high step reduction in rotor flux, which maximises the output torque in this region. Furthermore, limiting the stator voltage reference to the hexagonal boundary minimises the fake voltage extension and therefore prevents the natural reduction of q-axis current. This decreases the oscillations in q-axis current. In this chapter, the analysis of the stator voltage vector in the nonlinear modulation region based on the motor parameters and applied reference currents is also described. The proposed method is firstly presented analytically and then the simulation and experimental results are included to verify the control method.

## 6.2 Flux weakening based on voltage components

### 6.2.1 Voltage and current constraints as a function of voltage components

In this section, the current limitation is developed based on the voltage components. This tries to explain how the voltage components are used for producing the reference d-axis current. By neglecting the resistance voltage drop term ($r_s\, i^e_{dqs}$) and substituting (5.4) and (5.5) into (5.6), the current limitation boundary becomes:

$$(\frac{v^e_{qs}}{w_e\, L_s})^2 + (\frac{v^e_{ds}}{w_e\, \sigma L_s})^2 \leq (I_{s,max})^2 \tag{6.1}$$

Therefore, the torque equation (described in 3.33) can be derived by the simplified stator voltage components as:

$$T_e = -\frac{3}{2}\frac{P}{2}\frac{{L_m}^2}{\sigma L_r\, {L_s}^2 {w_e}^2} v^e_{qs} v^e_{ds} \tag{6.2}$$

As shown in Fig. 6.1a, the major axis of the current ellipse lies on the $v^e_{qs}$ axis due to of having the higher denominator in comparison with $v^e_{ds}$ (6.1). The zero slope of the current ellipse on the $v^e_{qs}$ axis needs to be considered in case of having a high level of resistance voltage drop. As shown in Fig. 6.1b, the voltage is now constrained by the hexagonal boundary rather than the inscribed circle. This hexagonal voltage boundary is rotating at the electrical speed $w_e$ . As demonstrated in Fig. 6.1b, the maximum and minimum radius of the rotating hexagonal voltage is limited between the inscribed and circumscribed circles of the hexagon. Therefore, the maximum voltage utilisation is achieved by keeping the magnitude of $v^e_{dqs}$ within the limitation range. When the stator voltage reaches to the limit, the dominant term of absorbing voltage is $w_e\, \frac{L_m\, \lambda^e_{dr}}{L_r}$ as can be realised from (5.2) and (5.3). In the limited voltage region, the only way to move beyond the base speed is by reducing $\lambda^e_{dr}$.

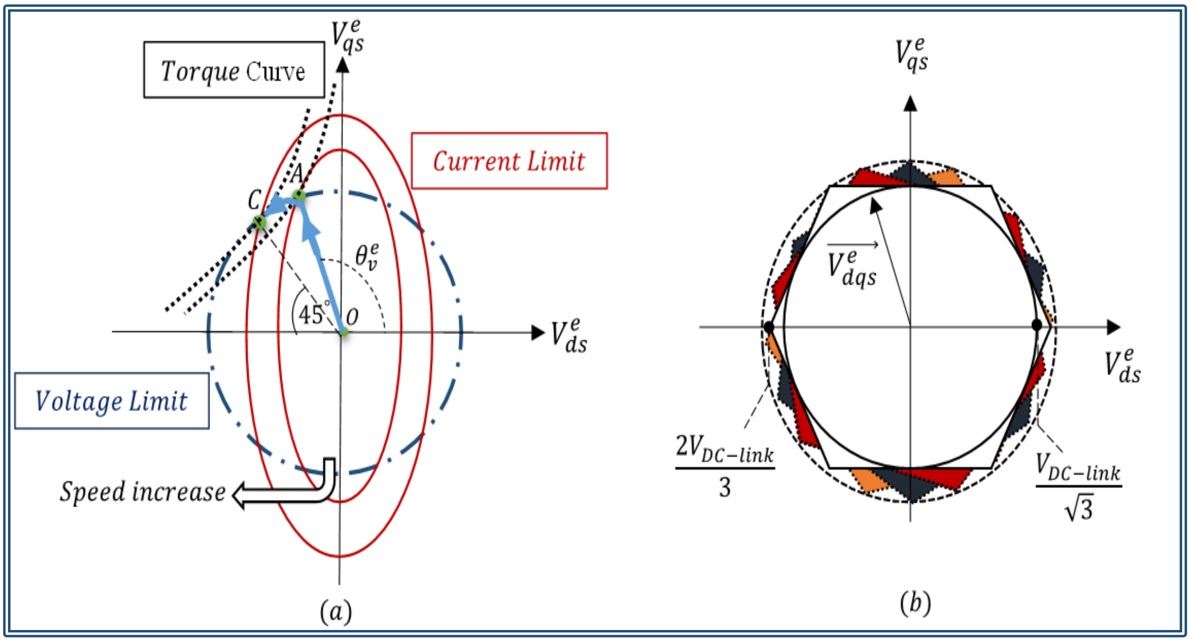


Fig. 6.1 (a) Current and voltage constraints for IM (b) Voltage trajectory in SVM

### 6.2.2 Stator voltage trajectory in CT, FWI and FWII

The operation of IM is divided into three speed regions to satisfy the current and voltage limitations. When the speed of IM is increasing, and it is below the base speed, the magnitude of $\vec{v}_{dqs}^e$ starts to rise from point O to A as shown in Fig. 6.1a. By neglecting the resistance voltage drop in (5.4) and (5.5), the angle of $\vec{v}_{dqs}^e$ in CT region (below the base speed) is calculated by:

$$\theta_v^e = \tan^{-1}\frac{-i_{ds\_rated}^{e*}}{\sigma i_{qs}^{e*}} \tag{6.3}$$

It can be realised from (6.3) that the angle of $\vec{v}_{dqs}^e$ depends on the leakage factor $\sigma$, desired flux producing current $i_{ds}^{e*}$ and torque producing currents $i_{qs}^{e*}$.

In CT region, $i_{ds}^{e*}$ is constant and its value depends on the flux level at rated conditions. To extract the maximum torque in constant torque region, $i_{qs}^{e*}$ needs to be defined as:

$$i_{qs}^{e*} = \sqrt{(I_{s,max})^2 - (i_{ds-rated}^{e*})^2} \tag{6.4}$$

By applying constant current in the CT region, the stator voltage reaches its maximum voltage at base speed. Under these circumstances, the speed cannot increase further when keeping the desired currents constant. This is because the back electromagnetic (EMF) component ($w_e \frac{L_m \lambda_{dr}^e}{L_r}$) needs to be controlled in a way that satisfies the voltage limitation. This is achieved by reducing $i_{ds}^{e*}$ in the FWI region. As shown in Fig .6.1a, in this region the voltage constraint is satisfied by forcing the operational point from A to C. As can also be realised from (5.4), (5.5) and Fig. 2a, the weakened flux causes a drop in $v_{qs}^e$ . Also $|v_{ds}^e|$ rises with increasing $i_{qs}^{e*}$ to extract maximum output torque. If the maximum torque is not required throughout FWI, then $i_{qs}^{e*}$ needs to be calculated based on the reference torque $T_e^*$ as follows:

$$i_{qs}^{e*} = \frac{4T_e^* L_r}{3PL_m^2 i_{ds}^e} \tag{6.5}$$

As the speed increases further, the current ellipse constraint becomes larger. As it reaches point C, the optimal operating condition is achieved by satisfying the voltage constraint. This is because, as demonstrated in (6.2), the maximum torque is obtained when the terms of stator voltages are defined as follows:

$$-v_{ds}^e = v_{qs}^e = \frac{V_{s,max}}{\sqrt{2}} \tag{6.6}$$

The FWII is always achieved at point C regardless of the operational speed. So, the current constraint is no longer followed because the intersection of voltage and current constraints happens outside of Point C. This prevents the maximum output torque being achieved in FWII. As the current limitation has not been followed, then the maximum acceptable $i_{qs}^{e*}$ is derived from (5.4) and (6.6) as:

$$i_{qs-max}^{e*} = \sqrt{\frac{(V_{s,max})^2}{2(w_e \sigma L_s)^2}} \tag{6.7}$$

As shown in Fig. 2.2, the production of $i_{ds}^{e*}$ in FWI and FWII is based on the closed loop stator voltage (Method A, Method B and Method D) or using active SVM switching periods (Method C). Methods A, B and D suffer from insufficient reference voltage, which prevents maximum extraction of $V_{DC}$ or increases the torque ripple by imposing fake voltage extension. This fake extension is minimised but still exists in Method C, which also sees the large step reduction of flux in transient period. To reduce the q-axis current ripple, a large step reduction in d-axis current for the transition from CT to FWI and

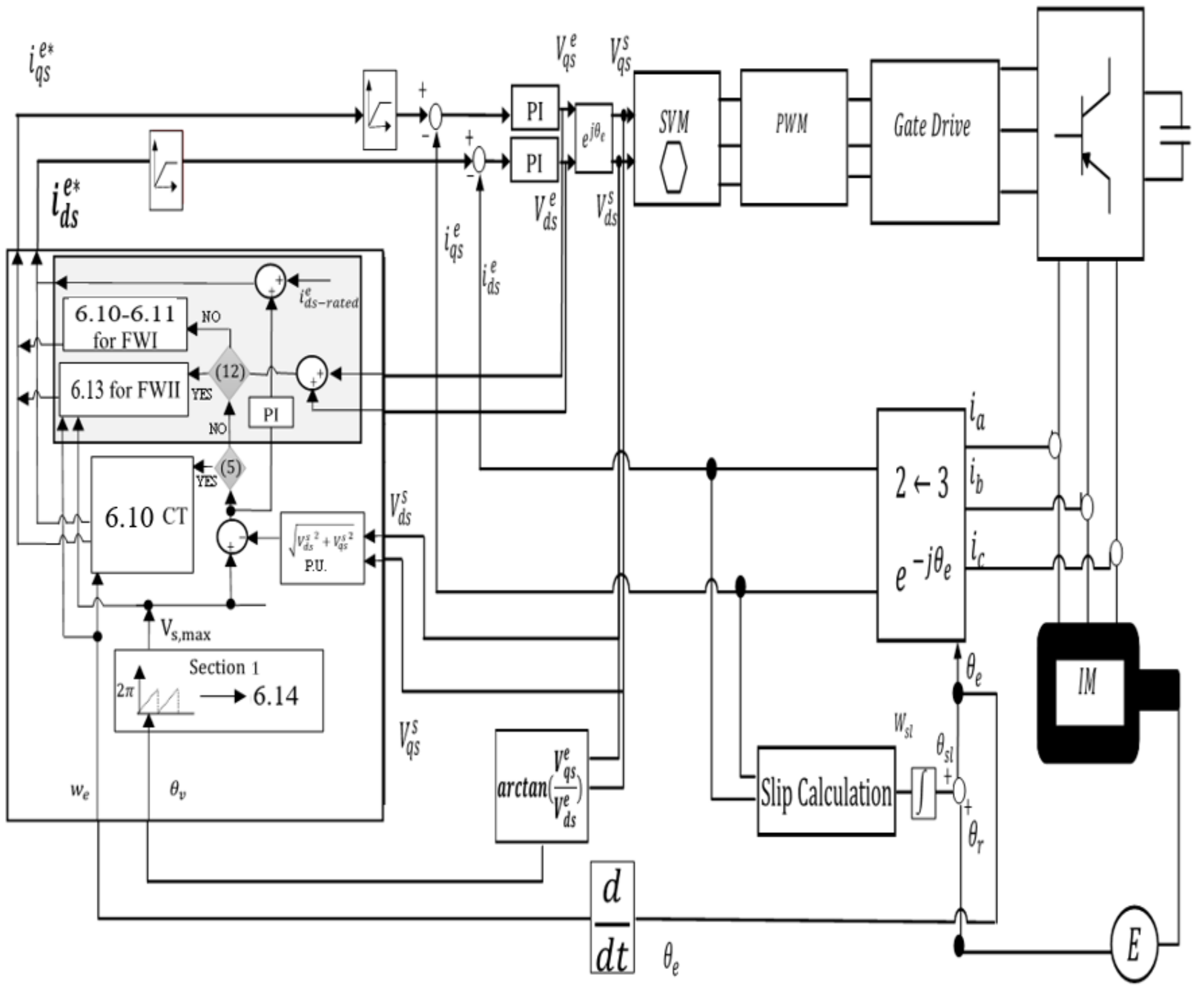


Fig. 6.2 Induction motor drive with proposed voltage control method

parameter sensitivity of the control algorithms in recognising the FWII, the improved closed-loop voltage control is presented in the next section.

### 6.3 The proposed closed loop voltage control

The proposed closed loop voltage control method for the field weakening region is shown in Fig. 6.2. Although this proposed method achieves the maximum output torque with full utilisation of the $V_{DC}$, the imposed fake voltage extension (explained in Method C in Fig. 2.2 and [30, 31]) caused by insufficient d-axis of voltage margin is minimised. This is the result of a well-defined d-axis reference current based on the difference of the hexagonal voltage boundary and stator voltage amplitude. This reference hexagonal voltage boundary is created based on the stator voltage angle $\theta_v$. To reduce the computation for creating the six sides of the hexagonal reference voltage, the equation of the first side is considered as the reference for all sectors as:

$$0 \le \theta_v < \frac{\pi}{3} \qquad {V_{s,max}}^2 = \frac{(\frac{2}{3}V_{DC})^2}{(\frac{2}{\sqrt{3}}\sin(\theta_v + \frac{\pi}{3}))^2} \tag{6.8}$$

As shown in Fig. 6.3, the amplitude variation of the reference hexagonal voltage $V_{s,max}$ is similar in all six sectors, and so (6.8) can be used for all sectors as $\theta_v$ is kept between 0 and $\frac{\pi}{3}$ by:

$$\theta_v = \theta_v - \left\lfloor \frac{\theta_v}{\frac{\pi}{3}} \right\rfloor \frac{\pi}{3} \tag{6.9}$$

In (6.9), $\left\lfloor \frac{3\theta_v}{\pi} \right\rfloor$ represents the floor function, giving the nearest integer to $\frac{3\theta_v}{\pi}$. Therefore, the maximum available voltage is extracted in the proposed control algorithm without injecting the fake extension voltage explained in Method B and C. As shown in Fig. 6.2, $V_{s,max}$ is compared with the magnitude of the stator voltage to determine the region of the operation. The CT region is achieved by applying $i^{e*}_{ds-rated}$ and (6.4) where the stator voltage magnitude has not reached to $V_{s,max}$ and the motor is operating below the base speed. Due to increased back EMF in higher speed operation, the stator voltage reaches $V_{s,max}$ and the rotor flux must be decreased.

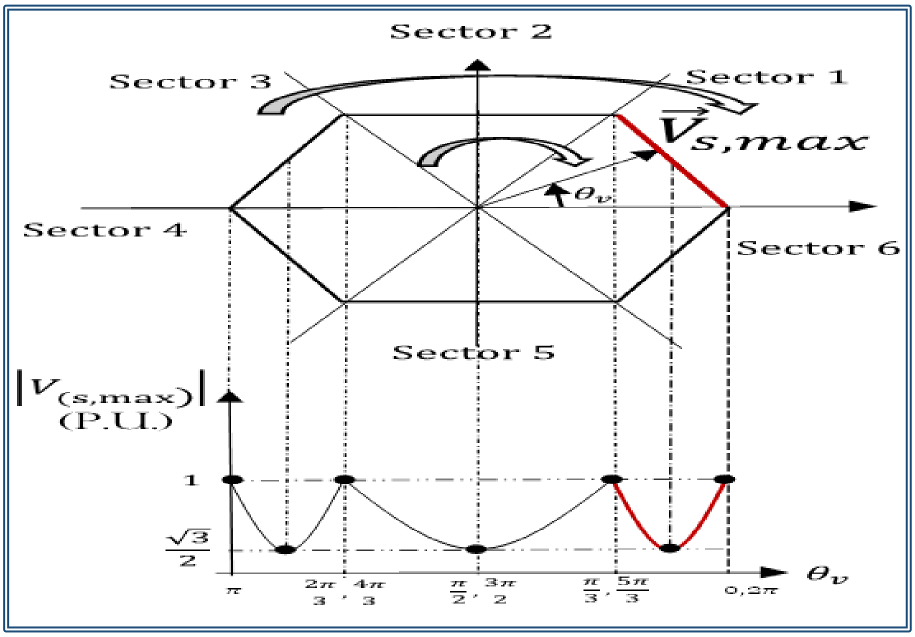


Fig. 6.3 Trajectory of reference voltage for the field weakening regions in the closed loop voltage control algorithm

The applied flux reduction is a result of the negative input of PI regulator $PI_{input}$ in the closed loop voltage control as follows:

$$PI_{input} = \left( \left(V_{s,max}\right) - \sqrt{(v_{ds}^{e})^{2} + \left(v_{qs}^{e}\right)^{2}} \right) \tag{6.10}$$

The reduced rotor flux is applied in both FWI and FWII regions. However as shown in Fig. 6.2, determination of maximum $i_{qs}^{e*}$ depends on the selected FW region. This selection is based on (6.6) where the d-q axis of stator voltage in the synchronous frame is compared. Therefore, the transition from FWI to FWII takes place as the magnitude of these stator voltage components becomes equal. The proposed transition from FWI to FWII is not sensitive to the motor parameters used in conventional methods. This requires $i_{qs}^{e}$ to be compared with $\frac{i_{ds}^{e}}{\sigma}$ to recognise the starting of FWII as explained in (6.3).

The dynamic performance of the closed-loop voltage control in the transition between or within the regions depends on the precise tuning of the inner loop PI controller. Unlike the active timing algorithm explained in Method C (Fig. 2.2), in the proposed method, the tuning of the PI controllers is not based on trial and error. Designing the appropriate gains of the PI controller is achieved by deriving the current transfer function for closed loop voltage feedback. This is accomplished by defining the $i_{ds}^{e*}$ in terms of the stator voltage as follows:

$$i_{ds}^{e*}(s) = PI_{input}(k_p + \frac{k_i}{s}) + i_{ds-rated}^{e} \tag{6.11}$$

The amplitude of $\vec{v}_{dqs}^{e}(s)$ used in (6.10) mainly consists of $v_{qs}^{e}$ in high speed operation due to the large value of back EMF. To express the $v_{qs}^{e}$ in (5.5) in terms of $i_{ds}^{e}$, $\lambda_{dr}^{e}$ needs to be defined in terms of current and rotor time constant as follows:

$$\left|\vec{v}_{dqs}^{e}(s)\right| = v_{qs}^{e}(s) = w_e \, \frac{{L_m}^{2} i_{ds}^{e}(s)}{L_r \, (1 + \tau_r s)} + w_e \, \sigma L_s \, i_{ds}^{e}(s) \tag{6.12}$$

Based on the derived stator voltage in terms of the stator current in (6.12), the applied $V_{s,max}$ in (6.10) can also be described as:

$$\left|\vec{v}_{dqs}^{e}(s)\right| = v_{qs}^{e}(s) = w_e \frac{{L_m}^2 i_{ds}^{e}(s)}{L_r(1+\tau_r s)} + w_e\,\sigma L_s\, i_{ds}^{e}(s) \tag{6.13}$$

By substituting (6.12) and (6.13) into the (6.10) and then (6.11), the transfer function of current can be calculated by:

$$\frac{i_{ds}^{e}(s) - i_{ds-rated}^{e}}{i_{ds}^{e*}(s) - i_{ds-rated}^{e}} = \frac{\Delta i_{ds}^{e}(s)}{\Delta i_{ds}^{e*}(s)} = \frac{\big(M(s)k_p - 1\big)s + M(s)k_i}{M(s)(k_p s + k_i)} \tag{6.14}$$

where $M(s) = w_e\, L_s\, \frac{1+\tau_r\sigma s}{1+\tau_r s}$ and the gains of the PI regulator are $k_p$ and $k_i$. The applied $i_{ds}^{e*}$ keeps the system stable at different speeds as a result of negative poles for the closed loop transfer function shown in (6.14). To design the PI controller, the $k_i$ gain needs to have a low value to make the alignment of one of the poles and zeroes close to zero on the real-imaginary axis. This low value selection of $k_i$ leads to a reduction in the large step change of $i_{ds}^{e*}$ for transition from CT to FWI. It also speeds up the tuning process due to only having to deal with the placement of another zero in (20). To trade-off between the oscillation of $i_{ds}^{e*}$ and acceleration of stator voltage response to $V_{S,max}$ , the $k_p$ is determined. The root-Locus and step response used for tuning the PI gains of the closed loop voltage controller are presented in Appendix E. It should be noted that the bandwidth of a closed loop system dictates how fast variation in reference currents can be tracked. The proposed method in this manuscript was tested on a 4 poles induction machine running up to 3,000RPM. This speed corresponds to 102Hz (electrical plus slip frequencies). The proposed method defines six parabolic variations in d-q axis of the reference currents per electrical cycle. Thus, the PI controller used with this method requires a bandwidth of 612Hz.

To explain how the stator voltage is maximised based on the proposed method, the variation of the stator voltage vector in the stationary and rotor frames is presented in Fig. 6.4 The proposed $i_{ds}^{e*}$ helps the stator voltage vector to move along the hexagonal voltage boundary as shown in Fig. 6.a. The angle of the hexagon voltage rotation in Fig. 6.4a is a result of the starting angle of stator voltage vector in the field weakening region calculated in (6.3). It should be noted that the corner of the rotated hexagonal stator voltage and fixed hexagonal voltage boundary could be aligned at the start of field-weakening region with optimised design of $\sigma$ and $i_{ds\_rated}^{e*}$. The hexagonal voltage in Fig .6.4a is achieved by 12 lines variation of stator voltage in the rotor frame in Fig. 6.4b which is the result of parabolic variation of reference voltage as explained in Fig. 6.3. Each of these lines reflects the half of the parabolic variation of the reference voltage as shown in Fig. 6.3 and Fig. 6.4b.

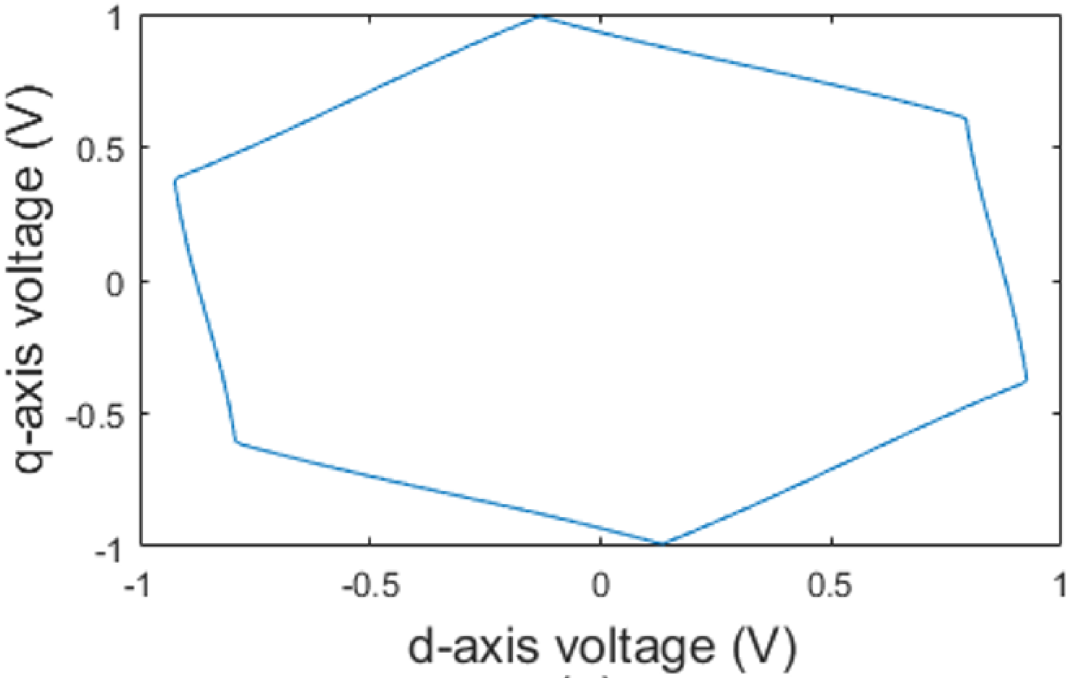


(a)

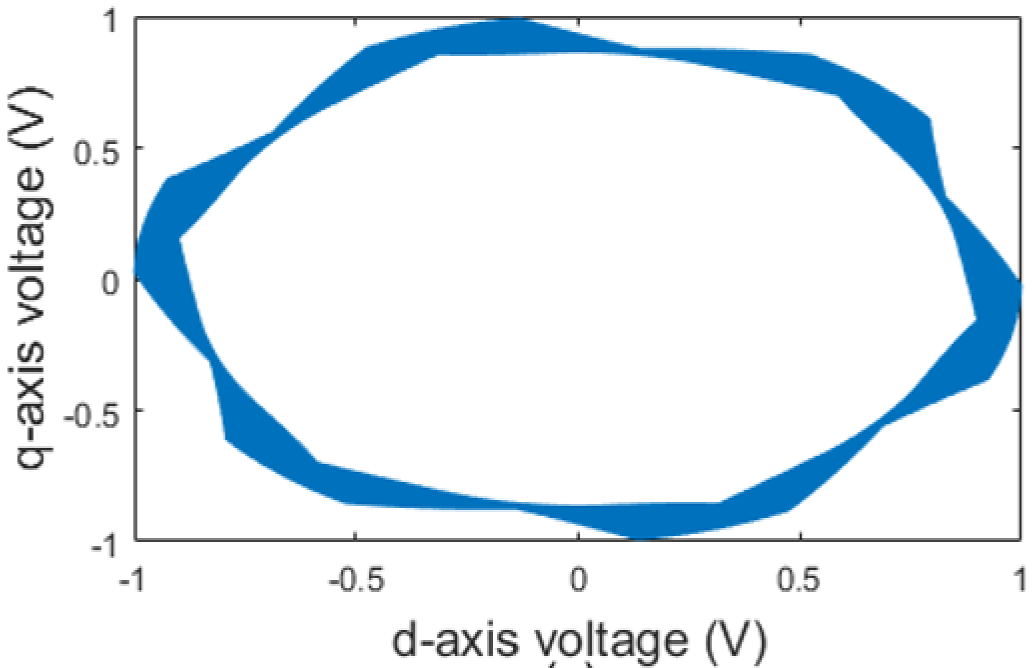


(c)

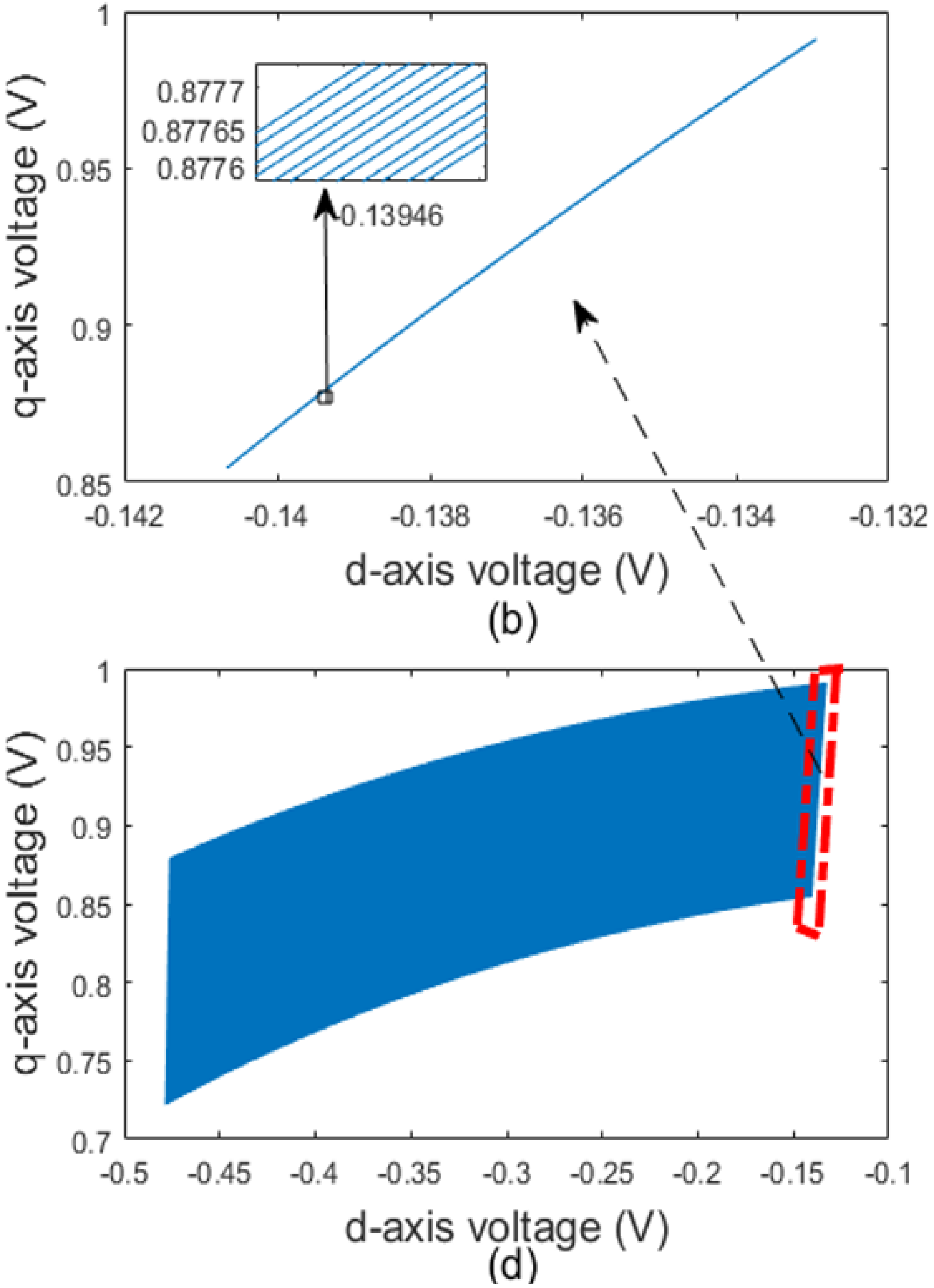


Fig. 6.4 Stator voltage trajectory (P.U.): (a) in the stationary frame for starting of field weakening (b) in the rotor frame for starting of field weakening (c) in stationary frame for field-weakening region (d) in rotor frame for field-weakening region

As explained in Section II and III, the field weakening region is entered by reducing the $i_{ds}^{e*}$, which causes the reduction in $v_{qs}^{e}$ as shown in Fig. 6.4d. This variation in $v_{qs}^{e}$ and $v_{ds}^{e}$ causes the stator voltage angle in rotor frame to change and then the hexagonal voltage rotates as shown in Fig. 6.4c. Therefore, the whole hexagonal voltage variation could be achieved by applying the proposed method, maximising the output torque and power.

### 6.4 Results

The control model described in Fig. 6.2 is implemented in CPU1 of the microcontroller. The currents controllers and SVM are realised in CPU1.CLA. The execution time of the control method and SVM in CPU1 and CPU1.CLA are 10.81us and 5.32us respectively and so comfortably fit in the 50-microsecond switching period.

#### 6.4.1 Simulation and experimental results

The proposed controller is applied to extract its maximum torque from the IM. In the experimental set-up, the output torque is measured by a torque transducer as the speed is adjusted with the dynamometer operated in speed mode control (Fig. 4.6). The simulation results and the experimental results of the proposed method are shown in Fig. 6.5 and Fig. 6.6 respectively. Figure. 6.7 also demonstrates the improvement of output torque and power of the test IM when compared with the conventional method (Method A in Fig. 2.2). Moreover, the merits of the proposed method in the transition period from constant torque to field weakening region are demonstrated and compared with Method C in Fig. 6.8.

##### 6.4.1.1 d-q axis currents, voltage and current constraints in CT and FW region

Fig. 6.5a1 shows the reduction in d-axis current in the field-weakening region based on the explanation given in Section 6.2 and Fig. 6.1. Fig. 6.5a2, a3 present the d-axis current for steady state condition where the motor is operating in 1,800 rpm and 2,500 rpm. Because of the model-based tuning for the closed loop voltage regulator explained in Section 6.3, the proposed d-axis current does not have a large step reduction in d-axis current for transition period. This is proven by Fig. 6.8 c and d where the produced d-axis current based on Method C experiences 30% more reduction in d-axis current from base speed to 1,800 rpm compared to the proposed method. Therefore, this causes a drop in the rotor flux and a consequent loss in the maximum output torque in the transition period for the Method C control methodology.

Fig. 6.5b1 demonstrates a q-axis current which satisfies the current and voltage constraints explained in Section 6.2.2 and 6.2.3. Fig. 6.5b2, b3 also demonstrate the q-axis current in steady-state condition where the motor speed is 1,800 rpm and 2,500 rpm. The q-axis current in the proposed method has 20% fewer oscillations in comparison with Method C for a speed of 1,700 rpm as shown in Fig. 6.8 e and f. This is the result of a high level of fake extension voltage in Method C as demonstrated in Fig. 6.8b, which cannot be provided by the inverter voltage, and consequently q-axis motor currents naturally must be dropped. These q-axis current oscillations produce torque ripple, which is more obvious in electric motors with a higher power rating. This is because the torque ripple produced in AC motors with a lower power rating is supressed by power train inertia.

Fig. 6.5c shows the resulting current boundary for the proposed method. As can be seen, the d-axis current is decreased to reduce the rotor flux at higher speeds. As demonstrated in this figure, the q-axis current is moving along the current limitation trajectory to produce the maximum output torque of the motor. The full hexagonal voltage limit is also confirmed in Fig. 6.5d, where the d-axis voltage catches the corner of the hexagonal boundary as described in Fig. 6.3 and proven with corresponding voltage waveforms as shown in Fig. 6.5e.

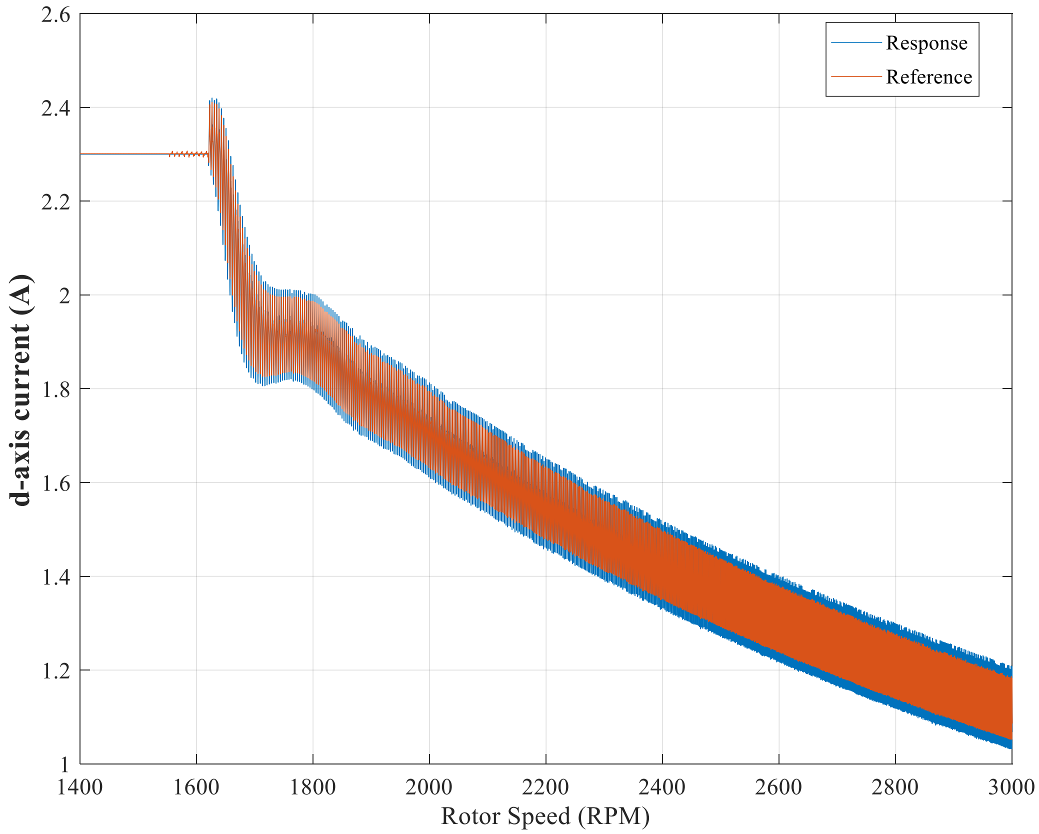
Response
Reference
d-axis current (A)
Rotor Speed (RPM)
2.6
2.4
2.2
2
1.8
1.6
1.4
1.2
1
1400
1600
1800
2000
2200
2400
2600
2800
3000

(a1)

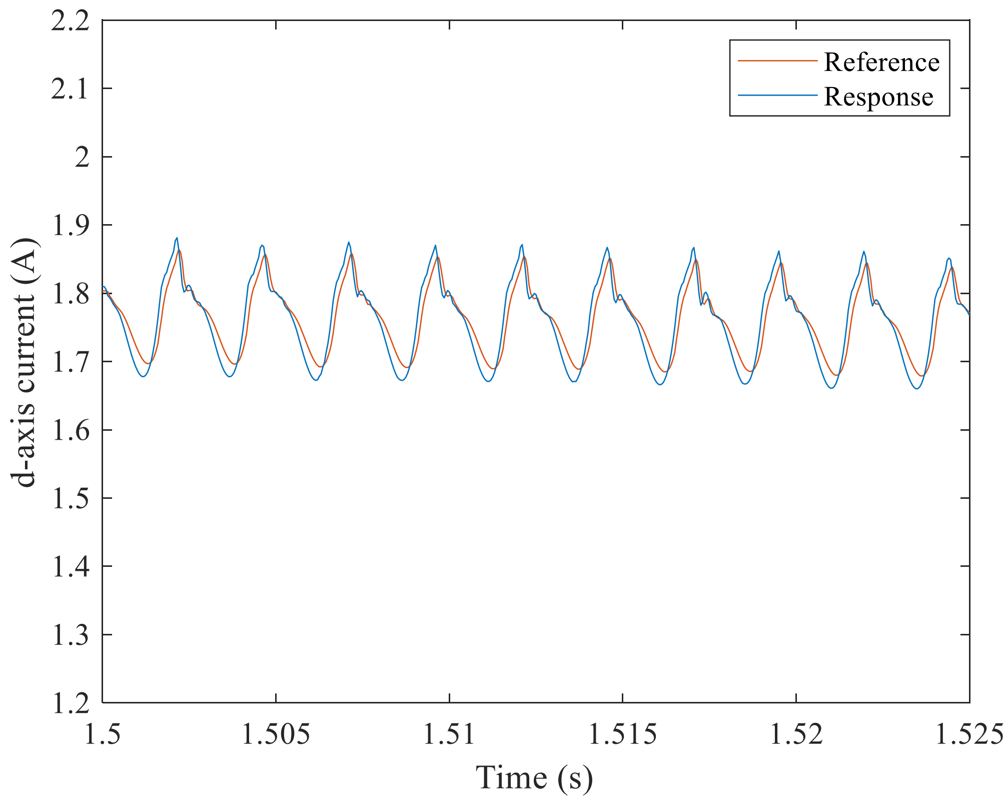
Reference
Response
d-axis current (A)
Time (s)
2.2
2.1
2
1.9
1.8
1.7
1.6
1.5
1.4
1.3
1.2
1.5
1.505
1.51
1.515
1.52
1.525

(a2)

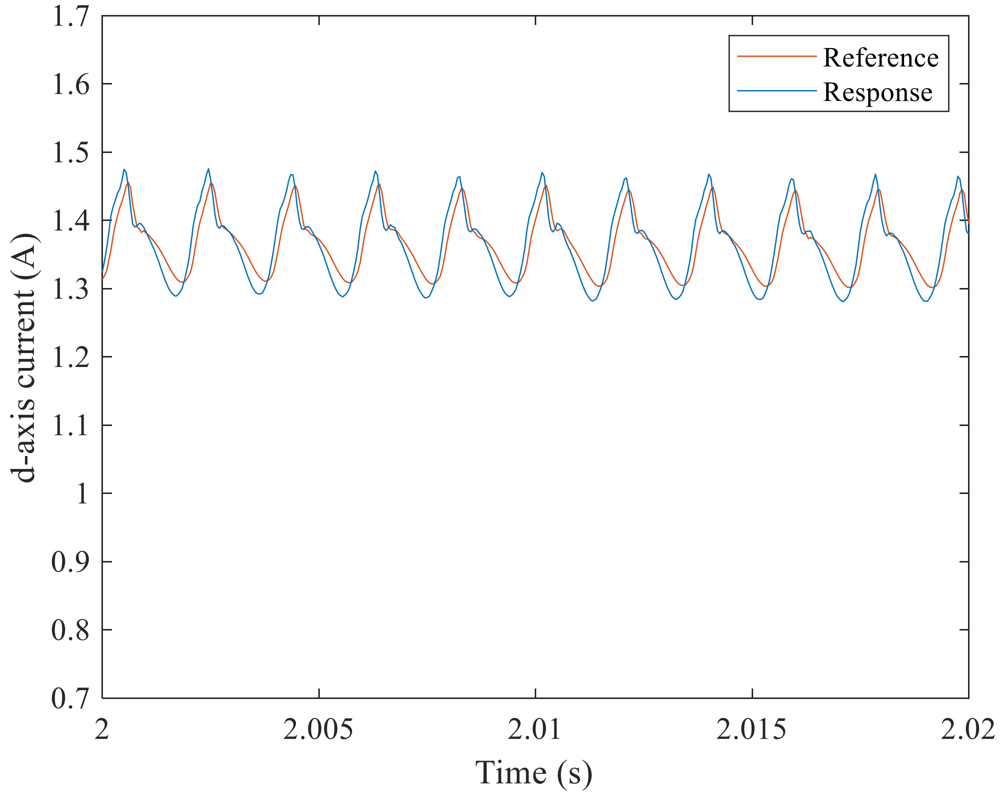
1.7
1.6
1.5
1.4
1.3
1.2
1.1
1
0.9
0.8
0.7
d-axis current (A)
Reference
Response
2
2.005
2.01
2.015
2.02
Time (s)

(a3)

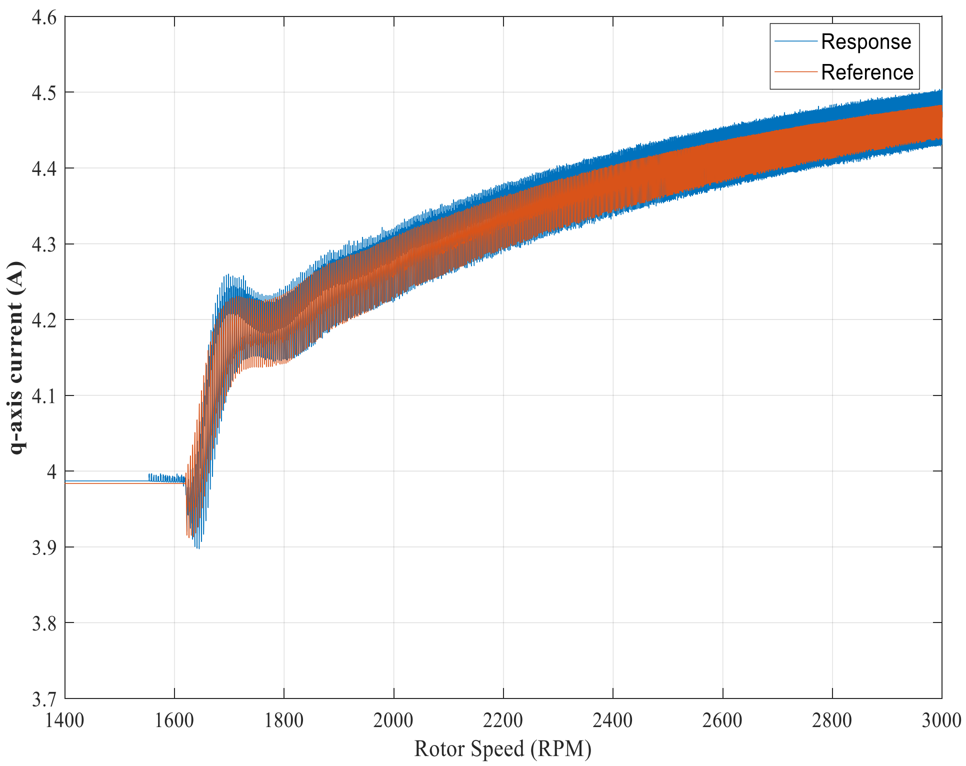
4.6
4.5
4.4
4.3
4.2
4.1
4
3.9
3.8
3.7
q-axis current (A)
Response
Reference
1400
1600
1800
2000
2200
2400
2600
2800
3000
Rotor Speed (RPM)

(b1)

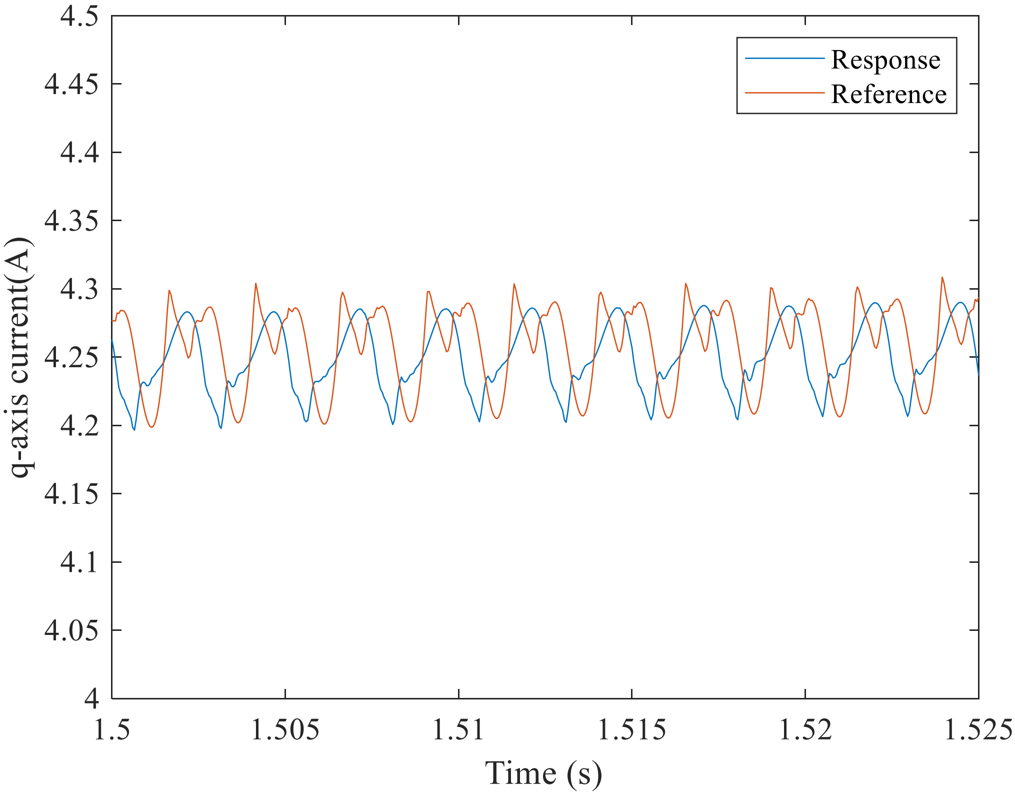

Response
Reference
4.5
4.45
4.4
4.35
4.3
4.25
4.2
4.15
4.1
4.05
4
q-axis current(A)
1.5
1.505
1.51
1.515
1.52
1.525
Time (s)


(b2)

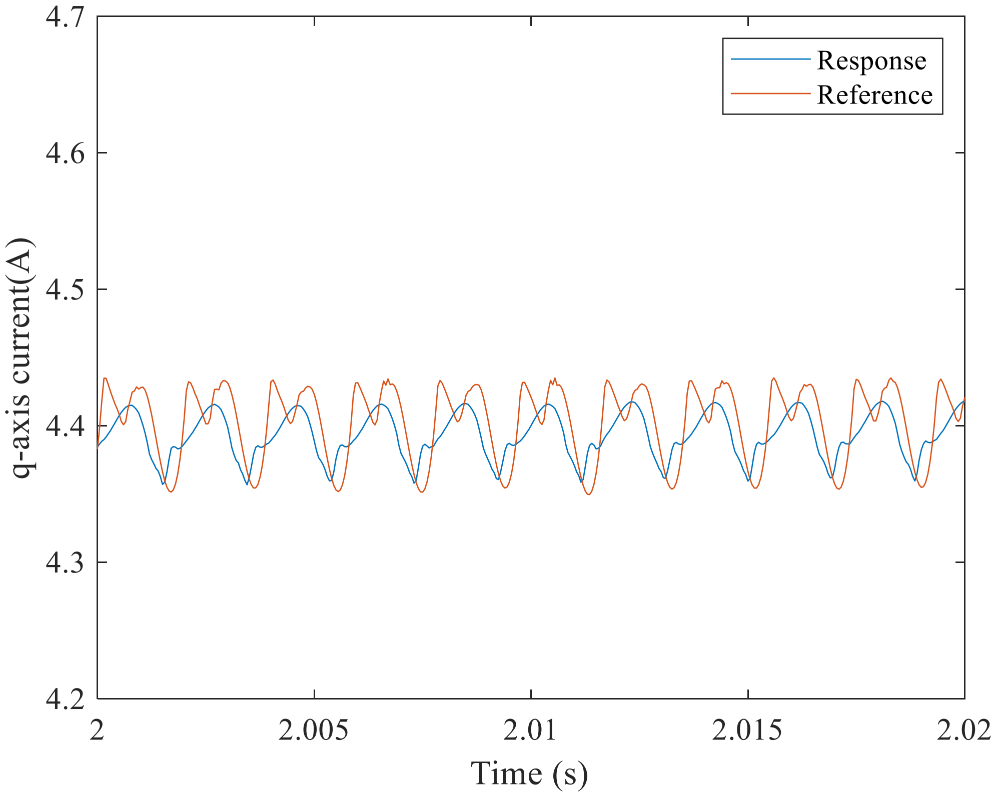

Response
Reference
4.7
4.6
4.5
4.4
4.3
4.2
q-axis current(A)
2
2.005
2.01
2.015
2.02
Time (s)


(b3)

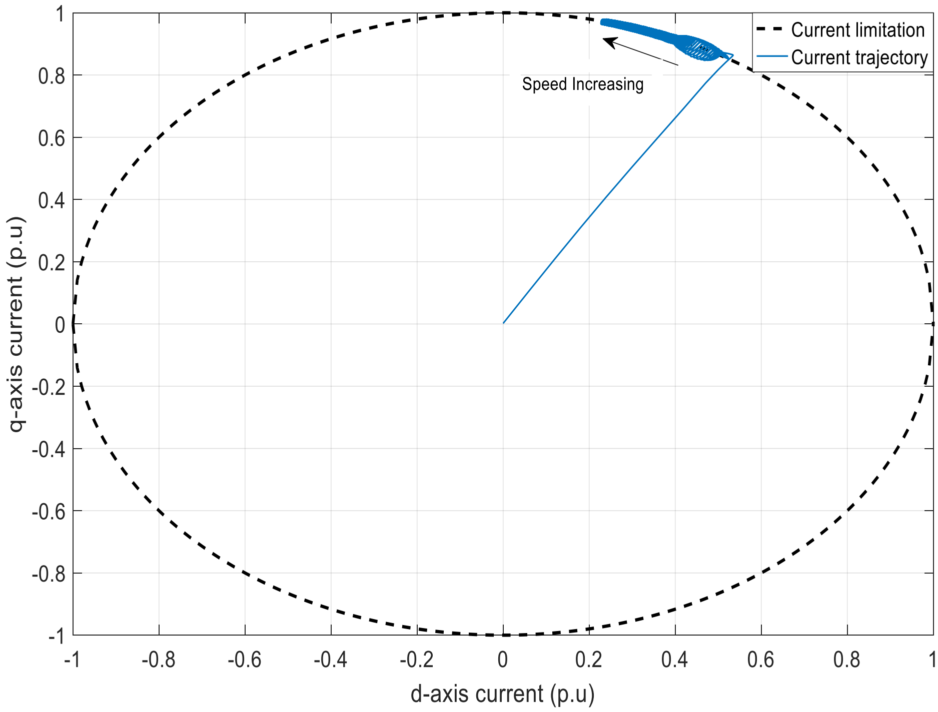
Current limitation
Current trajectory
Speed Increasing
q-axis current (p.u)
d-axis current (p.u)
1
0.8
0.6
0.4
0.2
0
-0.2
-0.4
-0.6
-0.8
-1
-1
-0.8
-0.6
-0.4
-0.2
0
0.2
0.4
0.6
0.8
1

(c)

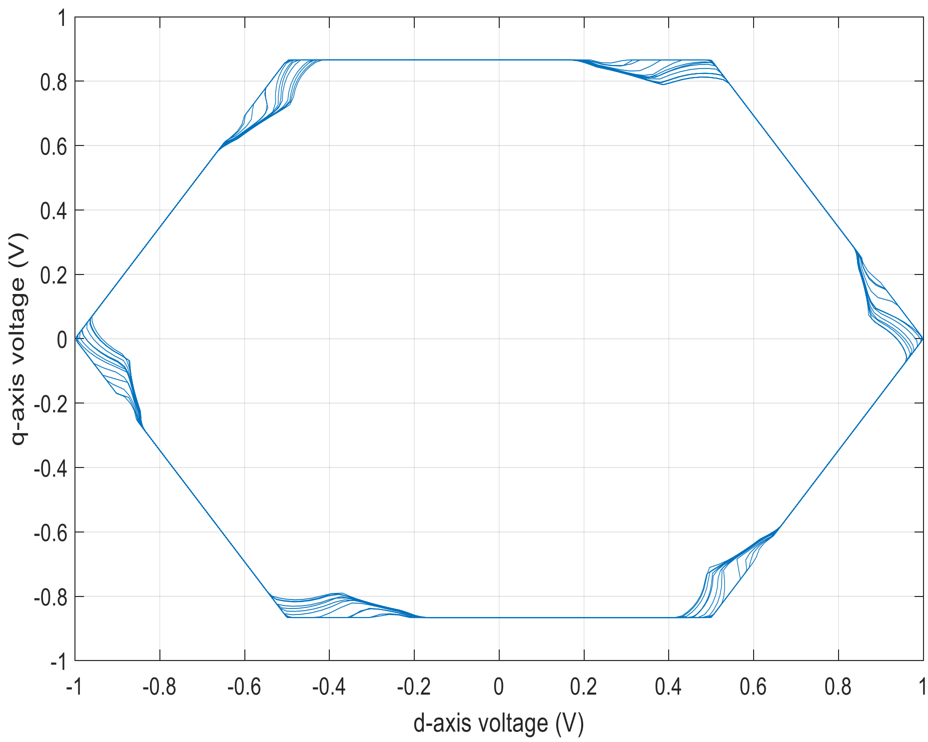
q-axis voltage (V)
d-axis voltage (V)
1
0.8
0.6
0.4
0.2
0
-0.2
-0.4
-0.6
-0.8
-1
-1
-0.8
-0.6
-0.4
-0.2
0
0.2
0.4
0.6
0.8
1

(d)

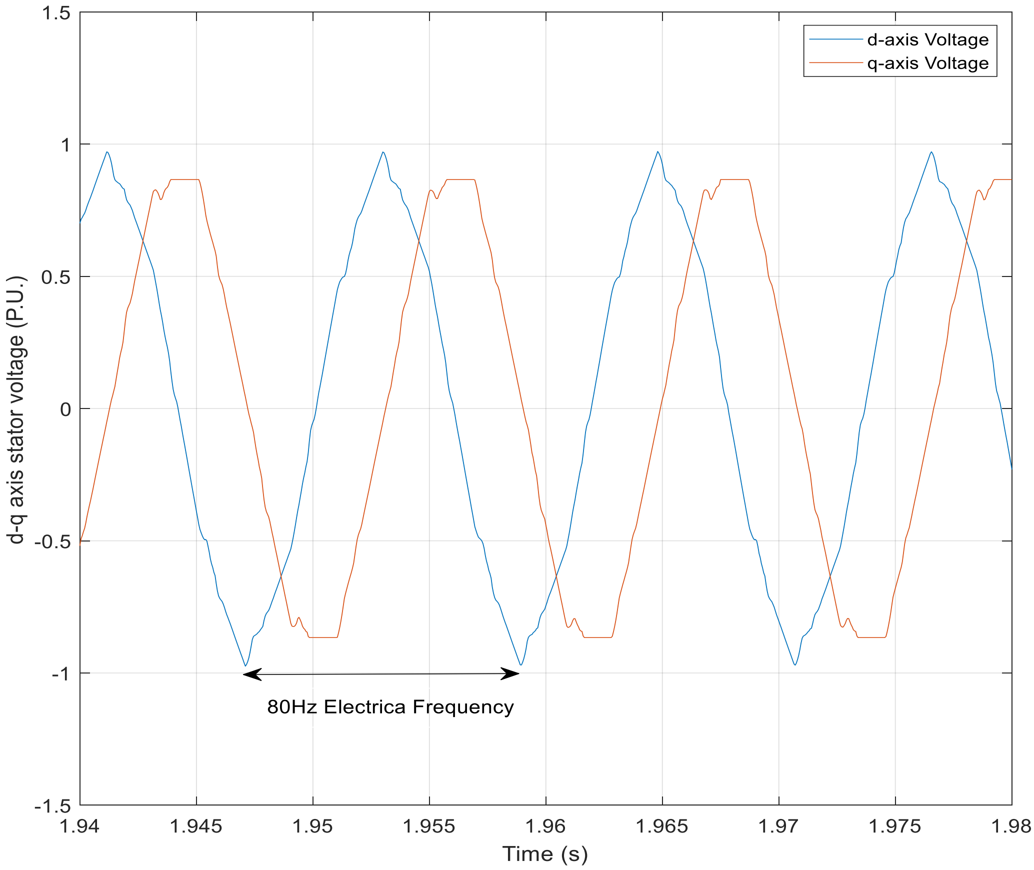


(e)

Fig. 6.5 Simulation results: d-axis current (a1) in speed range of 1,400rpm to 3,000rpm (a2) in steady-state condition with constant speed of 1,800rpm and 5.8N.m torque (a3) in steady-state condition with constant speed of 2,500rpm and 4N.m torque (b) q-axis current (b1) in speed range of 1,400rpm to 3,000rpm (b2) in steady-state condition with constant speed of 1,800rpm and 5.8N.m torque (b3) in steady-state condition with constant speed of 2,500rpm and 4N.m torque (c) current trajectory (P.U.) (d) voltage trajectory (P.U.) in rotor speed of 2,400rpm (e) d-q-axis of voltage (P.U.) in stationary frame at 2,400 rpm

As shown in Fig. 6.6, the experimental results have good correspondence with the simulation results. The d-q axis current waveforms presented in Fig. 6.6 a and b are captured using three digital to analogue converter (DAC) signals available on the microcontroller. These low-voltage analogue signals are passed to the oscilloscope and then filtered to eliminate the noise effects on DAC signals which are in a very low voltage range (0 to 3 V).

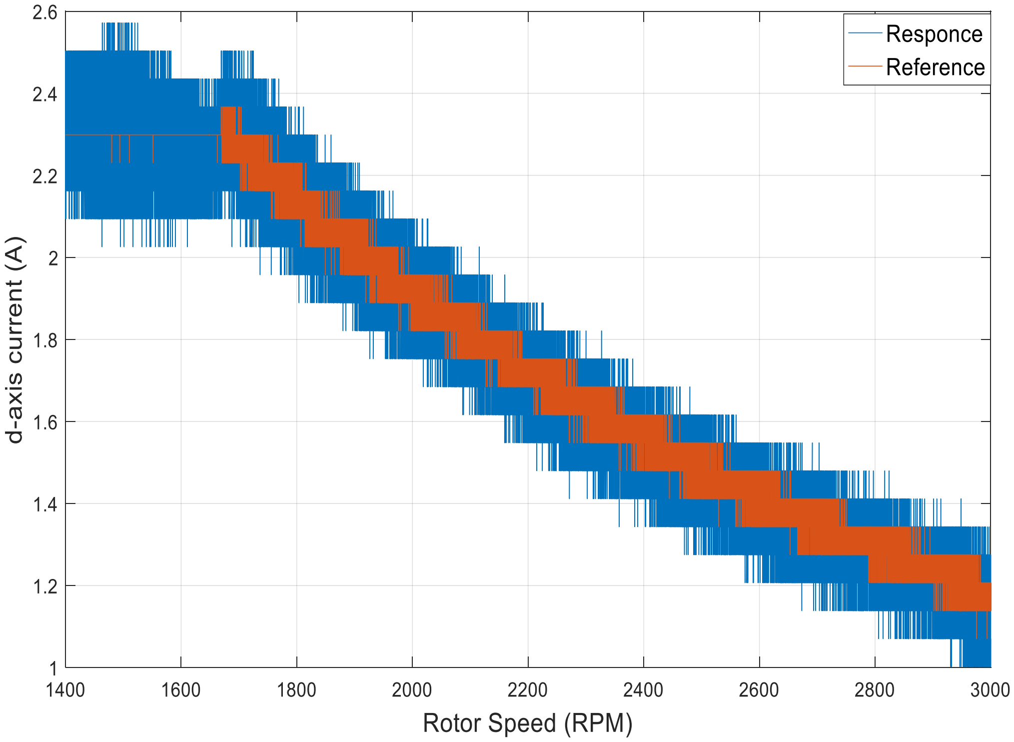
Responce
Reference
d-axis current (A)
Rotor Speed (RPM)
2.6
2.4
2.2
2
1.8
1.6
1.4
1.2
1
1400
1600
1800
2000
2200
2400
2600
2800
3000

(a)

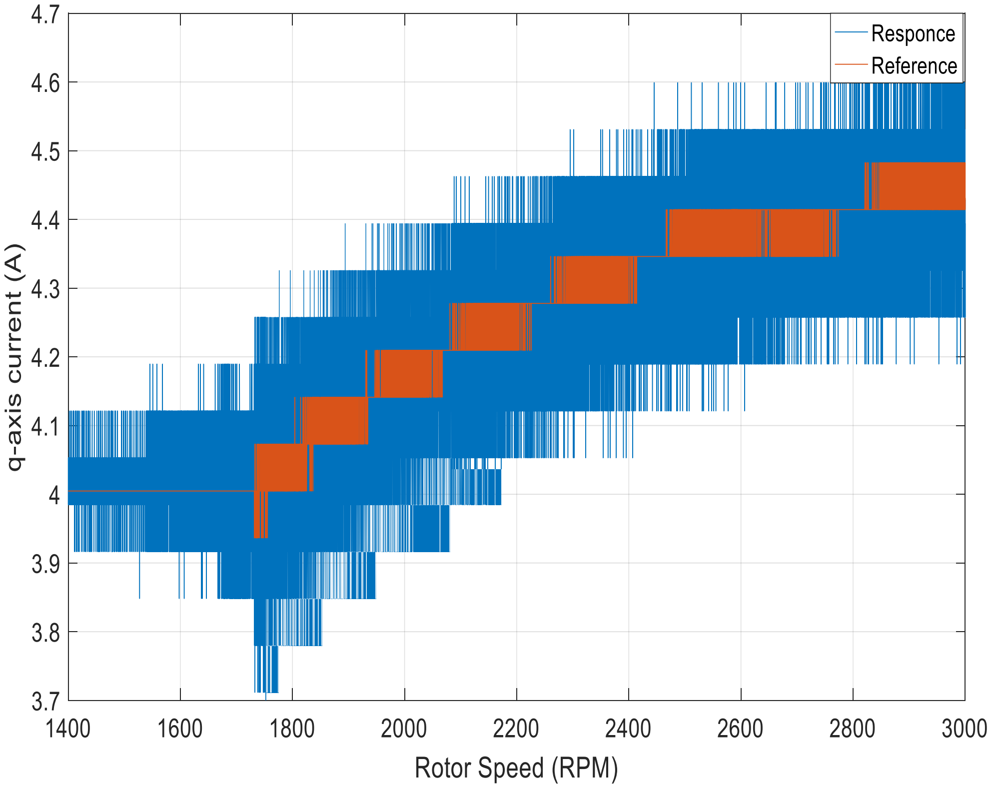
Responce
Reference
q-axis current (A)
Rotor Speed (RPM)
4.7
4.6
4.5
4.4
4.3
4.2
4.1
4
3.9
3.8
3.7
1400
1600
1800
2000
2200
2400
2600
2800
3000

(b)

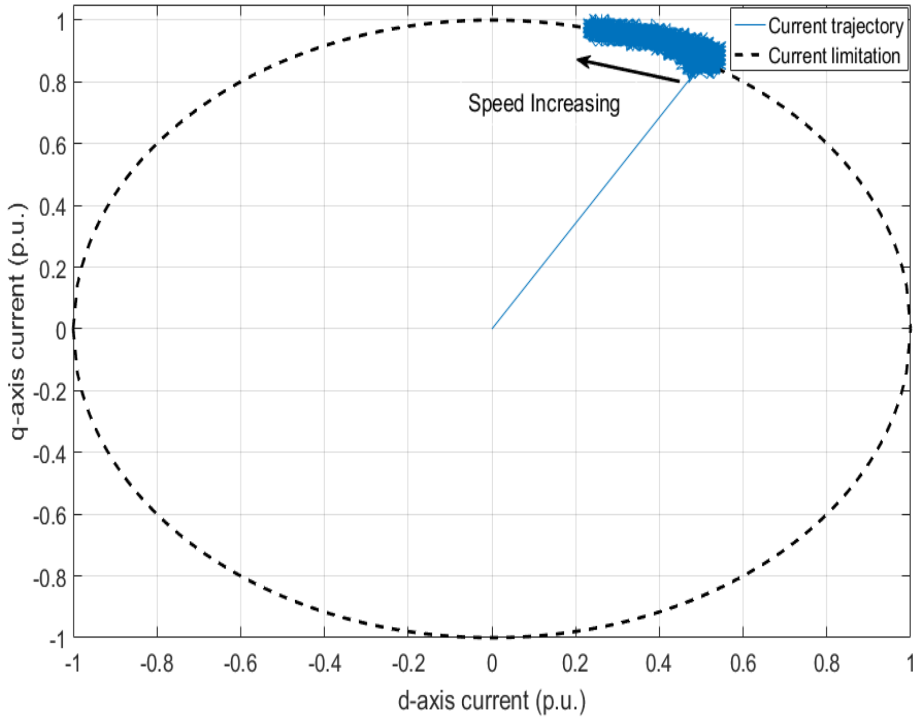

Current trajectory
Current limitation
Speed Increasing
q-axis current (p.u.)
d-axis current (p.u.)
1
0.8
0.6
0.4
0.2
0
-0.2
-0.4
-0.6
-0.8
-1


(c)

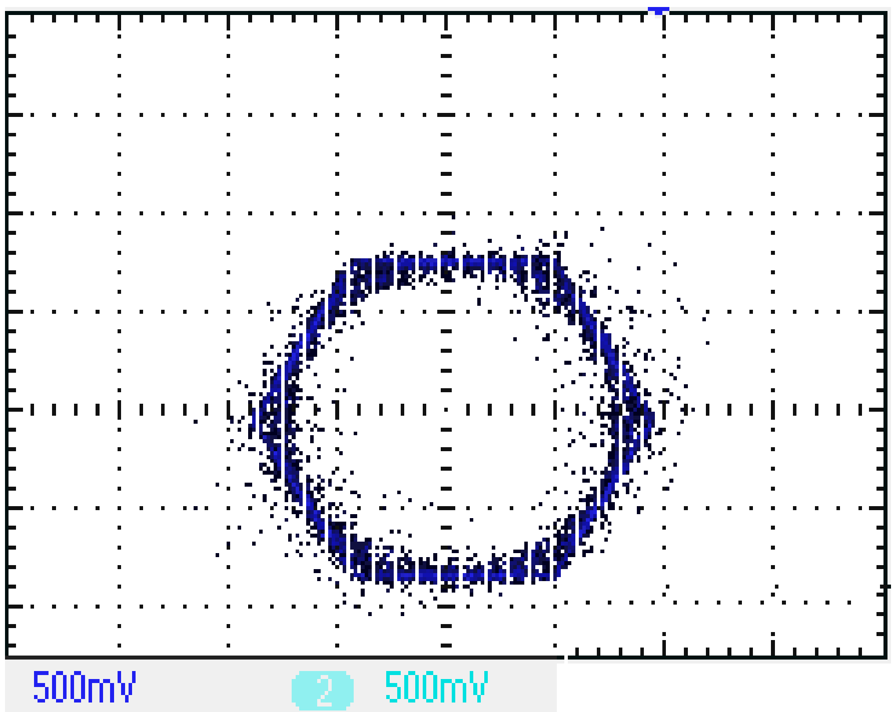

500mV
2
500mV


(d)

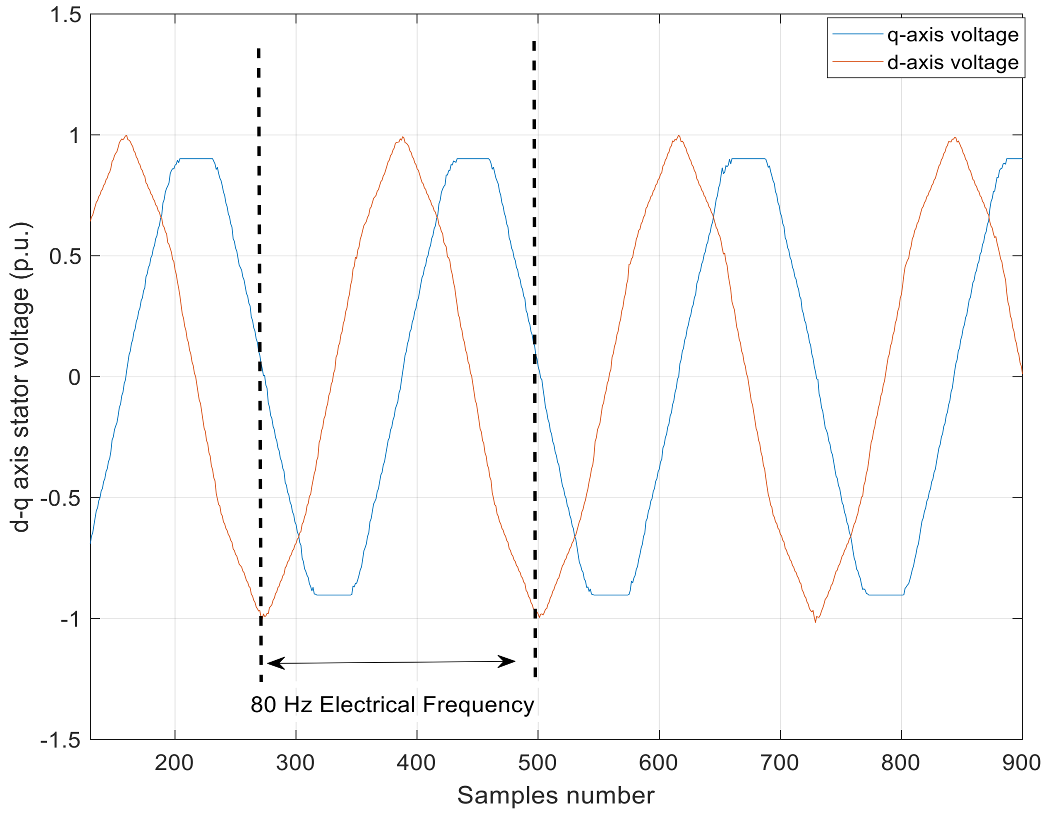


(e)

Fig. 6.6 Experimental results: (a) d-axis current. (b) q-axis current (c) current trajectory (P.U.) (d) voltage trajectory (P.U.) in rotor speed of 2,400rpm (e) d-q-axis of voltage (P.U.) in stationary frame at 2,400 rpm

### 6.4.1.2 Output torque and power in CT and FW region

The output torque and power were obtained with a torque transducer measuring the whole operational region. The speed is adjusted from 0 to 3,000 rpm by a dynamometer, which controls the PM load machine with a higher power rate compared to the test IM. In each operating speed, the proposed d-axis current is developed in order to maximise the utilisation of the inverter voltage. Figure 6.7 shows the measured torque and power for proposed and conventional voltage based control. As can be seen from the results, the output torque and power are increased in the FW region for the proposed scheme.

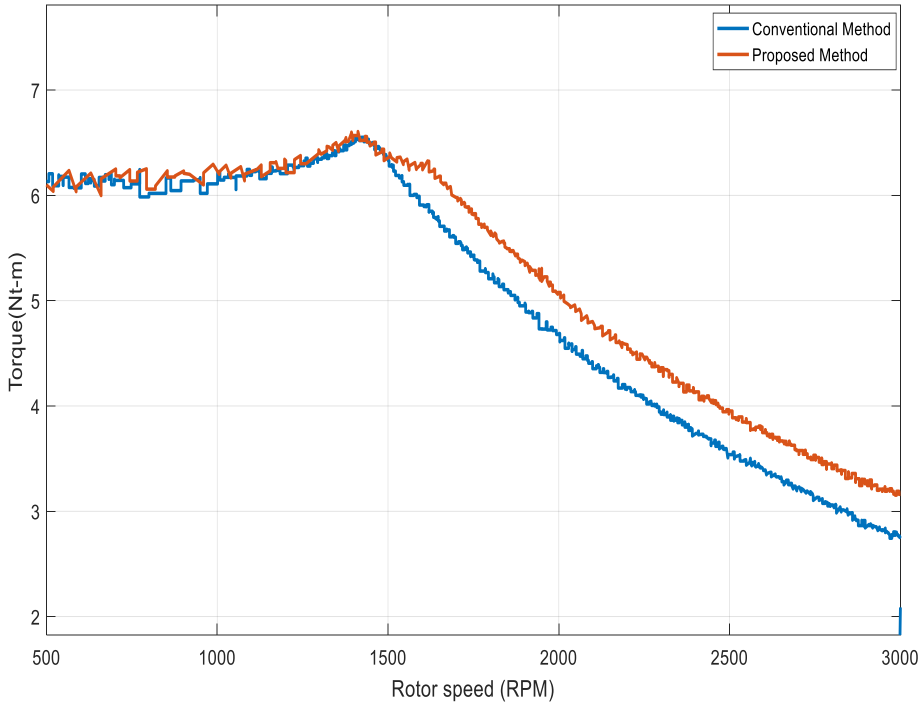


(a)

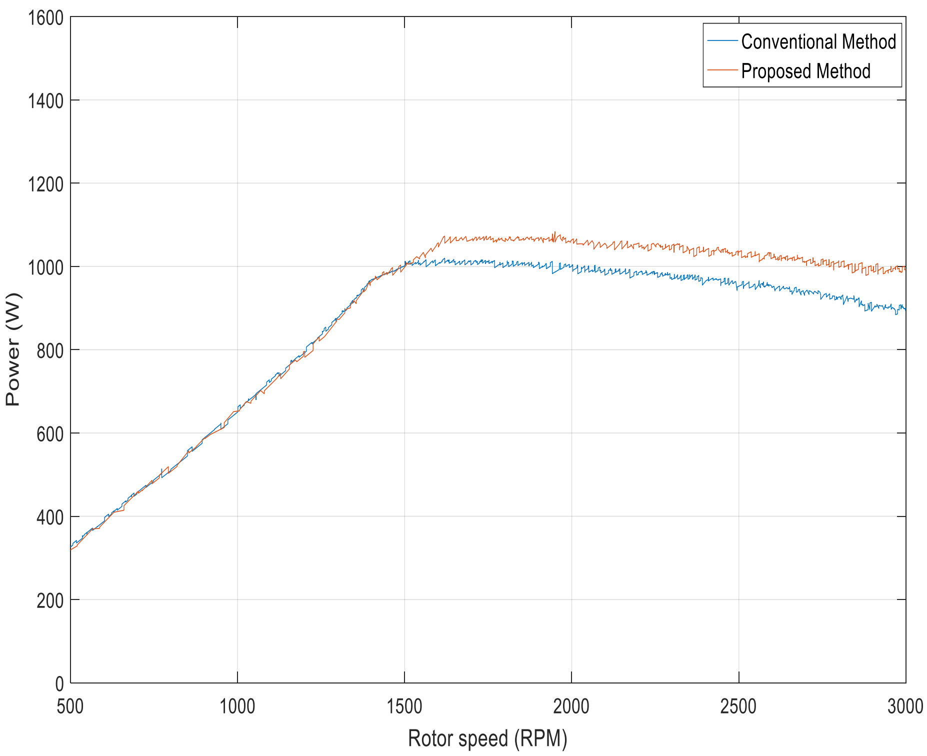


(b)

Fig. 6.7 Experimental comparison of proposed method and conventional method A in Fig.2.2. (a) Torque speed curve. (b) Power speed curve.

#### 6.4.1.3 Transient comparison of proposed method and active timing scheme

The comparison between torque and power waveforms for the proposed and conventional voltage based control in Fig .6.7 confirms the increment of inverter voltage utilisation. Further results are demonstrated in Fig. 6.8 where the proposed method is compared with the active timing scheme explained in Section 2.2.2.2. The results confirm that the fake extension voltage in active timing method impacts on the current ripple high reduction of d-axis current in the transition period from CT to FW region. As explained in detail in Section 6.4.1.1, these ripples are the result of not properly selecting the current reference. These current ripples then affects the stator voltage, which can be clearly seen in Fig. 6.8.

#### 6.4.1.4 Comparison of proposed methods in Chapter 5 and Chapter 6

This section provides the performance comparison of the proposed methods in Chapter 5 and Chapter6. In model-based control algorithm developed in Chapter 5, the reference d-axis current is calculated based on the position of stator voltage vector to achieve the hexagonal voltage boundary. This causes that the reference d-axis current (presented in Fig. 5.8a2, a3) has less oscillations comparing with proposed d-axis current (presented in Fig. 6.5a2, a3) in Chapter 6 where reference current is produced by the outer voltage loop controller. Although, the cycle-based control on stator voltage causes to produce more oscillations in reference currents, however the motor currents have less oscillations as the results more control on stator voltage vector. Therefore, the q-axis current in Fig. 6.5b1 has less oscillation comparing with Fig. 5.8b2. It worth mentioning that both methods satisfy the voltage and current constraints (shown in Fig. 6.6c, d and Fig. 5.10) however the closed-loop voltage controller requires extra regulator which add extra complexity to the control system. Although, both control algorithms require the accurate slip calculation the model-based control algorithm still is more sensitive to variation of motor parameters due to calculation of d-axis current in FW regions. The calculated G gain in transient period from CT to FW region helps the model-based control to have the smooth torque transition as shown in 5.13. This is also satisfied by closed-loop voltage controller where the voltage vector in FW region starts from last point from CT region as demonstrated in Fig. 6.7. It should be noted that the closed-loop voltage controller is more reliable in terms of dealing with the current controller fault. Therefore, this method is more practical in high-speed applications where the high torque accuracy is required.

Table 6.1 Performance comparison between model-based control and closed-loop voltage control algorithm

| | Smoother reference d-q axis currents | Current and voltage constraints | Maximising extraction of DC-link voltage | Extra regulator | Sensitive to motor parameters | Smooth torque transition from CT to FW |
|---|---|---|---|---|---|---|
| Model-based control | — | ✖ | ✖ | — | ✖ | ✖ |
| Closed-loop voltage control | ✖ | ✖ | ✖ | ✖ | — | ✖ |

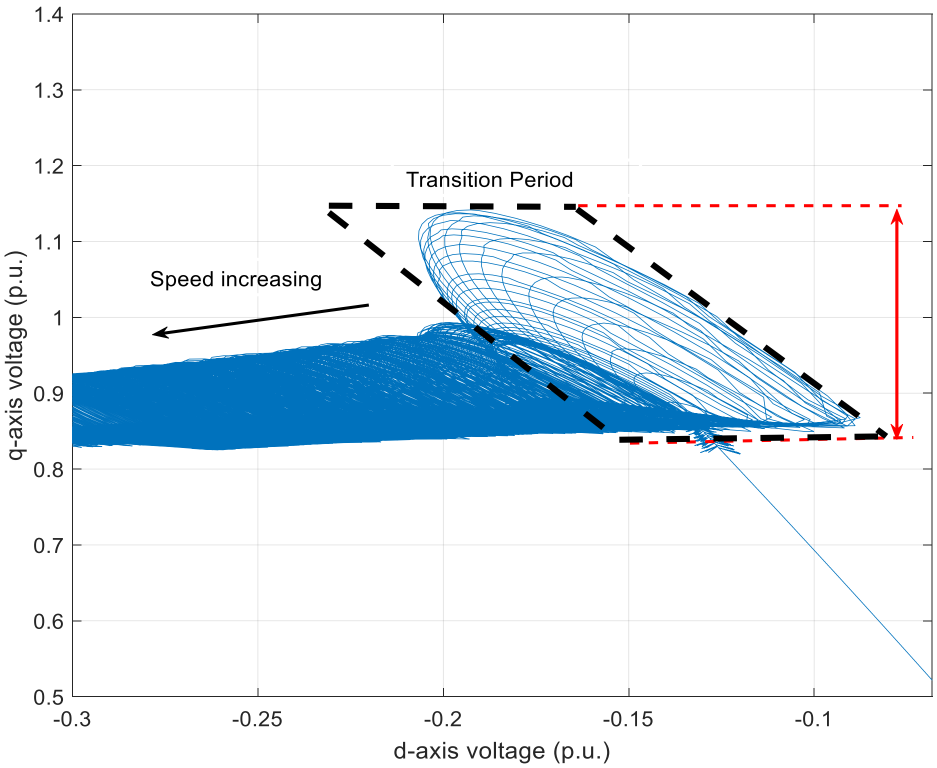
Transition Period
Speed increasing
q-axis voltage (p.u.)
d-axis voltage (p.u.)
1.4
1.3
1.2
1.1
1
0.9
0.8
0.7
0.6
0.5
-0.3
-0.25
-0.2
-0.15
-0.1

(a)

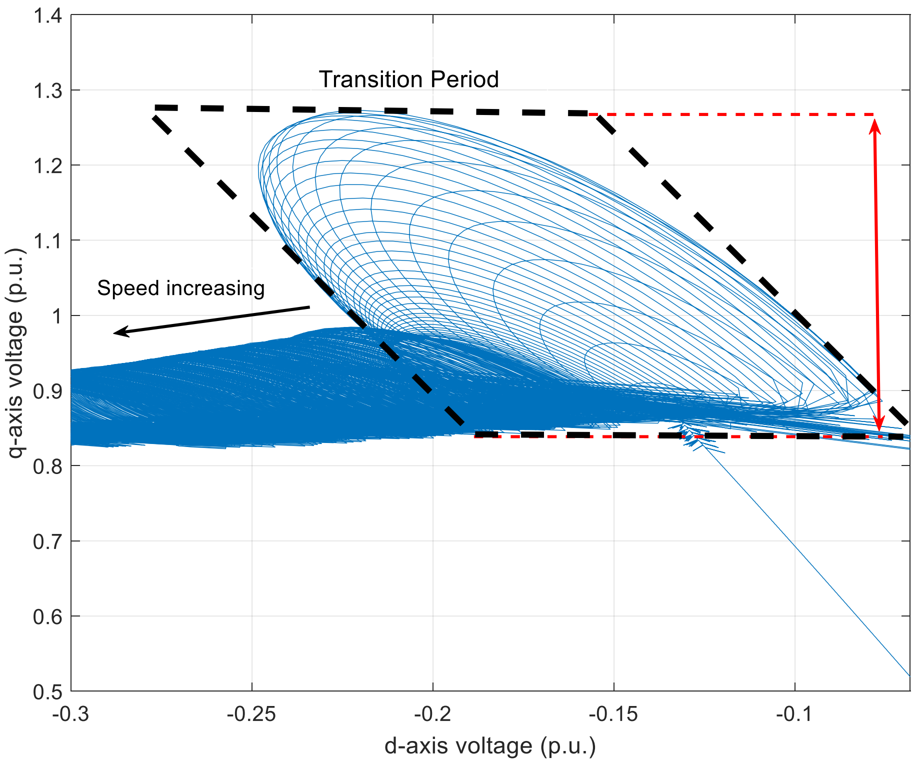
Transition Period
Speed increasing
q-axis voltage (p.u.)
d-axis voltage (p.u.)
1.4
1.3
1.2
1.1
1
0.9
0.8
0.7
0.6
0.5
-0.3
-0.25
-0.2
-0.15
-0.1

(b)

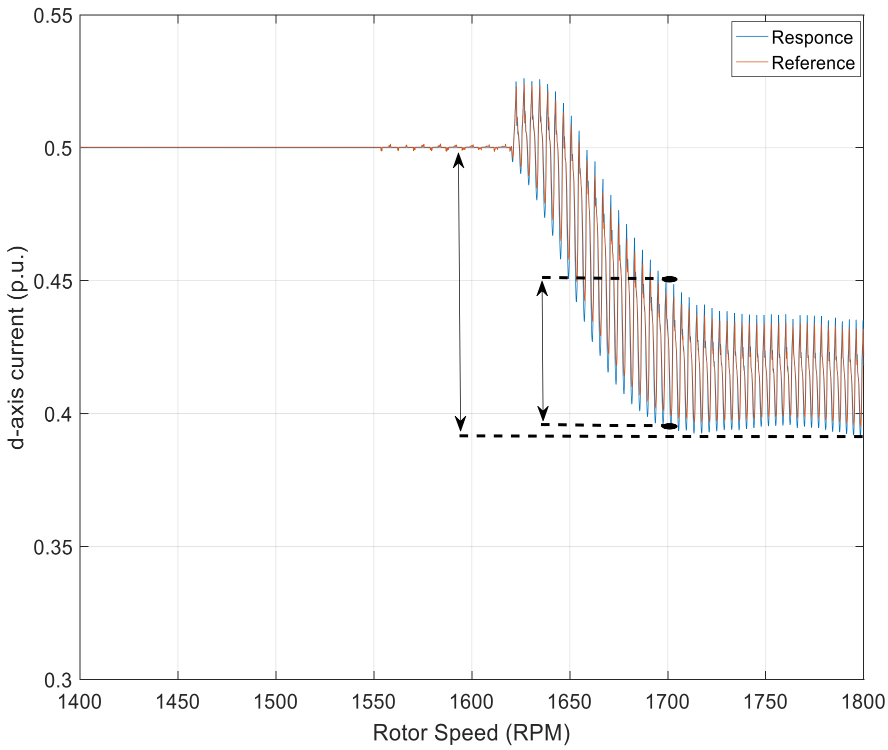

Responce
Reference
d-axis current (p.u.)
Rotor Speed (RPM)
0.55
0.5
0.45
0.4
0.35
0.3
1400
1450
1500
1550
1600
1650
1700
1750
1800


(c)

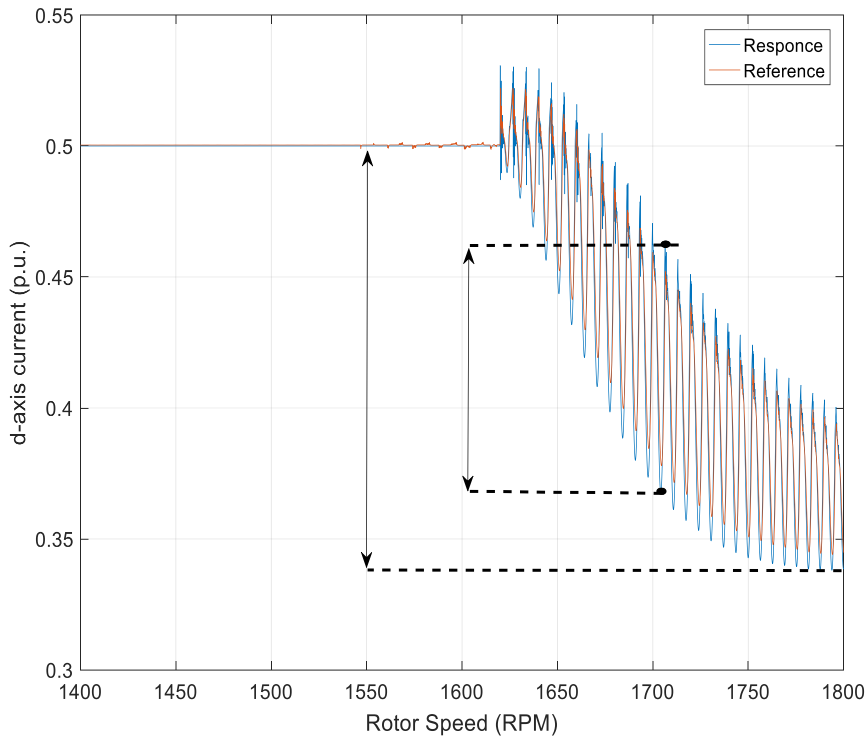

Responce
Reference
d-axis current (p.u.)
Rotor Speed (RPM)
0.55
0.5
0.45
0.4
0.35
0.3
1400
1450
1500
1550
1600
1650
1700
1750
1800


(d)

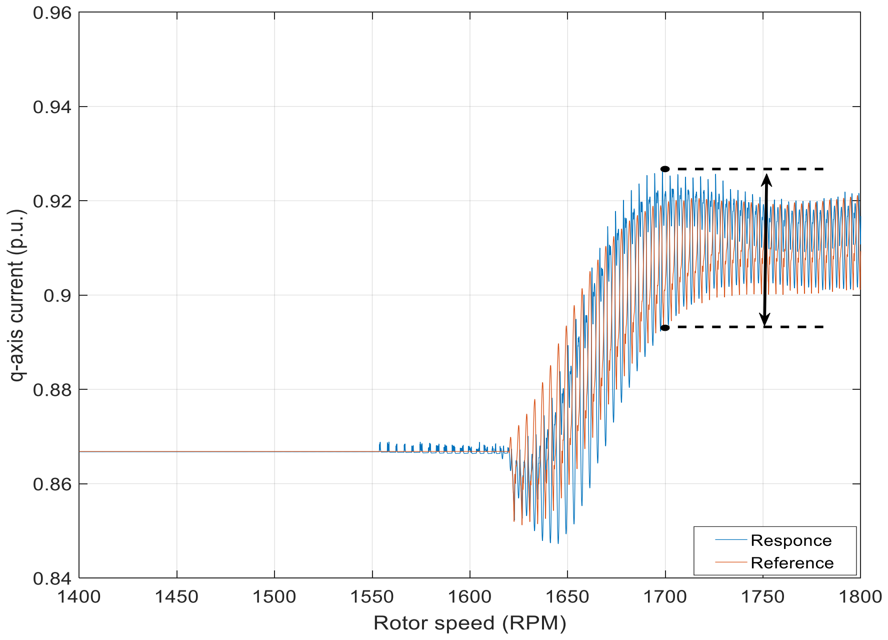


(e)

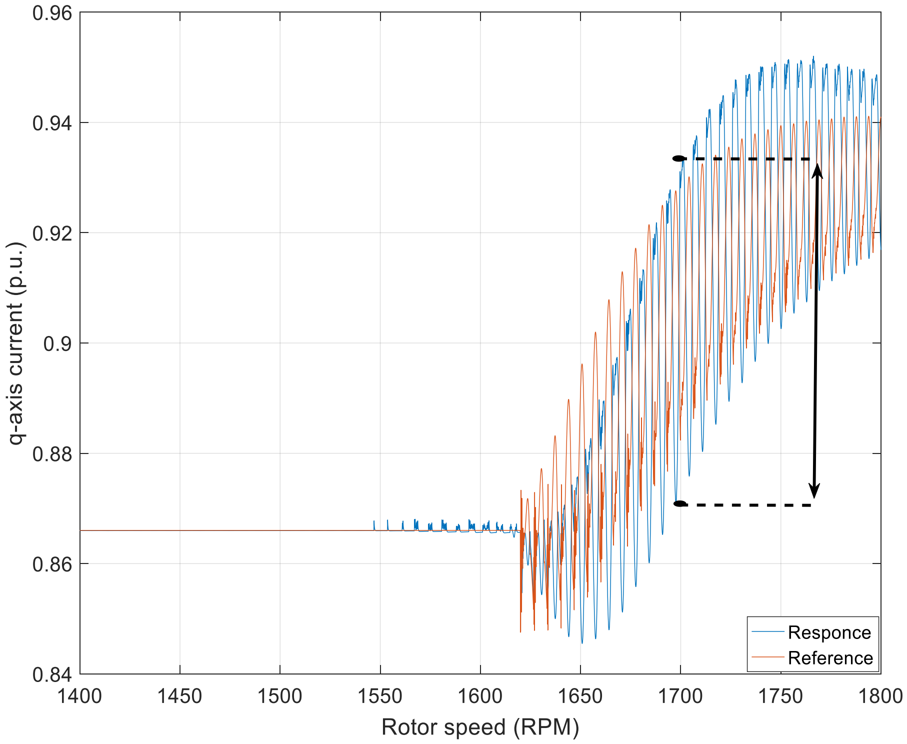


(f)

Fig. 6.8 Comparison between proposed method and Method C: (a) stator voltage of proposed method in synchronous frame (b) stator voltage of Method C in synchronous frame (c) d-axis current (P.U.) of proposed method (d) d-axis current (P.U.) of Method C (e) q-axis of current (P.U.) of proposed method (f) q-axis of current (P.U.) of Method C in Fig 2.2.

### 6.5 Summary

In this chapter, a new closed-loop voltage control is presented to maximise the utilisation of the inverter DC-link voltage in the field-weakening region. This is achieved by calculating the d-axis current based on the angular difference between the hexagonal voltage boundry and stator voltage magnitude for the corresponding angle of the stator voltage vector. As a result, the output torque and power of the motor is increased in the field weakening region. This method prevents the high step reduction in d-axis current for the transition period from CT to the FWI region. The method uses root-locos based tuning for the outer PI controller. Therefore, a smooth transition is achived without losing the maximum output torque due to a high step reduction in d-axis current and rotor flux. Furthermore~~,~~ the ripple in the q-axis current is reduced in comparison with the active timing method due to minimising the fake stator voltage and consequently reducing the drop in q-axis motor current. The mathematical analysis for extracting the hexagonal voltage and controlling the motor in different operational regions based on the applied d-q axis currents is presented in this chapter. The feasibility of the proposed method is also validated by thesimulation and experimental results.

# CHAPTER 7

# Estimation of Rotor Resistance and Magnetizing Inductance for Induction Motor Drives

## 7.1 Introduction

The proposed methods in Chapter 5 and Chapter 6 maximises the voltage utilization of DC-link voltage. Both methods require to have the accurate value of the motor parameters especially magnetising inductance as described in (5.9) to (5.13) in Chapter 5 and (6.5) to (6.7) in Chapter 6. In high power and speed IMs where the d-q axis of motor currents vary significantly in CT and FW regions, the magnetising inductance of the motor saturates. Therefore, the proper estimation of motor parameters are required for slip estimation and proper calculation of control algorithm. In this Chapter, a novel parameter estimation is described for an IM based on the combination of the Kalman-filter (KF) algorithm and model reference adaptive system (MRAS). In this method, the estimated rotor flux based on KF is utilised to define the magnetising inductance. To guarantee the accuracy of the utilised rotor flux and corresponding estimated magnetising inductance, the MRAS-flux-based feedback is added to the KF algorithm. Then, the estimated magnetising inductances and rotor flux are utilised to calculate the rotor resistance. This proposed method improves the accuracy of the state and parameters estimation of IM and also reduces the computation time process which exists on the extended KF algorithm EKF. The proposed estimation concept is mathematically proven and verified by simulation. This chapter also includes the mathematical development of EKF for estimating the rotor resistance and magnetising inductance. The developed EKF is then implemented and verified on the real-time processor.

## 7.2 EKF for estimating IM parameters

### 7.2.1 Nonlinear state estimator

As mentioned in KF section of Chapter 2, the stochastic state space model, which contains of process noise $\boldsymbol{w}(k)$ and measurement noise $\boldsymbol{v}(k)$, needs to be modelled as follows [79]:

$$E\{\boldsymbol{w}(k)\boldsymbol{w}(j)^T\} = \boldsymbol{Q}\delta_{kj} \qquad \boldsymbol{Q} \geq 0 \tag{7.1}$$

$$E\{\boldsymbol{v}(k)\boldsymbol{v}(j)^T\} = \boldsymbol{R}\delta_{kj} \qquad \boldsymbol{R} \geq 0$$

Where, $R$ , $Q$ and $\delta_{kj}$ are the constant scaler variance and Kronecker delta respectively. The measurement noise covariance matrix is considered to be a result of uncertainty of stator current measurement. The selection of the aforementioned value for the $\boldsymbol{R}$ matrix in (3.39) is the result of the percentage of measurements error. Finding the accurate value of the $\boldsymbol{Q}$ matrix in a practical experiment is based on trial and error and checking the captured data [59]. Therefore, the stochastic state space model can be developed by adding $\boldsymbol{w}(k)$ and $\boldsymbol{v}(k)$ to the discrete state space model as follow:

$$\boldsymbol{x}(k+1) = \boldsymbol{F}(k)\boldsymbol{x}(k) + \boldsymbol{G}(k)\boldsymbol{u}(k) + \boldsymbol{w}(k) \tag{7.2}$$

$$\boldsymbol{y}(k) = \boldsymbol{H}\boldsymbol{x}(k) + \boldsymbol{v}(k)$$

To solve the stochastic state space model, Gaussian distribution needs to be applied [80]. This solution needs the calculation of the state error covariance matrix ($\boldsymbol{P}(k)$) and the output error covariance matrix ($\boldsymbol{S}(k)$). The distribution mean vectors of state and output ($\hat{x}$ , $\hat{y}$) are two answers to the Gaussian distribution solution. These answers as the estimated variables could be achieved by applying the KF method. By considering the stochastic or random aspects of the system, the minimum variance estimator or KF is the appropriate estimation solution to estimate the states of the IM. It should also be considered that the major value of KF lies in its ability to estimate the unmeasurable states in the system. As shown in Fig. 3.10, the KF can be expressed in a predictor and corrector form as follows:

The estate prediction is derived by:

$$\hat{\boldsymbol{x}}(k+1/k) = \boldsymbol{F}(k)\hat{\boldsymbol{x}}(k/k) + \boldsymbol{G}(k)\boldsymbol{u}(k) \tag{7.3}$$

$$\boldsymbol{P}(k+1/k) = \boldsymbol{F}(k)\boldsymbol{P}(k/k)\boldsymbol{F}(k)^T + \boldsymbol{Q}$$

The state correction could also be given by:

$$\boldsymbol{K}(k+1/k)=\boldsymbol{P}(k+1/k)\boldsymbol{H}(k+1)^T[\boldsymbol{H}(k)\boldsymbol{P}\left(k+\frac{1}{k}\right)\boldsymbol{H}(k)^T+\boldsymbol{R}]^{-1} \quad (7.4)$$

$$\hat{\boldsymbol{x}}(k+1/k+1)=\hat{\boldsymbol{x}}(k+1/k)+\boldsymbol{K}(k+1)[\boldsymbol{y}(k+1)-\boldsymbol{H}(k+1)\hat{\boldsymbol{x}}(k+1/k)]$$

$$\boldsymbol{P}(k+1/k+1)=\boldsymbol{P}(k+1/k)-\boldsymbol{K}(k+1)\boldsymbol{H}(k+1)\boldsymbol{P}(k+1/k)$$

It should be noted that $\hat{\boldsymbol{x}}(k/k)$ and $\hat{\boldsymbol{x}}(k+1/k)$ are the estimation of the state in discrete sequence of $k$ which is based on the data available and includes $k$ and $k+1$ sequence respectively. As expressed in (7.3), the Kalman gain is also defined by $\boldsymbol{K}(k+1)$.

The parameters of an induction machine can be considered as an augmented state in the state vector to be estimated by the extended Kalman filter (EKF). In [93],$\frac{\frac{{L_m}^2}{L_r}r_r}{L_r}$, $\frac{1}{(\frac{{L_m}^2}{L_r})}$ are added to the KF, as explained in Section 3.4.1, as new states to estimate the magnetising inductance and rotor resistance. Selection of these variables as augmented states does not produce precise estimations because some parts of the Jacobian matrix are assumed to be constant. This causes the variation of estimated parameters to affect those variables whose values are considered constant. This leads to the fact that the updated Jacobian matrix in each interrupt service routine will not be corrected. So, the state prediction and correction algorithm in EKF does not update with the correct Jacobian matrix. Therefore, the constant variables such as $\sigma L_s$, $(\frac{-1+\sigma}{\sigma L_m})$ and $\frac{L_m}{\sigma L_s L_r}$ are considered in the Jacobian matrix for developing EKF in this chapter. These variables are approximately constant as $L_m$ and $r_r$ are varying. By adding the motor parameters ($L_m$ and $r_r$) as new states, the state space model becomes nonlinear as result of states multiplication. To solve the none-linear state estimation problem, the extended Kalman filter is used as the nonlinear state estimator [62]. In this algorithm, the time-varying parameter, which is included as an additional state, is defined as follows:

$$\boldsymbol{\theta}(k+1)=\boldsymbol{\theta}(k)+\boldsymbol{n}(k) \quad (7.5)$$

In (7.5), the unknown random disturbance is introduced by $n(k)$. Then, the extended state space model can be expressed by (7.6). It needs to be mentioned that the undefined variables in the following equations are already defined in Section 3.4.1.

$$\boldsymbol{x}(k+1) = \boldsymbol{F}(\theta(k),k)x(k) + \boldsymbol{G}(\theta(k),k)u(k) + \boldsymbol{w}(k) \tag{7.6}$$

By considering (3.38), the new state vector could be defined as:

$$\boldsymbol{z}(k) = \begin{bmatrix} x(k) \\ \theta(k) \end{bmatrix} \tag{7.7}$$

The augmented state model is then presented by:

$$\boldsymbol{z}(k+1) = \boldsymbol{f}\big(z(k),u(k)\big) + \boldsymbol{w}'(k) \tag{7.8}$$

Where;

$$\boldsymbol{z}(k+1) = \boldsymbol{f}\big(z(k),u(k)\big) + \boldsymbol{w}'(k) \tag{7.9}$$

$$\boldsymbol{f}\big(z(k),u(k)\big) = \begin{bmatrix} F(\theta(k),k)x(k) + G(\theta(k),k)u(k) \\ \theta(k) \end{bmatrix}$$

$$\boldsymbol{w}'(k) = \begin{bmatrix} w(k) \\ n(k) \end{bmatrix}$$

The output vector, which is not dependent on $\theta(k)$, can be explained as follows:

$$y(k) = Hx(k) + v(k) \tag{7.10}$$

As explained in Section 3.4.1, the mean value of the random vectors ($w'(k)$ $and$ $v(k)$) are assumed to be zero. This assumption is based on the intention of implementing the KF algorithm. The covariance of measurement noise and proses noise in EKF is given as follows:

$$\boldsymbol{E}\{v(k),v(j)^T\} = R\delta_{kj} \tag{7.11}$$

$$\boldsymbol{E}\left\{\begin{bmatrix} w(k) \\ n(k) \end{bmatrix}\begin{bmatrix} w(j) \\ n(j) \end{bmatrix}^T\right\} = \boldsymbol{E}\begin{Bmatrix} w(k)w(j)^T & w(k)n(j)^T \\ n(k)w(j)^T & n(k)n(j)^T \end{Bmatrix} = \begin{Bmatrix} Q_{ww} & Q_{wn} \\ Q_{nw} & Q_{nn} \end{Bmatrix}\delta_{kj}$$

The covariance of natural state uncertainty and covariance of the parameter disturbance vector are symbolised by $Q_{ww}$ and $Q_{nn}$. As a result of there being no correlation between the natural and parameters states, $Q_{nw} = Q_{wn} = 0$. The initial state error covariance matrix can be defined as follows:

$$\boldsymbol{P}(0) = \begin{bmatrix} P_{ww} & P_{wn} \\ P_{nw} & P_{nn} \end{bmatrix} \tag{7.12}$$

where, $P_{ww}$ and $P_{nn}$ describe the quality of the prior knowledge of natural states and parameter states repetitively. Any interdependence between natural states and parameters states is defined by $P_{wn}$ and $P_{nw}$.

### 7.2.2 State predication and state correction in EKF

To solve the EKF estimating the states and parameters of IM, the state prediction and state correction equations need to be implemented. The state prediction equation of EKF can be calculated by:

$$\boldsymbol{f}\big(z(k),u(k)\big) = \begin{bmatrix} F(\theta(k),k)x(k) + G(\theta(k),k)u(k) \\ \theta(k) \end{bmatrix} \tag{7.13}$$

$$\begin{bmatrix} i_{ds}^{s}(k+1) \\ i_{qs}^{s}(k+1) \\ \lambda_{dr}^{s}(k+1) \\ \lambda_{qr}^{s}(k+1) \\ \dfrac{1}{L_m}(k+1) \\ \dfrac{{L_m}^2}{L_r} r_r(k+1) \end{bmatrix} = \begin{bmatrix} A & 0 & B & C & 0 & 0 \\ 0 & A & -C & B & 0 & 0 \\ D & 0 & E & G & 0 & 0 \\ 0 & D & -G & E & 0 & 0 \\ 0 & 0 & 0 & 0 & 1 & 0 \\ 0 & 0 & 0 & 0 & 0 & 1 \end{bmatrix} \begin{bmatrix} i_{ds}^{s}(k) \\ i_{qs}^{s}(k) \\ \lambda_{dr}^{s}(k) \\ \lambda_{qr}^{s}(k) \\ \dfrac{1}{L_m}(k) \\ \dfrac{{L_m}^2}{L_r} r_r(k) \end{bmatrix} + \begin{bmatrix} \dfrac{t_s}{\sigma L_s} & 0 \\ 0 & \dfrac{t_s}{\sigma L_s} \\ 0 & 0 \\ 0 & 0 \\ 0 & 0 \\ 0 & 0 \end{bmatrix} \begin{bmatrix} v_{ds}^{s}(t) \\ v_{qs}^{s}(t) \end{bmatrix}$$

$$A = 1 + t_s\left(\frac{-r_s}{\sigma L_s} + \frac{-1+\sigma}{\sigma L_m} z(6)z(5)\right), B = t_s\frac{L_m}{\sigma L_s L_r}\big(z(5)^2 z(6)\big), C = t_s\frac{L_m}{\sigma L_s L_r}(\omega_r)$$

$$D = t_s\big(z(6)z(5)\big), E = 1 + t_s\big(-z(5)^2 z(6)\big), G = -t_s\omega_r$$

As can be deduced from (7.13), $\frac{1}{L_m}$ and $\frac{{L_m}^2}{L_r} r_r$ are considered as fifth and sixth states for the state space model of IM. $\omega_r$ is the electrical speed, which depends on the mechanical speed and number of motor poles. As shown in (7.2) and (7.3), the state correction and state prediction equation require the Jacobian matrix which is defined by:

$$\boldsymbol{F}(k) = \frac{\partial f(.)}{\partial z(k)} \|_{\hat{z}(k),u(k)} \rightarrow \boldsymbol{F}(k) = \begin{bmatrix} \dfrac{\partial f1}{\partial x1} & \cdots & \dfrac{\partial f1}{\partial xn} \\ \vdots & \ddots & \vdots \\ \dfrac{\partial fn}{\partial x1} & \cdots & \dfrac{\partial fn}{\partial xn} \end{bmatrix} \rightarrow \boldsymbol{F}(k) = \begin{bmatrix} A & 0 & B & C & H & M \\ 0 & A & -C & B & I & N \\ D & 0 & E & G & J & O \\ 0 & D & -G & E & T & S \\ 0 & 0 & 0 & 0 & 1 & 0 \\ 0 & 0 & 0 & 0 & 0 & 1 \end{bmatrix} \tag{7.14}$$

$$H = t_s z(1)\left(\frac{-1+\sigma}{\sigma L_m} z(6)\right) + t_s z(3)\frac{L_m}{\sigma L_s L_r}\big(2z(6)z(5)\big)$$

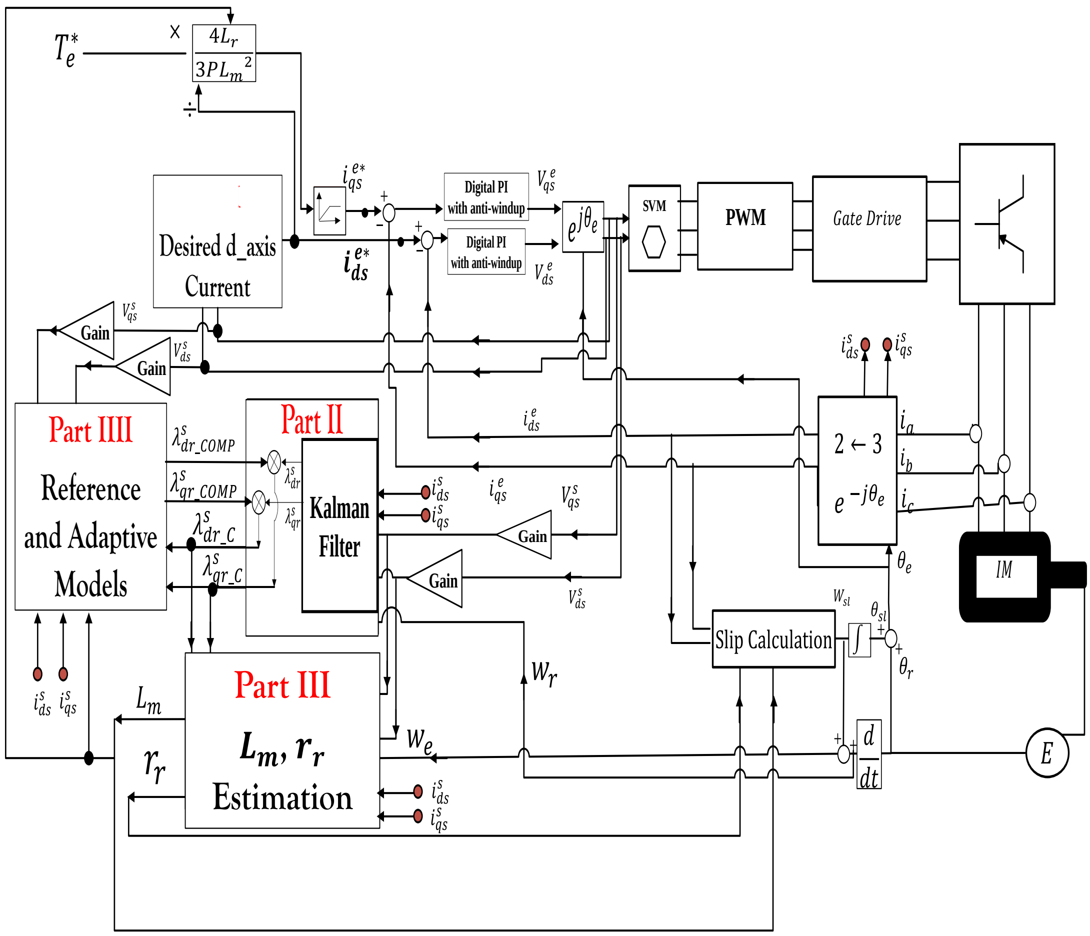

Fig. 7.1 Block diagram of the proposed method for parameter estimation of IM in the current-based control algorithm

$$I = t_s z(2)\left(\frac{-1+\sigma}{\sigma L_m} z(6)z\right) + t_s z(4)\frac{L_m}{\sigma L_s L_r}\big(2z(6)z(5)\big)$$

$$J = t_s\big(z(6)z(1)\big) - t_s z(3)\big(2z(6)z(5)\big), \qquad T = t_s\big(z(6)z(2)\big) - t_s z(4)\big(2z(6)z(5)\big)$$

$$M = t_s z(1)\left(\frac{-1+\sigma}{\sigma L_m} z(5)\right) + t_s z(3)\left(\frac{L_m}{\sigma L_s L_r} z(5)z(5)\right)$$

$$N = t_s z(2)\left(\frac{-1+\sigma}{\sigma L_m} z(5)\right) + t_s z(4)\left(\frac{L_m}{\sigma L_s L_r} z(5)z(5)\right)$$

$$O = t_s z(5)z(1) - t_s z(3)z(5)z(5), \qquad S = t_s z(5)z(2) - t_s z(4)z(5)z(5)$$

As can be seen from the developed EKF, many variables need to be defined and a huge computation process is needs to be considered. This means that the developed EKF could not be executed in one

PWM cycle when the switching frequency is high. It also needs huge memory space to save all defined variables and matrix indexes in (7.2) and (7.3). Furthermore, as shown in (7.11) and (7.12), selection of a state error covariance matrix applies more complexity to the developed EKF. Therefore, the proposed estimation method is developed for estimating stator inductance and rotor resistance. In this method, the extended part of EKF is removed which speeds up the process of execution and reduces the required memory spaces. This proposed method also produce more accurate estimation results, which are presented in Section 7.5.

### 7.3 Proposed estimation method

The accurate estimation of $L_m$ and $r_r$ is presented by Fig. 7.1 where a combination of MRAS, KF and mathematical modelling is used. As shown in Fig. 7.1, the proposed method consists of three controllers: Part II, Part III and Part IV, which are explained below.

#### 7.3.1 Part II: KF algorithm for flux estimation

In Part II, the KF algorithm estimates $\vec{\lambda}^s_{dqr}$ based on the description in Section 3.4.1. As shown in Fig. 7.2, the measured d-q axis of stator currents is compared with the components of the predicted stator

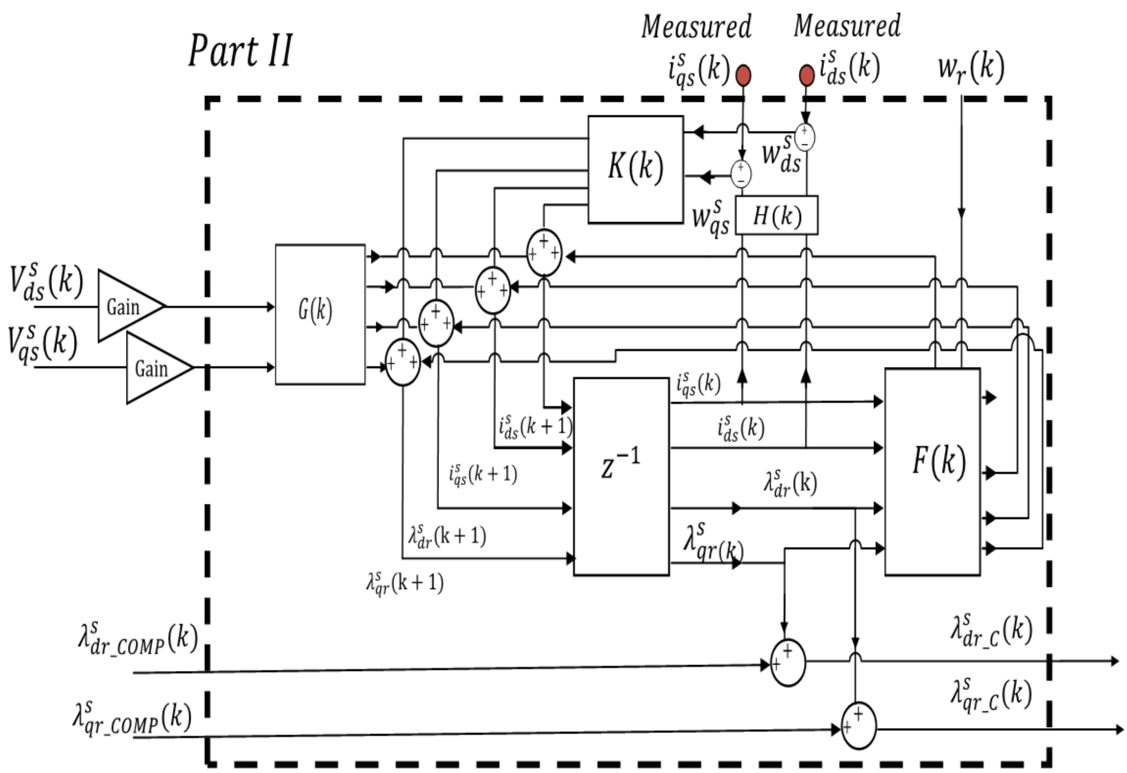


Fig. 7.2 Structure of KF estimator based on d-q axis of stator current and rotor flux IM model

current to produce the measurement error components $w_{ds}^{s}, w_{qs}^{s}$. The accuracy of the predicted stator current from one step to the next is indicated by the level of this error. Then, the gain matrix $K(k)$ is multiplied by the predicted error to form one of the state inputs. This input plays a key role in minimising the model output prediction error. The second states inputs are the results of the multiplication of states with the state feedback matrix $F(k)$, which is updated by an extra input $\omega_r(k)$. The last state inputs are formed by the stator voltage signals, which are extracted from the input of SVM algorithm, and multiplied by input gain matrix $G(k)$. It should be noted that $\frac{2V_{DC-LINK}}{3}$ is considered as the gain to produce the peak stator voltage from the scaled SVM input voltage. The described state inputs are verified by (7.2), (7.3) and (7.4).

As demonstrated in Fig. 7.2, the estimated $\vec{\lambda}_{dqr}^{s}$ on KF is added by the rotor flux compensator $\vec{\lambda}_{dqr\_COM}^{s}$, which is explained in Part IIII in this section, to provide the precise estimation of rotor flux $\lambda_{dqr\_C}^{s}$.

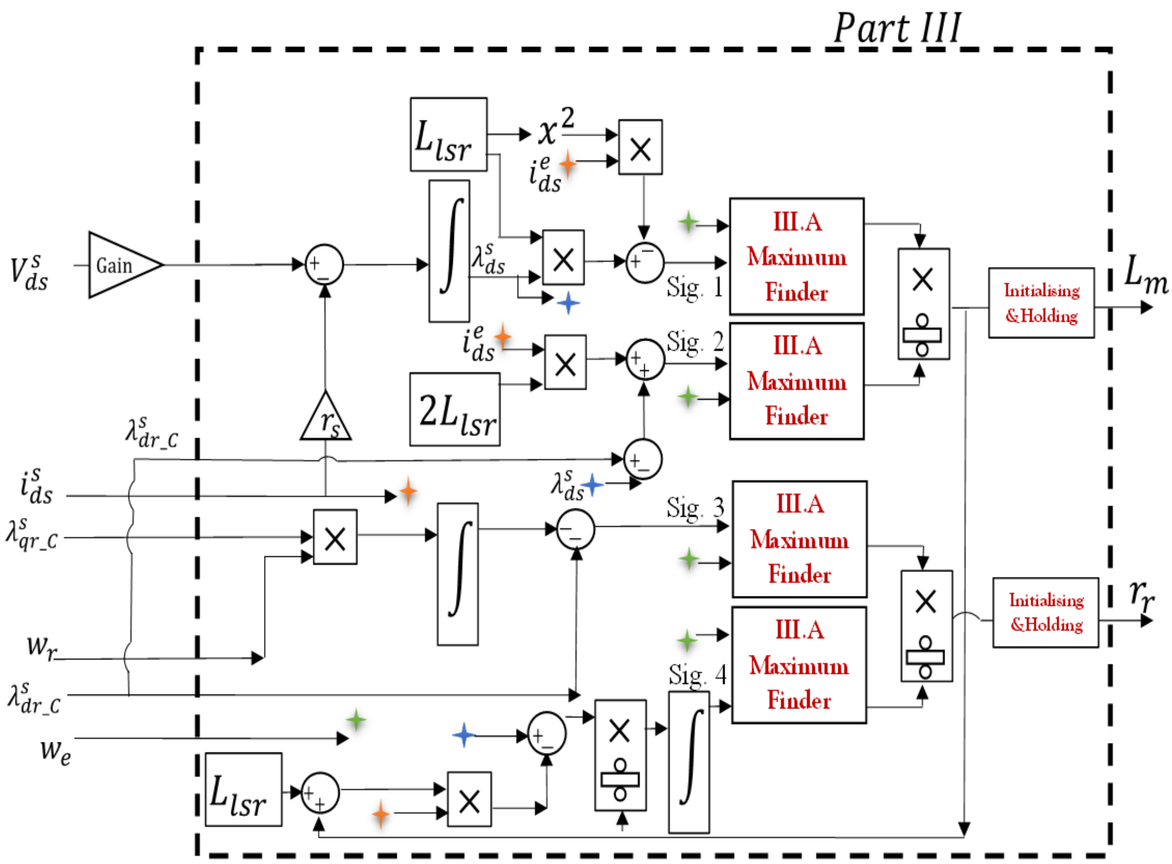

Fig. 7.3 Calculation of magnetizing inductance and rotor resistance of IM

### 7.3.2 Part III: Calculation of magnetizing inductance and rotor resistance

As shown in Fig. 7.3, the components of $\lambda_{dqr\_C}^{s}$ are utilised to calculate the magnetising inductance as follows:

$$\lambda_{ds}^{s} = L_s\, i_{ds}^{s} + L_m\, i_{dr}^{s} \tag{7.15}$$

$$i_{dr}^{s} = \frac{\lambda_{dr}^{s} - L_m i_{ds}^{s}}{L_r} \tag{7.16}$$

By substituting (7.16) within (7.15) and considering $L_r \cong L_s = L_m + L_{lsr}$, therefore:

$$L_m = \frac{\lambda_{ds}^{s} L_{lsr} - L_{lsr}{}^{2} i_{ds}^{s}}{\lambda_{dr}^{s} + 2L_{lsr} i_{ds}^{s} - \lambda_{ds}^{s}} \tag{7.17}$$

where, $\lambda_{ds}^{s}$ and $L_{lsr}$ are the d-axis of stator flux in stationary frame and rotor or stator leakage inductance. As shown in Fig. 7.3, calculated $L_m$ in (7.17) is used for estimating $r_r$:

$$\boldsymbol{V}_{dqr}^{r} = r_r \boldsymbol{i}_{dqr}^{r} + \frac{d\boldsymbol{\lambda}_{dqr}^{r}}{dt} \tag{7.18}$$

$$r_r = \frac{-\lambda_{dr}^{s} - \int \lambda_{qr}^{s}\, \omega_r dt}{\int \frac{\lambda_{ds}^{s} - i_{ds}^{s}(L_{lsr} + L_m)}{L_m} dt} \cong \frac{\frac{d\lambda_{dr}^{s}}{dt} - \lambda_{qr}^{s}\omega_r}{\frac{\lambda_{ds}^{s} - i_{ds}^{s}(L_{lsr} + L_m)}{L_m}} \tag{7.19}$$

As can be seen from (7.17) and (7.19), the rotor and stator flux and also the stator current in stationary frame are used. Therefore, the sinusoidal variation of variables is obvious. This gives their denominator the potential to have a zero value. To prevent this situation, the proposed Maximum-Finder method is applied as shown in Fig. 7.4. The Maximum-Finder mechanism holds the values of input signal for one electrical cycle and then passes its maximum in the next cycle. The frequency of a cycle is calculated based on the electrical speed $\omega_e$ which is the summation of $\omega_r$ and slip speed in IM. The calculated electrical frequency is applied to produce the ramp signal which is stepped up by using the PWM action counter. The ramp-generator is used by the Maximum-Finder mechanism to hold the corresponding signal for a specific frequency. It needs to be noticed that the ramp-generator becomes zero at the end of the time cycle period. Furthermore, as shown in Fig. 7.3, the initialising and holding mechanism are placed before realising the estimated values. These help the proposed method to pass the initial value of $L_m$ and $r_r$ in the starting condition and also it holds the last value when the maximum finder detects an unreasonable value for the signal.

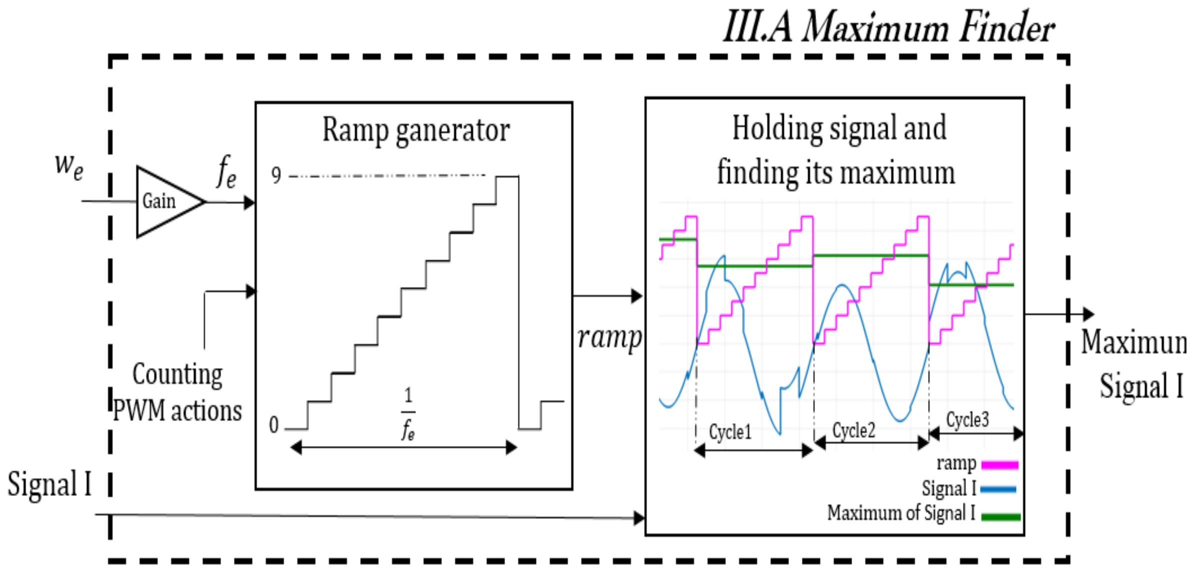


Fig. 7.4 Maximum- finder algorithm used to determine the maximum value of signals

### 7.3.3 Part IIII: MRAS flux observer for improving the estimated rotor flux in KF

As explained in Section 7.3, the uncertainty in the IM model is considered by describing the process noise covariance and the measurement noise covariance. Although the considered covariance in the IM model improves the described state space model in terms of model prediction the model could still be defined more precisely. It should be stated that the weak performance of KF, which is caused by the lack of an accurate selection of process and measurement noise covariance, is improved by applying the proposed compensator. As shown in Fig. 7.5, the rotor flux compensator components $\lambda^s_{dr\_COMP}$ and $\lambda^s_{qr\_COMP}$ are added by $\lambda^s_{dqr}$ to provide the precise estimation of rotor flux $\lambda^s_{dqr\_C}$.

As illustrated in Fig. 7.5, $\lambda^s_{dqr\_COMP}$ is the output of the PI controllers, which are trying to close the output of adaptive signals $\lambda^s_{dqr_adp}$to the reference signals $\lambda^s_{dqs}$. The defined $\lambda^s_{dqs}$ and $\lambda^s_{dqr\_adp}$ are achieved by:

$$\boldsymbol{\lambda}^s_{dqs} = \int \boldsymbol{V}^s_{dqs} - r_s \boldsymbol{i}^s_{dqs} \; dt \tag{7.20}$$

$$\boldsymbol{\lambda}^s_{dqr\_adp} = L_s \boldsymbol{i}^s_{dqs} + L_m \frac{\lambda^s_{dqr\_C} - L_m \boldsymbol{i}^s_{dqs}}{L_m + L_{lsr}} \tag{7.21}$$

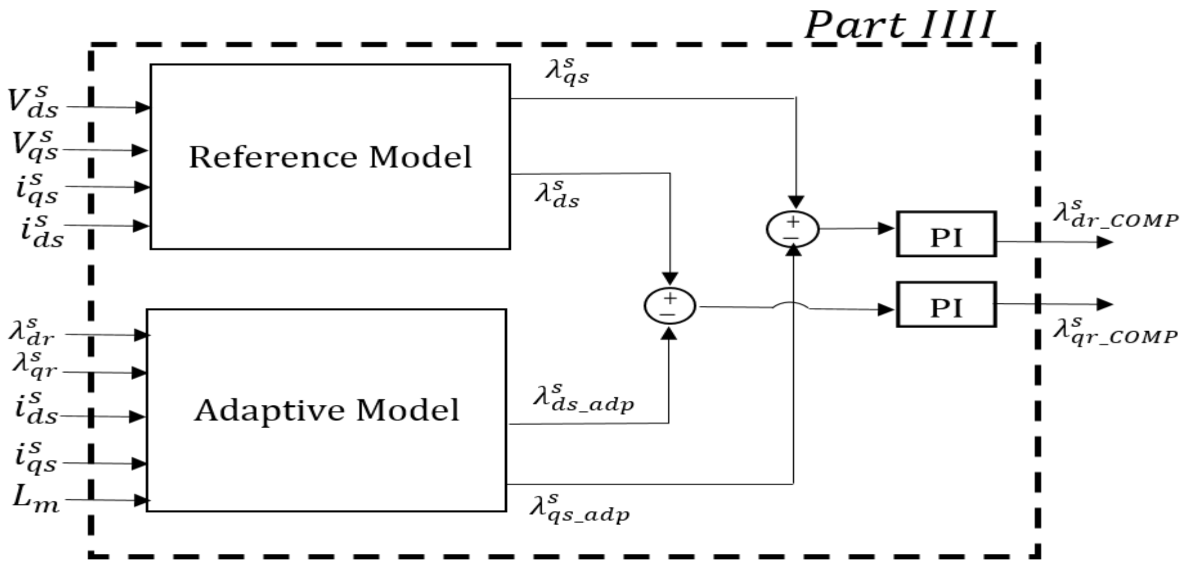


Fig. 7.5 Proposed MRAS flux observer mechanism to improve the KF flux estimator

As (7.21) illustrates, the estimated flux in the KF algorithm is used to improve the prediction of rotor flux in the proposed MRAS configuration. Therefore, the adaptive model can closely track the reference model when $\lambda_{dqr\_C}^s$ is properly achieved.

As discussed in Section 3.4, the stability of the MRAS observer needs to be analysed based on defined linear and nonlinear subsystems. As shown in Fig. 7.6, the stability of the proposed MRAS observer presented in Fig. 7.5 can be confirmed because the transfer function of the linear subsystem is positive and real. This satisfies the first condition of stability of the MRAS system explained in Section 3.4. The second condition of stability could also be satisfied by properly defining the adaption functions $\varphi_1(\varepsilon), \varphi_2(\varepsilon)$. First of all, the error vector needs to be defined as:

$$\varepsilon_d = \lambda_{ds}^s - \lambda_{ds\_adp}^s \tag{7.22}$$

$$\varepsilon_q = \lambda_{qs}^s - \lambda_{qs\_adp}^s \tag{7.23}$$

Therefore, the error vector and the output of the nonlinear function $W$ can be written as:

$$\varepsilon = [\varepsilon_d \quad \varepsilon_q]^T$$

$$\boldsymbol{W} = \left[\frac{-L_m}{L_r}\left(\lambda_{dr}^s - \lambda_{dr\_C}^s\right) - L_s\sigma i_{ds}^s \quad \frac{-L_m}{L_r}\left(\lambda_{qr}^s - \lambda_{qr\_C}^s\right) - L_s\sigma i_{qs}^s\right] \tag{7.24}$$

As can be realised from Fig. 7.6, $\lambda_{dr\_C}^s$ and $\lambda_{qr\_C}^s$ in above can be rewritten based on $\varphi_1(\varepsilon), \varphi_2(\varepsilon)$ as follow:

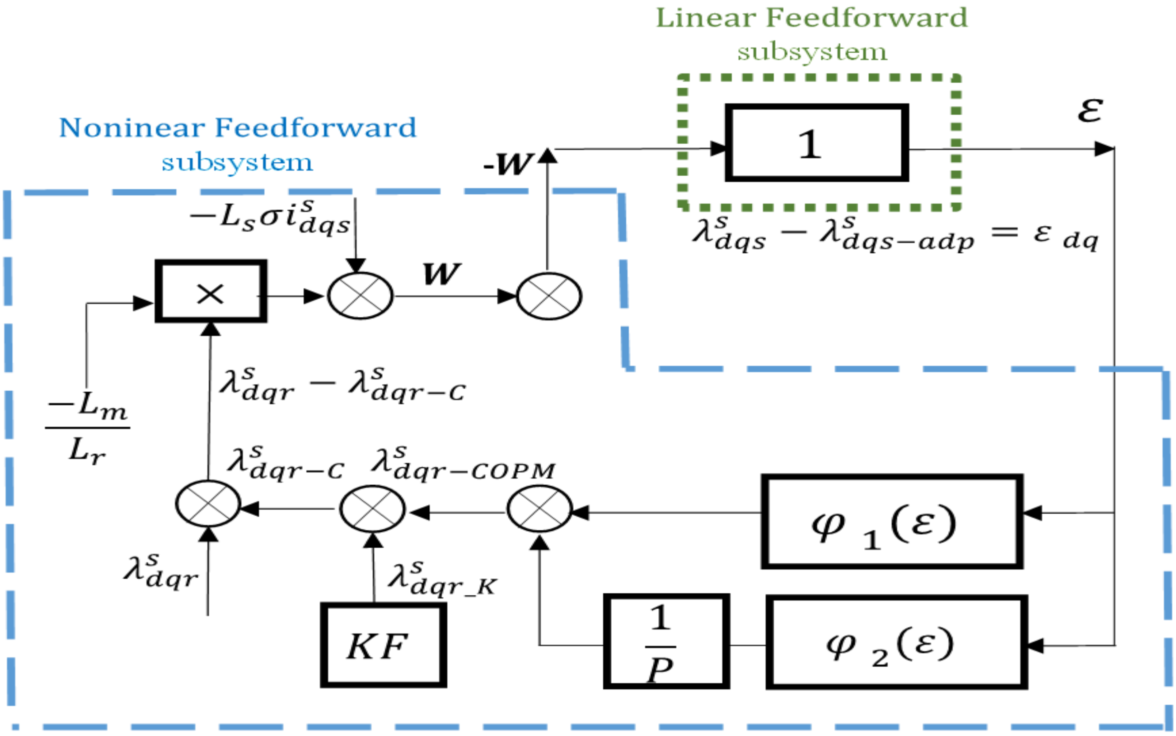


Fig. 7.6 The linear and nonlinear subsystems of the stator flux MRAS observer

$$\lambda^s_{dr\_C} = \varphi_1(\varepsilon) + \int_0^t \varphi_2(\varepsilon)\,dt + \lambda^s_{dr\_K} \tag{7.25}$$

$$\lambda^s_{qr\_C} = \varphi_1(\varepsilon) + \int_0^t \varphi_2(\varepsilon)\,dt + \lambda^s_{qr\_K} \tag{7.26}$$

Therefore, the inequality in 3.43 can be satisfied if the following functions are used:

$$\varphi_1(\varepsilon) = K_p\left(\lambda^s_{dqs} - \lambda^s_{ds_{adp}}\right) = K_p\varepsilon_{dq} \tag{7.27}$$

$$\varphi_2(\varepsilon) = K_i\left(\lambda^s_{dqs} - \lambda^s_{dqs_{adp}}\right) = K_i\varepsilon_{dq} \tag{7.28}$$

The positive $K_p$ and $K_i$ gains in (7.27) and (7.28) guarantee the second condition of MRAS stability. To validate the performance of the developed EKF and proposed estimation method, the simulation and real-time-emulator-based results are provided in the next section.

## 7.4 Results

### 7.4.1 Real time and simulation results for developed EKF in steady state condition

Figure. 7.7 shows the block diagram of implemented EKF in F28377d. The IM is emulated in the CPU2 of the microcontroller as explained in Section 4.2. In this test, the switching frequency and sampling frequency are fixed to 10KHz which is enough to run the EKF algorithm and plant emulator in the CPU2. It needs to be mentioned that the RK4 is solved only once to keep the running time within one PWM cycle. To improve the accuracy of the numerical solver (RK4), two instances of solving need to be considered. As shown in Appendix D, the running time of EKF and RK4 in CPU2 is 79us which is in the range of 100us for 10KHz switching frequency.

As shown in Fig. 7.8 and 7.9, the data are captured for 1,000 samples and each sample corresponds to 100 us. Therefore, the timing period for the captured data is 100 milliseconds. Figure 7.8a and b demonstrate the measured and estimated stator flux which are almost equal. The estimated rotor flux components are also illustrated in Fig. 7.8c which could be verified by (7.13) when the desired currents

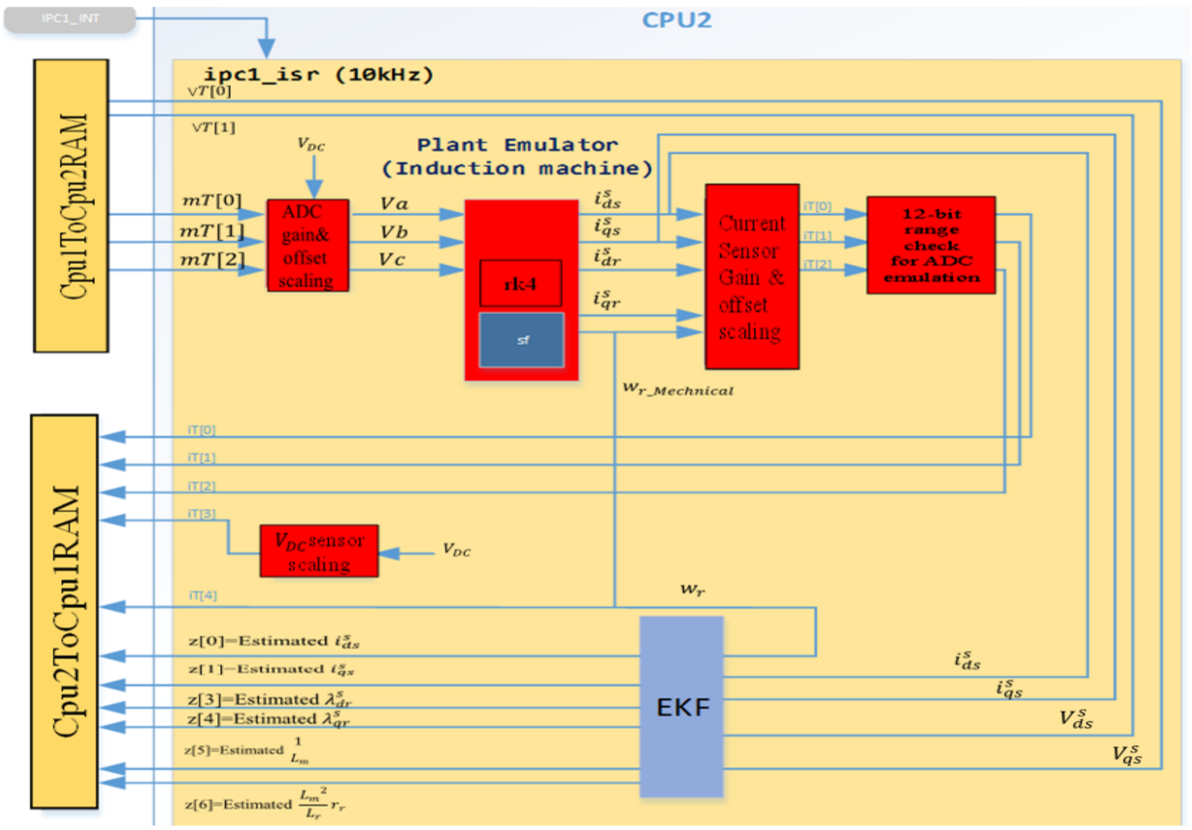


Fig. 7. 7 Implementation of the extended Kalman filter and induction motor emulator in F28377d

$i_{ds}^{e*} = 2.3A$ and $i_{qs}^{e*} = 3.98A$ are applied. The estimated rotor and stator flux are then used by (3.41) and (3.42) based on (7.13) and (7.14) to estimate the rotor resistance and magnetising inductance. As shown in Fig. 7.8d, the augmented states $\frac{1}{L_m}$ and $\frac{{L_m}^2}{L_r} r_r$ have values of 4.65 and 0.52 respectively. Therefore, the estimated $L_m$ and $r_r$ could be calculated as 0.201H and 2.51Ω based on the values of augmented states.

The simulation results for the developed EKF are also demonstrated in Appendix D. As can be deduced from the simulation results captured in the steady-state condition, the estimated magnetising inductance is closer to its measured value. This is a result of a more accurate flux estimation, which is achieved in the simulation where the numerical solver is not restricted to run only one time in a PWM cycle.

As shown in Appendix D, the indexes of the gain matrix for the developed EKF follow a pattern which can be used in a real-time emulator to reduce he expectation time and save memory spaces. This pattern is derived by:

$$\boldsymbol{K}(k) = \begin{bmatrix} k_{11} & k_{12} \\ k_{11} & k_{12} \\ k_{31} & k_{32} \\ -k_{32} & -k_{31} \\ k_{51} & k_{52} \\ k_{52} & -k_{51} \end{bmatrix} \tag{7.29}$$

By having this developed pattern (7.29), six indexes of gain matrix are enough to produce the whole indexes of $K(k)$.

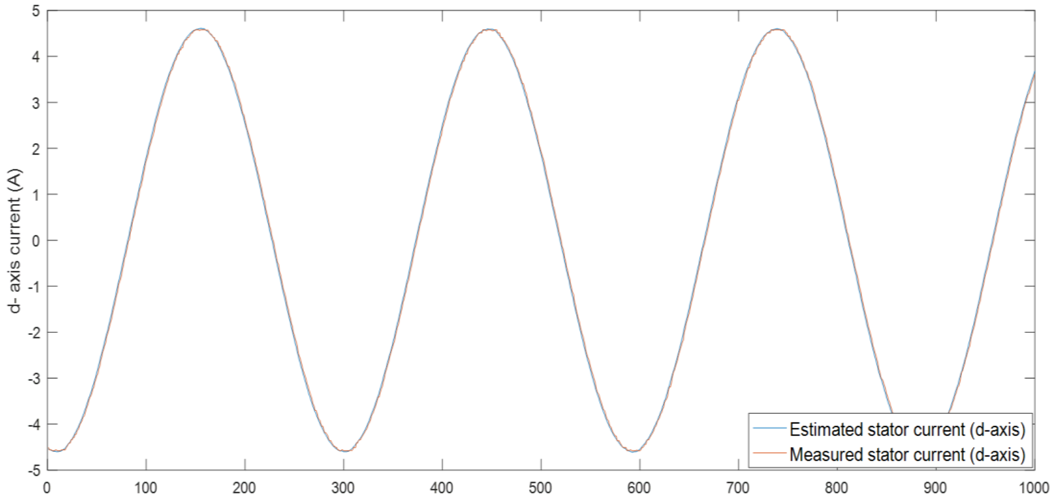


(a)

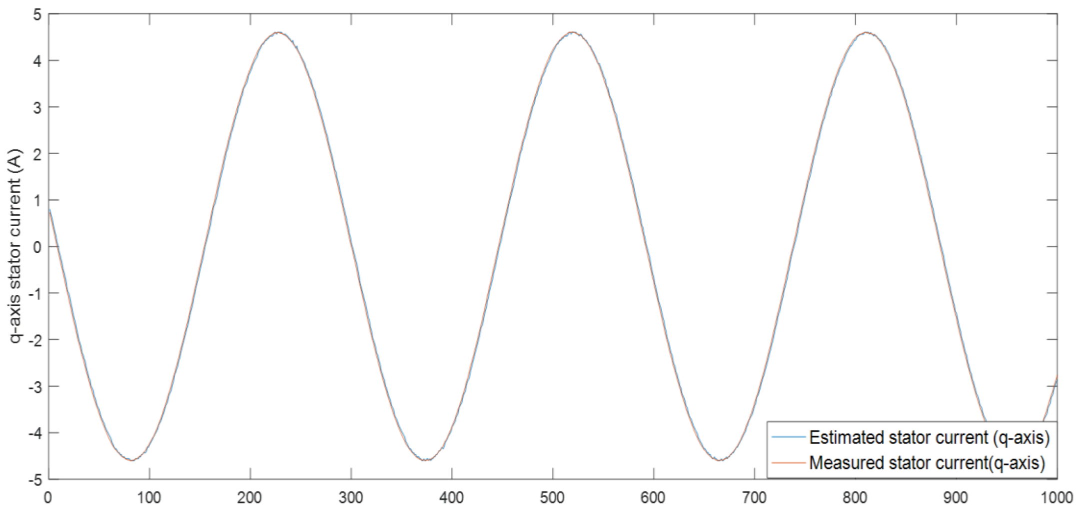


(b)

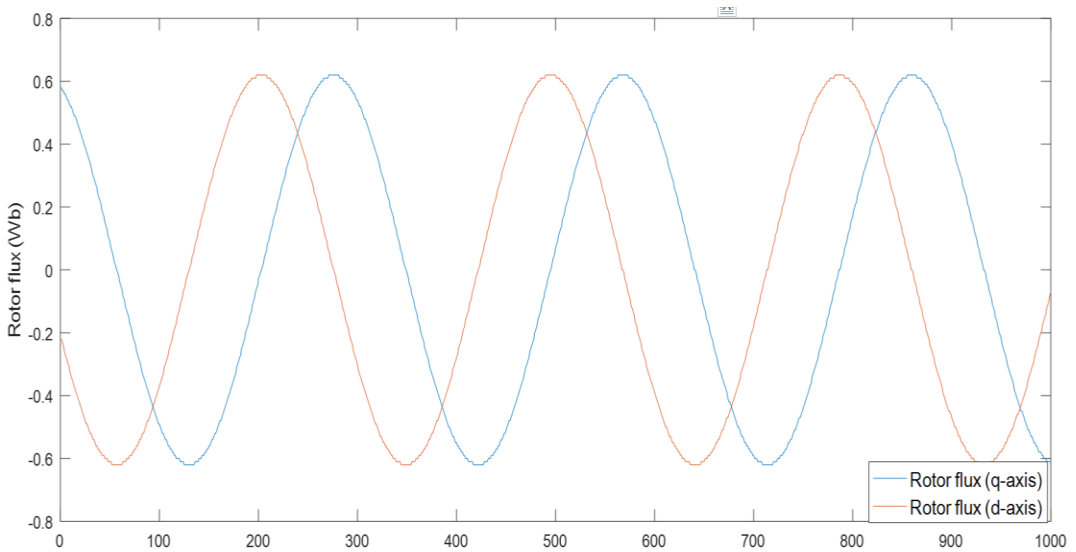


Samples (100ms)

(c)

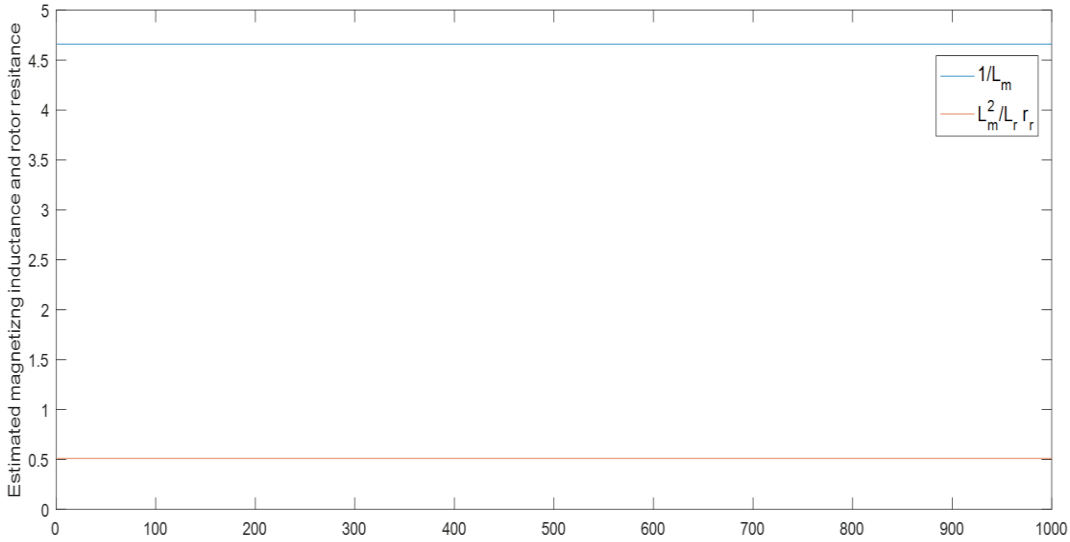


Samples (100ms)

(d)

Fig. 7. 8 Estimation results of EKF in real-time emulator F28377D (a) d-axis stator current (b) q-axis stator current (c) d-q axis rotor flux (d) q-axis (d) ($\frac{1}{L_m}$ and $\frac{{L_m}^2}{L_r}r_r$).

**7.4.2 Real time and simulation results for developed EKF in transient condition**

To analyse the performance of the developed EKF, the magnetizing inductance used in the IM model is changed to half of its initial value for the real time emulator and simulation. Therefore, the performance of EKF is monitored in transient and steady state condition where the estimated states and parameters are settled. As shown in Fig. 7.9a and b, the components of estimated stator current are not changed because the applied reference current has not had any changes. As demonstrated in Fig. 7.9c and d, the components of the rotor flux reach to half of their initial values. These variations of rotor flux are verified by (3.20), which shows the rotor flux changes directly as a function of $L_m$. Figure 7.9 e and f also demonstrate the estimation of augmented states $\frac{1}{L_m}$ and $\frac{{L_m}^2}{L_r}r_r$ in transient and steady state conditions. These results show that the developed EKF technique recognises $L_m$ variation and augmented state $\frac{1}{L_m}$ finally settled on 8.8 which is almost double its estimation in Section 7.5.1. As can be seen from the blue trace in Fig. 7.9f, the other augmented state $\frac{{L_m}^2}{L_r}r_r$ reaches to 0.21, which shows the estimated $r_r$ has a value of 2.046 Ω. Simulink results are provided in Appendix D to verify the captured results from the real time-emulator.

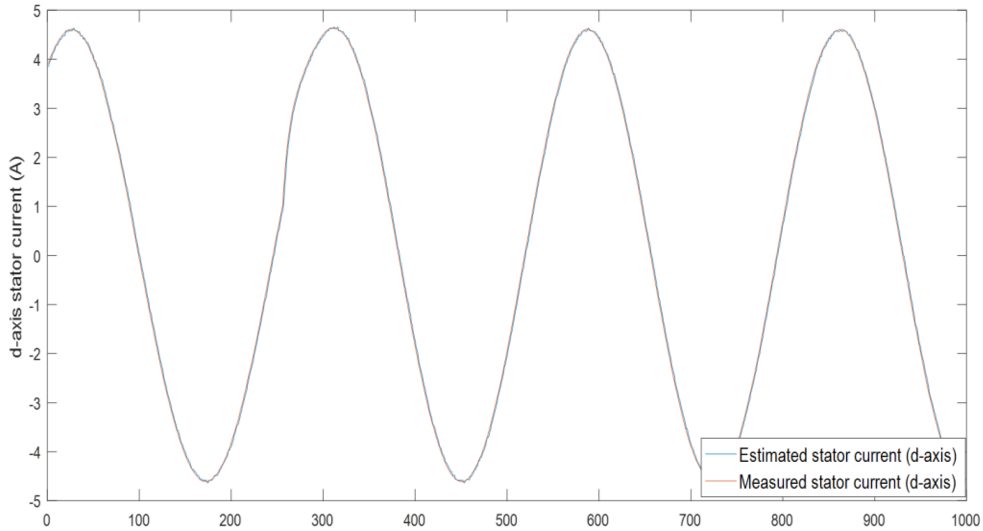
d-axis stator current (A)
Estimated stator current (d-axis)
Measured stator current (d-axis)

(a)

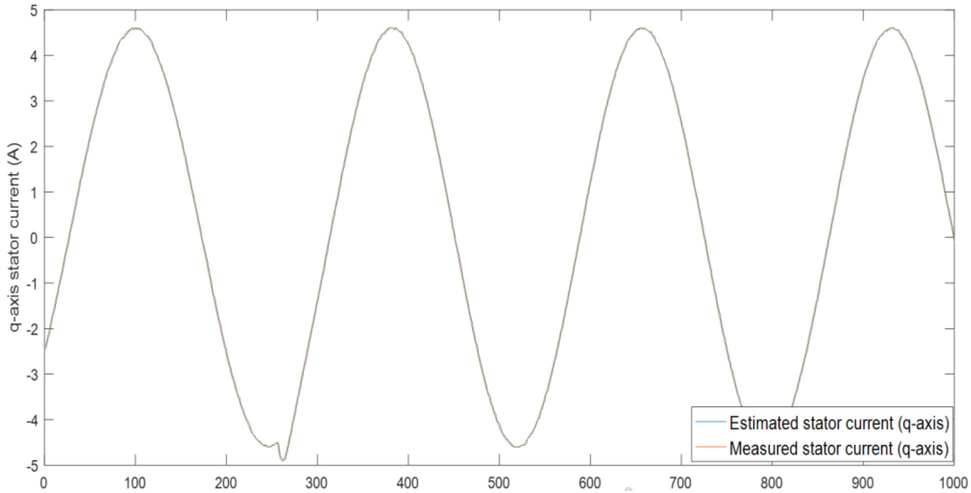
q-axis stator current (A)
Estimated stator current (q-axis)
Measured stator current (q-axis)

(b)

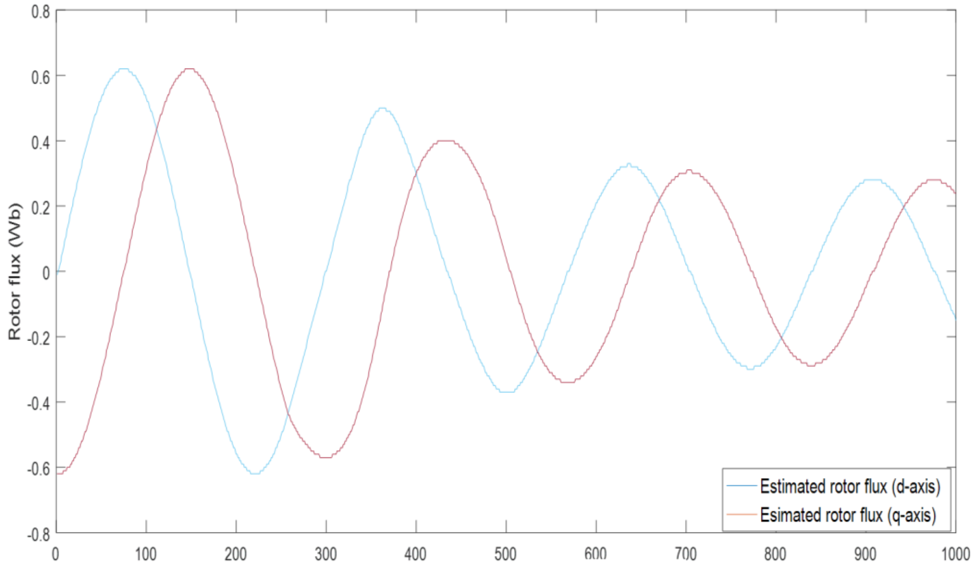
Rotor flux (Wb)
Estimated rotor flux (d-axis)
Esimated rotor flux (q-axis)

(c)

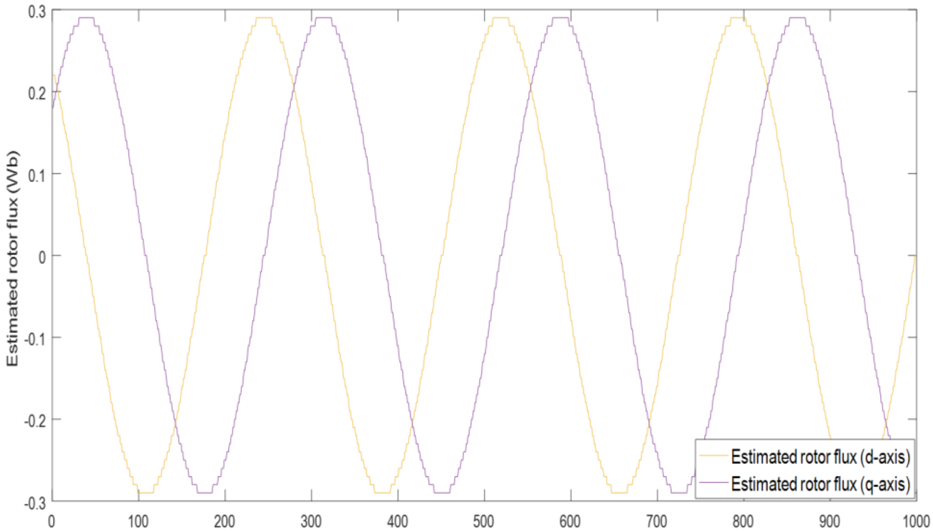


(d)

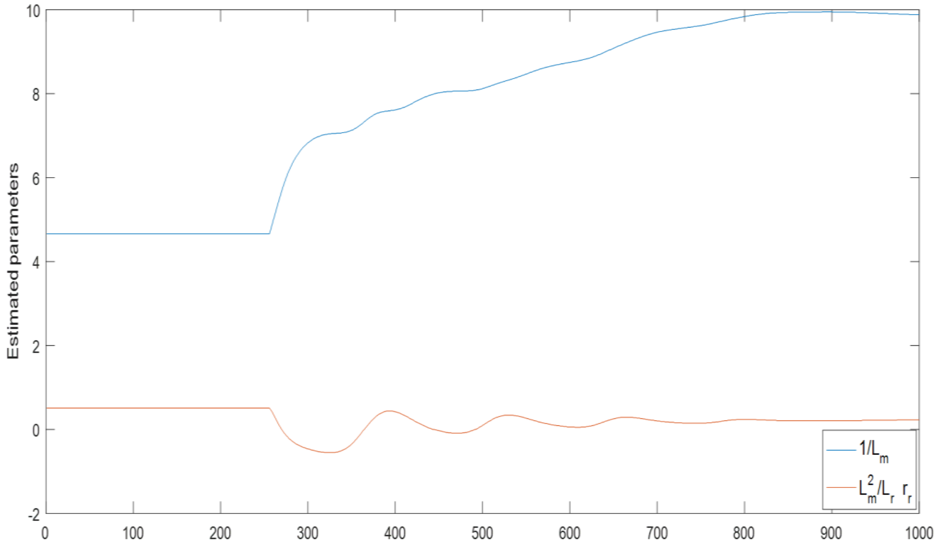


(e)

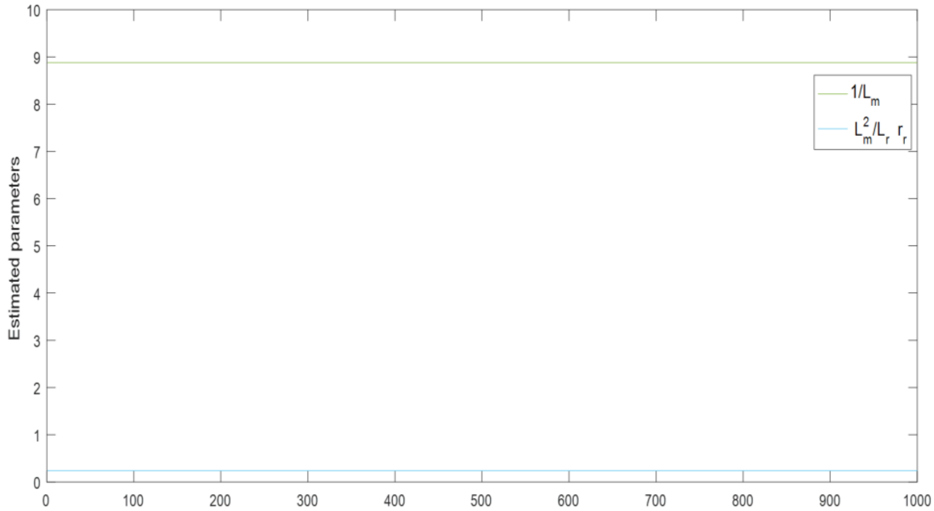


(f)

Fig. 7. 9 Results of estimated states in real-time emulator F28377D (a) d-axis stator current (b) q-axis stator current (c) transient rotor flux in d-q axis (d) steady-state rotor flux in d-q axis (e) estimated $(\frac{1}{L_m}$ and $\frac{{L_m}^2}{L_r}r_r)$ in transient operation (f) estimated $(\frac{1}{L_m}$ and $\frac{{L_m}^2}{L_r}r_r)$ in steady-state operation

### 7.4.3 Simulation results for proposed estimation method

#### 7.4.3.1 Results for steady state condition

The performance of the proposed algorithm explained in Section 7.4 has been tested and verified by MATLAB Simulink. In this simulation, the discrete model is created based on the sampling frequency of 20KHz. As shown in Fig. 7.10a and b, the rotor flux components are estimated precisely based on the proposed method where the estimated rotor flux in KF is added by MRAS-based compensator terms. This means that the correct amplitude for the numerator and denominator of (7.13) and (7.15) are achieved as shown in Fig. 7.10c to f. These amplitudes are used in Maximum-Finder mechanism explained in Section 4.4.2 to calculate $L_m$ and $r_r$. As demonstrated in Fig. 7.10c and d and 7.10e and f, the maximum numerator and denominator signals derived in (7.13) and (7.15) respectively are captured and held in each fundamental frequency. Eventually, these maximum values are divided to estimate $L_m$ and $r_r$ which are shown in Fig. 7.10g and 7.10h. The comparison of estimated values and Table 4.4 confirms the ability of the proposed method to produce the precise parameters estimation. It needs to be clarified that the compensators' terms produced by the MRAS configuration guarantee the accurate estimation of rotor flux components in the KF algorithm.

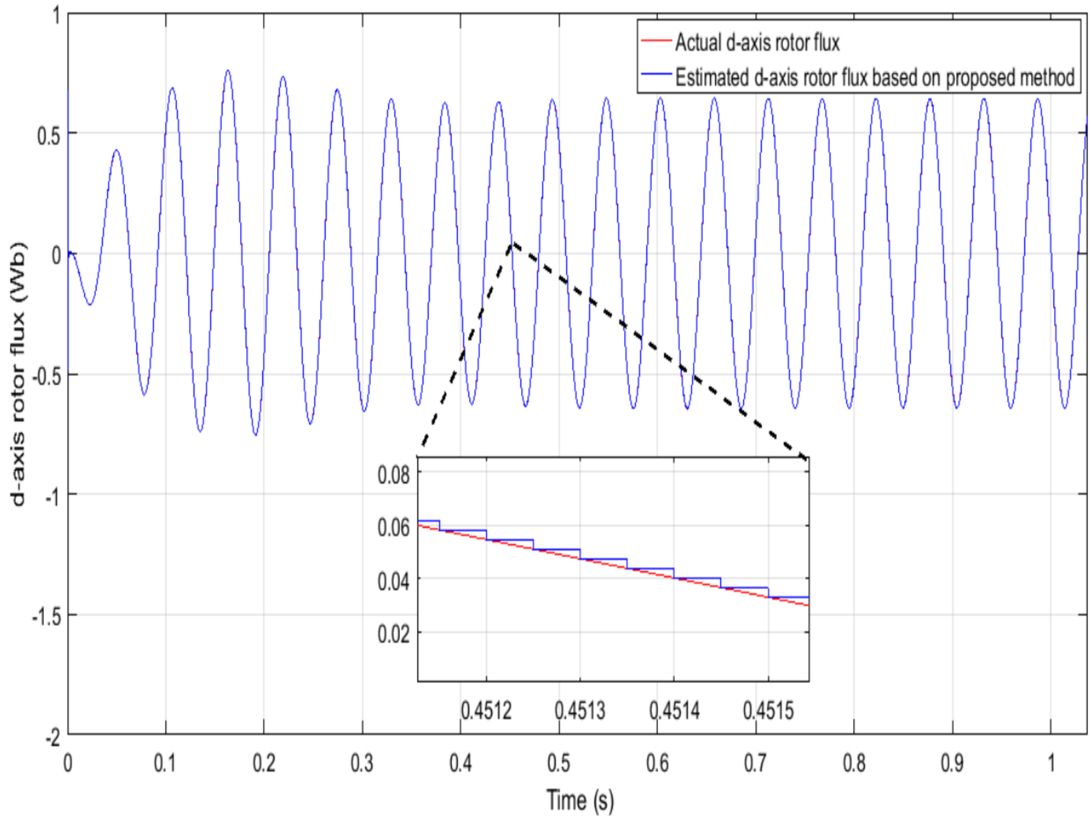
Actual d-axis rotor flux
Estimated d-axis rotor flux based on proposed method
d-axis rotor flux (Wb)
Time (s)
1
0.5
0
-0.5
-1
-1.5
-2
0
0.1
0.2
0.3
0.4
0.5
0.6
0.7
0.8
0.9
1
0.08
0.06
0.04
0.02
0.4512
0.4513
0.4514
0.4515

(a)

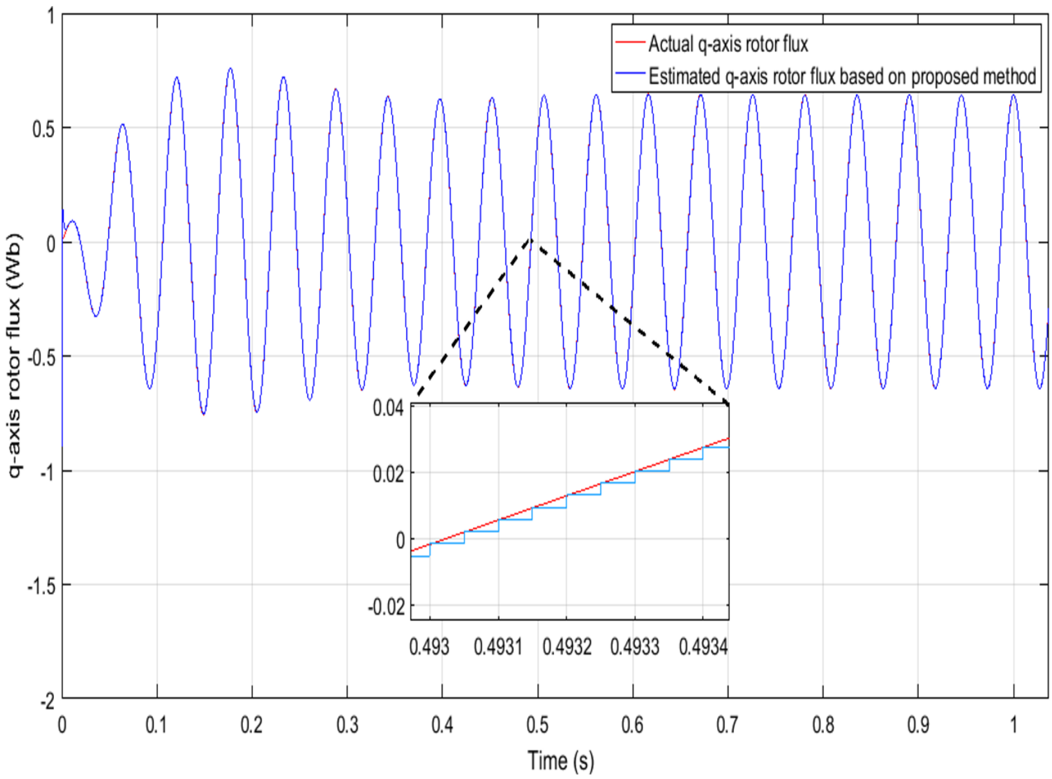
Actual q-axis rotor flux
Estimated q-axis rotor flux based on proposed method
q-axis rotor flux (Wb)
Time (s)
1
0.5
0
-0.5
-1
-1.5
-2
0
0.1
0.2
0.3
0.4
0.5
0.6
0.7
0.8
0.9
1
0.04
0.02
0
-0.02
0.493
0.4931
0.4932
0.4933
0.4934

(b)

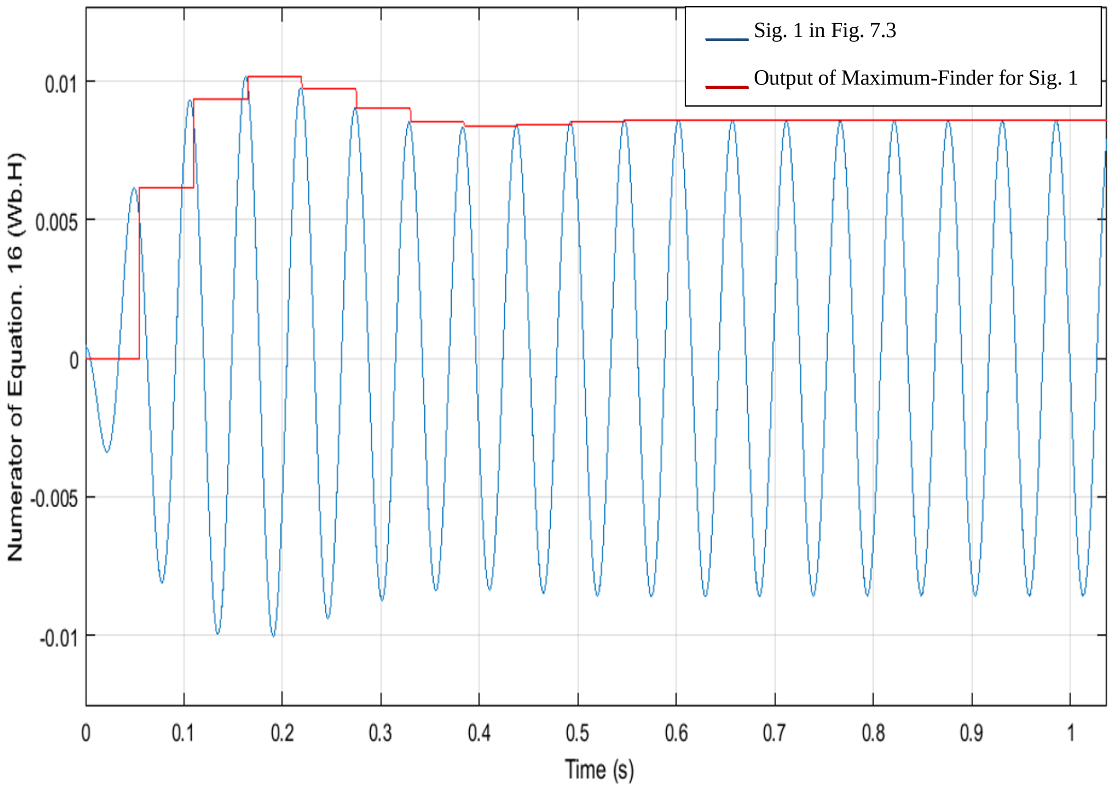
Sig. 1 in Fig. 7.3
Output of Maximum-Finder for Sig. 1
Numerator of Equation. 16 (Wb.H)
0.01
0.005
0
-0.005
-0.01
0
0.1
0.2
0.3
0.4
0.5
0.6
0.7
0.8
0.9
1
Time (s)

(c)

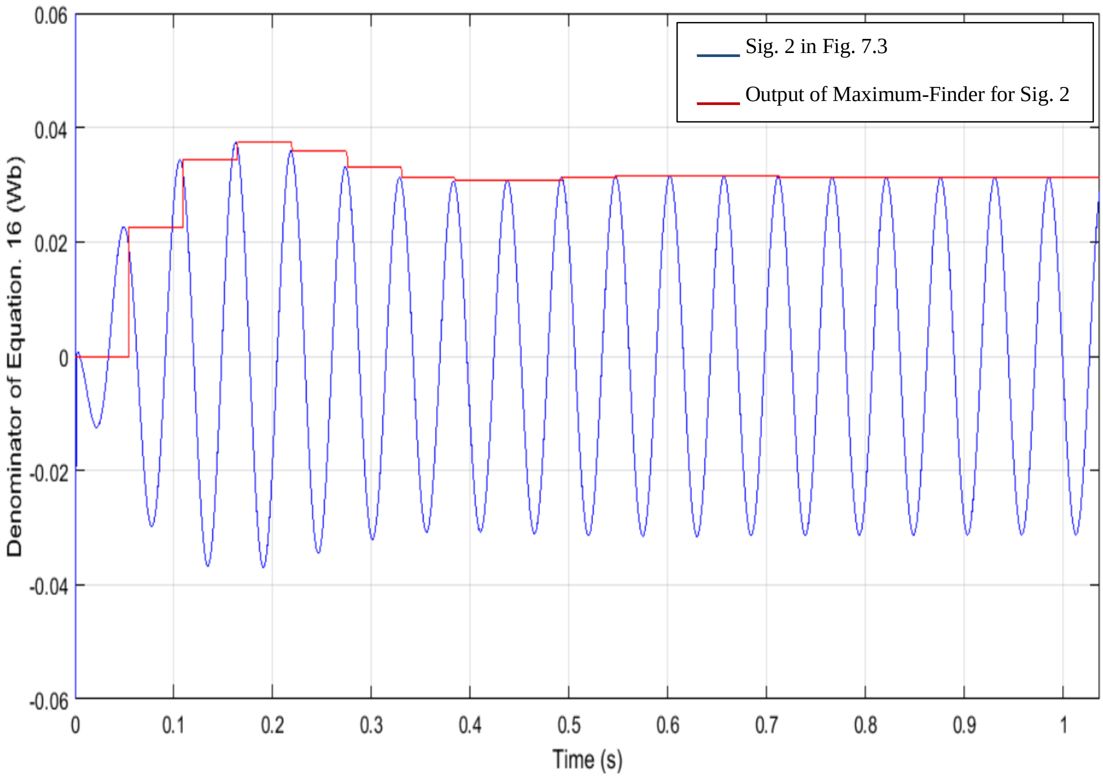
Sig. 2 in Fig. 7.3
Output of Maximum-Finder for Sig. 2
Denominator of Equation. 16 (Wb)
0.06
0.04
0.02
0
-0.02
-0.04
-0.06
0
0.1
0.2
0.3
0.4
0.5
0.6
0.7
0.8
0.9
1
Time (s)

(d)

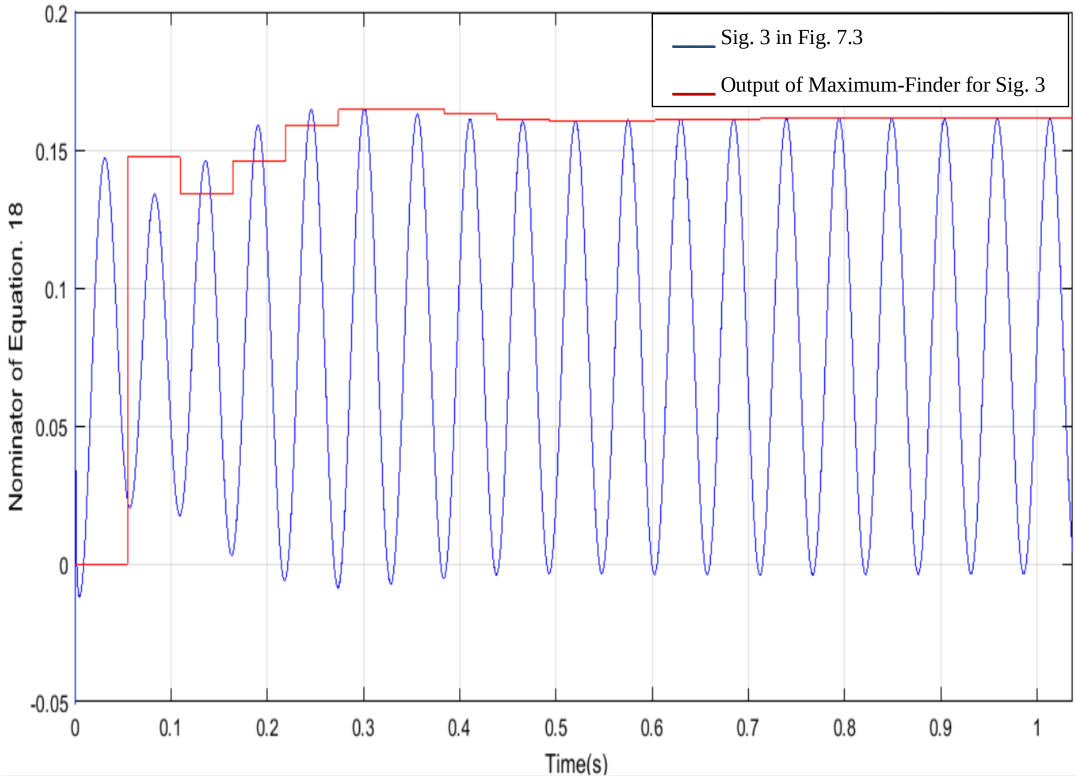
Sig. 3 in Fig. 7.3
Output of Maximum-Finder for Sig. 3
Nominator of Equation. 18
0.2
0.15
0.1
0.05
0
-0.05
0
0.1
0.2
0.3
0.4
0.5
0.6
0.7
0.8
0.9
1
Time(s)

(e)

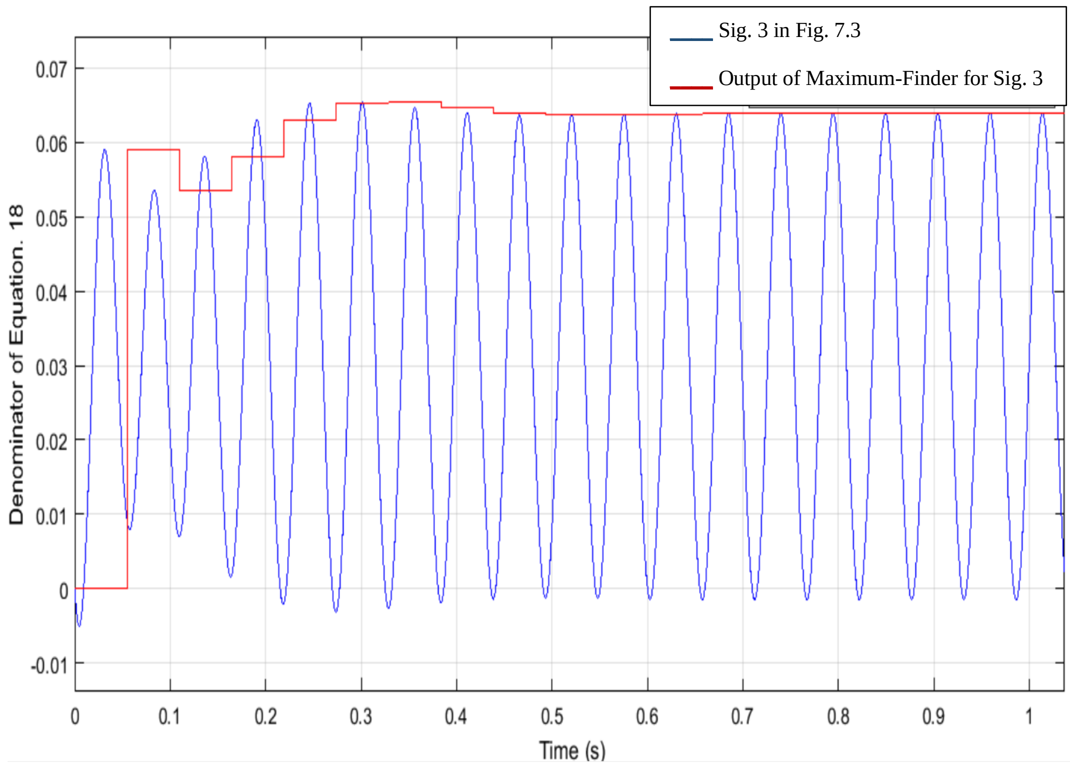
Sig. 3 in Fig. 7.3
Output of Maximum-Finder for Sig. 3
Denominator of Equation. 18
0.07
0.06
0.05
0.04
0.03
0.02
0.01
0
-0.01
0
0.1
0.2
0.3
0.4
0.5
0.6
0.7
0.8
0.9
1
Time (s)

(f)

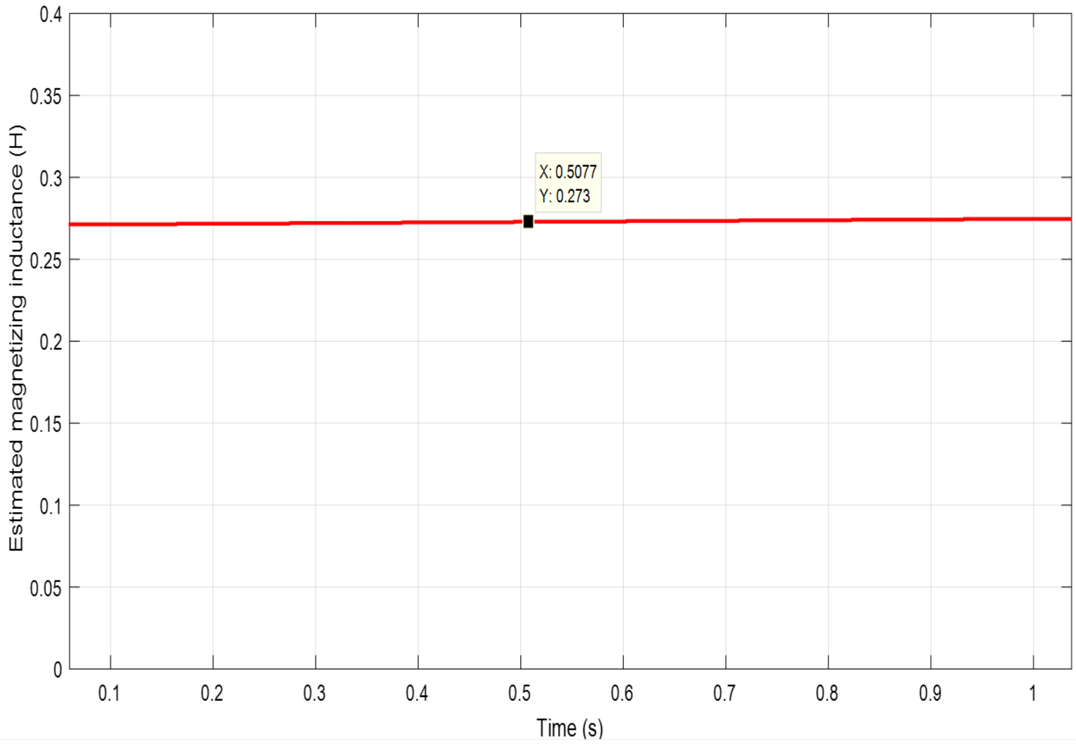


(g)

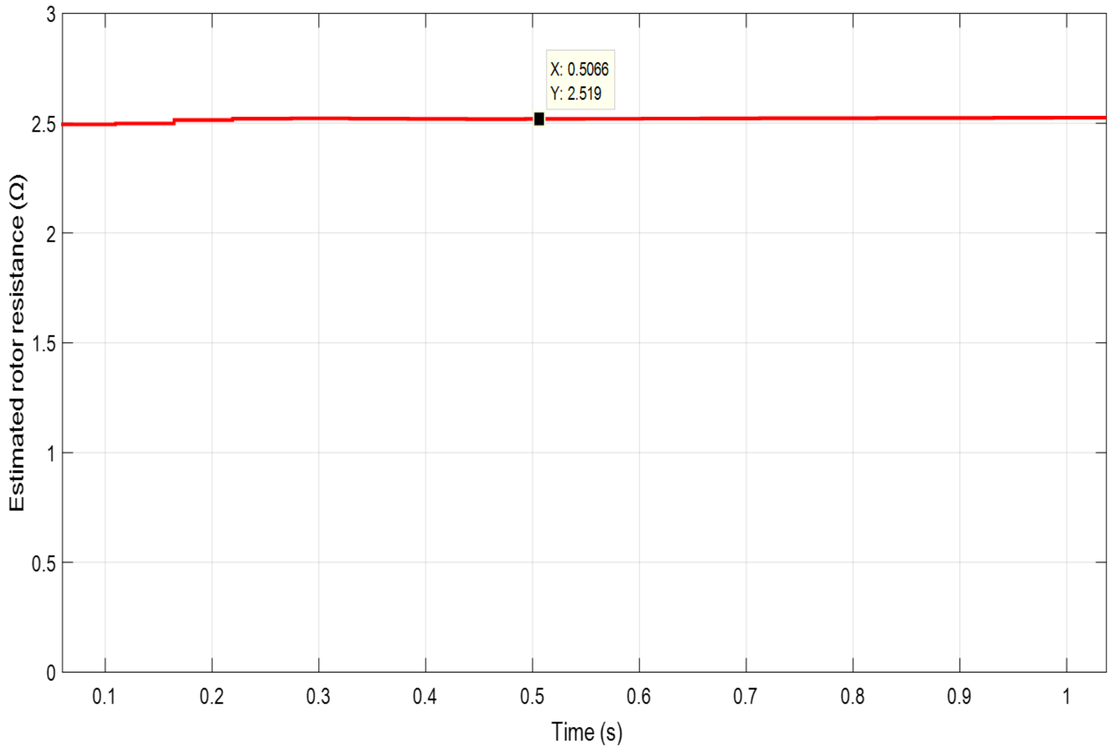


(h)

Fig. 7.10 Results of proposed estimation technique (a) Estimated d-axis rotor flux (b) Estimated q-axis rotor flux (c) Numerator signal of (16) (d) Denominator signal of (16) (e) Numerator signal of (18) (f) Denominator signal of (18) (g) Estimated $L_m$ (h) Estimated $r_r$

#### 7.4.3.2 Results for proposed estimation method in speed variation condition

Figure. 7.11 shows the performance of the proposed method when the speed has several upward and downward step changes. As shown in Fig. 7.11a, the mechanical speed is increased from 50rad/s to 200rad/sec and then reduced to its initial level. The speed modification impacts on the stator flux in the reference model as developed on (7.20). This happens due to the fact that the stator voltage has a proportional ratio with speed. This causes the flux compensator terms (explained in Section 7.4.2) to vary as the function of speed which is demonstrated in Fig. 7.11b. This varies the effects on the numerator and denominator of (7.17) and (7.19) which consequently impact on the estimated $L_m$ and $r_r$. However, the ratio of change for numerator and denominator signals is not significant as the result of using the maximum finder mechanism explained in Fig. 7.4. Consequently, as shown in Fig. 7.11c and d, the estimated $L_m$ and $r_r$ have a variation of less than 8% of the actual value.

As demonstrated in Fig. 5.2 and Fig. 6.2, the proper estimation of the magnetising inductance and rotor resistance are the key for satisfying the FOC in IMs. The correct values of magnetising inductance and rotor resistance are used for slip estimation mechanism which is required by control algorithm to allow the IMs to produce the demanded torque.

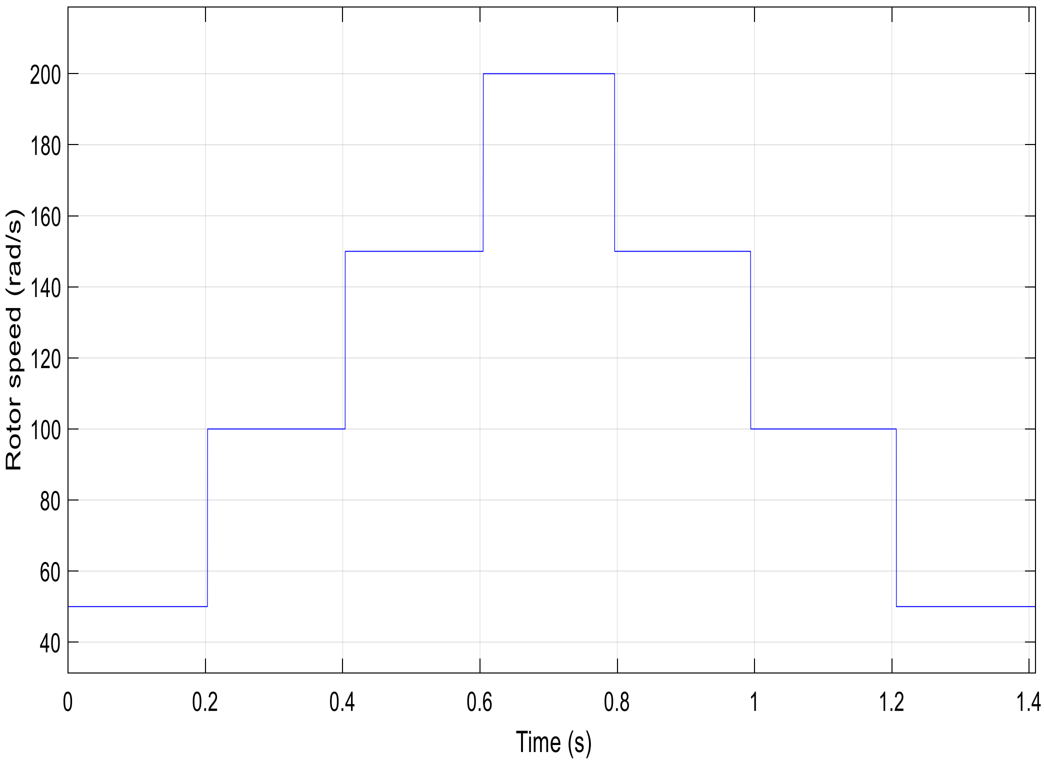

Rotor speed (rad/s)
200
180
160
140
120
100
80
60
40
0
0.2
0.4
0.6
0.8
1
1.2
1.4
Time (s)

(a)

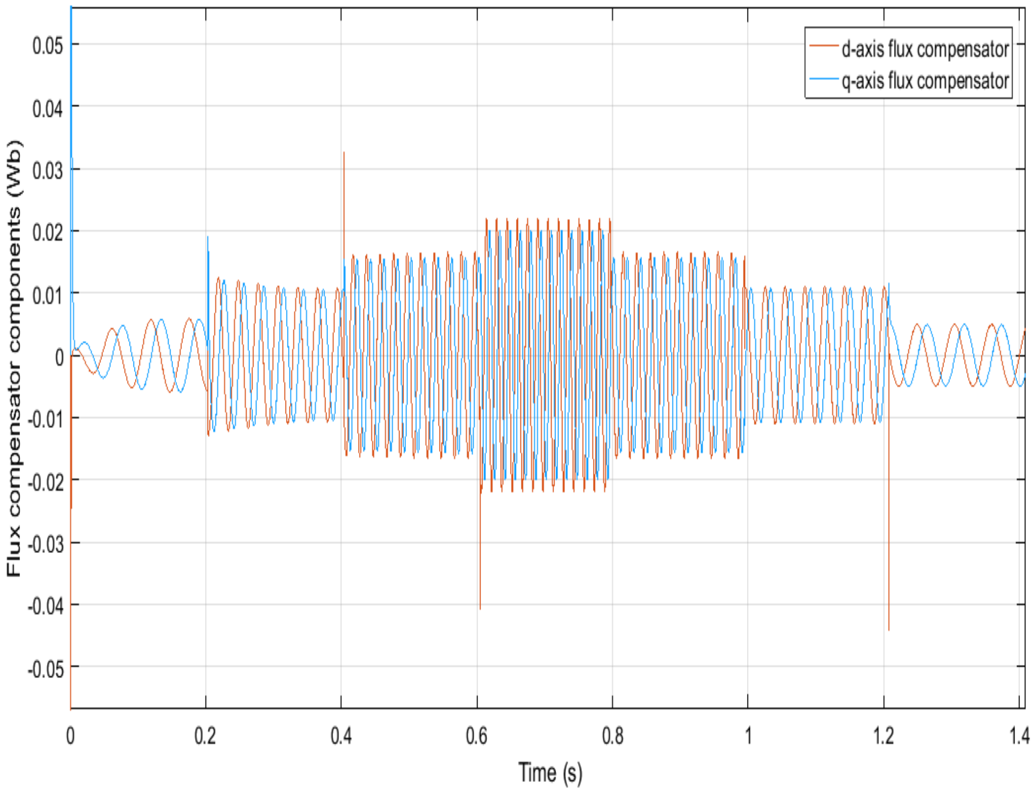

d-axis flux compensator
q-axis flux compensator
Flux compensator components (Wb)
0.05
0.04
0.03
0.02
0.01
0
-0.01
-0.02
-0.03
-0.04
-0.05
0
0.2
0.4
0.6
0.8
1
1.2
1.4
Time (s)

(b)

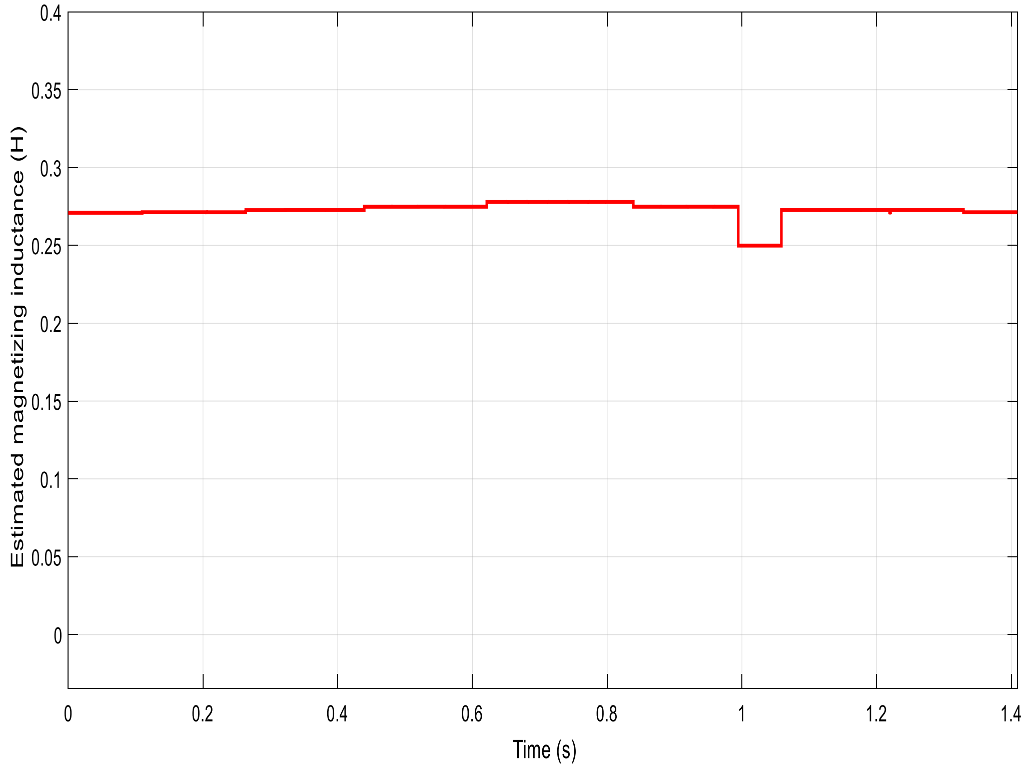


(c)

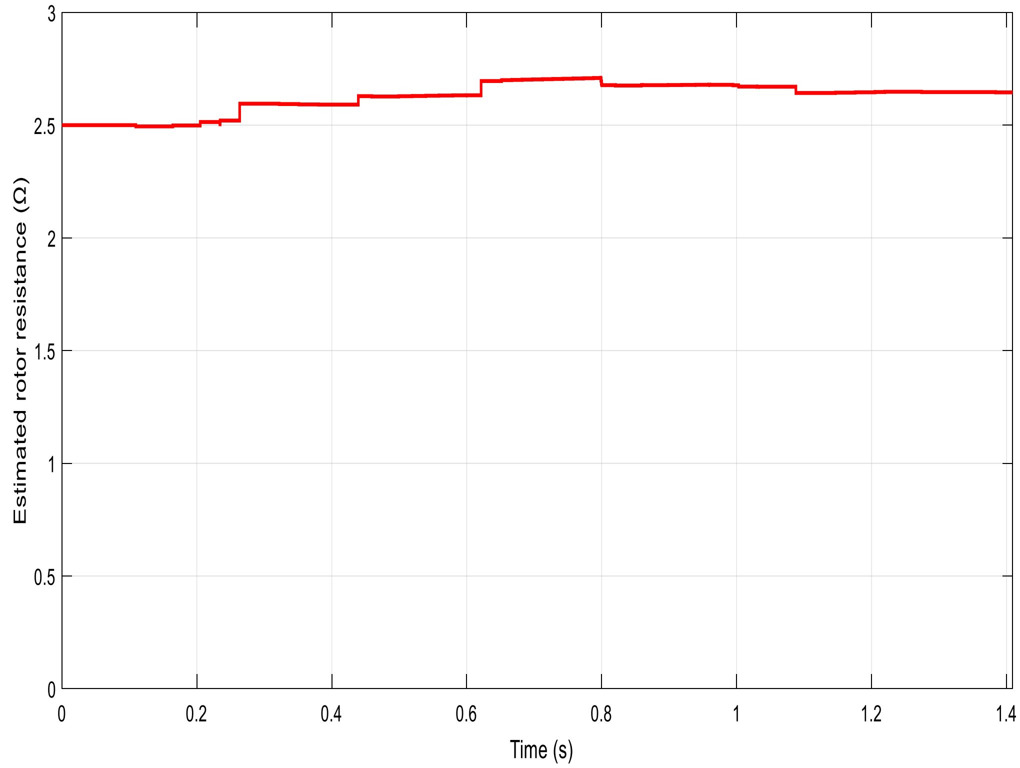


(d)

Fig. 7.11 Results for the proposed method in speed variation condition: (a) Several step changes in mechanical speed (b) Components of flux compensator (c) Estimated $L_m$ (d) Estimated $r_r$

#### 7.4.3.3 Results for the proposed estimation method in step change of $L_m$

The final verification of the proposed parameters estimation technique can be achieved when the magnetising inductance is changed to half of the actual value. In this situation, the numerator and denominator of (7.17) are shown in Fig. 7.12a and b. As shown in (7.13), the numerator becomes less as a result of changing the magnetizing inductance, and the denominator almost behaves the same as before in the steady-state stage. As shown in Fig. 7.12c, the estimated $L_m$ reaches half when the motor magnetising inductance changes to half. It is important to note that the maximum finder in the proposed scheme detects the transient stage where the maximum of the signals becomes unreasonable compare with the previous hold values. In this situation, the estimated $L_m$ has not been updated based on the maximum finder outputs and it hold the last value. This can be demonstrated in the transient stage of Fig. 7.12a and b where the maximum finder determines the maximum value of signals; however, the estimated $L_m$ has not been updated as shown in Fig. 7.12.c. As Fig. 7.12.d highlights, the estimated $r_r$ is still very close to the actual value with less than 4% difference. It needs to be mentioned that in a real test of IM, the variation of $L_m$ depends on the magnetising current which usually changes smoothly as a function of $i_{ds}^e$ and $i_{qs}^e$. Therefore, this simulation test demonstrates the proper performance of the proposed scheme in a worst-case scenario where the magnetising inductance becomes half within one step change.

As described in proposed methods in Chapter 5 and Chapter 6, the correct value of the magnetising inductance is also required in field weakening regions. This helps the IMs to have the smooth transition from CT to FW. This means that the produced torque in FWI region starts from the last point in CT. Furthermore, the maximum power per voltage which already described (5.8),(5.9) and (6.1),(6.2) could be satisfied and the IMs can produce its maximum torque for FW regions.

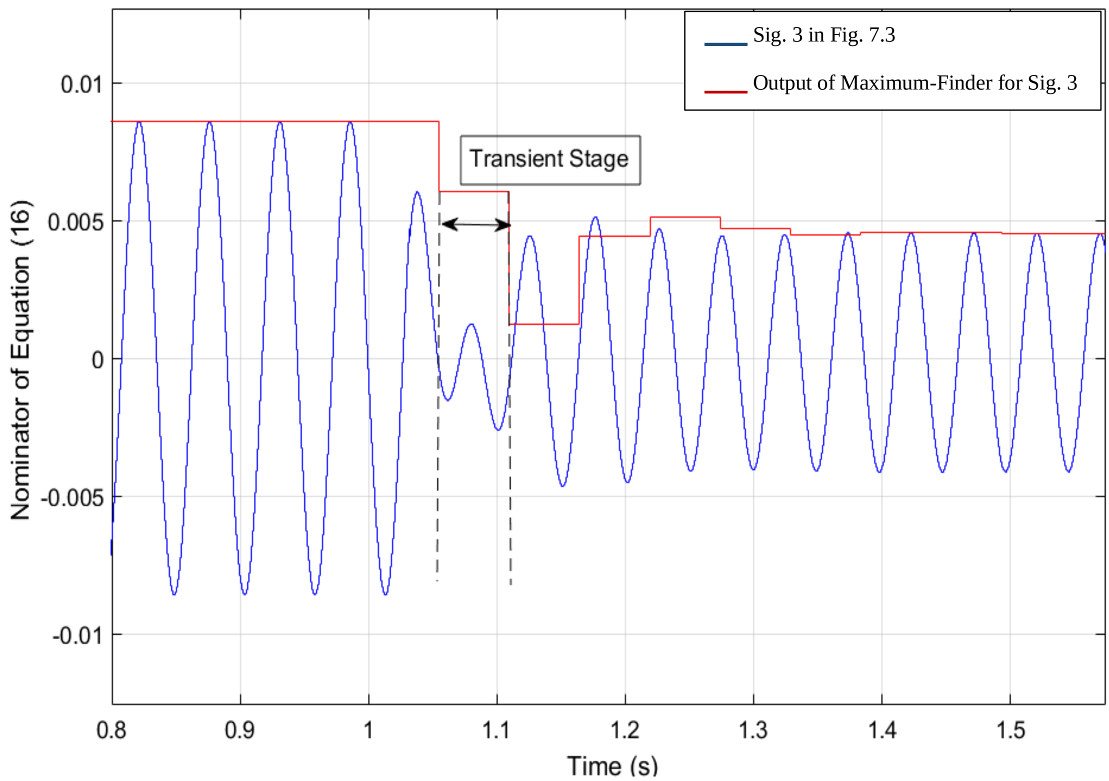
Sig. 3 in Fig. 7.3
Output of Maximum-Finder for Sig. 3
Transient Stage
0.01
0.005
0
-0.005
-0.01
Nominator of Equation (16)
0.8
0.9
1
1.1
1.2
1.3
1.4
1.5
Time (s)
(a)

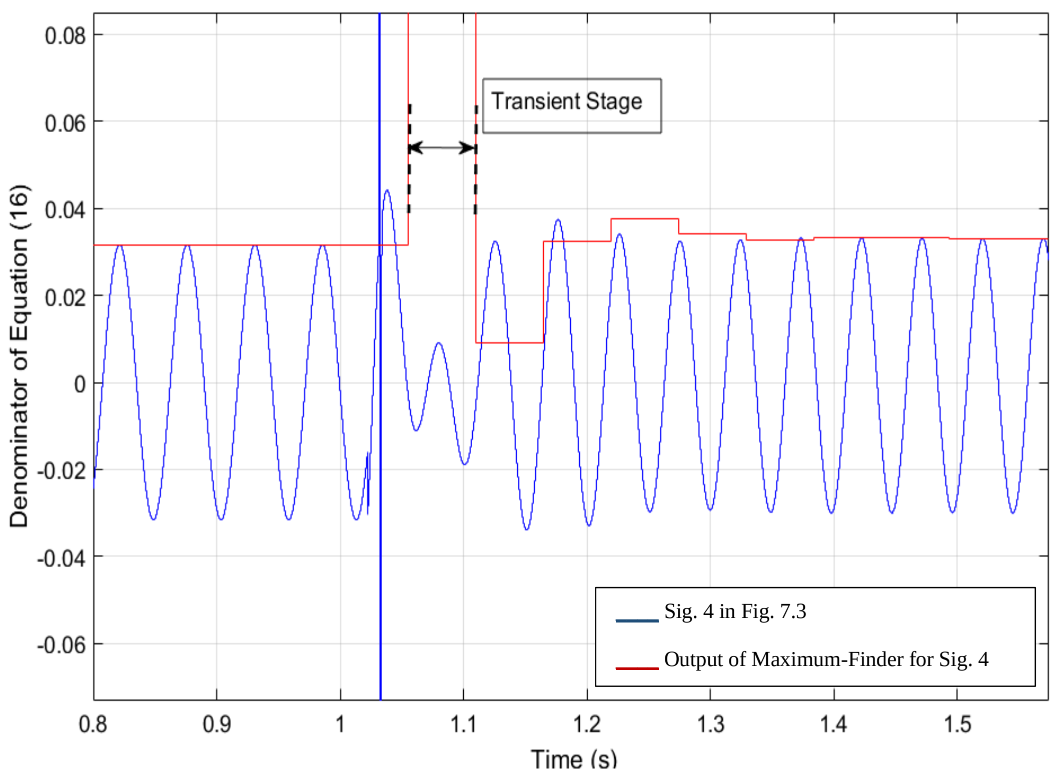
Transient Stage
0.08
0.06
0.04
0.02
0
-0.02
-0.04
-0.06
Denominator of Equation (16)
Sig. 4 in Fig. 7.3
Output of Maximum-Finder for Sig. 4
0.8
0.9
1
1.1
1.2
1.3
1.4
1.5
Time (s)
(b)

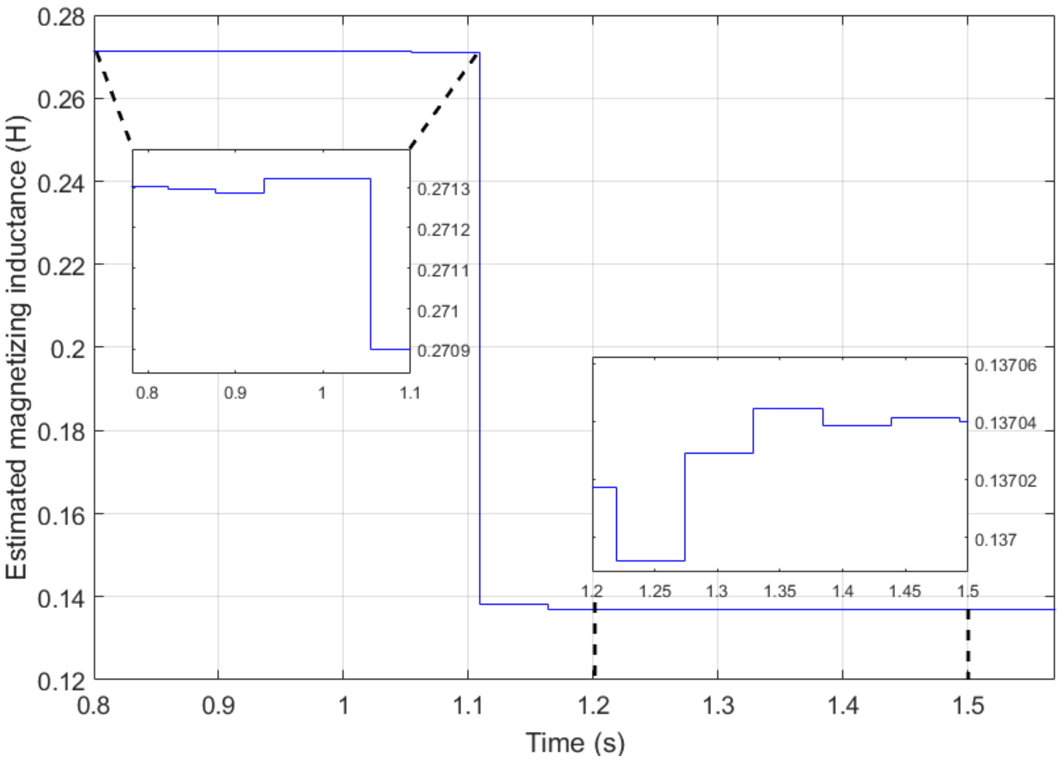


(c)

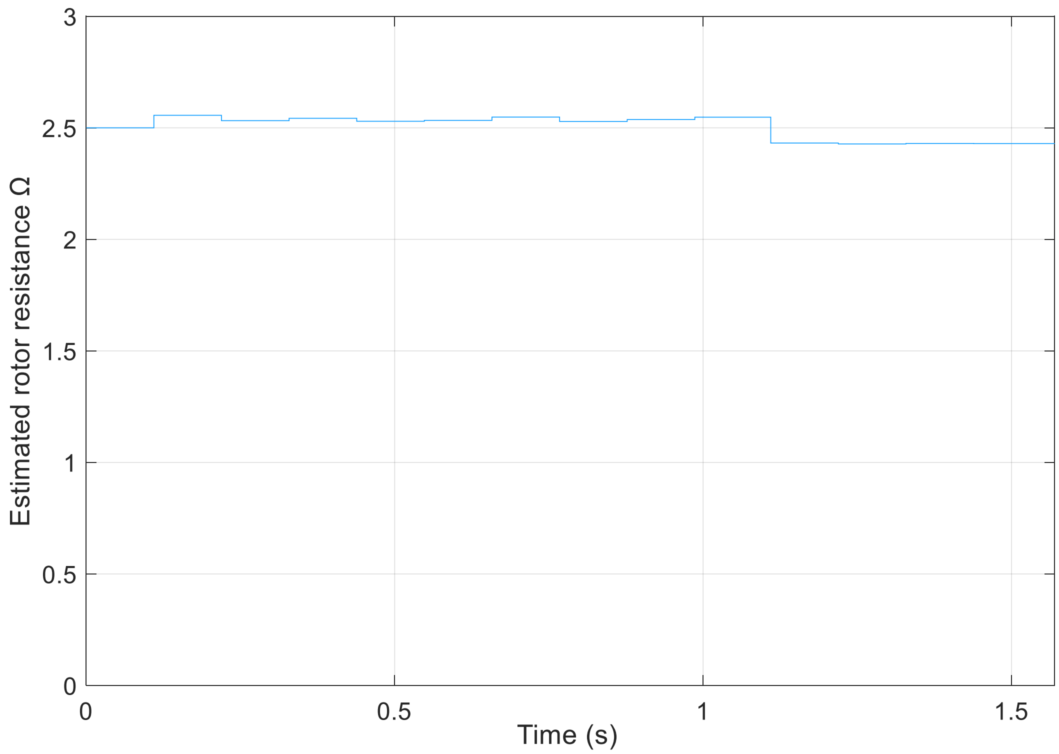


(d)

Fig. 7.12 Results for the proposed method in step change of $L_m$ (a) numerator signal of (7.13) (b) Denominator signal of (7.13) (c) Estimated $L_m$ (d) Estimated $r_r$

**7.5 Summary**

In this chapter, a developed EKF and the proposed estimation method, which is a combination of KF and MRAS, are mathematically derived and successfully implemented to estimate the magnetising inductance and rotor resistance of IM. In the developed EKF, the new augmented states, which creates a precise Jacobean matrix and consequently more accurate estimation results, are used in the state space matrix. The developed EKF is then implemented in the real time controller and its performance has been analysed. The results show that this technique needs the long execution time and huge memory space. Furthermore, the results demonstrates that the developed EKF is able to estimate the motor parameters in different condition; however, the estimated parameters have 15 to 20 % error from actual values. Therefore, the new estimation method which improves the flux estimation of KF by the developed MRAS compensator, is proposed. The accurate calculation of magnetising inductance and rotor resistance is then achieved by having the accurate estimated flux and proposed maximum-finder mechanism. The results verify the feasibility of the proposed control method in different operational conditions and it proves that the estimated parameters have a maximum 8% error from the actual values. In this method, the Jacobian matrix dimension is also reduced a as the result of removing augmented states from the state space model. This obviously reduces the execution time and required memory spaces of the controller.

# CHAPTER 8

# Summary and Future Work

## 8.1 Introduction

During the course of this research, several control schemes based on mathematical modelling and the voltage feedback mechanism were successfully developed to maximise the voltage utilisation of DC-link voltage in the field-weakening region. In these methods, flux-producing current is designed based on the position of the stator voltage vector to push the stator voltage to the hexagonal voltage boundary. This consequently causes a smooth transition from constant torque to field weakening, and it also increases the output torque and power of the electric machine without applying extra regulators or injecting step reduction in the d-axis current. This research also developed and proposed two parameter estimation techniques based on EKF and combined MRAS with KF to improve the accuracy of online estimation techniques. In these methods, the flux estimator mechanism is improved by modifying the Jacobian matrix calculation or flux compensator feedback. The performance of developed control schemes was investigated by using MATLAB Simulink, a plant emulator-based setup and experimental test bench. This chapter provides the overall conclusion of the included chapters along with the contributions and results of this research. Finally, possible future works are suggested to extend the research.

## 8.2 Research summary and conclusions

As discussed before, the electric drives play an important role in controlling the traction applications. In electric drives, the methodology for controlling the inverters is vital as the result of maximising the utilisation of inverter voltage enlarges the torque speed curve of electric machines. This allows motors to accelerate faster without requiring additional changes to the configuration of designed motor. Maximising inverter output voltage is achieved by controlling voltage modulation which determines the level of inverter extracted voltage from the DC-link voltage. Therefore, a control scheme is required to push the voltage modulation to an acceptable higher level and it should be able to deliver smooth torque in transient from different speed regions and also in individual operational speed points.

After a comprehensive review of the different control methods provided in Chapter 2, the model-based algorithm and closed-loop voltage feedback methods were concluded as the most suitable candidates among the current control schemes. However, in these methods, the utilised inverter output voltage is still limited to the inscribed voltage circle inside the hexagonal voltage boundary. Furthermore, fake voltage extensions, which consequently create more currents and torque ripples, were produced on the developed control methods. Therefore, it was found to radically modify both versions of these control algorithms in order to maximise the voltage utilisation without applying fake voltage extension or step reduction on currents. Therefore, a new control scheme was proposed in Chapter 5 to maximise the voltage extraction from DC-link voltage in model-based control techniques. This was achieved by calculating reference d-q axis currents based on maximum achievable voltage in SVM. In this method, the reference stator voltage, which was defined by the stator voltage angle and hexagonal voltage boundary, compensated the difference voltage between linear and nonlinear areas for the field-weakening region. This proposed scheme developed the new voltage trajectory, which allows the electric motor to have higher flux-producing current and more back-EMF. This consequently caused the electric motor to produce higher torque and power in the field-weakening region. The proposed scheme also provided a smooth transition from the constant torque region to the field-weakening region without applying extra regulators or calculating the base speed. This was achieved by matching the values of the flux and torque-producing currents in the transient point between different operational regions. The proposed scheme was successfully implemented and tested in Simulink and the test bench setup for the constant torque and field-weakening regions. Chapter 5 also explained that the proposed model-based scheme requires the motor parameters in calculating the desired currents. Therefore, a closed-loop voltage control scheme, which is less dependent on motor parameters, was developed and tested in Chapter 6.

In Chapter 6, the novel closed-loop voltage-based algorithm is used to maximise the voltage utilisation of the inverter in the field-weakening region. In this method, the reference flux-producing current is developed in the voltage control loop where the comparison of the stator voltage vector with a hexagonal voltage limitation was addressed. This allows the electric motor to have maximum available d-axis current and produce higher electromagnetic torque and output power. This is achieved without applying a fake voltage extension and consequently torque ripples which is the case with conventional voltage-based control methods. Furthermore, the proposed method does not apply the step reduction of current, which happens in active timing voltage control methods, during the transient region from the constant torque region to the field-weakening region. A comprehensive analysis of the proposed stator voltage vector, which was tried to be pushed around hexagonal voltage limitation, is also described in detail in this chapter. The proposed scheme was then successfully validated and tested in Simulink and in the lab environment at different operational speeds. The proposed methods in Chapter 5 and Chapter 6 can also be applied for the permanent magnet motors. This needs to have the corresponding mathematical modelling of voltage and current constraints for permanent magnet motors. Therefore, Appendix A presented mathematical models of interior and surface mounted permanent magnet machines in stationary and rotary frames. It should be noted that there is not any rotor current in permanent magnet motor where the designed permanent magnets in rotor produce the rotor flux. Therefore in permanent magnet motors, there is not a lag for the rotor flux such as IMs. This causes that the proposed d-axis reference current in Chapter 5 and Chapter 6 can be better tracked by the motor currents.

As also explained in Chapter 6, the motor parameters were not used in closed-loop voltage control; however, the slip speed was still estimated based on motor parameters. The variation of motor parameters can be neglected in low-power-rate AC motors where the stator current components do not have significant changes. However, to apply this scheme for a higher power rate of AC motors, it is essential to estimate the magnetising inductance and rotor resistance. The variation of these motor parameters could be significant in high-power-rate AC motors, which have huge stator current changes in different operational regions. Therefore, the accurate estimation of these motor parameters is required in order to have precise FOC. Therefore, Chapter 2 and Chapter 7 provided a literature review for motor parameters estimation methods and also provided the full mathematical description of the Kalman-filter and MRAS algorithms as two main states and parameters estimation methods. Online estimation techniques are seen to be the most reliable scheme where the estimated parameters can be used to run the system. However, providing the accurate estimation of magnetising inductance and rotor resistance at the same time based on the developed estimation method still requires more improvement. It was found that a more accurate flux estimation mechanism can help the developed module to provide better estimation results. Therefore, Chapter 7 proposed a parameter estimation technique based on the Kalman filter and model reference adaptive system. In this chapter, the extended Kalman filter, which was developed based on the new Jacobian matrix, was proposed to provide an accurate estimation of magnetising inductance and rotor resistance. The performance of the developed extended Kalman filter was then validated and tested in Simulink and experimenter kit where an IM was emulated in the CPU2 of the controller. To improve the accuracy of parameter estimation and reduce the computation time, the new combined model of the Kalman filter and MRAS was proposed. In this method, the compensated flux terms in MRAS were added to estimate the flux vector in the Kalman-filter algorithm. These terms were then used in the proposed maximum finder mechanism to calculate the magnetising inductance and rotor resistance. The results proved that more accurate estimation of motor parameters can be achieved with the proposed estimation technique. Furthermore, the dimension of the Jacobian matrix was reduced by removing segmented states from the state space model, which reduces the required memory space and computational time. It needs to be mentioned that accurate estimation of the flux vector presented in Chapter 7 based on combined Kalman filter and MRAS can also be used for sensor less control method. This can help the sensor-less control mechanism for low speed region where the accuracy of the estimated flux is very important.

### 8.3 Future works

- Further research is required to investigate the performance of the proposed model-based control scheme in very high-speed operation, where the fundamental frequency is approximately 10 times that of the sampling frequency. The suggested idea is to use three main points of designed parabolic reference voltage in each sector to calculate d-axis reference current as the stator voltage vector is rotating.

- This research has investigated how maximising the voltage utilisation from the DC-link voltage affects the output torque and power of the electrical machine. However, further research is also required to analyse the power electronic losses and current harmonics components in case of maximising voltage extraction.
- Additional work is required to combine the model-based algorithm with the proposed estimation techniques for a high-current-rate induction machine where variation of the magnetising inductance is significant.
- Further research is required to analyse the performance of the closed-loop voltage mechanism in transition from the constant torque region to field weakening region for high-power rate induction motor, which could have step changes in the slip speed.
- Further research is also required to analyse the performance of the proposed flux vector estimation, which is combined model of Kalman filter and MRAS, for sensor-less control methods

# Appendix A

# Dynamic Model and Control of Interior Permanent Magnet Machine

---

## A.1 Introduction of Permanent Magnet Machines

Due to the roro structure of the Permanent Magnet machines, this type of machines are used in many kind of applications such as electric vehicles which require the wide operation area of constant power. The reason of having the wide range of power speed range is that the reluctance torque incorporate in field weakening region. Using permanent magnet instead of winding in rotor structure causes the reduction in losses which means the efficiency improvement. The other reason, which helps the PM machines to have the higher rate of efficiency, is that these machines can operate in unity power factor because of synchronous performance.

The PM machines can be classified in sinusoidal excited PM motors (or Permanent Magnet Synchronous Motor) and trapezoidal excited PM motors (or Brushless DC Motors) [94]. The surface permanent magnet and interior permanent magnet machines are two main type of PMSMs. Table A.1

Table A. 1 Comparison of SPM and IPM motors

| | **SPMSM** | **IPMSM** |
|---|---|---|
| **Permanent Magnet Usage** | large | small |
| **Location of Permanent Magnet** | surface | cavities |
| **Saliency Ration ($\frac{L_q}{L_d}$)** | 1 | >1 |
| **Reluctance Torque usage** | no | yes |
| **Speed range** | small | large |

Appendix A

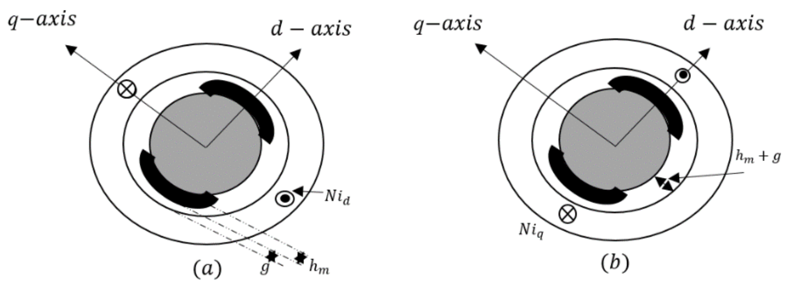


Fig. A. 1 Flux path for SPMSM

demonstrates the comparison between surface permanent magnet synchronous machine (SPMSM) and interior Permanent magnet synchronous machine (IPMSM).

### A.2 Inductance calculation in SPMSM and IPMSM

The value of the stator inductances play a vital role in determining the value of the reluctance torque. So, calculation of these stator reluctance should be completely understood before analysing the torque equation for PM machines.

By considering the flux path of SPMSM in d and q axis, the inductances can be calculated as follow [95]:

$$\frac{B}{\mu_{pm}}2h_m + \frac{B}{\mu_0}2g + \frac{B}{\mu_{Fe}}l_{core} = Ni_d \quad \text{A.1}$$

Because the permeability of the iron is much higher than air gap, so the last term of equation can be neglected (A.2).

$$\frac{B}{\mu_{pm}}2h_m + \frac{B}{\mu_0}2g = Ni_d \quad if\ \mu_0 = \mu_{pm}\ \ then\ B = \frac{\mu_0 N}{2(g+h_m)}i_d \quad \text{A.2}$$

Then, the magnetic flux ($\phi$) can be defined in terms of calculated magnetic field (A.3).

$$N\phi = NB * A = L_d i_d \rightarrow L_d = \frac{\mu_0 N^2 A}{2(g+h_m)} \quad \text{A.3}$$

By writing the magnetic flux equation in q axis, the same inductance value will be defined.

$$L_q = \frac{\mu_0 N^2 A}{2(g+h_m)} \quad \text{A.4}$$

So, the SPMSM cannot have the reluctance torque because the d and q axis of stator inductance are

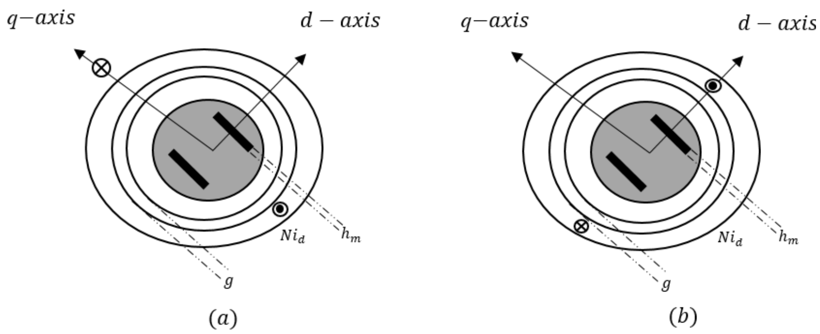


Fig. A. 2 Flux path for IPM

equal. This problem is solved in permanent magnet machine by placing the magnet in cavities instead of surface. The flux path in IPMSM has been shown in Fig. A.2. By calculating the inductance from flux equations, it can be clearly demonstrated that the $L_q > L_d$ (A.5).

$$L_d = \frac{\mu_0 N^2 A}{2(g+h_m)}, L_q = \frac{\mu_0 N^2 A}{2(g)} \qquad \text{A.5}$$

**A.3 IPMSM Dynamics in synchronous reference frame**

The stator voltage equation for IPMSM in synchronous reference frame can be obtained from the stator voltage equation in stationary frame:

$$V_{dq}^s = r_s i_{dq}^s + \frac{d(\lambda_{dq}^s)}{dt} \rightarrow V_{dq}^s = r_s i_{dq}^s + \frac{d(L_s i_{dq}^s - \frac{3}{2} L_\delta e^{2\theta_e} i_{dq}^{s*} + \psi_m e^{j\theta_e})}{dt} \qquad \text{A.6}$$

This stationary model is used for sensor less control of IPM machine in signal injection techniques. But for developing the IPM model in Matlab simulation, the synchronous model is used since it does not have any none-linear component such as triangular functions.

As it can be seen in above equation, the stator flux leakage formatting from stator current and rotor flux. The aforementioned stator voltage can be transferred into the synchronous frame by multiplication both side in $e^{-\theta_e}$.

$$V_d^e = r_s i_d^e + (L_s - \frac{3}{2} L_\delta) \frac{d(i_d^e)}{dt} - w_e (L_s + \frac{3}{2} L_\delta) i_q^e \rightarrow r_s i_d^e + (L_d) \frac{d(i_d^e)}{dt} - w_e (L_q) i_q^e \qquad \text{A.7}$$

$$V_q^e = r_s i_q^e + \left(L_s + \frac{3}{2} L_\delta\right) \frac{d(i_q^e)}{dt} + w_e \left(L_s - \frac{3}{2} L_\delta\right) i_q^e + w_e \varphi_m \rightarrow r_s i_q^e + \left(L_q\right) \frac{d(i_q^e)}{dt} + w_e (L_d) i_d^e + w_e \varphi_m$$

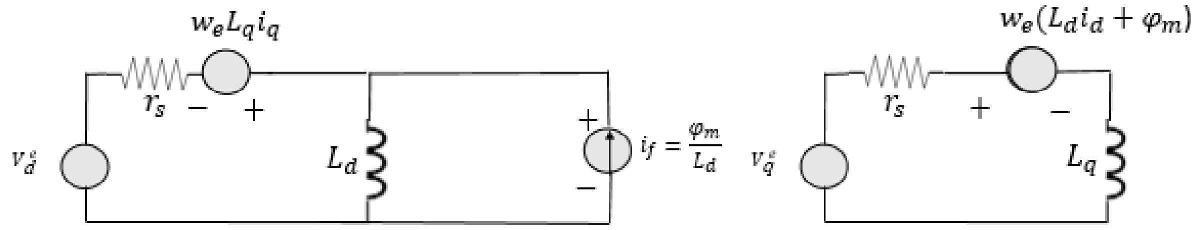


Fig. A. 3 Equivalent circuit for IPM

According to stator voltage equation in synchronous frame, the equivalent circuit of IPM machine is shown in Fig. A.3. The virtual current source $(i_f)$ is the result of rotor flux. The dynamic equation of IPM machine can be defined by using the aforementioned voltage equation.

$$\frac{d}{dt}\begin{bmatrix} i_d^e \\ i_q^e \end{bmatrix} = \begin{bmatrix} \frac{-r_s}{L_d} & w_e \frac{L_q}{L_d} \\ -w_e \frac{L_d}{L_q} & \frac{-r_s}{L_q} \end{bmatrix} \begin{bmatrix} i_d^e \\ i_q^e \end{bmatrix} - \frac{w_e \varphi_m}{L_q} \begin{bmatrix} 0 \\ 1 \end{bmatrix} + \begin{bmatrix} \frac{V_d^e}{L_d} \\ \frac{V_q^e}{L_q} \end{bmatrix} \quad \text{A.8}$$

### A.4 Torque and power equation in IPM

Torque equation is derived by using the stator flux linkage and stator current in synchronous frame.

$$T_e = \frac{3P}{4}\left(\lambda_{dq}^e \times i_{dq}^e\right) = \frac{3P}{4}\begin{vmatrix} \vec{i} & \vec{j} & \vec{k} \\ \lambda_{ds}^e & \lambda_{qs}^e & 0 \\ i_d^e & i_q^e & 0 \end{vmatrix} = \frac{3P}{4}\left(\lambda_{ds}^e i_q^e - \lambda_{qs}^e i_d^e\right) = \frac{3P}{4}\left[\varphi_m i_q^e + \left(L_d - L_q\right) i_d^e i_q^e\right] \quad \text{A.9}$$

The torque equation consisted of electro-magnetic torque based on the rotor flux and reluctance torque based on the inductance asymmetry. The power equation of Interior permanent magnet machine can be obtained by using the simplified voltage equation which are not consisted of the losses and derivation components (Equation 10).

$$V_d^e = r_s i_d^e + \left(L_s - \frac{3}{2}L_\delta\right)\frac{d(i_d^e)}{dt} - w_e\left(L_s + \frac{3}{2}L_\delta\right) i_q^e \rightarrow V_d^e = -w_e(L_q) i_q^e \quad \text{A.10}$$

$$V_q^e = r_s i_q^e + \left(L_s + \frac{3}{2}L_\delta\right)\frac{d(i_q^e)}{dt} + w_e\left(L_s - \frac{3}{2}L_\delta\right) i_q^e + w_e\varphi_m \rightarrow V_q^e = +w_e(L_d) i_d^e + w_e\varphi_m$$

Then, the power equation in d-q axis can be defined by:

$$P = \frac{3}{2}\left(V_d^e i_d^e + V_q^e i_q^e\right) = \frac{3}{2} w_e\left(\varphi_m i_q^e + \left(L_d - L_q\right) i_d^e i_q^e\right) \quad \text{A.11}$$

Appendix A

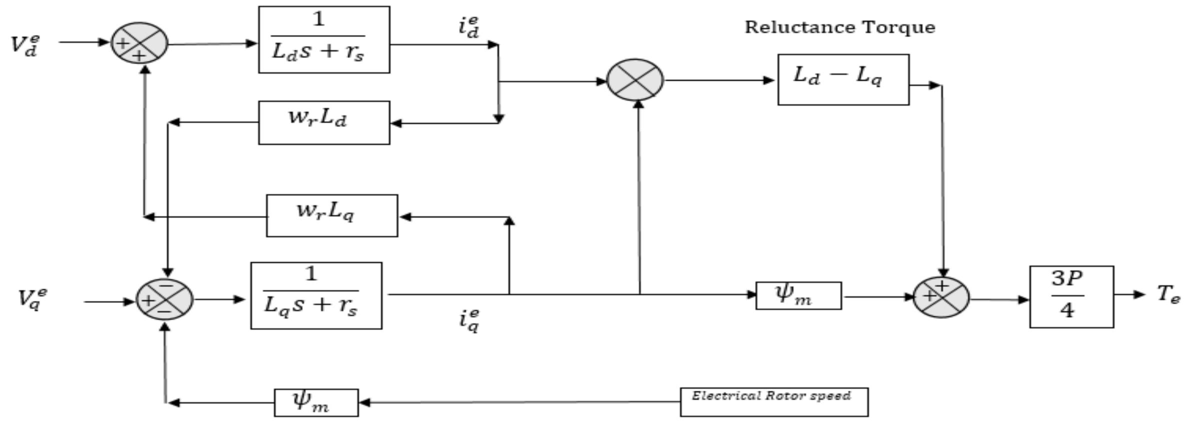


Fig. A. 4 Dynamic model of IPM

Because in IPM machine, the electrical rotor speed and speed of synchronous frame rotating is same, so the power equation for IPM can be expressed in terms of mechanical speed by:

$$P = \frac{3P}{4} w_r(\varphi_m i_q^e + (L_d - L_q) i_d^e i_q^e) \quad \text{A.12}$$

So by using the equation describing the IPM in synchronous frame, the dynamic model of IPM is presented by Fig. A.4. The mechanical equation (A.13) should be used in order to define the electrical rotor speed.

$$\mathrm{J}\frac{dw_r}{dt} + \mathrm{B}w_r = T_e - T_L \quad \text{A.13}$$

So, the electrical speed can be determined from the IPM dynamic by adding the mechanical equation (Fig. A.5).

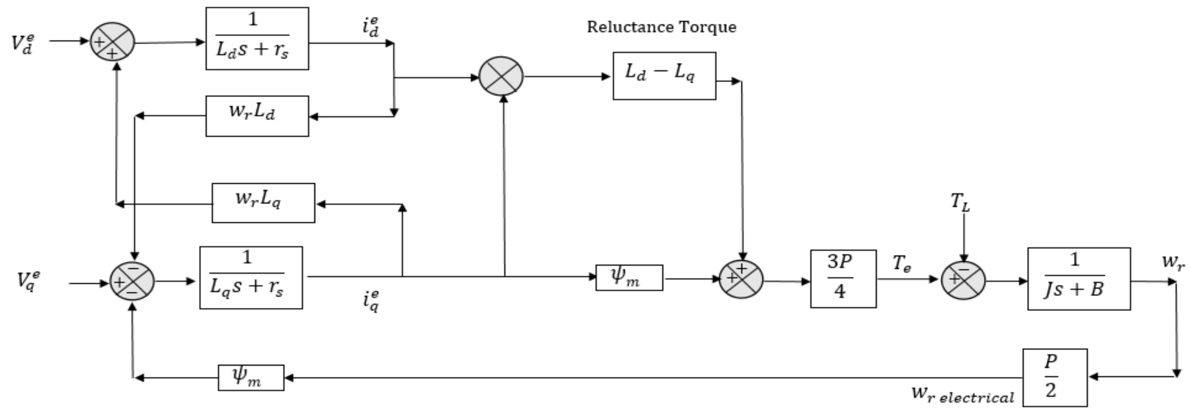


Fig. A. 5 IPM dynamic by adding the mechanical equation

**A.5 Control of IPM**

One of the typical method that can be used for control the IPM machine is current controller. In current control method, the sensed currents are transferred to the two axis (d-q) in synchronous frame. To implement this transformer, the flux angle is used. The value of the flux angle is extracted by resolver and then its value has been modified to position or velocity by using the converter. Then, the transferred currents are compared with desired current and pass from PI controllers. The tuned PI controllers try to keep the currents of machine close to the desired currents.

The back EMF and decoupling terms has to be compensated to produce the input voltage of space vector modulation. These compensation terms can be neglected in current control methods because the PI controller can compensate the coupling and back EMF.

$$V_{ds}^{e} = \mathrm{PI}\ (i_d^{e*} - i_d^{e}) - w_e(L_q)i_q^{e} \qquad \text{A.14}$$

$$V_{qs}^{e} = \ \mathrm{PI}(i_d^{e*} - i_d^{e}) + w_e(L_d)i_d^{e} + \ w_e\varphi_m$$

The current controller of IPM machine can be designed as follow:

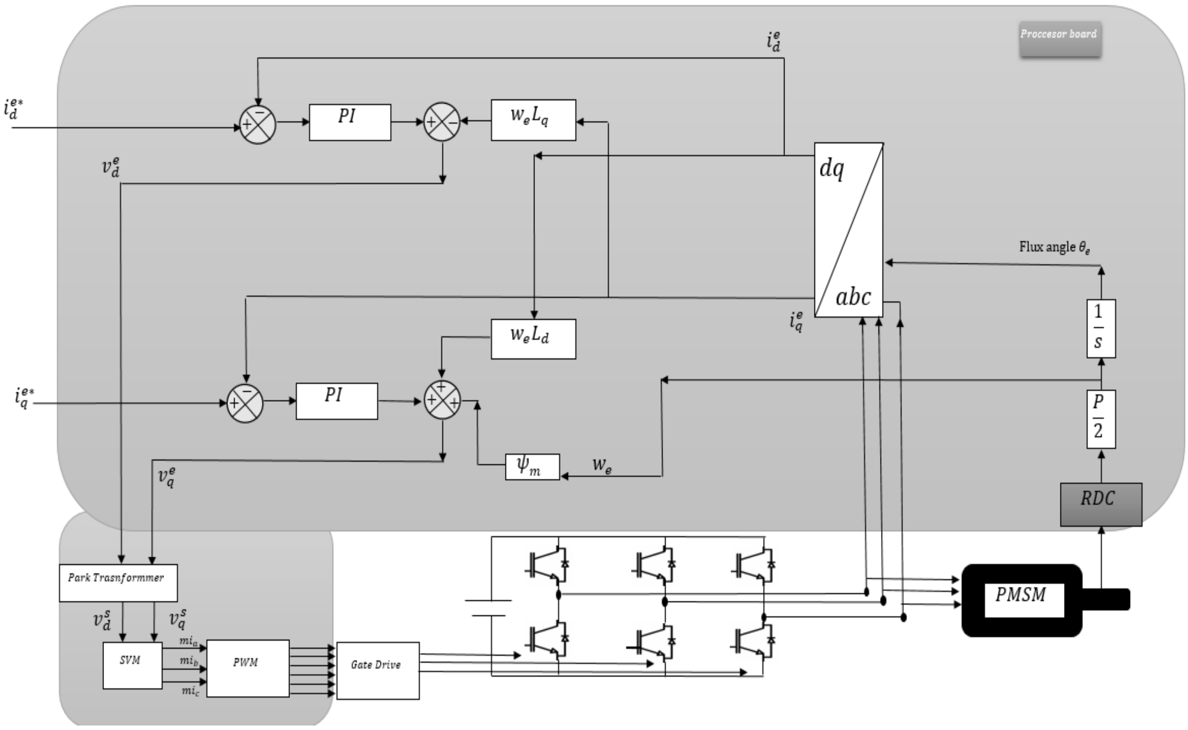


Fig. A. 6 Control block diagram for IPM

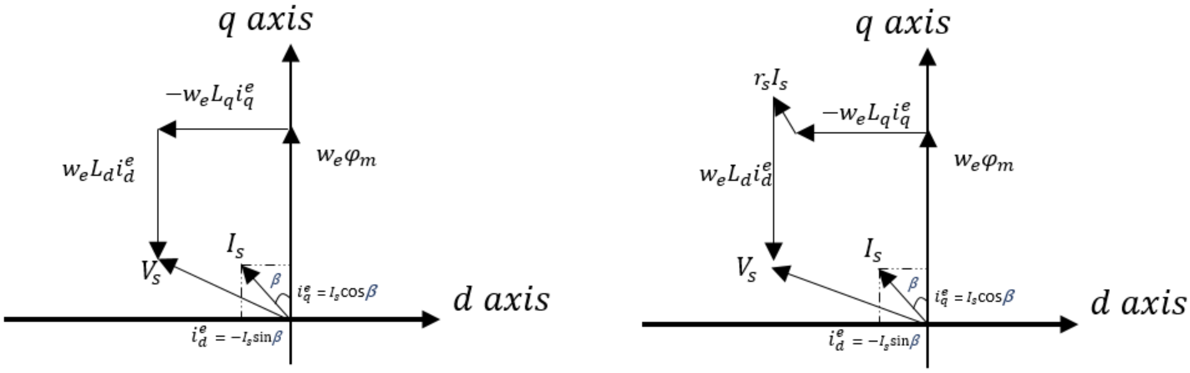


Fig. A. 7 Phasor diagram for IPM

In the above diagram, all of the dark part of the figure can be designed in F28377D which is the floating point microprocessor of C2000 family. The main part of this current controller defines the appropriate level of desired currents ($i_d^{e*}$ and $i_q^{e*}$). The value of the desired currents plays the key role in control of IPM machine to operate in different level of torque and power.

### A.6 Designing the desired currents

To control the currents of interior permanent magnet machine, the phasor diagram should be analysed. The phasor diagram of IPM machine are analysed by considering the stator resistance and without considering stator resistance in steady state condition. By considering stator voltage A.7 in synchronous frame, the phasor diagram can be drawn as shown in Fig. A.7. The reason of existing the back EMF in q axis can be expressed by showing the stator voltage vector:

$$V_s^e = V_{ds}^e + jV_{qs}^e \rightarrow V_s^e = -w_e\left(L_q\right)i_q^e + j(+w_eL_di_d^e + \ w_e\varphi_m) \qquad \text{A.15}$$

The back EMF component has contained of imaginary symbol ($j$) which causes that it will appear on q axis. As it can be seen in the Equation 15, the value of back EMF will be increased by raising the Machine speed. So, this increment of back EMF is compensated by increasing the value of $i_d^e$ in negative direction to satisfy the available voltage from inverter. This is the subject called field weakening operation.

The current control method is categorised to constant torque, constant power and constant power speed regions. To force the motor to operate in these three regions, the appropriate level of the currents need to be introduced. Before explaining about current controller methods, it should be considered that there

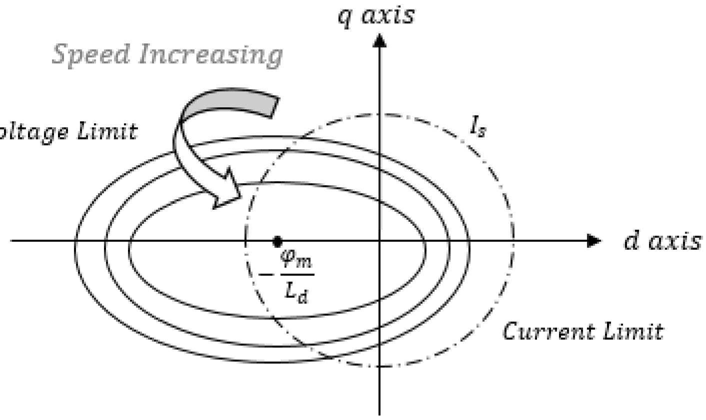


Fig. A. 8 Current and voltage constraint for IPM

are two constraint for motor drive control. The first constraint which is from the power converter side is the maximum voltage that inverter can provide from the dc link voltage. The next constraint belong to the rated current level that the machine can be accepted. The current and voltage limitation can be described by a circle and ellipse as follow:

$$(i_d^e)^2 + (i_q^e)^2 \leq (I_s)^2 \qquad \text{A.16}$$

$$(V_{ds}^e)^2 + (V_{qs}^e)^2 \leq (V_s)^2 \rightarrow (-w_e L_q i_q^e)^2 + (w_e L_d i_d^e + w_e \varphi_m)^2 \leq (V_s)^2$$

$$\rightarrow \frac{{i_q^e}^2}{(V_s)^2/(w_e L_q)^2} + \frac{(i_d^e + i_f)^2}{(V_s)^2/(w_e L_d)^2} \leq 1$$

As it can be realized from voltage constraint equation, increasing the speed of the machine causes that the ellipse shrinks to the centre point which is $(-i_f, 0) = (-\frac{\varphi_m}{L_d}, 0)$. The ellipse has the d axis as the major axis because $(V_s)^2/(w_e L_d)^2 > (V_s)^2/(w_e L_q)^2$. As explained before, the reason behind this is that the $L_d < L_q$. So, the current and voltage constraint behave as demonstrated Fig.A.8 for different speed value. To analysis the current controller in different machines operation region, the torque equation of IPM machine should be described. As expressed before, the torque equation of IPM consisted of magnetic component and reluctance component:

$$\mathrm{T} = \frac{3P}{4}\left[\varphi_m i_q^e - \left(L_q - L_d\right) i_d^e i_q^e\right] \qquad \text{A.17}$$

The $i_d^e$ and $i_q^e$can be modified in terms of the maximum level of current limitation (Fig. A.7). So, the torque equation is defined as follow:

$$\mathrm{T} = \frac{3P}{4}\left[\varphi_m i_q^e - \left(L_q - L_d\right) i_d^e i_q^e\right] = \frac{3P}{4}\left[\varphi_m I_s cos\beta \; + \frac{1}{2}\left(L_q - L_d\right) I_s^2 sin\,(2\beta)\right] \qquad \text{A.18}$$

It should be noted that the speed of changing the reluctance torque is twice faster than the magnetic torque. Thus by using a high rate of $L_q/L_d$, the high level of torque is obtained. Now by understanding the effect of the two axis stator currents on electrical torque, the current control methods can be described by details.

### A.6.1 Current Control Methods

As mentioned before, in SPMSM the value of the d and q axis of stator inductance are equal($L_q = L_d$). This leads to that the reluctance torque will not appeare in torque equation for SPMSM. So, the level of the torque can be adjusted just by controlling the value of $i_q^e$ and keeping $i_d^e$ at zero value. In contrast, in IPMs, there are numerous combination of d and q axis currents that can be defined to produce the same level of the torque. Selection the suitable combination depends on the desired performance that engineers tend to extract from the machines [96]. In this Appendix, the current control methods which can provide maximum torque per ampere, maximum power and Maximum Torque/Flux are explained.

### A.6.2 Maximum Torque per Ampere (MTPA)

The motor works on the maximum torque rate for a fixed stator current limitation at appropriate current angle ($\beta$). To find the current angle which can produce the maximum torque of the machine, the derivation of the torque versus the current angle applied (Equation 18).

$$T = \frac{3P}{4}\left[\varphi_m I_s cos\beta \; + \frac{1}{2}\left(L_q - L_d\right) I_s^2 \sin\,(2\beta)\right] \rightarrow \frac{\partial T}{\partial \beta} = 0 \rightarrow \beta = \sin^{-1}\left[\frac{-\varphi_m + \sqrt{{\varphi_m}^2 + 8(L_q - L_d)^2 I_s^2}}{4(L_q - L_d) I_s}\right]$$

Thus the desired currents $i_d^{e*}$ and $i_q^{e*}$ for first stage of operation (MTPA) are defined as follow:

$$i_d^{e*} = -I_s \sin(\beta) \rightarrow i_d^{e*} = \frac{1}{4\left(L_q - L_d\right)}\left(\varphi_m - \sqrt{{\varphi_m}^2 + 8(L_q - L_d)^2 I_s^2}\;\right) \qquad \text{A.19}$$

Appendix A

$$i_q^{e*} = I_s \cos(\beta) \rightarrow i_q^{e*} = I_s \cos(\sin^{-1}\left[\frac{-\varphi_m + \sqrt{{\varphi_m}^2 + 8(L_q - L_d)^2 I_s^2}}{4(L_q - L_d)I_s}\right])$$

The operation of the IPM with defined specification (Table A.2) in the maximum Torque Per ampere demonstrated in Matlab simulation.

In this stage of operation, the values of $i_d^{e*}$ and $i_q^{e*}$ are constant because the value of current angle just depends on the machine parameters. As the result of constant desired current, the torque level is kept at constant value (Figure 10). In this control stage, the machine speed is raising before the base speed where the modulation index is reaching to the maximum limit. As explained before, the maximum limitation of modulation index in space vector modulation is one.

Table A. 2 Parameters of tested IPM

| | | | | |
|---|---|---|---|---|
| Number of Poles | 6 | | Power (rated) | 8.8 KW |
| Dc link Voltage | 300V | | Base Speed | 2600 RPM |
| $L_d$ | 3.05 mH | | Current (rated) | 40 A |
| $L_q$ | 6.2 mH | | Flux ($\varphi_m$) | 0.0948 Wb |

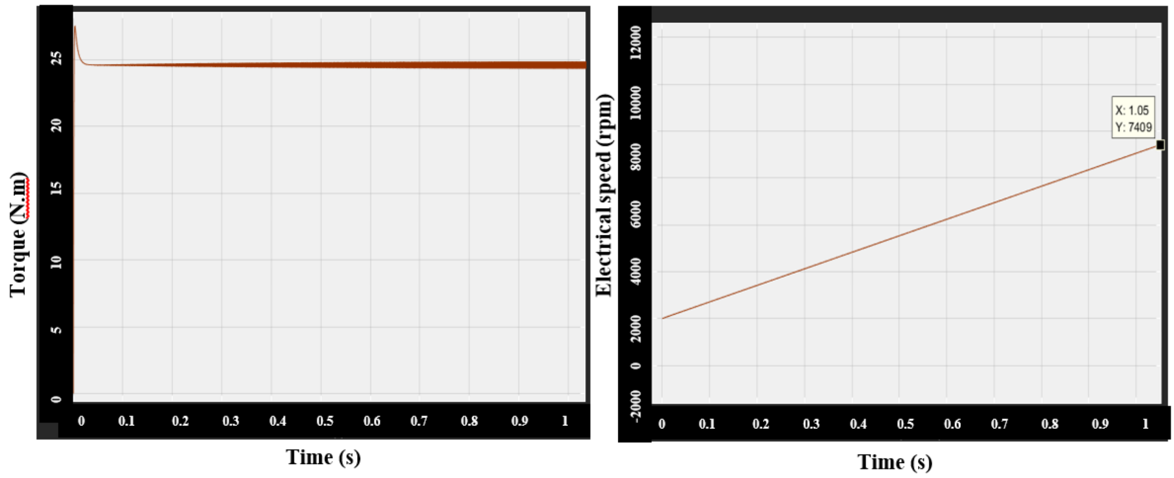


Fig. A. 9 Torque and speed for IPM

As shown in Fig. A.9, the electrical motor speed which is $\frac{P}{2}$ of mechanical speed reach to the 7400 RPM in MTPA operation stage. That means that the mechanical speed is closing to the base speed (2600 RPM). In this level of speed, the modulation index is reaching to one which means that the maximum available voltage provided by the inverter (Fig. A.10). It should be noted that AC motor are designed in a way to catch the rated in maximum available voltage value.

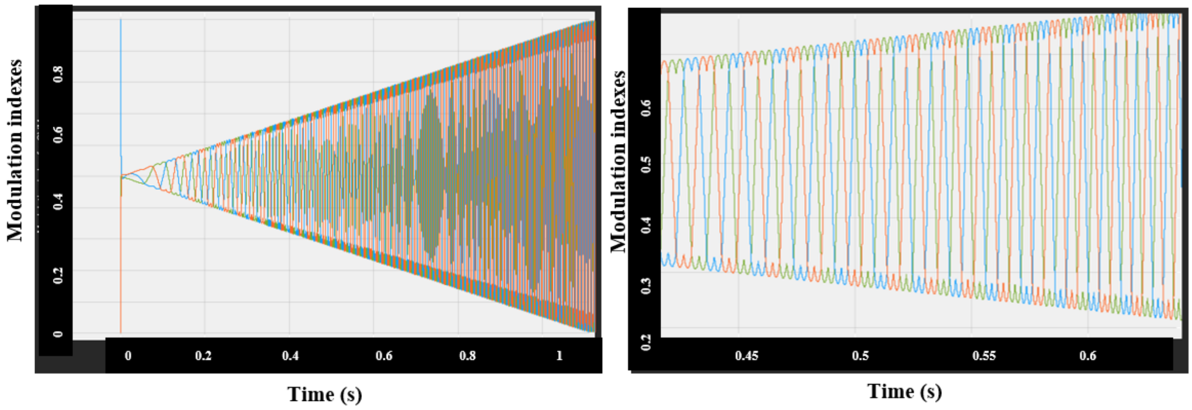


Fig. A. 10 Modulation index for IPM

As explained in phasor diagram (Fig. A.7), the incensement of back EMF as the result of speed raising should be compensated by decreasing the value of $i_d^e$. So by going to the field weakening regions, the machine finds the chance to catch higher speed rate. The reason of calling these regions as field weakening is that the stator flux in synchronous frame for IPM can be expressed by:

$$\lambda_{ds}^e = L_d i_d^e + \varphi_m \tag{A.21}$$

$$\lambda_{qs}^e = L_q i_q^e$$

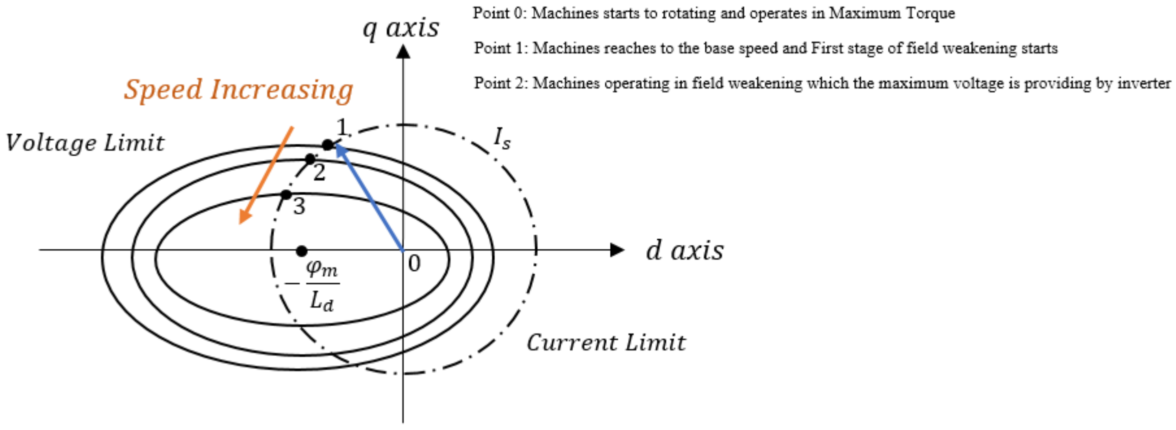


Fig. A. 11 Performance of IPM in current and voltage constraint

because in field weakening $i_d^e$ and $i_q^e$ need to be decreased, so the stator flux in d and q axis have to be reduced.

### A.6.3 maximum Power

In first stage of field weakening the desired current should be designed in such way that the maximum power performance can be achieved. In this stage, the desired currents moving on the current and voltage limitation. As explained before, the voltage ellipse shrinking to the center when the speed is increasing. So, it forces the current angle to increase that means increasing the $i_d^{e*}$ and reducing$i_q^{e*}$.By using the power equation in A.12 and considering the voltage and current constraint, the value of desired currents can be calculated. The key idea to find desired current is applying Kuhn-Tucker theorem [97]. In this theorem, the power equation is defined as objective function and the voltage and current constraint as the conditions.

Max $P_e\ (i_q^e, i_d^e)$ under $c_1\left(i_q^e, i_d^e\right) \leq 0,\quad c_2\left(i_q^e, i_d^e\right) \leq 0$ where A. 22

$$c_1\left(i_q^e, i_d^e\right) = (i_d^e)^2 + (i_q^e)^2 - (I_s)^2$$

$$c_2\left(i_q^e, i_d^e\right) = \varepsilon^2\left((i_q^e)^2 + ((i_d^e) + \frac{\varphi_m}{L_d})^2\right) - \frac{(V_s)^2}{(w^2 L_d^2)} \text{ Where } \varepsilon^2 = (L_q/L_d)^2$$

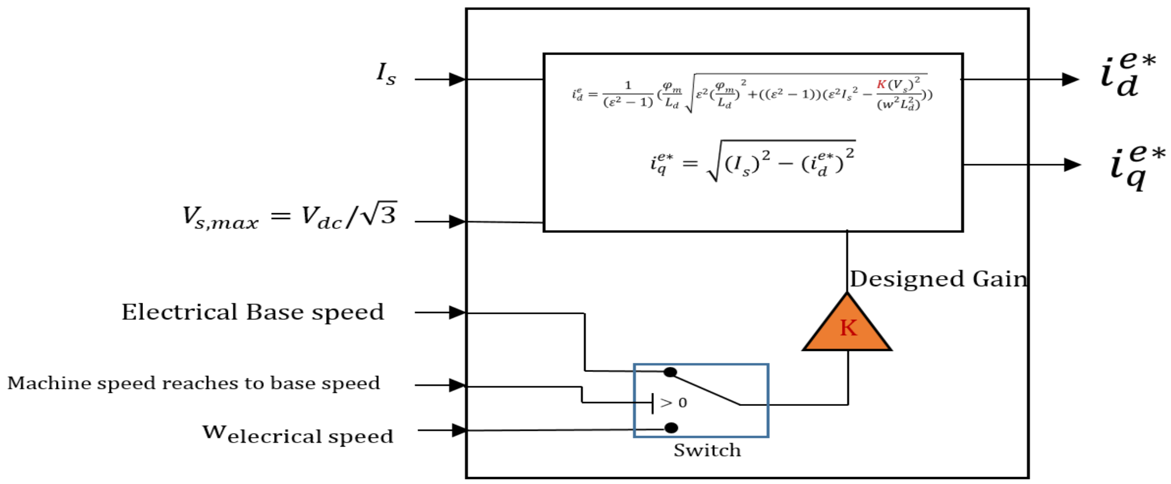


Fig. A. 12 The control schemed used for producing desired currents in first stage field weakening

These two conditions are satisfied by the points which are placed on the current and voltage constraints($c_1 = c_2 = 0$) . So by finding $(i_q^e)^2$ in current limitation equation and substituting in voltage constant equation, the desired currents can be achieved (A.23).

$$c_1(i_q^e, i_d^e) = 0 \rightarrow (i_q^e)^2 = (I_s)^2 - (i_d^e)^2 \tag{A.23}$$

$$c_2(i_q^e, i_d^e) = 0 \rightarrow i_d^e = \frac{1}{(\varepsilon^2-1)}\left(\frac{\varphi_m}{L_d}\sqrt{\varepsilon^2\left(\frac{\varphi_m}{L_d}\right)^2 + \left((\varepsilon^2-1)\right)\left(\varepsilon^2 I_s{}^2 - \frac{(V_s)^2}{(w^2L_d^2)}\right)}\right), i_q^{e*} = \sqrt{(I_s)^2 - (i_d^{e*})^2}$$

In above equation, the negative $i_d^e$ answers has been accepted because these negatives value just can provide the field weakening operation. So as shown in A.23, the desired $i_d^{e*}$ in first stage of field weakening depends on electrical motor speed, maximum available voltage and the rate current (Fig. A.12). The block diagram illustrates that before the reference currents are considered as the desired currents, their value should be matched by the desired current in MTPA. This causes that the motor move to field weakening without torque ripple and the torque rate in starting point of field weakening is aligned with maximum torque level. To achieve this requirement, the gain is designed for this specific machine with the value of 0.98. To design the gain value, the base speed is used before the machine

Appendix A

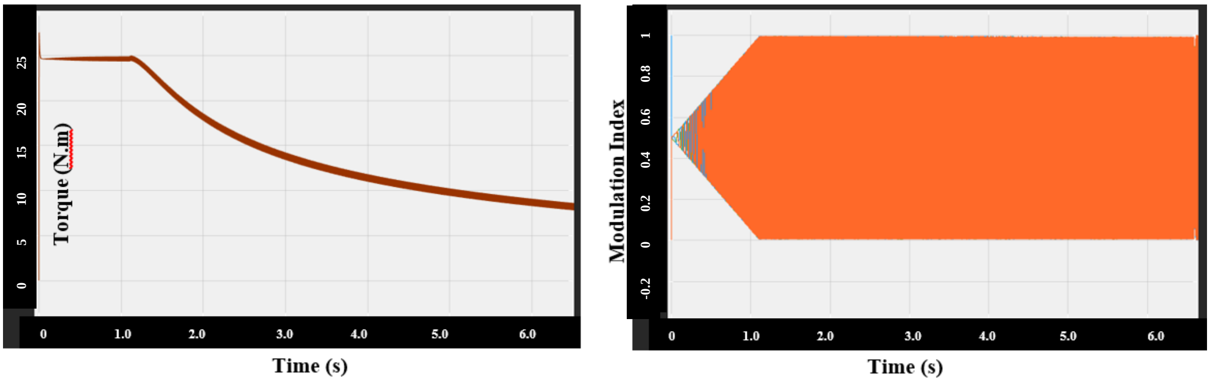


Fig. A. 13 Torque and modulation index in second stage field weakening

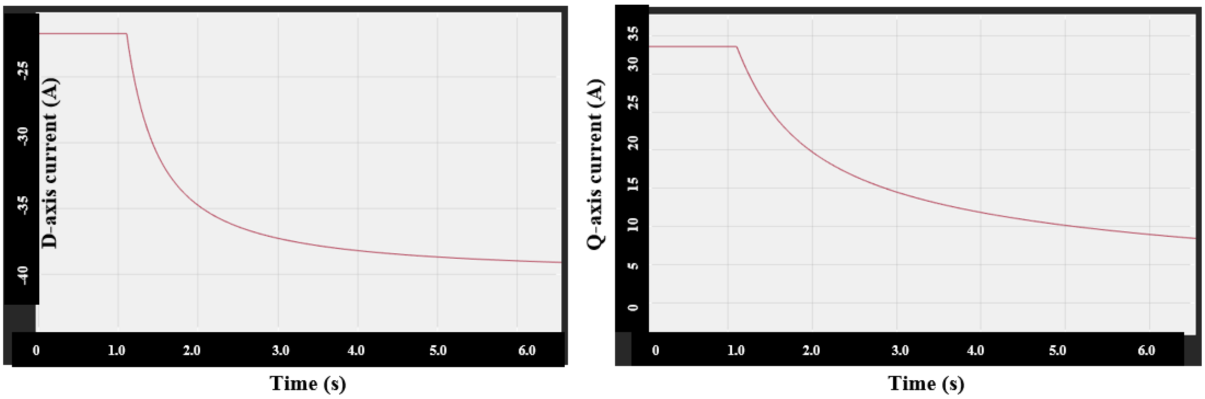


Fig. A. 14 Desired currents produced in control block

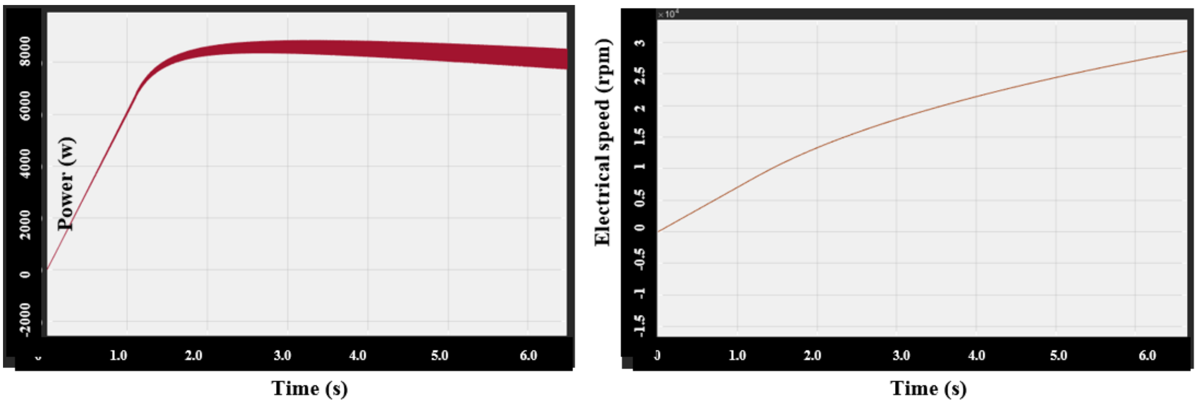


Fig. A. 15 Power and electrical speed

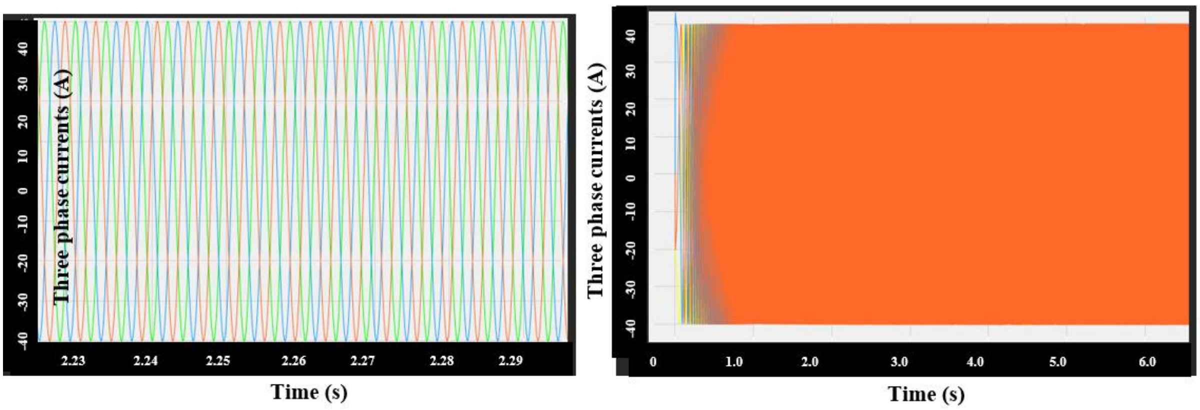


Fig. A. 16 Three phases Stator currents

reaches to that speed and then the real machine speed will be considered in the loop when the machine pass the base speed. As shown in Fig. A.14, the value of desired currents in both axis are decreasing to provide field weakening. Because these desired currents are placed in current and voltage constraints, so the maximum power can be produced for the machine. Fig. A.15, shows that the power reaches to the rated value in first stage of field weakening which confirm the performance of the control method. The three phase currents have the peak value same with the rated current value. It shows that desired designed currents($i_d^{e*}, i_q^{e*}$) are moving on the current constraint circuit so the peak of three phase current kept constant but the frequency is enhancing. The frequency of the current signals are increasing in order to raising the speed of the machine. The speed of the machine depends on the applied input current frequency. It should be noticed that the machines current is close to the rated value which can produce the maximum torque for the machine. So if the machine was asked to control on speed mode, then the phase current will be reduced when the machine was closing to the reference speed. The reason behind this is that in speed mode control, the desired $i_q^{e*}$ is coming from the clos loop speed loop. Thus, the reference $i_q^{e*}$ will decrease as long as the machine is closing to the reference speed.

### A.6-4 Maximum Torque/Flux control

The second stage of field weakening (high speed range) for IPM machine can be achieved if the center of voltage ellipse placed inside the current constraint. It is because that the desired currents can still be controlled by using the maximum torque/flux control. This high speed motor operation called second stage of field weakening and can be achieved if $I_s > \frac{\varphi_m}{L_d}$. As it was explained before, this stage is used for producing an extreme high speed. So, the voltage ellipse needs to be closed to the center which is $(-\frac{\varphi_m}{L_d}, 0)$. In this region, the desired currents are defined in such way to produce the maximum torque per flux.

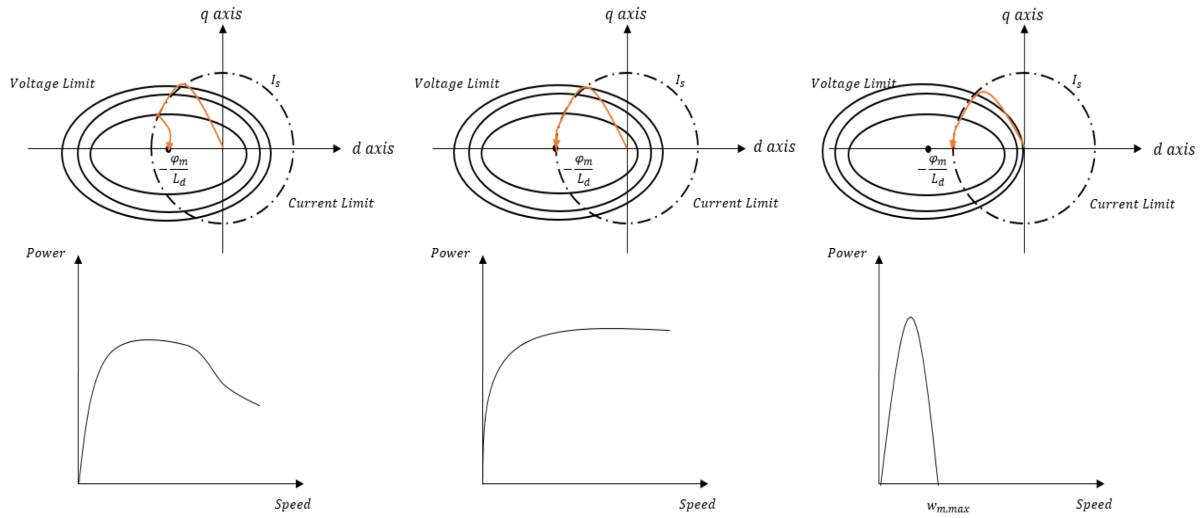


Fig. A. 17 The effect of centre of voltage ellipse constraint on motor output power

In second stage field weakening, the desired currents are placed on the voltage ellipse and because the flux follows the voltage equation, the maximum torque per flux can be achieved as follow:

$$(\lambda_q)^2 + \lambda_d{}^2 = (\frac{V_s}{w_e})^2 \rightarrow (L_d i_q^e)^2 + (L_d i_d^e + \varphi_m)^2 = (\frac{V_s}{w_e})^2 \rightarrow i_d^e = \frac{\lambda_d - \varphi_m}{L_d}, i_q^e = \frac{(\frac{V_s}{w_e})^2 - \lambda_d{}^2}{L_q^2}$$

So now, the torque equation can be expressed in terms of d-axis flux (A.25).

$$T_e^2 = \left(\frac{3P}{4}\right)^2 \left(\lambda_d - L_q \frac{\lambda_d - \varphi_m}{L_d}\right)^2 \left(\frac{(\frac{V_s}{w_e})^2 - \lambda_d{}^2}{L_q^2}\right) \qquad \text{A.25}$$

By taking the derivation of the torque with respect to d-axis of rotor flux, the maximum flux can be calculated (A.26).

$$\lambda_d = \frac{-L_q \varphi_m + \sqrt{L_q^2 \varphi_m{}^2 + 8(L_d - L_q)^2 (\frac{V_s}{w_e})^2}}{4(L_d - L_q)} \qquad \text{A.26}$$

Then, the desired currents in second stage field weakening are determined in terms of the d-axis stator flux as follow:

$$i_d^{e*} = \frac{\lambda_d - \varphi_m}{L_d} \qquad \text{A. 27}$$

$$i_q^{e*} = \frac{(\frac{V_s}{w_e})^2 - \lambda_d^{\ 2}}{L_q^2} \qquad \text{A. 28}$$

As it was expected, the amplitude of desired currents are reduced because the voltage ellipse shrinks to the centre which is inside of the current circle limitation.

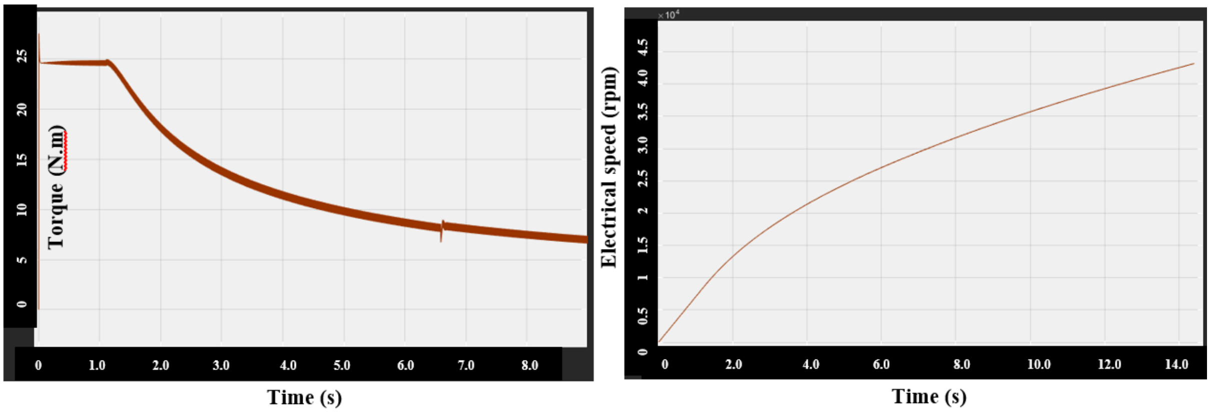

Fig. A. 18 Torque and speed of IPM

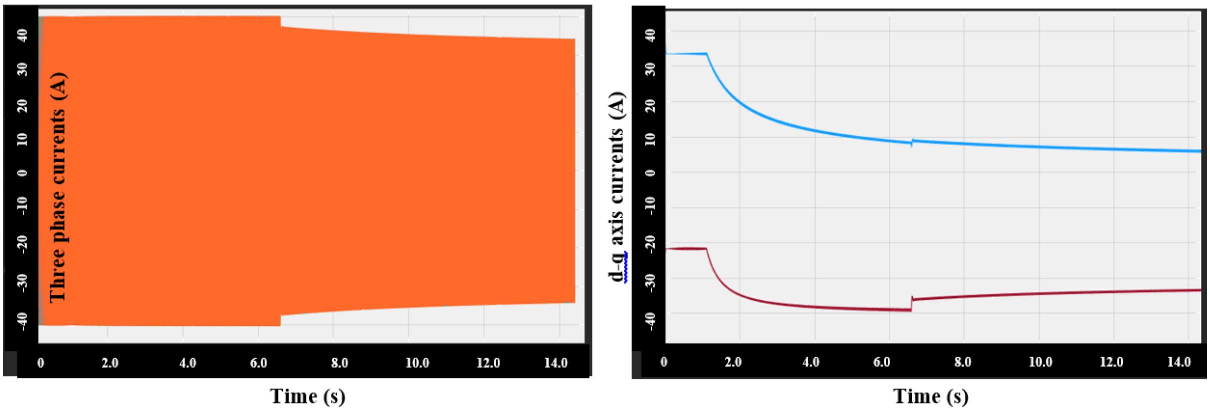

Fig. A. 19 Three phase currents and d-q axis measured currents

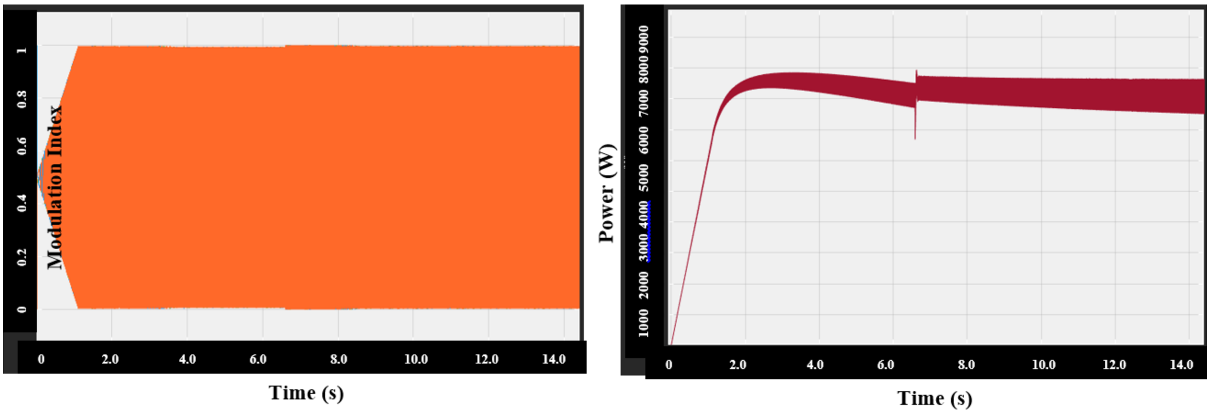

Fig. A. 20 Modulation index and power of IPM

It should be mentioned that the carrier signal has the frequency of 10 kHz and the hexagon limit boundary has been considered in space vector modulation design. Furthermore, the digital PI controllers has been designed and the sampling frequency of 10 kHz considered. Proportional and integral gains of both PI controllers have been tuned by 0.05 and 0.0008 respectively. The integrator clamp is imitated between 2 and -2. The combination of the explained current control methods leads to the motor operate in very high level speed and the constant torque, constant power and constant torque/flux are utilized. It should be mentioned here that the back EMF and coupling terms has not been compensated in control methods so the PI controllers are the main elements to produce the inputs of the space vector modulation.

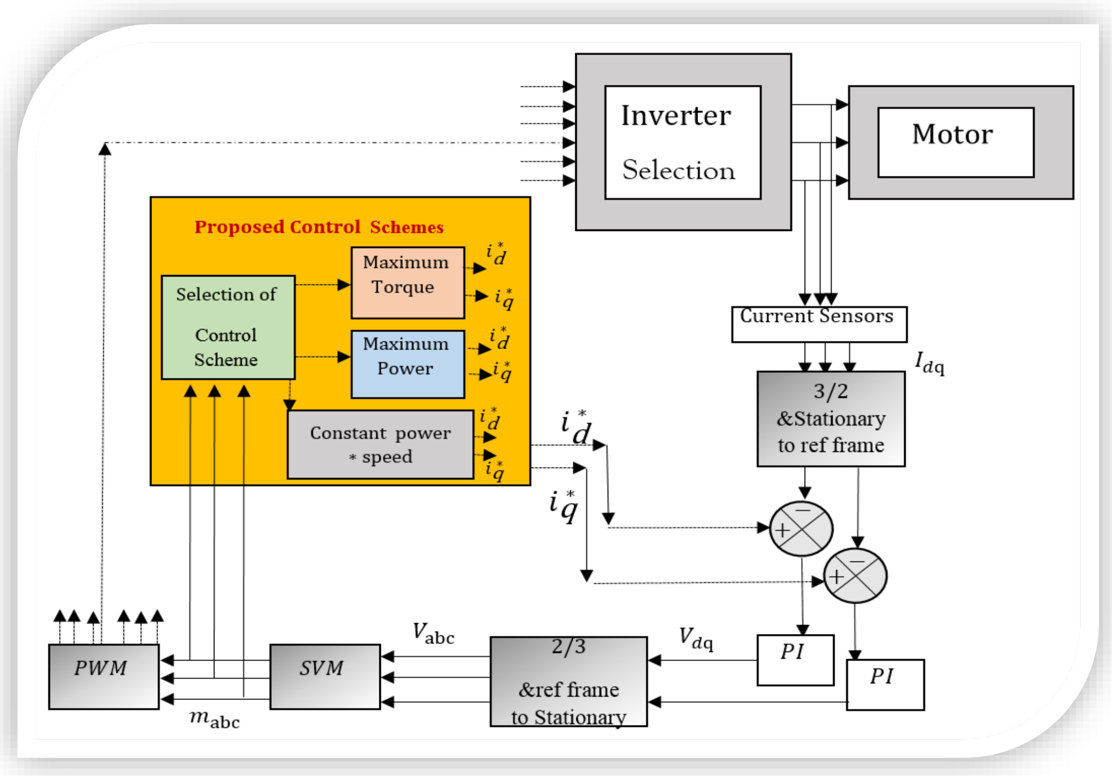


Fig. A. 21Complete Control diagram of IPM

# Appendix B

# Runge-Kutta 4th order Method

The ordinary differential equations (ODE) for mathematical modelling of an IM are solved in CPU2 of microcontroller by using a well-known numerical solution. For general ODE, $\frac{dy}{dx} = f(x, y)$ with having the initial condition of $y_i$ at $x_i$, the value of $y_{i+1}$ at $x_{i+1} = (x_i + h)$ can be determined by:

$$y_{i+1} = y_i + \frac{1}{6}(k_1 + 2k_2 + 2k_3 + k_4) \qquad B.1$$

where $k_1$ to $k_4$ can be defined by:

$$k_1 = f(x_i, y_i) \qquad B.2$$

$$k_2 = f\left(x_i + \frac{1}{2}h, y_i + \frac{1}{2}k_1 h\right)$$

$$k_3 = f\left(x_i + \frac{1}{2}h, y_i + \frac{1}{2}k_2 h\right)$$

$$k_4 = f(x_i + h, y_i + k_3 h)$$

It needs to be mentioned that B.1 is equated to first five term of Taylor series:

$$y_{i+1} = y_i + \frac{dy}{dx}|_{x_i, y_i}(x_{i+1} - x_i) + \frac{1}{2!}\frac{d^2y}{dx^2}|_{x_i, y_i}(x_{i+1} - x_i)^2 + \frac{1}{3!}\frac{d^3y}{dx^3}|_{x_i, y_i}(x_{i+1} - x_i)^3$$
$$+ \frac{1}{4!}\frac{d^4y}{dx^4}|_{x_i, y_i}(x_{i+1} - x_i)^4 \qquad B.3$$

The results for emulated induction machine in F28377d is validated by Matlab Simulink for contant torque and field weakening regions in Fig. B1.

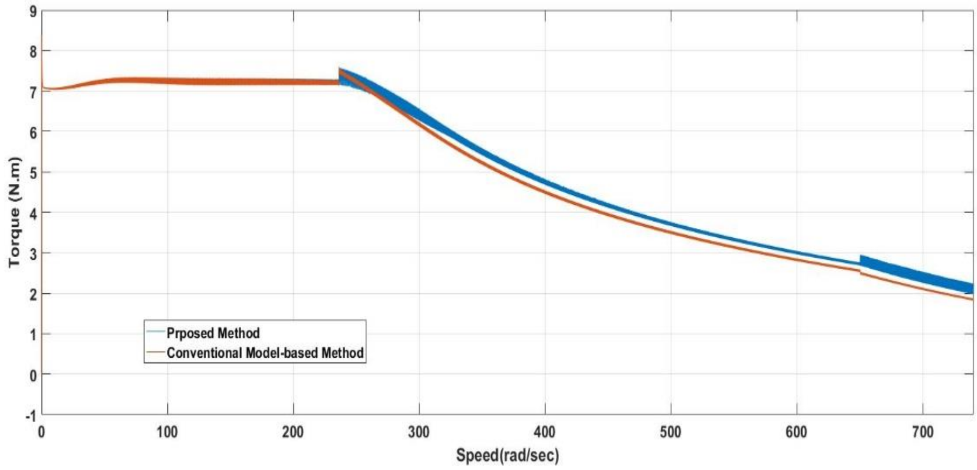


(a)

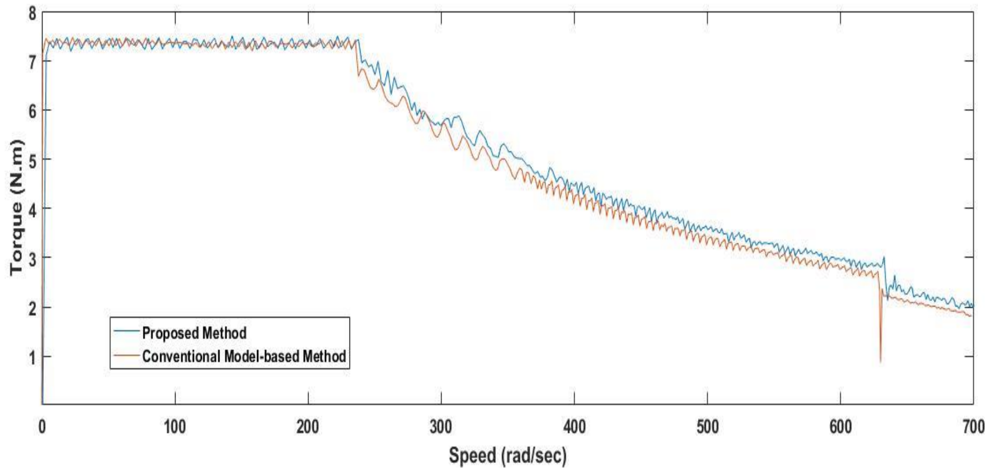


(b)

Fig. B 1 Torque-speed result for tested IM emulated in (a) Matlab Simulink (b) F28377d microcontroller board

# Appendix C

# Filter design

## C.1 Required cut-off frequency in input of the ADC channel of microcontroller

Selecting the cut-off frequency of RC filter in input of the ADC depends on the sampling rate. To design the optimal low pass filter, the equivalent Thevenin resistance of the circuit needs to be calculated. Then, the value of the filter capacitor is selected to satisfy the required cut-off frequency.

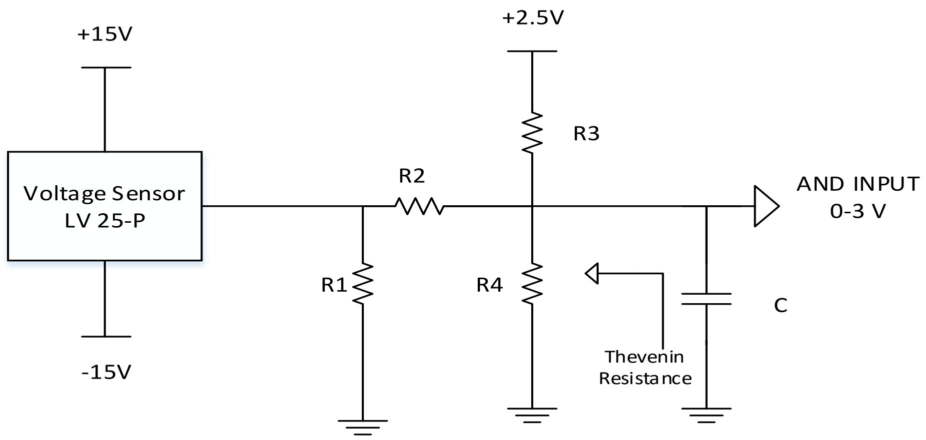


Fig. C. 1 Design of filter for input of ADC channel

As the output voltage of the sensor is higher than 3 V, so the amplifier does not to be placed in output of the sensor. Designing the resistors depend on the voltage produced by the sensor. Then, this voltage need to be decrease to 0-3 Volt which is the acceptable rate of input of ADC.

So, the Thevenin resistance can be calculated by:

$$R_{th} = R3 \,|\, \; R4 \,|\, \; R2$$

And the cut-off frequency of the filter is:

| Time scale per division | Record length (Points) | Sampling rate (number of samples /second) |
|---|---|---|
| 40 us | 100K | 250M |
| | 1M | 1G |
| 200 us | 125K | 62.5M |
| | 1M | 500M |
| 1 ms | 125K | 12.5M |
| | 1.25M | 125M |
| 100 ms | 125K | 12.5 K |
| | 1.25M | 1.25M |
| 1s | 125K | 12.5K |
| | 1.25M | 125.5K |
| 10s | 125K | 1.25K |
| | 1.25M | 12.5K |

Table C. 1 Sampling rate for different time scale in TEKTRONIX 2000

$$f_C = \frac{1}{2\pi R_{th} C}$$

The corner frequency is close to 220 KHz which allows to controllers to compensate the error of measured and desired signals. Considering the law bandwidth frequency causes that the significant difference between actual and measured signal as some harmonics content are already taken off from it.

**C.2 Designing the digital filter in oscilloscope for capturing DAC signals:**

There is one digital filter placed in oscilloscope. The bandwidth of this filter is in range of 600Hz to 100MHz. The maximum sampling rate for the oscilloscope is 100MSample per second.

The rate of the sampling rate of the oscilloscope depends on:

- the time scale per division of the oscilloscope
- record length which specified the number of points

So, changing the bandwidth of the digital filter does not change the sampling rate. The sampling rate for different time scale are demonstrated at Table C.1 for Oscilloscope model TEKTRONIX 2000.

It can be assumed that the maximum speed of the machine in first stage of field weakening is 7000RPM. So maximum frequency of signals provided by DAC is 233Hz. That means the time takes for one complete rotating cycle (360 electrical degree) is 4.29ms. For reference d-q currents signals (in my proposed method), six quadratic shapes are produced. So, the required time for one quadratic shape in maximum speed is 4.29ms/6 (0.715ms). If assume that 10 points are required in one quadratic (0.715ms), so the minimum samples for 1 second is close to 14k Samples. Now if the time scale division put in 10s with record length of 1.25Mpoint, so the 12.5k samples per second can be achieved. This rate is close with the required samples (14k samples/second) which is calculated for maximum speed. As the maximum frequency of signal is 1.4 KHz (1/.715ms), this is near .1 of sampling frequency (12.5 KHz).

### C.3 Over-current and voltage trip

The over-current trip is the procedure that keeps the power switches and motor isolations safe in an over-current situation. As the initial step for activating the over-current trip, the voltage-current characteristic of the current sensor needs to be measured. Figure C.2 shows that the 3.1V output voltage is produced by the current sensor as the 15A rms current is applied. To protect the power switches and induction machine in an over-current situation, the threshold value for the comparator control register needs to be defined. The high/low DAC shadow threshold depends on the maximum /minimum acceptable current for CAS 15-NP. The produced output voltage of the current sensor is between 0.375V and 4.625V for input current range -15A rms to 15A rms. In a zero measured current, the produced sensor voltage is 2.5V. The output sensor voltage is passed from resistor divider to define the acceptable voltage range for ADC which is 0-3V. Before the ADC data is passed to software, the scaling factor and offset can be applied to it by using post-processing block (PPB). Then this ADC data is changed to analogue by using DAC to be compared with high and low DAC value shadow registers. This threshold value is defined to enable the trip zone. It should be noticed that the threshold value are defined based

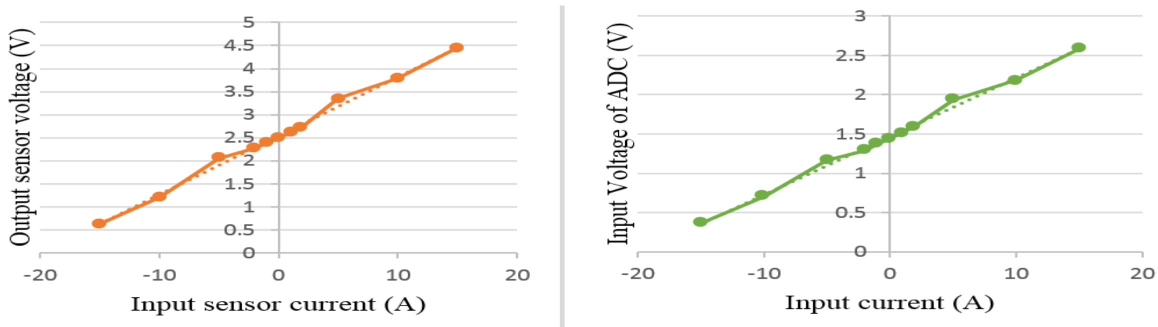


Fig. C.2 Step response of CAS 15-NP current sensor on the rated current of the load and power switch. The power switches used in three-phase inverter is IRG4PH50UDPbF, which accepts 24A continuous collector current in 100℃ case temperature.

The threshold current trip values should be considered as double the value of motor rated current. The reason for selecting the aforementioned range is to consider the effects of the PWM ripple and acceleration/deceleration condition in transient mode. In this experimental test, the rated current of machine is 4.6A rms. So, the threshold current trip is defined between 13A and -13A. The high and low DAC value in the shadow register of comparator register (CMPSS) is configured as shown in Fig. C.3.

In initial step of this test, the constant current is applied to the sensor directly by using the DC-power supply to find the high and low DAC value as the threshold value. By monitoring the produced ADC value in the (GUI), the ADC value of 1,000 samples for +5A and -5A can be measured. As shown in Fig. C.4, the average measured values for +5A and -5A are 2500 and 1475 respectively. After this initial low current test, the desired current trip level for 13A and -13A can be measured and therefore, the corresponding DAC value for these current rates could be set as 3230 and 400 respectively. The defined current trip level is then used by on-chip comparator in order to trip the PWMs. It needs to be pointed out that there are four 16 bits ADC channels in F28377D. To synchronise the process of sampling and holding, each ADC is used separately for one current measurements.

As a result of directly applying DC current to the sensors, the temperature of the sensor increases. This causes some additional offset in measurement. So, it's more reliable to set the threshold level by applying the modulation pulse test.

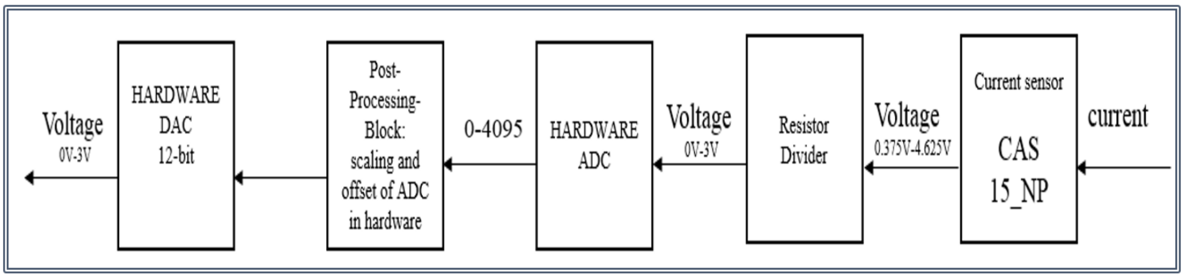


Fig. C.3 Produced DAC value for the applied input current

### C.4 Modulation pulse test to validate the performance of PWM trip in over-current situation

To produce a pulse for modulation signal, the interrupt service routine counter is used. The counter value is increased one by one in each PWM cycle. The created pulse single has 50ms width in 5s time period. The reason for producing the pulse width of 50ms is that it provides enough time for the current signal to settle in the resistor-inductor (R-L) load. The required settling time is 5 times that of the R-L time constant. The produced modulation pulse is then applied to the R-L load to calibrate the maximum

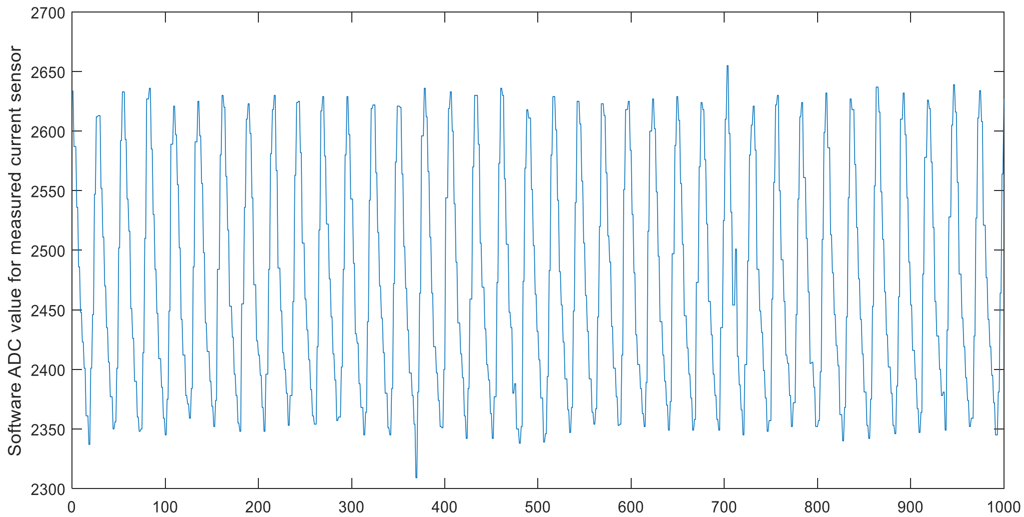


Number of samples

(a)

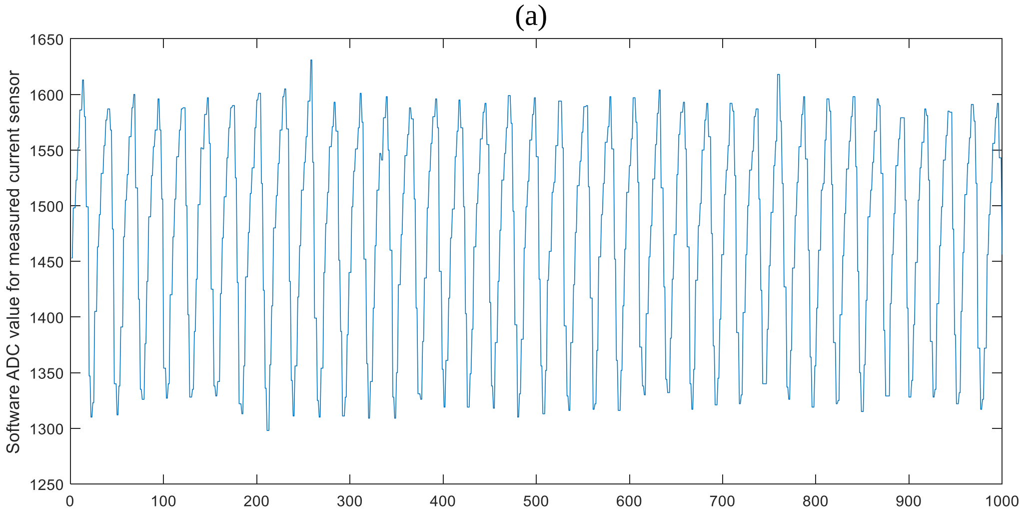


Number of samples

(b)

Fig. C.4 The ADC value of 1,000 samples data for (a) +5A and (b) -5A level of current trip as shown in Fig. C.5. It needs to be noticed that the amplitude of the modulation pulse must be set to the maximum level, which could be calculated based on the time period of switching frequency $T_{PWM}$ and the time period of clock $T_{TBCLK}$ for PWM.

As shown in Fig. C.5b, the applied modulation pulse passes the DC-link voltage to R-L load for 50ms. It creates the current which increases exponentially to reach the steady-state rate of 13.07A. Therefore, the threshold value of the current trip, which was already measured in the over-current activation section, is not precisely defined to trigger the PWM trip for 13A current. The slight reduction in the DAC value in the shadow register causes the PWM trip to be activated when the current passes 13A (Fig. 4.14c). Therefore, if the current trip happens in one short trip, the PWM signals will not be produced any more and the switches will be turned off.

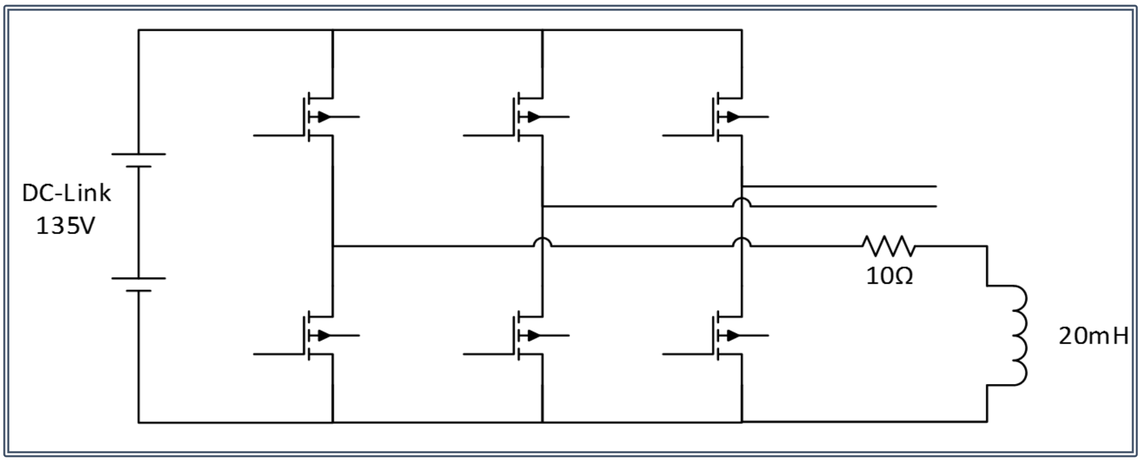


(a)

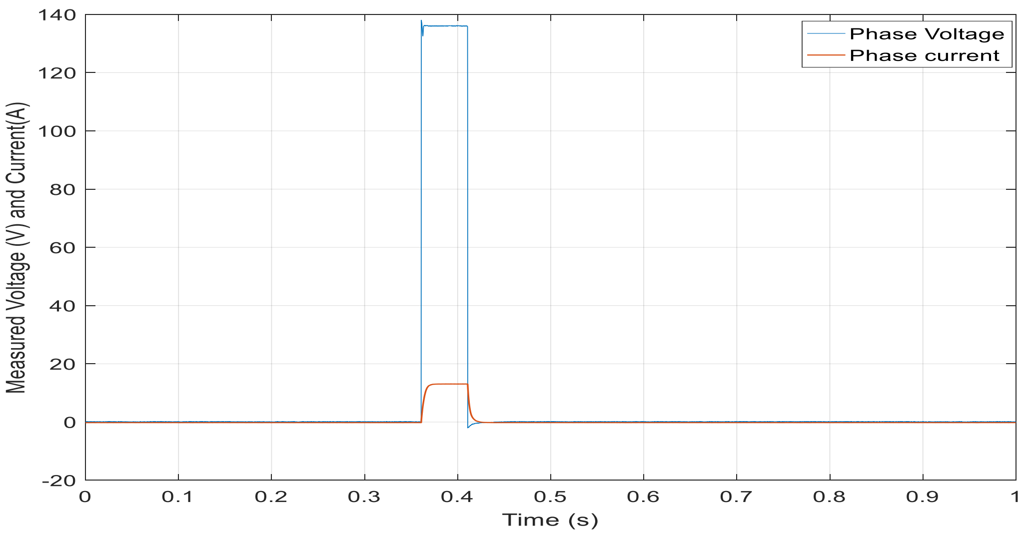


(b)

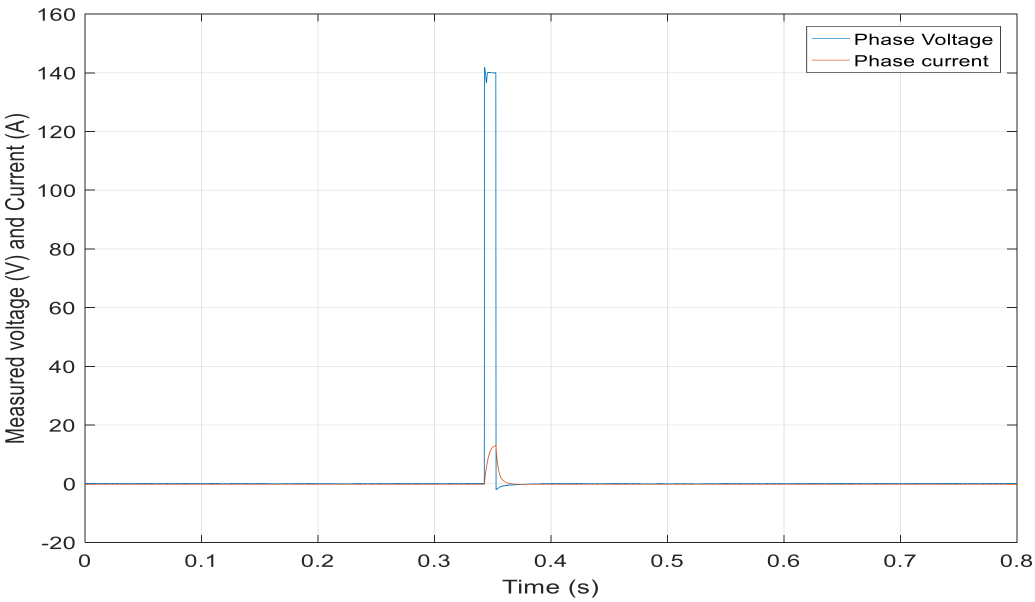


(c)

Fig. C.5 (a) Circuit configuration for calibrating the highest current trip (b) Phase voltage and current for R-L load under pulse modulation test (c) Phase voltage and current for R-L load under pulse modulation test in current trip mode

The lower trip level could also be calibrated based on the configuration shown in Fig. C.6. In this test, the 50ms pulse is applied to the lower legs to produce the negative current in the R-L load.

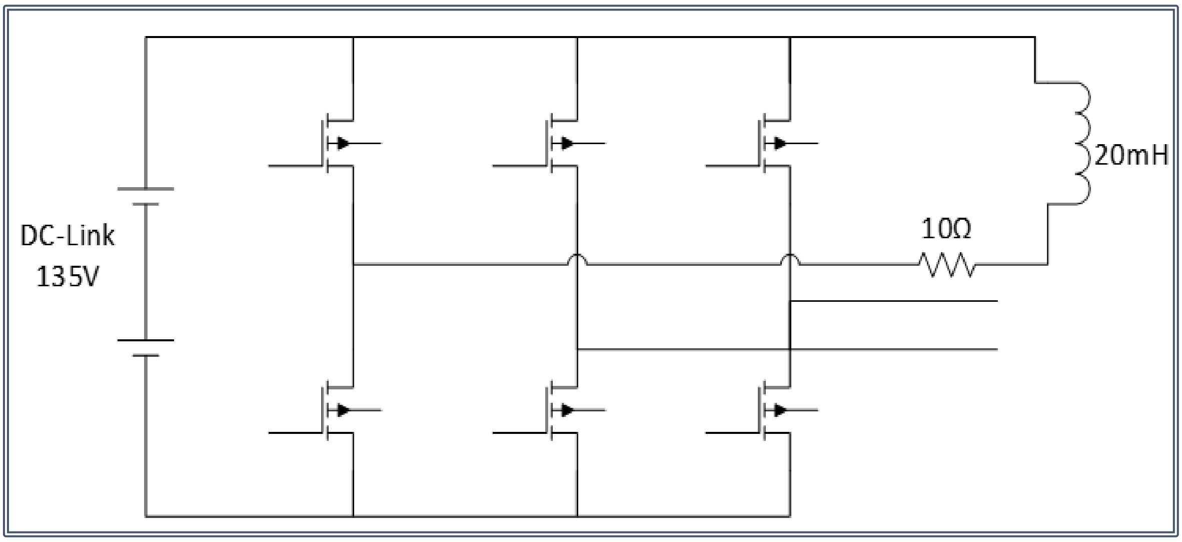


(a)

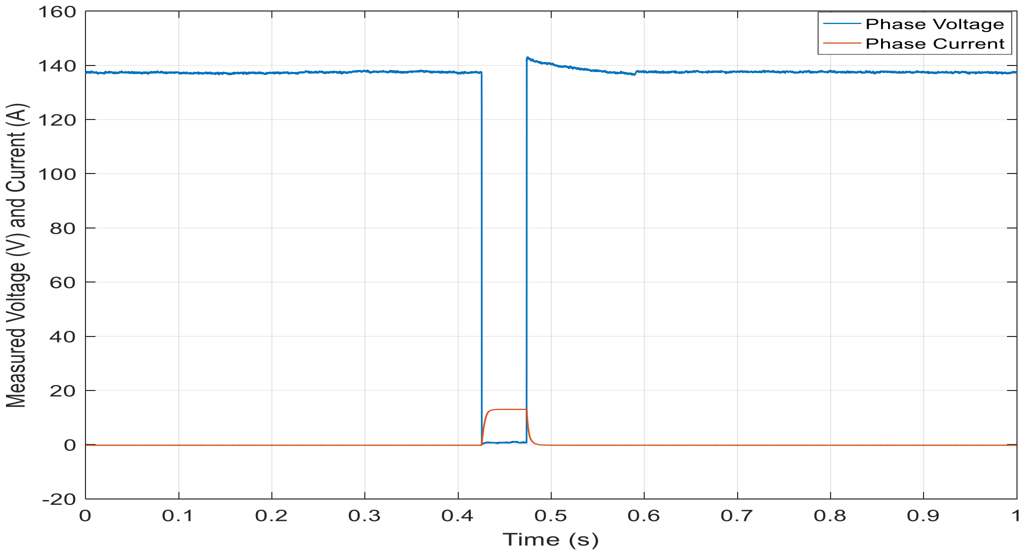


(b)

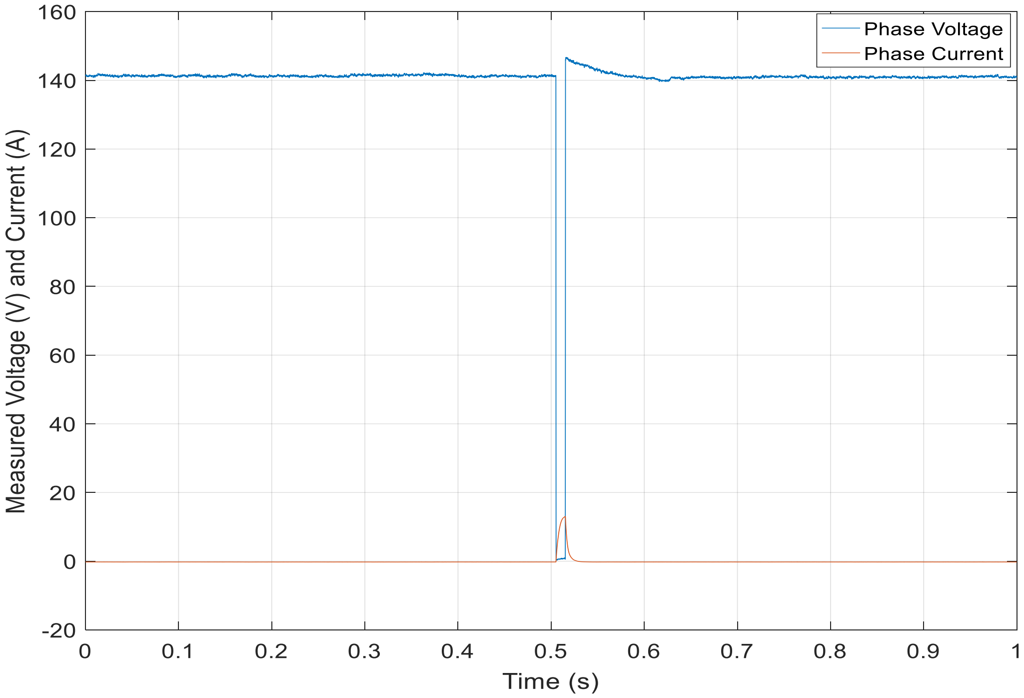


(c)

Fig. C.6 (a) Circuit configuration for calibration of the lower current trip (b) Phase voltage and current for R-L load under pulse modulation test (c) Phase voltage and current for R-L load under pulse modulation test in current trip mode

### C.4.1 Break-chopper control for over-voltage condition

In re-generating mode, the power will transfer back from motor to power converter. As shown in Fig. C.7a, the forth leg of the inverter is used to prevent damage to the DC-power supply in the configured test set-up. It is important to be noticed that the re-generated power charges up the batteries in traction applications [86].

Appendix C

Two power switches in the fourth leg are controlled by the hysteresis algorithm based on the threshold level. In the initial test, this chopper leg is designed to protect the DC-link power supply. So, the 50 Ohm chopper resistor is of a suitable value. However, in the re-generating test condition, the higher resistor with an appropriate heatsink which has the ability to kill the whole power rate of 2.2 KW, should be used. To control the fourth leg, where the break chopper resistor is connected, a proper threshold level needs to be designed. This limitation is selected based on the applied DC-link voltage. For 300 DC-link voltage, the threshold level of 320V to 350V is suitable (Fig. C.7c). Therefore, the lower switch of the fourth leg will be turned on if the DC-link voltage passes 320V. This causes the re-generated power to pass through the brake chopper resistor. It should also be pointed out that the upper

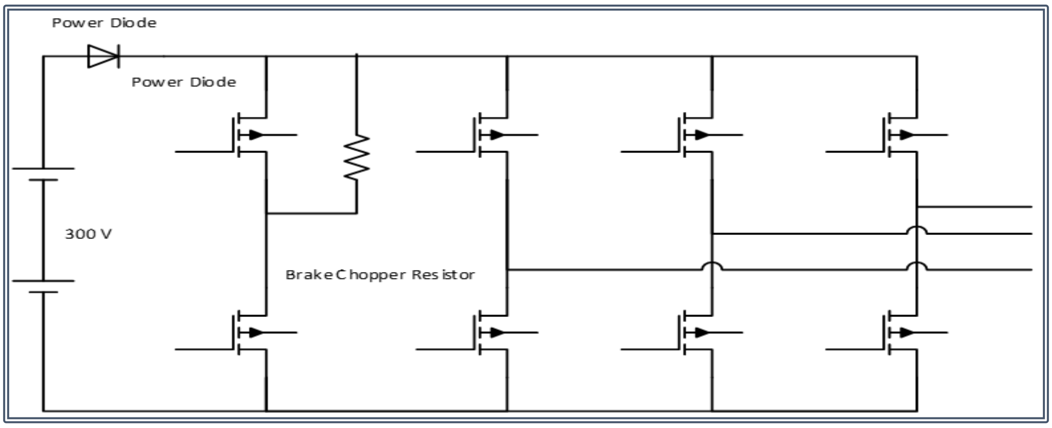


(a)

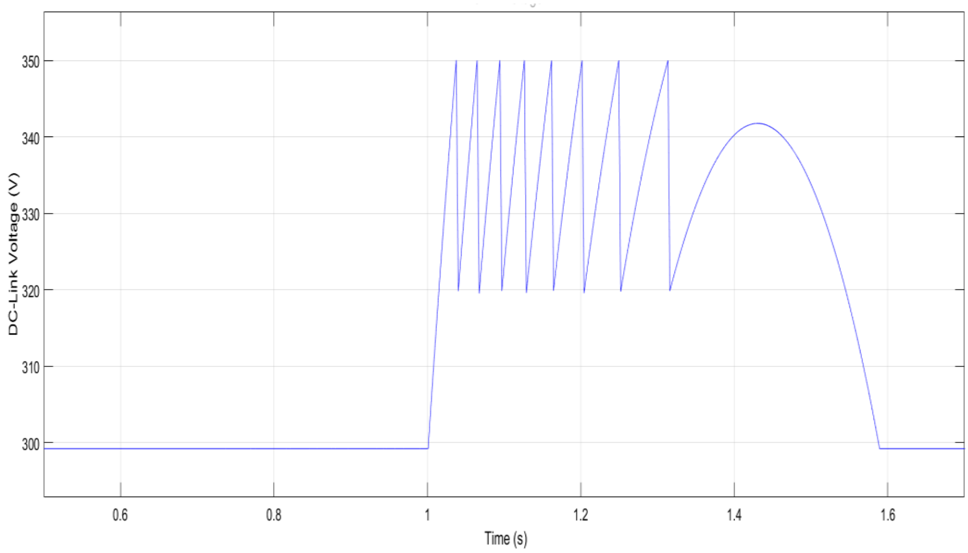


(b)

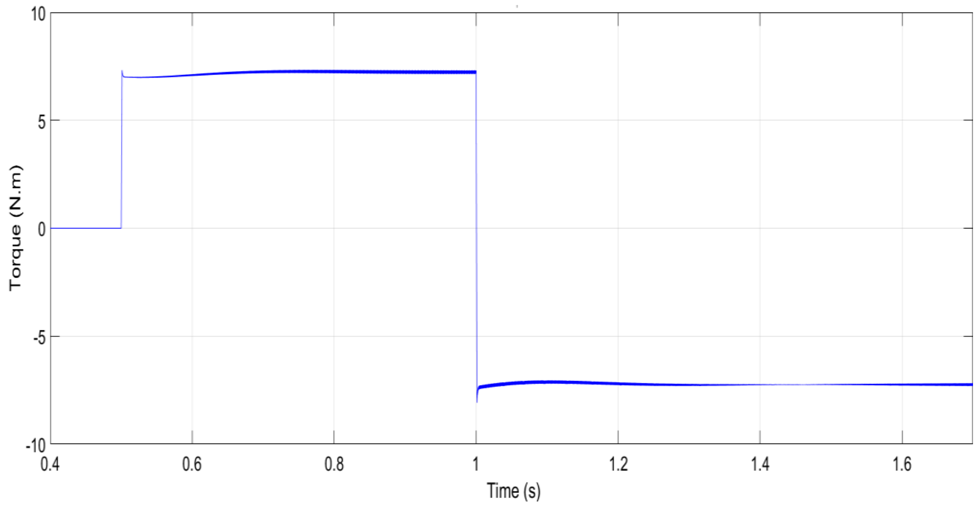


(c)

Fig. C.7 (a) Break chopper configuration (b) DC-Link variation in re-generating mode (c) Generating and re-generating torque of IM

power switch in the fourth leg is always kept off by making the connection between gate and emitter [87]. In regeneration mode, the power can damage the DC power supply. So, making the series connection of DC-power supply and diode protects the power supply. The ADD-A-Pak power standard diode with average forward current of 100A and up to 1600V is selected. As can be seen from the data-sheet of diode, the instantaneous forward voltage is close to 0.8V for 10A, which is the maximum extracted current from the DC supply. So, continuous dissipating power will be 5W, which is not significant and therefore does not need a heatsink. But for safety reasons, a suitable heatsink with thermal resistance of 0.9℃/W is selected to allow the power diode to have an acceptable junction temperature of 37℃. Protecting the IM and power inverter of over current and voltage provides safe conditions to have the position sensor in the control system.

# Appendix D

# Gain Matrix in Extended Kalman-Filter

---

In first step, the EKF is implemented in Matlab simulation in the switching frequency of 20KHz. The reference d-q axis currents (in synchronous frame) are considered as 2.3A and 3.98A respectively. The estimation is validated as the induction machine is rotating with the mechanical speed of 100 rad/sec. The estimated and measured d-q axis of stator flux in stationary frame are demonstrated in Fig. D.1. As shown in Fig. D.1, the estimated d-q axis currents are exactly compliance with the measured values. The estimated d-q axis of rotor flux are also compared with the actual rotor flux which used in making the model of machine (Fig. D.1 (c, d)). As shown in Fig. D.1 (e), the estimated magnetizing inductance is $\frac{1}{4.257} = 0.235$ H. The actual magnetizing inductance is 0.2709. This shows that the error of estimation is lower than 12%. The estimated rotor resistance can be calculated from estimated state $\frac{{L_m}^2}{L_r} r_r$ which has the value of 0.565. So by considering constant leakage rotor inductance ($L_{lr} = 0.0133\ H$) and estimated $L_m$, the value of the estimated rotor resistance is 2.1880Ω. As the simulation is running, the value of the $L_m$in machine modelled changed to the half and the process of the EKF is analysed as shown in Fig. D.2. As the reference current signal are not changed to the new value, so the estimated stator currents sensor do not have any variation in magnitude. As expected from rotor flux equations, the estimated rotor flux drops to half as the magnetizing inductances changed to half. As the value of the magnetizing current is suddenly changed to the half (which is not the case in practical as it changes gradually), the estimated values varied not accurately for few second and then converge to expected levels. As shown in Fig. D.2(f), the estimated magnetizing inductance is $\frac{1}{8.25} = 0.1220$ H. This estimated value is very close to half of the inductance (0.2709/2 H).

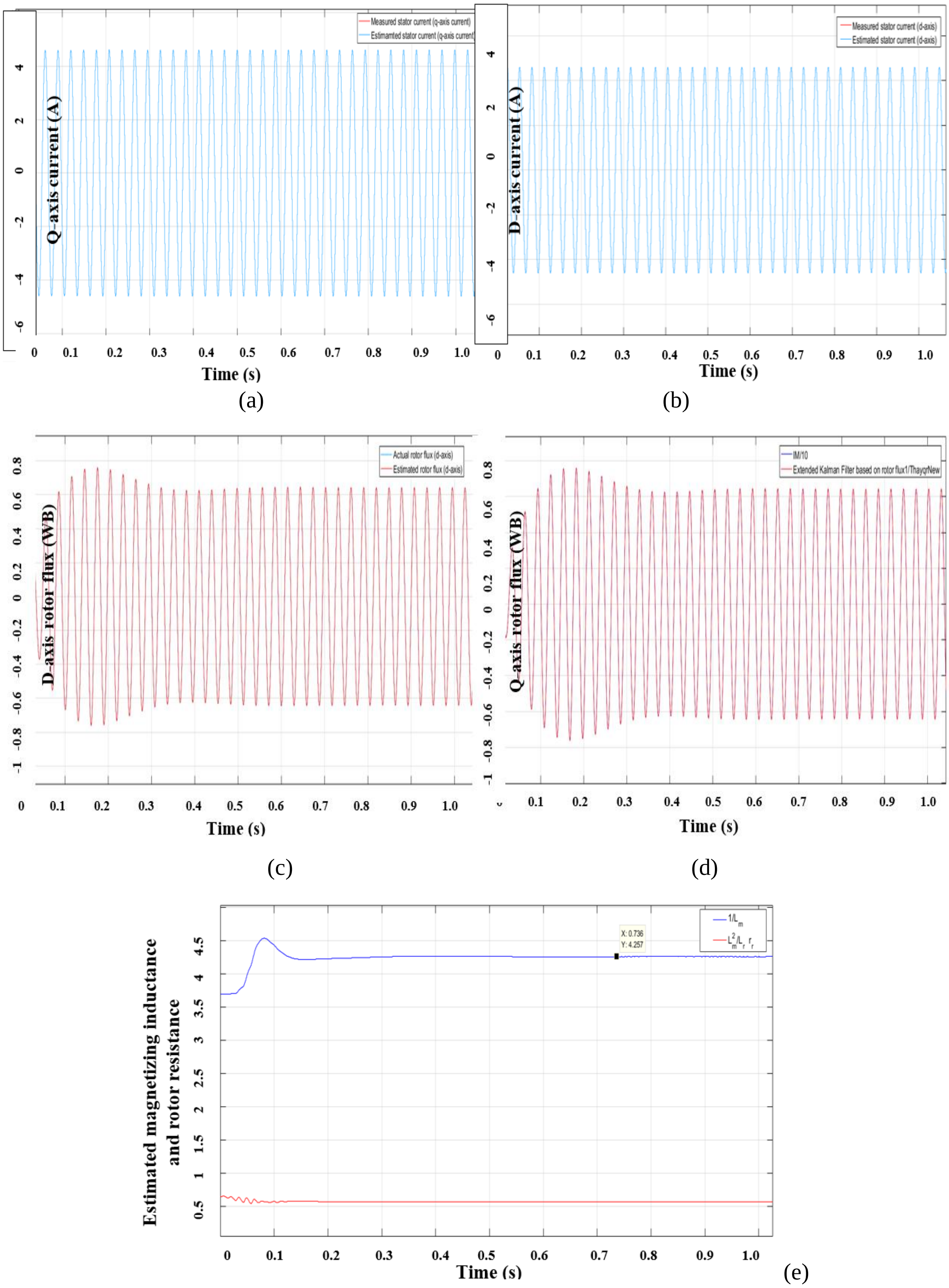


Fig. D. 1Estimated states in stationary frame for applied $i_{ds}^{e*} = 2.3A$ , $i_{qs}^{e*} = 3.98\ A$. (a) q-axis stator current (b) d-axis stator current (c) d-axis rotor flux (d) q-axis rotor flux (e) estimated parameters ($\frac{1}{L_m}$ and $\frac{{L_m}^2}{L_r} r_r$).

Appendix D

To demonstrate the observability of the defined non-liner Jacobian matrix, the conversion of the state error covariance matrix (P) need to be proved. As shown in Fig. D.3, the conversion of each index of matrix demonstrated.

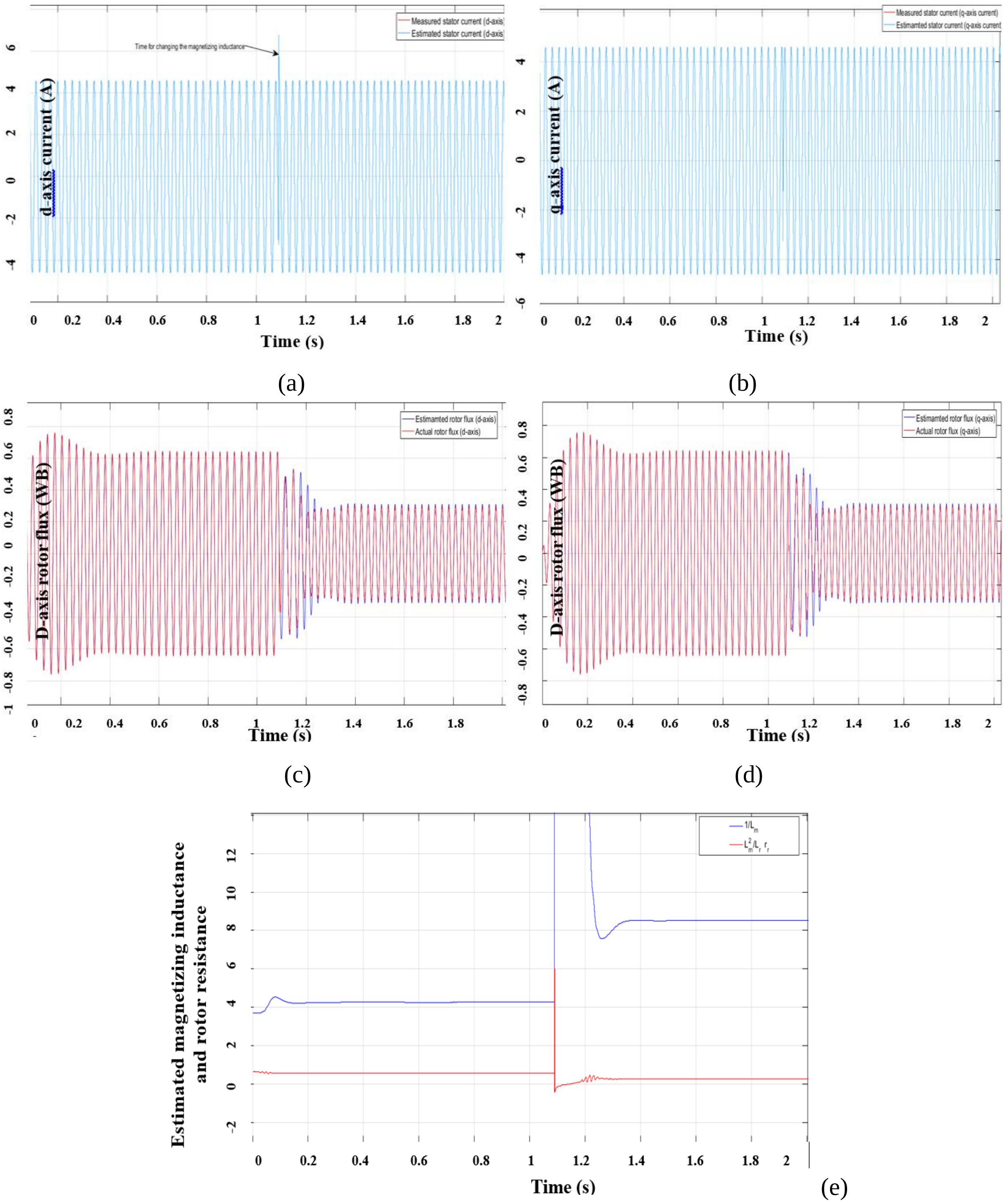


Fig. D.2 Estimated states as magnetizing inductance changed to half (a) q-axis stator current (b) d-axis stator current (c) d-axis rotor flux (d) q-axis rotor flux (e) estimated parameters ($\frac{1}{L_m}$ and $\frac{{L_m}^2}{L_r}r_r$).

As shown in Fig. D.3, the indexes of first forth row of the P matrix oscillate around the zero. P1(1) and P2(2) are the only two index which have the constant level in these matrix rows. These indexes are related to estimated d-q axis stator currents which are the two measurable states in extended Kalman filter. In two last row of P matrix, P5(5) and P6(6) change their value to double and half respectively. This is because of fifth and six state of the z matrix need to be changed to correctly estimate the parameters estimation. The convergence of the index of P matrix is essential for accurate estimation algorithms. If the P matrix diverge, it leads to the estimated states go to infinity and wrong value. To analyze the performance of the gain matrix (K), the first, second and third pairs of matrix row are demonstrated in Fig. D.4.

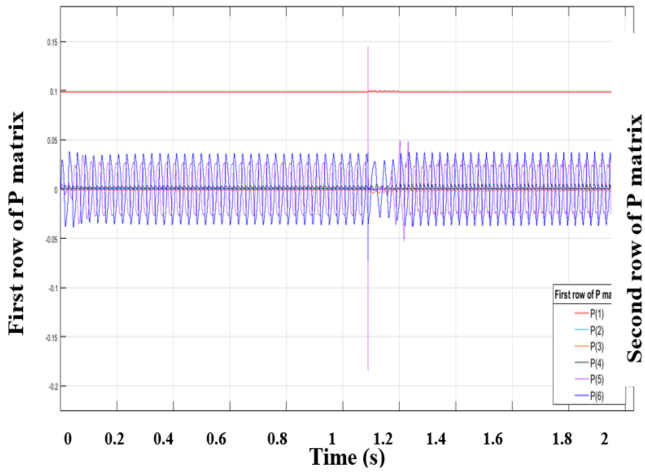


(a)

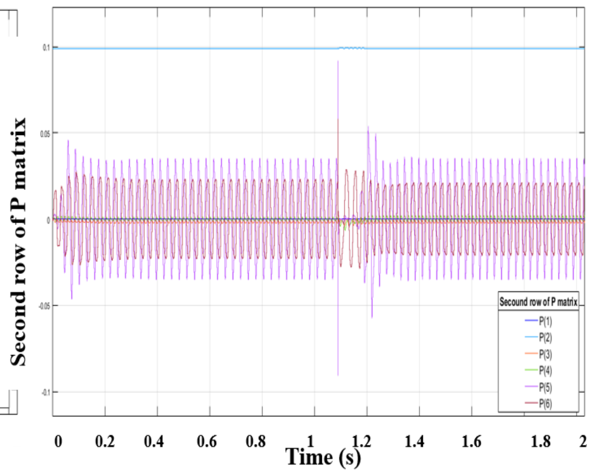


(b)

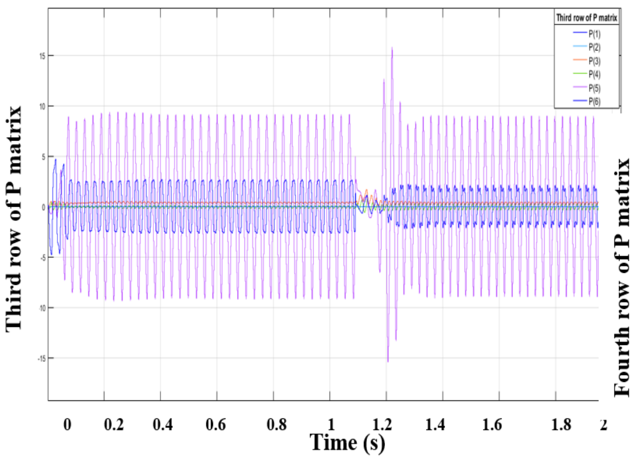


(c)

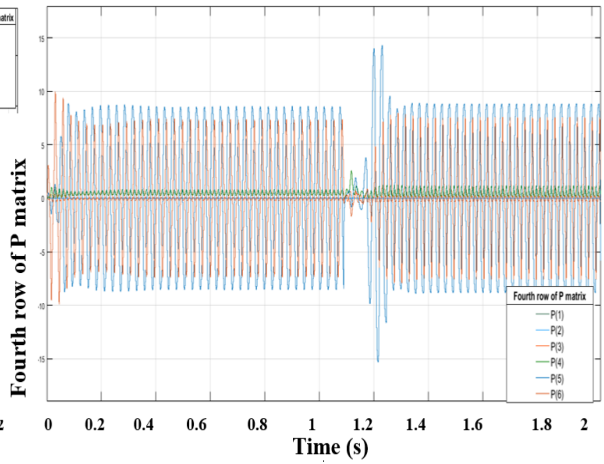


(d)

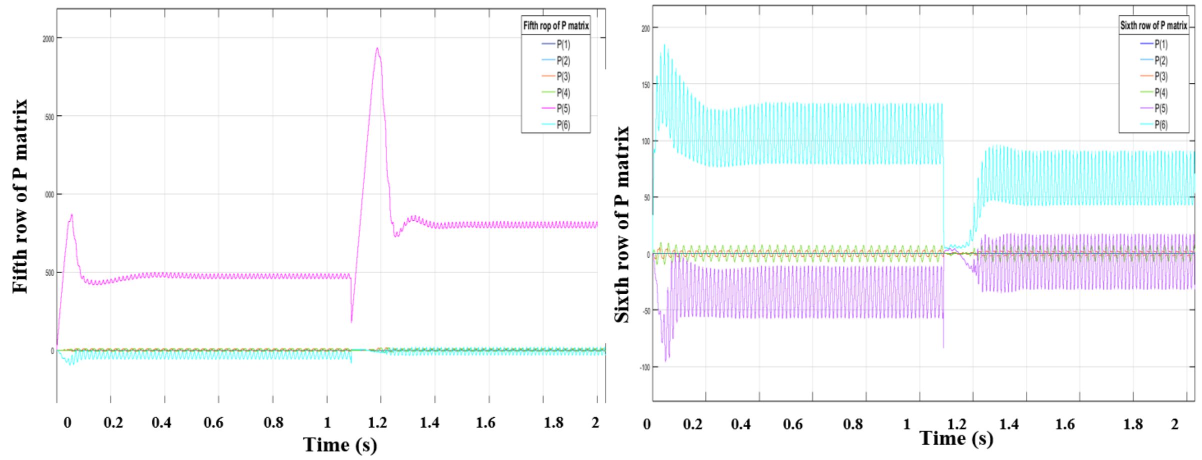


Fig. D. 3 State error covariance matrix (P). (a) First row (b) Second row (c) Third row (d) Fourth row (e) Fifth row (f) Sixth row

By considering the some approximation, K3(1)-K3(2) and K4(2)-K4(1) are the negetive of each other. As can be realized from above figure, the K5(2) and K6(1) are equal and K5(1) should be negative to produce K6(2). So, the Kalmna gain matrix can be provided by:

$$K(k) = \begin{bmatrix} k_{11} & k_{12} \\ k_{11} & k_{12} \\ k_{31} & k_{32} \\ -k_{32} & -k_{31} \\ k_{51} & k_{52} \\ k_{52} & -k_{51} \end{bmatrix} \qquad D.1$$

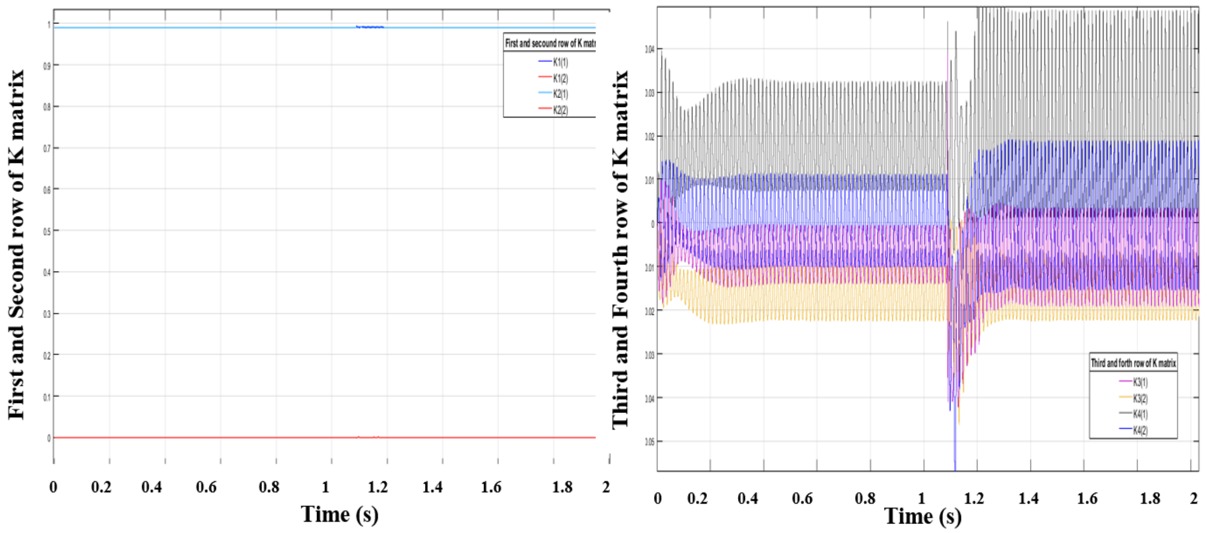


(a) (b)

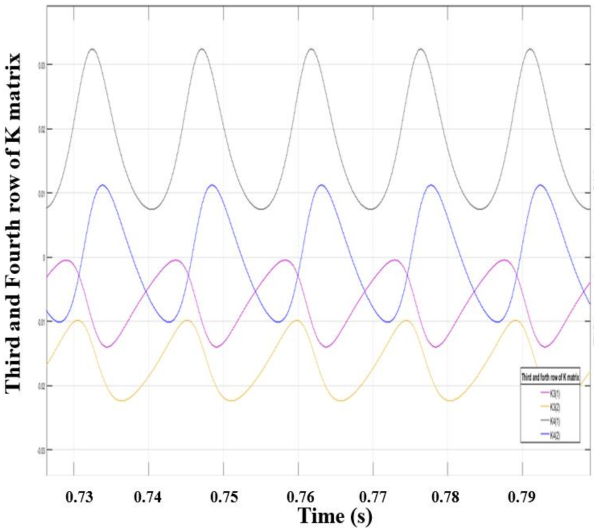


(c)

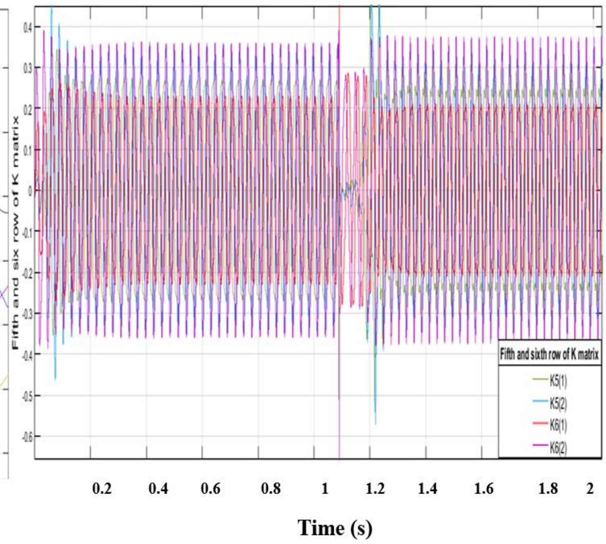


(d)

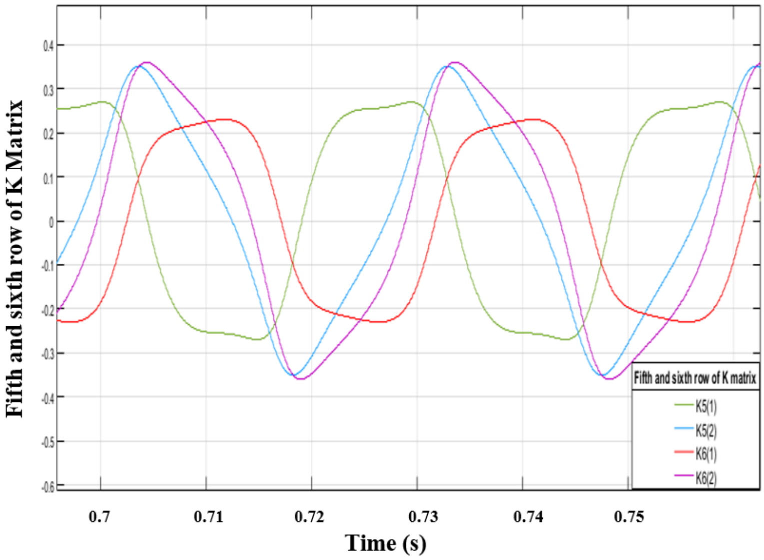


(e)

Fig. D. 4 Gain matrix ((K)) indexes. (a) First and second row (b) Third and fourth row (c) Third and fourth row (d) Fifth and sixth row (e) Fifth and sixth row

# Appendix E

# Root-Locus of Poles and Zeros for Closed Loop Voltage Controller

As described in chapter 6, the Back EMF is the main term of the stator voltage in high speed operation. Therefore, the stator voltage can be rewritten by E.1 where rotor flux is described as a function of $i_{ds}^{e}$:

$$v_{dqs}^{e}(s) = v_{qs}^{e}(s) = w_e \frac{{L_m}^2 i_{ds}^{e}(s)}{L_r\,(1+\tau_r s)} + w_e\,\sigma L_s\, i_{ds}^{e}(s) \qquad \text{E.1}$$

The reference voltage, which is calculated by hexagonal voltage boundary, can also be expressed in terms of the d-q axis currents as follow:

$$V_{S,max} = w_e \frac{L_m\, i_{ds}^{e*}(s)}{L_r\,(1+\tau_r s)} + w_e\,\sigma L_s\, i_{ds}^{e*}(s) \qquad \text{E.2}$$

Therefore, the $i_{ds}^{e*}(s)$ can be derived in the closed loop voltage control method as follow:

$$i_{ds}^{e*}(s) = PI_{input}(k_p + \frac{k_i}{s}) + i_{ds-rated}^{e} \qquad \text{E.3}$$

by substituting E.1 and E.2 in E.3, therefore:

$$i_{ds}^{e*}(s) = \left(w_e\,\frac{1+\sigma\tau_r s}{1+\tau_r s}\right)(i_{ds}^{e*}(s) - i_{ds}^{e}(s))(k_p + \frac{k_i}{s}) + i_{ds-rated}^{e} \qquad \text{E.4}$$

Reducing $i_{ds-rated}^{e}$ form $i_{ds}^{e*}$ and $i_{ds}^{e}$, the closed loop transfer function can be written as follow:

$$\frac{\Delta i_{ds}^{e}(s)}{\Delta i_{ds}^{e}(s)} = \frac{\big(M(s)k_p - 1\big)s + M(s)k_i}{M(s)(k_p s + k_i)} \qquad \text{E. 5}$$

where $M(s) = w_e\, L_s\,\frac{1+\tau_r\sigma s}{1+\tau_r s}$. As shown in Fig. E1, the applied $i_{ds}^{e*}$ keeps the close loop system stable as a result of negative poles in derived closed loop transfer function in E.1. Fig. E1 shows that one of the zeros of E.5 cancel a pole which is close to the zero in real-imaginary axis. This can be achieved by proper selection of $k_i$ which is a low value for the tested induction motor based on E.5. After cancelling one of the pole of E.5, the position of the other zero can be determined by considering the trade-off between the oscillation of $i_{ds}^{e*}$ and acceleration of stator voltage response to $V_{S,max}$. Figure E.1 shows different step respond for the closed loop system when different $k_p$ is considered.

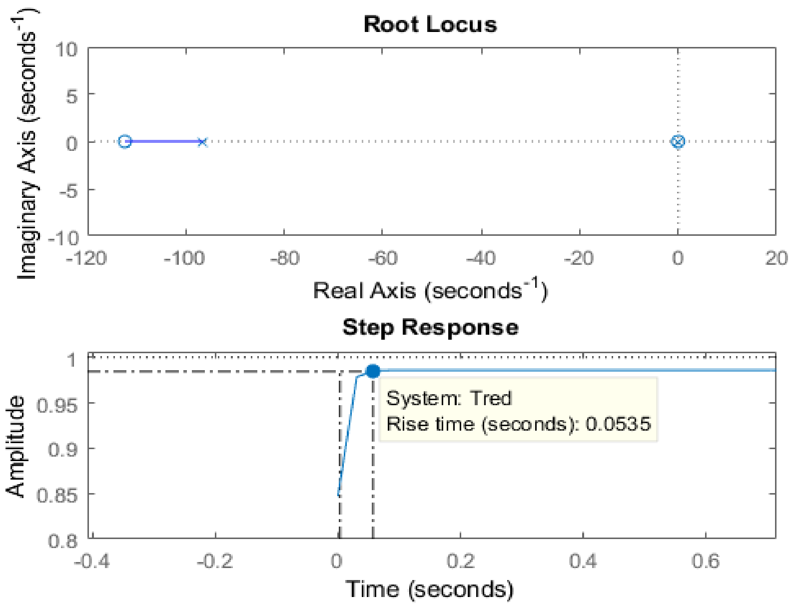


(a)

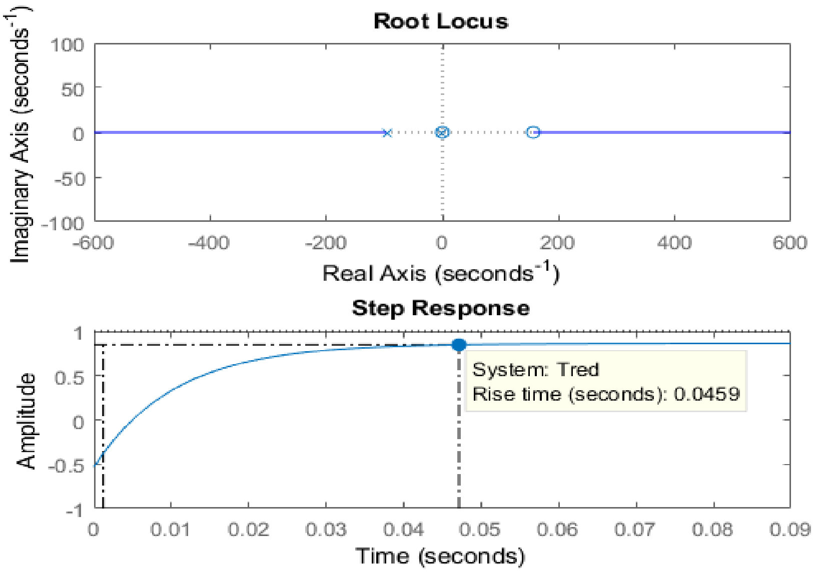


(b)

Fig. E. 1 Root-locus and step response for the closed loop voltage controller with same integral gain and different proportional gain (a) $k_p = 0.8$ and $k_i = 0.006$ (b) $k_p = 0.08$ and $k_i = 0.006$

# Appendix F

# The Algorithm C code for Extended Kalman-Filter and Plant Emulator in Cpu2 of F28377D

---

```
// FILE:   run_cpu02.c//REZA

// AUTHOR: H Gashtil

// PROJECT: \\\\\\\\\\Extended Kalman Filter_Induction Machine_GCB_cpu02

// This code runs on CPU2 and communicates with CPU1 via the IPC

// Also at present, CPU2 communicates with CPU2.CLA using a SW triggered Task


#define PI 3.14159265358979323846264338327950

#define TWOPI (2*PI)

#define TWOPIBY3 (2*PI/3)

#define FOURPIBY3 (4*PI/3)

#define ROOT3 1.7320508                    // Square root of 3


#include "F28x_Project.h"

#include <math.h>


#pragma DATA_SECTION(VT,"Cpu1ToCpu2RAM")//input voltage of svm for EKF

float VT[2]={0,0};

#pragma DATA_SECTION(Currentdq,"Cpu1ToCpu2RAM")// d-q axis of stator current

float Currentdq[2];


// Transferring calculated modulation indexes from Cpu1 to Cpu2

#pragma DATA_SECTION(mT,"Cpu1ToCpu2RAM")
```

Appendix F

```
int16_t mT[4];


#pragma DATA_SECTION(iT,"Cpu2ToCpu1RAM")
int16_t iT[5];
#pragma DATA_SECTION(T,"Cpu2ToCpu1RAM") // Defined for monitoring Torque
float   T=0;  //By reza for monitoring torque


#pragma DATA_SECTION(z,"Cpu2ToCpu1RAM") // Defined for EKF - four motor states and Lm, rr
float   z[6]={0,0,0,0,3.6914,.6473};
#pragma DATA_SECTION(xm,"Cpu2ToCpu1RAM") // for monitoring ids,iqs,idr,iqr
float   xm[5];  //By reza for monitoring torque
#pragma DATA_SECTION(um,"Cpu2ToCpu1RAM") // Defining for monitoring va,vb,vc
#pragma DATA_SECTION(un,"Cpu2ToCpu1RAM") // Defining for monitoring vds,vqs
#pragma DATA_SECTION(xn,"CpuToCla1MsgRAM")
int16_t xn=0;
#pragma DATA_SECTION(yn,"Cla1ToCpuMsgRAM")
int16_t yn=0;
…………………………………………………………………………………………………..
#define Lm (0.2709)
#define Lr (0.2842)
#define Ls (0.2842)
#define O (0.0914060035429) //leankage coefficient:(O=1-((Lm^2)/((Lr)*(Ls))))
#define P (4)  // number of poles
#define rr (2.5067) //rotor resistance
#define rs (2.291) //stator resistance
#define ts (.0001) //switching time for 10 KHz but in simulation for low switching is still kept at 20Khz eventhoght the sampling of zoh is 10KHz
#define wr (2*pi*20)  // electrical speed considered at constant and w slip considered at 0.0433 (for ide and iq=2)
#define a0 (-rs/(O*Ls))
#define a1 (wr*(1-O)/(O))
#define a2 (Lm/(O*Ls*(Lr/rr)))
#define a3 (Lm*wr/(O*Ls))
```

```
#define a4 (1/(O*Ls))

// coefficient for d(ids)/dt equation with variables speed (w) so the speed in above equations removed

#define A0 (-rs/(O*Ls))

#define A1 ((1-O)/(O))// w removed from a1

#define A2 (Lm/(O*Ls*(Lr/rr)))

#define A3 (Lm/(O*Ls))// w removed from a3

#define A4 (1/(O*Ls))



// coefficient for d(iqs)/dt equation

#define b0 -(wr*(1-O)/(O))

#define b1 (-rs/(O*Ls))

#define b2 -(Lm*wr/(O*Ls))

#define b3 (Lm/(O*Ls*(Lr/rr)))

#define b4 (1/(O*Ls))


// coefficient for d(ids)/dt equation with variables speed (w) so the speed in above equations removed

#define B0 -((1-O)/(O)) //b0 whithout w

#define B1 (-rs/(O*Ls))

#define B2 -(Lm/(O*Ls))//b2 without w

#define B3 (Lm/(O*Ls*(Lr/rr)))

#define B4 (1/(O*Ls))


// coefficient for d(idr)/dt equation

#define c0 ((Lm*rs)/(O*Lr*Ls))

#define c1 (-(Lm*wr)/(O*Lr))

#define c2 (-(1)/(O*(Lr/rr)))

#define c3 (-(wr)/(O))

#define c4 (-(Lm)/(O*Lr*Ls))


// coefficient for d(ids)/dt equation with variables speed (w) so the speed in above equations removed
```

Appendix F

```
#define C0 ((Lm*rs)/(O*Lr*Ls))

#define C1 (-(Lm)/(O*Lr))// c1 without w

#define C2 (-(1)/(O*(Lr/rr)))

#define C3 (-(1)/(O))// c3 without w

#define C4 (-(Lm)/(O*Lr*Ls))



// coefficient for d(iqr)/dt equation

#define d0 ((Lm*wr)/(O*Lr))

#define d1 ((Lm*rs)/(O*Lr*Ls))

#define d2 ((wr)/(O))

#define d3 (-(1)/(O*(Lr/rr)))

#define d4 (-(Lm)/(O*Lr*Ls))

// coefficient for d(ids)/dt equation with variables speed (w) so the speed in above equations
removed

#define D0 ((Lm)/(O*Lr))//d0 without

#define D1 ((Lm*rs)/(O*Lr*Ls))

#define D2 ((1)/(O))  //d2 without w

#define D3 (-(1)/(O*(Lr/rr)))

#define D4 (-(Lm)/(O*Lr*Ls))

…………………………………………………………………………….

#define h 100e-6 //changed by reza to 50e-6 from 25e-6 (which was for 2 times rk4 operation in
20Khz).  if one times rk4 is run the h will be double

#define h_div_2 h/2

#define h_div_6 h/6

#if 1

// LA 100-P sensor settings

#define CT_GAIN1    13.65

#define CT_GAIN2    13.65

#define CT_GAIN3    13.65

#define CT_OS1      2207

#define CT_OS2      2206

#define CT_OS3      2195
```

```
#endif
typedef float  vec3[3];           // used with RK4 solver
typedef float  vec4[4];               //Defined for Induction machine states vector(ids,iqd,idr,iqr)
typedef float  vec2[2];              // Defined for Induction machine d-q voltage vector (vds,vqs)
typedef float  vec5[5];
typedef float  vec6[6];
// ISRs
interrupt void ipc1_isr(void);
interrupt void ipc2_isr(void);
__interrupt void Cla1Task1();
__interrupt void Cla1Task2();
__interrupt void Cla1Task3();
__interrupt void Cla1Task4();
__interrupt void Cla1Task5();
__interrupt void Cla1Task6();
__interrupt void Cla1Task7();
__interrupt void Cla1Task8();
…………………………………………………………………………………………….
void Timer1_Init(void);               // Init Timer 1 - to trigger plant emulator ISR
void CLA_configClaMemory(void);
void CLA_initCpu1Cla1(void);
void SetUpLookUpTable(void);           // Set up cos/sin lookup tables
void sf(vec2 u, vec5 x, vec5 f);       // u is vector of vds and vqs, x is state vector, and f is derivative of
state voctor
void rk4(vec2 u, vec5 x);
void EstimationLm(vec2 SVMinV,vec6 EsSt, vec5 IM);
vec5 MotorStates;
__interrupt void cla1Isr1();
__interrupt void cla1Isr2();
__interrupt void cla1Isr3();
__interrupt void cla1Isr4();
__interrupt void cla1Isr5();
__interrupt void cla1Isr6();
```

Appendix F

```
__interrupt void cla1Isr7();
__interrupt void cla1Isr8();


……………………………………………………………………………………….
// Global variables
int temp1=0, temp2=0;
long ISR_count1 = 0;              // useful for timing
char flag;
vec3  um;// used by RK4 solver,  xm used
vec2  un;                         // used for vds and vqs
vec2 VoltageInput;
int angle1;                       // angle used by load model (RK4)
float cos_t[360];
float sin_t[360];
void main(void)
{
   InitSysCtrl();
// Configure CLA memory spaces and CLA task vectors
   CLA_configClaMemory();
   CLA_initCpu1Cla1();
   SetUpLookUpTable();      // set up sine and cosine tables for use within RK4 solver
…………………………………………………………………………………..
   // Initialise RK4 state vector
   xm[0] = 0;
   xm[1] = 0;
   xm[2] = 0;
   xm[3] = 0;
   xm[4] = 50; // Defined to make for states (ids,iqs,idr,iqr)
  //Initialization of z matrix for Lm stimation. Add for extended KAlman filter
   z[0]=0;
   z[1]=0;
   z[2]=0;
```

```
  z[3]=0;
  z[4]=3.6914;
  z[5]=0.6473;
   DINT;
   InitPieCtrl();
   IER = 0x0000;
   IFR = 0x0000;
// Initialize the PIE vector table
   InitPieVectTable();
// Map ISR functions
   EALLOW;
   PieVectTable.IPC1_INT = &ipc1_isr;        // IPC1 interrupt
   PieVectTable.IPC2_INT = &ipc2_isr;        // IPC2 interrupt
   EDIS;
   PieCtrlRegs.PIEIER1.bit.INTx14 = 1;    // Enable IPC1 ISR
// Enable global interrupts and higher priority real-time debug events:
   IER |= M_INT1;                  // Enable PIE group 1 interrupts (ADCs, IPCs)
   //IER |= M_INT3;                    // Enable PIE group 3 interrupts (EPWM1 - EPWM12)
   IER |= M_INT13;                 // Enable CPU interrupt 13 for Timer 1
   EINT;                          // Enable Global interrupt INTM
   ERTM;                          // Enable Global real-time interrupt DBGM
// Let CPU1 know that CPU2 is ready
   IpcRegs.IPCSET.bit.IPC17 = 1;      // Set IPC17 to release CPU1
// L forever
   while(1)
   {
      GpioDataRegs.GPBDAT.bit.GPIO34 = 0;       // Turn on LED D3
      DELAY_US(1000 * 250);                // ON delay
      GpioDataRegs.GPBDAT.bit.GPIO34 = 1;       // Turn off LED D3
      DELAY_US(1000 * 250);                // ON delay
   }
}
```

Appendix F

```
//--------------------------------------------------------------------------------------------------
interrupt void ipc1_isr(void)
{
   float va,vb,vc;    // inverter leg voltages (emulator)
   float vn;          // star-point voltage (emulator)
   float vdc=600;     // inverter dc link voltage (emulator changed by reza from 12 to 48)
   //float ma=0,mb=0,mc=0;
   GpioDataRegs.GPCSET.bit.GPIO67 = 1;        // Set test point high (HSEC-132)
   // Read data from CPU1
   temp1 = (Uint16) IpcRegs.IPCRECVDATA;
   temp2 = (Uint16) IpcRegs.IPCRECVADDR;
   xn = temp1;                           // deposit data in CPU2->CPU2.CLA message RAM
#if 1
………………………………………………………………………………………………………..
   // Execute plant emulator model- Induction Machine
   angle1 = mT[3];
   // Calculate inverter leg voltages
  va = 0.0002*vdc*mT[0];
   vb = 0.0002*vdc*mT[1];
   vc = 0.0002*vdc*mT[2];
   // Calculate star-point voltage
   vn = 0.333333*(va + vb + vc);
   // Calculate motor phase voltages
   um[0] = va - vn;
   um[1] = vb - vn;
   um[2] = vc - vn;
   //defining the vds and vqs from 3 to 2 trasnformation
   un[0]=0.666666*um[0] - 0.333333*um[1] - 0.333333*um[2];//(2/3)*um[0]-(1/3)*um[1]-
(1/3)*um[2];   //vds
   un[1]=0.577350*(um[1] - um[2]); //(1/ROOT3)*(um[1]-um[2]);   //vqs
   // input voltage for EKF are same with input voltage of SVM
```

```
   VoltageInput[0]=(VT[0]*vdc*2)/(5000*3);//(VT[0]*0.08);// (VT[0]*vdc*2)/(5000*3)---vdc=600,
5000 is because of 10KHz switching

   VoltageInput[1]=(VT[1]*vdc*2)/(5000*3);//(VT[1]*0.08);//(VT[1]*vdc*2)/(5000*3)

    MotorStates[0]=Currentdq[0];

    MotorStates[1]=Currentdq[1];

    MotorStates[2]=xm[2];

    MotorStates[3]=xm[3];

    MotorStates[4]=xm[4];//motor speed


       // Execute RK4 ODE solver to calculate motor phase currents

rk4(un,xm);

    EstimationLm(VoltageInput,z,MotorStates); //EstimationLm(VoltageInput,z,xm);/// z is the state
matrix. xm is the measured three phase current. Voltage input is the input voltage of SVM in cla1

        iT[0] = (int16_t) (CT_GAIN1*(xm[0]) + CT_OS1);//(int16_t) (CT_GAIN1*(xm[0]) + CT_OS1);      //
ia , xm[0] is ids which can be considerd as ia from 2 to 3 transformation

        iT[1] = (int16_t) (CT_GAIN2*(-.5*xm[0]+.8660254*xm[1]) + CT_OS2);//(int16_t)
(CT_GAIN2*((-.5*xm[0])+(.5*ROOT3*xm[1])) + CT_OS2);       // ib is -ids+(sqrt(3)/2)*iqs

        iT[2] = (int16_t) (CT_GAIN3*(-.5*xm[0]-.8660254*xm[1]) + CT_OS3); //(int16_t)
(CT_GAIN3*((-.5*xm[0])-(.5*ROOT3*xm[1])) + CT_OS3);       // ic  is -ids-(sqrt(3)/2)*iqs

// torque equation : T=1.5*P/2*Lm*(x[1]*x[2]-x[0]x[3])

        T= .8127*(xm[1]*xm[2]-xm[0]*xm[3]);

    // Limit phase A current measurement to 12-bit ADC range

    if(iT[0] > 4095)

        iT[0] = 4095;

    if(iT[0] < 0)

        iT[0] = 0;

    // Limit phase B current measurement to 12-bit ADC range

    if(iT[1] > 4095)

        iT[1] = 4095;

    if(iT[1] < 0)

        iT[1] = 0;

    // Limit phase C current measurement to 12-bit ADC range

    if(iT[2] > 4095)

        iT[2] = 4095;
```

```
    if(iT[2] < 0)
        iT[2] = 0;


    // The dc link voltage sensor only measures a positive voltage and hence there is no offset
    iT[3] = (int16_t) (9.923*vdc);            // vdc


    // the electrical speed of machine , xm[4] comes from RK4 as the rotor speed and 23.11905 should
be added in cpu1.cla as slip speed
    iT[4] = (int16_t) xm[4]*0.5*P;//*P+23.1195;// the mechanical speed multiplied by P/2 to make
electrical speed
    // calculating


    ISR_count1++;   // not used at present


    //Return from interrupt house keeping
    IpcRegs.IPCACK.bit.IPC1 = 1;              // Clear IPC1 bit
    PieCtrlRegs.PIEACK.all = PIEACK_GROUP1;    // Acknowledge PIE group 1 to enable further
interrupts
    GpioDataRegs.GPCCLEAR.bit.GPIO67 = 1;      // Set test point low (HSEC-132)
}
//-----------------------------------------------------------------------------------------------------
// This ISR is currently not doing anything significant
interrupt void ipc2_isr(void)
{
    //GpioDataRegs.GPCSET.bit.GPIO68 = 1;          // Set test point high (HSEC-133)
    // Read data from CPU1
    temp1 = (Uint16) IpcRegs.IPCRECVDATA;
    temp2 = (Uint16) IpcRegs.IPCRECVADDR;
    IpcRegs.IPCSENDADDR = (Uint16) 8*temp2;



    // Return from interrupt house keeping
    IpcRegs.IPCACK.bit.IPC2 = 1;              // Clear IPC2 bit
```

```
   PieCtrlRegs.PIEACK.all = PIEACK_GROUP1;    // Acknowledge PIE group 1 to enable further
interrupts

   //GpioDataRegs.GPCCLEAR.bit.GPIO68 = 1;    // Set test point low (HSEC-133)

}

//----------------------------------------------------------------------------------------


   MemCfgRegs.MSGxINIT.bit.INIT_CLA1TOCPU = 1;                // Initialise CLA1ToCPUMsgRAM

   while(MemCfgRegs.MSGxINITDONE.bit.INITDONE_CLA1TOCPU != 1) {};  // Wait until done


   MemCfgRegs.MSGxINIT.bit.INIT_CPUTOCLA1 = 1;                // Initialise CPUToCLA1MsgRAM

   while(MemCfgRegs.MSGxINITDONE.bit.INITDONE_CPUTOCLA1 != 1) {};  // Wait until done


   // Set up program and data memory blocks for use by CLA1


   MemCfgRegs.LSxMSEL.bit.MSEL_LS0 = 1;       // Allocate LS0 RAM to CLA1

   MemCfgRegs.LSxCLAPGM.bit.CLAPGM_LS0 = 1;   // Set LS0 as program memory



   MemCfgRegs.LSxMSEL.bit.MSEL_LS1 = 1;       // Allocate LS1 RAM to CLA1

   MemCfgRegs.LSxCLAPGM.bit.CLAPGM_LS1 = 0;   // Set LS1 as data memory


   MemCfgRegs.LSxMSEL.bit.MSEL_LS2 = 1;       // Allocate LS2 RAM to CLA1

   MemCfgRegs.LSxCLAPGM.bit.CLAPGM_LS2 = 0;   // Set LS2 as data memory


   EDIS;

}

//----------------------------------------------------------------------------------------

void CLA_initCpu1Cla1(void)

{

   // Code executed in CLA is in the form of interrupt driven Tasks (max of 8 Tasks).

   // CPU1 must load Task vectors into CLA1 MVECT registers

   // Compute all CLA task vectors

   // On Type-1 CLA the MVECT registers accept full 16-bit task addresses
```

```
EALLOW;
Cla1Regs.MVECT1 = (uint16_t)(&Cla1Task1);
Cla1Regs.MVECT2 = (uint16_t)(&Cla1Task2);
Cla1Regs.MVECT3 = (uint16_t)(&Cla1Task3);
Cla1Regs.MVECT4 = (uint16_t)(&Cla1Task4);
Cla1Regs.MVECT5 = (uint16_t)(&Cla1Task5);
Cla1Regs.MVECT6 = (uint16_t)(&Cla1Task6);
Cla1Regs.MVECT7 = (uint16_t)(&Cla1Task7);
Cla1Regs.MVECT8 = (uint16_t)(&Cla1Task8);

Cla1Regs.MCTL.bit.IACKE = 1;    // Enable IACK instruction to allow CPU1 software triggers of CLA1
Tasks

//Cla1Regs.MIER.all = 0x00FF;   // Enable CLA1 Task1-8 interrupts
Cla1Regs.MIER.all = 0x0081;     // Enable CLA1 Task 1 & Task 8 interrupts

// When a CLA1 Task is complete it can signal this via a CPU1 interrupt.
// Configure vectors for end-of-task interrupt for all 8 tasks
PieVectTable.CLA1_1_INT = &cla1Isr1;
PieVectTable.CLA1_2_INT = &cla1Isr2;
PieVectTable.CLA1_3_INT = &cla1Isr3;
PieVectTable.CLA1_4_INT = &cla1Isr4;
PieVectTable.CLA1_5_INT = &cla1Isr5;
PieVectTable.CLA1_6_INT = &cla1Isr6;
PieVectTable.CLA1_7_INT = &cla1Isr7;
PieVectTable.CLA1_8_INT = &cla1Isr8;

// Set CLA1 task trigger sources
// IMPORTANT: A modification was required in F2837xD_SysCtrl.h to identify "DmaClaSrcSelRegs"
to this source file.
DmaClaSrcSelRegs.CLA1TASKSRCSEL1.bit.TASK1 = 0; // Trigger Task 1 on SW
DmaClaSrcSelRegs.CLA1TASKSRCSEL1.bit.TASK2 = 0; // Trigger Task 2 on SW
DmaClaSrcSelRegs.CLA1TASKSRCSEL1.bit.TASK3 = 0; // Trigger Task 3 on SW
```

```
    DmaClaSrcSelRegs.CLA1TASKSRCSEL1.bit.TASK4 = 0; // Trigger Task 4 on SW
    DmaClaSrcSelRegs.CLA1TASKSRCSEL2.bit.TASK5 = 0; // Trigger Task 5 on SW
    DmaClaSrcSelRegs.CLA1TASKSRCSEL2.bit.TASK6 = 0; // Trigger Task 6 on SW
    DmaClaSrcSelRegs.CLA1TASKSRCSEL2.bit.TASK7 = 0; // Trigger Task 7 on SW
    DmaClaSrcSelRegs.CLA1TASKSRCSEL2.bit.TASK8 = 0; // Trigger Task 8 on SW

    // Enable CLA interrupts at the group and subgroup levels
    PieCtrlRegs.PIEIER11.all = 0xFFFF;          // Enable all 8 task end CPU interrupts
    IER |= (M_INT11);                           // Enable CPU interrupt level 11 (CLA)

    EDIS;
}
//----------------------------------------------------------------------------------------
#if 1
void Timer1_Init()
{
    // Set up CPU Timer 1
    //CpuTimer1Regs.PRD.all  = 0x270F;  // Initialize timer period to 50us
    CpuTimer1Regs.PRD.all  = 0x0FA0;    // Initialize timer period to 20us
    //CpuTimer1Regs.PRD.all  = 0x1F40;  // Initialize timer period to 40us
    //CpuTimer1Regs.PRD.all  = 0x3E80;  // Initialize timer period to 80us
    // Initialize pre-scale counter to divide by 1 (i.e. clocking at SYSCLKOUT)
    // Timing checks with scope confirmed that SYSCLKOUT = 200MHz
    CpuTimer1Regs.TPR.all  = 0;
    CpuTimer1Regs.TPRH.all = 0;

    CpuTimer1Regs.TCR.bit.TIE = 1;  // timer interrupt enabled
    CpuTimer1Regs.TCR.bit.TSS = 0;  // run timer
    CpuTimer1Regs.TCR.all = 0x4000;     //
}
#endif
//----------------------------------------------------------------------------------------
```

Appendix F

```
// Set up cosine and sine lookup tables of 360 elements

// useful for modulation signals and reference frame transformations

void SetUpLookUpTable(void)

{

  Uint16 i;

  float angle;


  for(i=0; i < 360; ++i)

  {

    angle = TWOPI*i/360;

    cos_t[i] = cos(angle);

    sin_t[i] = sin(angle);

  }

}

//------------------------------------------------------------------------------------------

#if 1

void sf(vec2 u, vec5 x, vec5 f)  // x is the 4*1 vector of current states in Induction
machine(ids,iqs,idr,iqr) and f is the derivation of state vector and u is vds and vqs

{

f[0] = A0*x[0]+A1*x[1]*x[4]*0.5*P+a2*x[2]+A3*x[3]*x[4]*0.5*P+A4*u[0]; //the 0.5*P multiplied to
mechanical speed(x[4]) to make the electrical speed which is used in equations

f[1] = B0*x[0]*x[4]*0.5*P+B1*x[1]+B2*x[2]*x[4]*0.5*P+B3*x[3]+B4*u[1];

f[2] = C0*x[0]+C1*x[1]*x[4]*0.5*P+C2*x[2]+C3*x[3]*x[4]*0.5*P+C4*u[0];

f[3] = D0*x[0]*x[4]*0.5*P+D1*x[1]+D2*x[2]*x[4]*0.5*P+D3*x[3]+D4*u[1];

  //T=(1.5*.5*P*(Lm)*(x[1]*x[2]-x[0]*x[3]))//  mechanical torque equation//sw= (1/J)*T-(B/J)*w


f[4]=0;//(.5418*(x[1]*x[2]-x[0]*x[3]));//if J=2.5-->1.5*.5*P*(Lm)/J=.3251-----and if
32.5080=1.5*.5*P*(Lm)/J//if B/J==6.4 when the speed want to keep close to 90---//-6.4*x[4])));//-
0.25*x[4]   B=0;j=.025;// This equations is for B=5e-4 and j= .002which used in matlab simulation
f[4]=(42.5*(x[1]*x[2]-x[0]*x[3]))-0.25*x[4]

//this is for B=20e-4 which causes the maximum mechanical speed of 150 f[4]=(42.5*(x[1]*x[2]-
x[0]*x[3]))-1*x[4]

}

//--------------------------------------------------------------------
```

Appendix F

```
void rk4(vec2 u, vec5 x)     //u vectore consisted of vds and vqs (which are used in sf function) and x vector consisted of ids,iqs,idr,iqr

/* Runga-Kutta 4th Order Solver */

{

   int k;

   vec5    p,m1,m2,m3,m4;

   for (k=0; k<5; ++k)

      p[k] = x[k];

   sf(u,p,m1);


   for (k=0; k<5; ++k)

      p[k] = x[k] + h_div_2*m1[k];

   sf(u,p,m2);


   for (k=0; k<5; ++k)

      p[k] = x[k] + h_div_2*m2[k];

   sf(u,p,m3);


   for (k=0; k<5; ++k)

      p[k] = x[k] + h*m3[k];

   sf(u,p,m4);


   for (k=0; k<5; ++k)

      x[k] += (h_div_6)*(m1[k] + 2*m2[k] + 2*m3[k] + m4[k]);

}
```

……………………………………………………………………………………………………………………

```
void EstimationLm(vec2 SVMinV, vec6 EsSt, vec5 IM)  //states are ids iqs thayqr and thaydr //x is the calculated current signal (we just used x(1) and x(2))

{

static vec6 P1={.001, 0, 0, 0, 0, 0},P2={0, .001, 0, 0, 0, 0},P3={0, 0, .001, 0, 0, 0},P4={0, 0, 0, .001, 0, 0},P5={0, 0, 0, 0, 0, 0},P6={0, 0, 0, 0, 0, 0};

vec6 aa1, aa2,aa3,aa4,aa5,aa6,Q1,Q2,Q3,Q4,Q5,Q6;

vec6   M1,M2,M3,M4,M5,M6,H1,H2,KH1,KH2,KH3,KH4,KH5,KH6;
```

vec6 FP1,FP2,FP3,FP4,FP5,FP6,EsStOLD,KHP1,KHP2,KHP3,KHP4,KHP5,KHP6; // Pvectore // aa1 to aa6 are the row of coefficient matrix of digital state space model of ids,iqs,thaydr,thayqr---Q1 to Q6 coefficient process noise--- M1 to M6 are P*H ---H1 to H2 are y=Hx+v(k)----- KH1 to 6 are the first row to sixth row of the matrix of K*H---FP is the F*P matrix---ab1 to ab6 are matriz used for elements of F' matrix

vec2 K1,K2,K3,K4,K5,K6,G1,G2,G3,G4,G5,G6,Jacob1,Jacob2,Jacob3,Jacob4,R1,R2,Inv1,Inv2,YHz1; //K are the kalman gain--G the coefficinet of Ax+bY which is the b matrix. six 1*2 vectores-- Jacob1 is a1_7F and a1_8F in matlab code--R1 and R2 noise coefficient--R1,R2 are the measured noise as the result of uncertainity of stator current measured---Inv1 to Inv6 are the inverse part of K matrix

```
int L; //for loop

float CI;// for matrix inverse determinal


//a11 to a16 in matlab code

aa1[0]=1+ts*((-rs/(O*Ls))+(((-1+O)/(O*Lm))*EsSt[5]*EsSt[4]));//1+ts*((-rs/(O*Ls))+(((-1+O)/(O))*EsSt[5]*EsSt[4]*EsSt[4])); // in matlab the the array cannot statrt from zero Ex, z(0) does not existence. but in ccs z(0) is not existed. so, all the equistions are changed to one lower. so z(5) in matlab changed to z(4) in ccs

  aa1[1]=0;

  aa1[2]=((Lm)/(O*Ls*Lr))*(EsSt[4]*EsSt[4]*EsSt[5])*ts;

  aa1[3]=2*IM[4]*ts*(((Lm)/(O*Ls*Lr)));//wr changed to 2*IM[4] which is electrical speed

  aa1[4]=0;

  aa1[5]=0;


  //a21 to a26 in matlab code

  aa2[0]=0;

  aa2[1]=1+ts*((-rs/(O*Ls))+(((-1+O)/(O*Lm))*EsSt[5]*EsSt[4]));

  aa2[2]=-2*IM[4]*ts*(((Lm)/(O*Ls*Lr)));//wr changed to 2*IM[4]

  aa2[3]=((Lm)/(O*Ls*Lr))*(EsSt[4]*EsSt[5]*EsSt[4])*ts;

  aa2[4]=0;

  aa2[5]=0;


  //a31 to a36 in matlab code

  aa3[0]=ts*EsSt[5]*EsSt[4];

  aa3[1]=0;

  aa3[2]=1-ts*EsSt[4]*EsSt[5]*EsSt[4];

  aa3[3]=-ts*2*IM[4];//wr changed to 2*IM[4]
```

```
aa3[4]=0;
aa3[5]=0;

//a41 to a46 in matlab code
aa4[0]=0;
aa4[1]=ts*EsSt[5]*EsSt[4];
aa4[2]=ts*2*IM[4];//wr changed to 2*IM[4]
aa4[3]=1-ts*EsSt[4]*EsSt[5]*EsSt[4];
aa4[4]=0;
aa4[5]=0;

//a51 to a56 in matlab code
aa5[0]=0;
aa5[1]=0;
aa5[2]=0;
aa5[3]=0;
aa5[4]=1;
aa5[5]=0;


//a61 to a66 in matlab code
  aa6[0]=0;
  aa6[1]=0;
  aa6[2]=0;
  aa6[3]=0;
  aa6[4]=0;
  aa6[5]=1;

  // G matrix which is same b matrix in Ax+bY
  G1[0]=ts/(O*Ls);
  G1[1]=0;
  G2[0]=0;
```

```
G2[1]=ts/(O*Ls);
G3[0]=0;
G3[1]=0;
G4[0]=0;
G4[1]=0;
G5[0]=0;
G5[1]=0;
G6[0]=0;
G6[1]=0;
//The jacobian matrix values:  a15_F a16_8F...
 // Jacob1[0]=ts*EsSt[0]*(((-1+O)/(O))*EsSt[5]*2*EsSt[4])+ts*EsSt[2]*((Lm)/(O*Ls*Lr))*(EsSt[5]*2*EsSt[4]); //  %d(FF)/dz(5);
 // Jacob1[1]=ts*EsSt[0]*(((-1+O)/(O))*EsSt[4]*EsSt[4])+ts*EsSt[2]*((Lm)/(O*Ls*Lr))*(EsSt[4]*EsSt[4]); //%d(FF)/dz(6);

//  Jacob2[0]=ts*EsSt[1]*(((-1+O)/(O))*EsSt[5]*2*EsSt[4])+ts*EsSt[3]*((Lm)/(O*Ls*Lr))*(EsSt[5]*2*EsSt[4]); //%d(FF)/dz(5);
//  Jacob2[1]=ts*EsSt[1]*(((-1+O)/(O))*EsSt[4]*EsSt[4])+ts*EsSt[3]*((Lm)/(O*Ls*Lr))*(EsSt[4]*EsSt[4]); //%d(FF)/dz(6);

//  Jacob3[0]=-EsSt[2]*ts*EsSt[5]*2*EsSt[4];//%d(FF)/dz(5);
//   Jacob3[1]=EsSt[1]*ts*EsSt[4]-ts*EsSt[4]*EsSt[2]*EsSt[4];//%d(FF)/dz(6);

//   Jacob4[0]=-EsSt[3]*ts*EsSt[5]*2*EsSt[4];//%d(FF)/dz(5);
//   Jacob4[1]=EsSt[1]*ts*EsSt[4]-EsSt[3]*ts*EsSt[4]*EsSt[4];//%d(FF)/dz(6);

  Jacob1[0]=ts*EsSt[0]*(((-1+O)/(O*Lm))*EsSt[5])+ts*EsSt[2]*((Lm)/(O*Ls*Lr))*(EsSt[5]*2*EsSt[4]); //%%  %d(FF)/dEsSt[5];
  Jacob1[1]=ts*EsSt[0]*(((-1+O)/(O*Lm))*EsSt[4])+ts*EsSt[2]*((Lm)/(O*Ls*Lr))*(EsSt[4]*EsSt[4]);// %%%d(FF)/dEsSt[5];

  Jacob2[0]=ts*EsSt[1]*(((-1+O)/(O)*Lm)*EsSt[5])+ts*EsSt[3]*((Lm)/(O*Ls*Lr))*(EsSt[5]*2*EsSt[4]); //%d(FF)/dEsSt[4]
  Jacob2[1]=ts*EsSt[1]*(((-1+O)/(O)*Lm)*EsSt[4])+ts*EsSt[3]*((Lm)/(O*Ls*Lr))*(EsSt[4]*EsSt[4]); //%d(FF)/dEsSt[5]
```

```
Jacob3[0]= EsSt[0]*ts*EsSt[5]-
EsSt[2]*ts*EsSt[5]*2*EsSt[4];//%d(FF)/dEsSt[4];//%%%d(FF)/dEsSt[5];

Jacob3[1]=EsSt[0]*ts*EsSt[4]-ts*EsSt[4]*EsSt[2]*EsSt[4];//%%%d(FF)/


Jacob4[0]=EsSt[1]*ts*EsSt[5]-EsSt[3]*ts*EsSt[5]*2*EsSt[4];//%%%d(FF)/dEsSt[5];

Jacob4[1]=EsSt[1]*ts*EsSt[4]-EsSt[3]*ts*EsSt[4]*EsSt[4];//%%%d(FF)/dEsSt[5];

// Jacob5[0]=0; is aa5[4]

// Jacob5[1]=0;    aa5[5]


//Jacob6[0]=0;

//Jacob6[1]=0;


//definition the measured noise matrix R=2*2 and process noise coefficient Q=6*6


R1[0]=.1;

R1[1]=0;

R2[0]=0;

R2[1]=.1;


Q1[0]=10;

Q1[1]=0;

Q1[2]=0;

Q1[3]=0;

Q1[4]=0;

Q1[5]=0;


Q2[0]=0;

Q2[1]=10;

Q2[2]=0;

Q2[3]=0;

Q2[4]=0;

Q2[5]=0;
```

```
Q3[0]=0;
Q3[1]=0;
Q3[2]=0;
Q3[3]=0;
Q3[4]=0;
Q3[5]=0;

Q4[0]=0;
Q4[1]=0;
Q4[2]=0;
Q4[3]=0;
Q4[4]=0;
Q4[5]=0;

Q5[0]=0;
Q5[1]=0;
Q5[2]=0;
Q5[3]=0;
Q5[4]=1;
Q5[5]=0;

Q6[0]=0;
Q6[1]=0;
Q6[2]=0;
Q6[3]=0;
Q6[4]=0;
Q6[5]=1;

//state pridection equations
EsStOLD[0]=EsSt[0];
EsStOLD[1]=EsSt[1];
```

```
            EsStOLD[2]=EsSt[2];
            EsStOLD[3]=EsSt[3];
            EsStOLD[4]=EsSt[4];
            EsStOLD[5]=EsSt[5];

EsSt[0]=aa1[0]*EsStOLD[0]+aa1[1]*EsStOLD[1]+aa1[2]*EsStOLD[2]+aa1[3]*EsStOLD[3]+aa1[4]*EsStO
LD[4]+aa1[5]*EsStOLD[5]+(G1[0]*SVMinV[0]+G1[1]*SVMinV[1]);

EsSt[1]=aa2[0]*EsStOLD[0]+aa2[1]*EsStOLD[1]+aa2[2]*EsStOLD[2]+aa2[3]*EsStOLD[3]+aa2[4]*EsStO
LD[4]+aa2[5]*EsStOLD[5]+(G2[0]*SVMinV[0]+G2[1]*SVMinV[1]);

EsSt[2]=aa3[0]*EsStOLD[0]+aa3[1]*EsStOLD[1]+aa3[2]*EsStOLD[2]+aa3[3]*EsStOLD[3]+aa3[4]*EsStO
LD[4]+aa3[5]*EsStOLD[5]+(G3[0]*SVMinV[0]+G3[1]*SVMinV[1]);

EsSt[3]=aa4[0]*EsStOLD[0]+aa4[1]*EsStOLD[1]+aa4[2]*EsStOLD[2]+aa4[3]*EsStOLD[3]+aa4[4]*EsStO
LD[4]+aa4[5]*EsStOLD[5]+(G4[0]*SVMinV[0]+G4[1]*SVMinV[1]);

EsSt[4]=aa5[0]*EsStOLD[0]+aa5[1]*EsStOLD[1]+aa5[2]*EsStOLD[2]+aa5[3]*EsStOLD[3]+aa5[4]*EsStO
LD[4]+aa5[5]*EsStOLD[5]+(G5[0]*SVMinV[0]+G5[1]*SVMinV[1]);

EsSt[5]=aa6[0]*EsStOLD[0]+aa6[1]*EsStOLD[1]+aa6[2]*EsStOLD[2]+aa6[3]*EsStOLD[3]+aa6[4]*EsStO
LD[4]+aa6[5]*EsStOLD[5]+(G6[0]*SVMinV[0]+G6[1]*SVMinV[1]);


                // for calculating P1 faster. Firstly the F*P is calculated as FP
                for (L=0; L<6; ++L)

FP1[L]=aa1[0]*P1[L]+aa1[1]*P2[L]+aa1[2]*P3[L]+aa1[3]*P4[L]+Jacob1[0]*P5[L]+Jacob1[1]*P6[L];
                for (L=0; L<6; ++L)

FP2[L]=aa2[0]*P1[L]+aa2[1]*P2[L]+aa2[2]*P3[L]+aa2[3]*P4[L]+Jacob2[0]*P5[L]+Jacob2[1]*P6[L];
                for (L=0; L<6; ++L)

FP3[L]=aa3[0]*P1[L]+aa3[1]*P2[L]+aa3[2]*P3[L]+aa3[3]*P4[L]+Jacob3[0]*P5[L]+Jacob3[1]*P6[L];
                for (L=0; L<6; ++L)

FP4[L]=aa4[0]*P1[L]+aa4[1]*P2[L]+aa4[2]*P3[L]+aa4[3]*P4[L]+Jacob4[0]*P5[L]+Jacob4[1]*P6[L];
                for (L=0; L<6; ++L)

FP5[L]=aa5[0]*P1[L]+aa5[1]*P2[L]+aa5[2]*P3[L]+aa5[3]*P4[L]+aa5[4]*P5[L]+aa5[5]*P6[L];
```

Appendix F

```
            for (L=0; L<6; ++L)

FP6[L]=aa6[0]*P1[L]+aa6[1]*P2[L]+aa6[2]*P3[L]+aa6[3]*P4[L]+aa6[4]*P5[L]+aa6[5]*P6[L];

// P=FP*F'+Q   ---- The first row of the matrix in below matrix the Q is applied directly

P1[0]=FP1[0]*aa1[0]+FP1[1]*aa1[1]+FP1[2]*aa1[2]+FP1[3]*aa1[3]+FP1[4]*Jacob1[0]+FP1[5]*Jacob1
[1]+Q1[0];

P1[1]=FP1[0]*aa2[0]+FP1[1]*aa2[1]+FP1[2]*aa2[2]+FP1[3]*aa2[3]+FP1[4]*Jacob2[0]+FP1[5]*Jacob2
[1]+Q1[1];

P1[2]=FP1[0]*aa3[0]+FP1[1]*aa3[1]+FP1[2]*aa3[2]+FP1[3]*aa3[3]+FP1[4]*Jacob3[0]+FP1[5]*Jacob3
[1]+Q1[2];

P1[3]=FP1[0]*aa4[0]+FP1[1]*aa4[1]+FP1[2]*aa4[2]+FP1[3]*aa4[3]+FP1[4]*Jacob4[0]+FP1[5]*Jacob4
[1]+Q1[3];

P1[4]=FP1[0]*aa5[0]+FP1[1]*aa5[1]+FP1[2]*aa5[2]+FP1[3]*aa5[3]+FP1[4]*aa5[4]+FP1[5]*aa5[5]+Q1
[4];

P1[5]=FP1[0]*aa6[0]+FP1[1]*aa6[1]+FP1[2]*aa6[2]+FP1[3]*aa6[3]+FP1[4]*aa6[4]+FP1[5]*aa6[5]+Q1
[5];

           //The secound Row

P2[0]=FP2[0]*aa1[0]+FP2[1]*aa1[1]+FP2[2]*aa1[2]+FP2[3]*aa1[3]+FP2[4]*Jacob1[0]+FP2[5]*Jacob1
[1]+Q2[0];

P2[1]=FP2[0]*aa2[0]+FP2[1]*aa2[1]+FP2[2]*aa2[2]+FP2[3]*aa2[3]+FP2[4]*Jacob2[0]+FP2[5]*Jacob2
[1]+Q2[1];

P2[2]=FP2[0]*aa3[0]+FP2[1]*aa3[1]+FP2[2]*aa3[2]+FP2[3]*aa3[3]+FP2[4]*Jacob3[0]+FP2[5]*Jacob3
[1]+Q2[2];

P2[3]=FP2[0]*aa4[0]+FP2[1]*aa4[1]+FP2[2]*aa4[2]+FP2[3]*aa4[3]+FP2[4]*Jacob4[0]+FP2[5]*Jacob4
[1]+Q2[3];

P2[4]=FP2[0]*aa5[0]+FP2[1]*aa5[1]+FP2[2]*aa5[2]+FP2[3]*aa5[3]+FP2[4]*aa5[4]+FP2[5]*aa5[5]+Q2
[4];
```

P2[5]=FP2[0]*aa6[0]+FP2[1]*aa6[1]+FP2[2]*aa6[2]+FP2[3]*aa6[3]+FP2[4]*aa6[4]+FP2[5]*aa6[5]+Q2[5];

//The Third Row

P3[0]=FP3[0]*aa1[0]+FP3[1]*aa1[1]+FP3[2]*aa1[2]+FP3[3]*aa1[3]+FP3[4]*Jacob1[0]+FP3[5]*Jacob1[1]+Q3[0];

P3[1]=FP3[0]*aa2[0]+FP3[1]*aa2[1]+FP3[2]*aa2[2]+FP3[3]*aa2[3]+FP3[4]*Jacob2[0]+FP3[5]*Jacob2[1]+Q3[1];

P3[2]=FP3[0]*aa3[0]+FP3[1]*aa3[1]+FP3[2]*aa3[2]+FP3[3]*aa3[3]+FP3[4]*Jacob3[0]+FP3[5]*Jacob3[1]+Q3[2];

P3[3]=FP3[0]*aa4[0]+FP3[1]*aa4[1]+FP3[2]*aa4[2]+FP3[3]*aa4[3]+FP3[4]*Jacob4[0]+FP3[5]*Jacob4[1]+Q3[3];

P3[4]=FP3[0]*aa5[0]+FP3[1]*aa5[1]+FP3[2]*aa5[2]+FP3[3]*aa5[3]+FP3[4]*aa5[4]+FP3[5]*aa5[5]+Q3[4];

P3[5]=FP3[0]*aa6[0]+FP3[1]*aa6[1]+FP3[2]*aa6[2]+FP3[3]*aa6[3]+FP3[4]*aa6[4]+FP3[5]*aa6[5]+Q3[5];

//The Forth Row

P4[0]=FP4[0]*aa1[0]+FP4[1]*aa1[1]+FP4[2]*aa1[2]+FP4[3]*aa1[3]+FP4[4]*Jacob1[0]+FP4[5]*Jacob1[1]+Q4[0];

P4[1]=FP4[0]*aa2[0]+FP4[1]*aa2[1]+FP4[2]*aa2[2]+FP4[3]*aa2[3]+FP4[4]*Jacob2[0]+FP4[5]*Jacob2[1]+Q4[1];

P4[2]=FP4[0]*aa3[0]+FP4[1]*aa3[1]+FP4[2]*aa3[2]+FP4[3]*aa3[3]+FP4[4]*Jacob3[0]+FP4[5]*Jacob3[1]+Q4[2];

P4[3]=FP4[0]*aa4[0]+FP4[1]*aa4[1]+FP4[2]*aa4[2]+FP4[3]*aa4[3]+FP4[4]*Jacob4[0]+FP4[5]*Jacob4[1]+Q4[3];

P4[4]=FP4[0]*aa5[0]+FP4[1]*aa5[1]+FP4[2]*aa5[2]+FP4[3]*aa5[3]+FP4[4]*aa5[4]+FP4[5]*aa5[5]+Q4[4];

P4[5]=FP4[0]*aa6[0]+FP4[1]*aa6[1]+FP4[2]*aa6[2]+FP4[3]*aa6[3]+FP4[4]*aa6[4]+FP4[5]*aa6[5]+Q4[5];

```
//The fifth Row

P5[0]=FP5[0]*aa1[0]+FP5[1]*aa1[1]+FP5[2]*aa1[2]+FP5[3]*aa1[3]+FP5[4]*Jacob1[0]+FP5[5]*Jacob1
[1]+Q5[0];

P5[1]=FP5[0]*aa2[0]+FP5[1]*aa2[1]+FP5[2]*aa2[2]+FP5[3]*aa2[3]+FP5[4]*Jacob2[0]+FP5[5]*Jacob2
[1]+Q5[1];

P5[2]=FP5[0]*aa3[0]+FP5[1]*aa3[1]+FP5[2]*aa3[2]+FP5[3]*aa3[3]+FP5[4]*Jacob3[0]+FP5[5]*Jacob3
[1]+Q5[2];

P5[3]=FP5[0]*aa4[0]+FP5[1]*aa4[1]+FP5[2]*aa4[2]+FP5[3]*aa4[3]+FP5[4]*Jacob4[0]+FP5[5]*Jacob4
[1]+Q5[3];

P5[4]=FP5[0]*aa5[0]+FP5[1]*aa5[1]+FP5[2]*aa5[2]+FP5[3]*aa5[3]+FP5[4]*aa5[4]+FP5[5]*aa5[5]+Q5
[4];

P5[5]=FP5[0]*aa6[0]+FP5[1]*aa6[1]+FP5[2]*aa6[2]+FP5[3]*aa6[3]+FP5[4]*aa6[4]+FP5[5]*aa6[5]+Q5
[5];

//The sixth Row

P6[0]=FP6[0]*aa1[0]+FP6[1]*aa1[1]+FP6[2]*aa1[2]+FP6[3]*aa1[3]+FP6[4]*Jacob1[0]+FP6[5]*Jacob1
[1]+Q6[0];

P6[1]=FP6[0]*aa2[0]+FP6[1]*aa2[1]+FP6[2]*aa2[2]+FP6[3]*aa2[3]+FP6[4]*Jacob2[0]+FP6[5]*Jacob2
[1]+Q6[1];

P6[2]=FP6[0]*aa3[0]+FP6[1]*aa3[1]+FP6[2]*aa3[2]+FP6[3]*aa3[3]+FP6[4]*Jacob3[0]+FP6[5]*Jacob3
[1]+Q6[2];

P6[3]=FP6[0]*aa4[0]+FP6[1]*aa4[1]+FP6[2]*aa4[2]+FP6[3]*aa4[3]+FP6[4]*Jacob4[0]+FP6[5]*Jacob4
[1]+Q6[3];

P6[4]=FP6[0]*aa5[0]+FP6[1]*aa5[1]+FP6[2]*aa5[2]+FP6[3]*aa5[3]+FP6[4]*aa5[4]+FP6[5]*aa5[5]+Q6
[4];

P6[5]=FP6[0]*aa6[0]+FP6[1]*aa6[1]+FP6[2]*aa6[2]+FP6[3]*aa6[3]+FP6[4]*aa6[4]+FP6[5]*aa6[5]+Q6
[5];


//state correction equations

H1[0]=1;// Y=Hx+v
```

```
        H1[1]=0;
        H1[2]=0;
        H1[3]=0;
        H1[4]=0;
        H1[5]=0;
        H2[0]=0;
        H2[1]=1;
        H2[2]=0;
        H2[3]=0;
        H2[4]=0;
        H2[5]=0;
    // The M matrix is P*H'

        M1[0]=P1[0]*H1[0]+P1[1]*H1[1]+P1[2]*H1[2]+P1[3]*H1[3]+P1[4]*H1[4]+P1[5]*H1[5];// Kalman gain 6*2
        M1[1]=P1[0]*H2[0]+P1[1]*H2[1]+P1[2]*H2[2]+P1[3]*H2[3]+P1[4]*H2[4]+P1[5]*H2[5];

        M2[0]=P2[0]*H1[0]+P2[1]*H1[1]+P2[2]*H1[2]+P2[3]*H1[3]+P2[4]*H1[4]+P2[5]*H1[5];
        M2[1]=P2[0]*H2[0]+P2[1]*H2[1]+P2[2]*H2[2]+P2[3]*H2[3]+P2[4]*H2[4]+P2[5]*H2[5];

        M3[0]=P3[0]*H1[0]+P3[1]*H1[1]+P3[2]*H1[2]+P3[3]*H1[3]+P3[4]*H1[4]+P3[5]*H1[5];
        M3[1]=P3[0]*H2[0]+P3[1]*H2[1]+P3[2]*H2[2]+P3[3]*H2[3]+P3[4]*H2[4]+P3[5]*H2[5];

        M4[0]=P4[0]*H1[0]+P4[1]*H1[1]+P4[2]*H1[2]+P4[3]*H1[3]+P4[4]*H1[4]+P4[5]*H1[5];
        M4[1]=P4[0]*H2[0]+P4[1]*H2[1]+P4[2]*H2[2]+P4[3]*H2[3]+P4[4]*H2[4]+P4[5]*H2[5];

        M5[0]=P5[0]*H1[0]+P5[1]*H1[1]+P5[2]*H1[2]+P5[3]*H1[3]+P5[4]*H1[4]+P5[5]*H1[5];
        M5[1]=P5[0]*H2[0]+P5[1]*H2[1]+P5[2]*H2[2]+P5[3]*H2[3]+P5[4]*H2[4]+P5[5]*H2[5];

        M6[0]=P6[0]*H1[0]+P6[1]*H1[1]+P6[2]*H1[2]+P6[3]*H1[3]+P6[4]*H1[4]+P6[5]*H1[5];
        M6[1]=P6[0]*H2[0]+P6[1]*H2[1]+P6[2]*H2[2]+P6[3]*H2[3]+P6[4]*H2[4]+P6[5]*H2[5];
```

```
//R 2*2 measured noise coefficient
// R1[0]=0.01;
// R1[1]=0;
// R2[0]=0;
//R2[1]=0.01;

// Calculation of inverse matrix determinal

CI=(1/((H2[0]*M1[1]+H2[1]*M2[1]+H2[2]*M3[1]+H2[3]*M4[1]+H2[4]*M5[1]+H2[5]*M6[1]+R2[1])*(H1[0]*M1[0]+H1[1]*M2[0]+H1[2]*M3[0]+H1[3]*M4[0]+H1[4]*M5[0]+H1[5]*M6[0]+R1[0])-(((H1[0]*M1[1]+H1[1]*M2[1]+H1[2]*M3[1]+H1[3]*M4[1]+H1[4]*M5[1]+H1[5]*M6[1]+R1[1]))*((H2[0]*M1[0]+H2[1]*M2[0]+H2[2]*M3[0]+H2[3]*M4[0]+H2[4]*M5[0]+H2[5]*M6[0]+R2[0])))));

//inv(H*M+R)= 2*2 matrix

Inv1[0]=CI*(H2[0]*M1[1]+H2[1]*M2[1]+H2[2]*M3[1]+H2[3]*M4[1]+H2[4]*M5[1]+H2[5]*M6[1]+R2[1]);
Inv1[1]=-CI*(H1[0]*M1[1]+H1[1]*M2[1]+H1[2]*M3[1]+H1[3]*M4[1]+H1[4]*M5[1]+H1[5]*M6[1]+R1[1]);
Inv2[0]=-CI*(H2[0]*M1[0]+H2[1]*M2[0]+H2[2]*M3[0]+H2[3]*M4[0]+H2[4]*M5[0]+H2[5]*M6[0]+R2[0]);

Inv2[1]=CI*(H1[0]*M1[0]+H1[1]*M2[0]+H1[2]*M3[0]+H1[3]*M4[0]+H1[4]*M5[0]+H1[5]*M6[0]+R1[0]);

// Kalman gain M*Inv = 6*2 matrix

K1[0]=M1[0]*Inv1[0]+M1[1]*Inv2[0];
K1[1]=M1[0]*Inv1[1]+M1[1]*Inv2[1];

K2[0]=M2[0]*Inv1[0]+M2[1]*Inv2[0];
K2[1]=M2[0]*Inv1[1]+M2[1]*Inv2[1];

K3[0]=M3[0]*Inv1[0]+M3[1]*Inv2[0];
K3[1]=M3[0]*Inv1[1]+M3[1]*Inv2[1];
```

```
K4[0]=M4[0]*Inv1[0]+M4[1]*Inv2[0];
K4[1]=M4[0]*Inv1[1]+M4[1]*Inv2[1];

K5[0]=M5[0]*Inv1[0]+M5[1]*Inv2[0];
K5[1]=M5[0]*Inv1[1]+M5[1]*Inv2[1];

K6[0]=M6[0]*Inv1[0]+M6[1]*Inv2[0];
K6[1]=M6[0]*Inv1[1]+M6[1]*Inv2[1];

//state correction
//firstly ym-Hz is calculated
YHz1[0] =
(H1[0]*EsSt[0]+H1[1]*EsSt[1]+H1[2]*EsSt[2]+H1[3]*EsSt[3]+H1[4]*EsSt[4]+H1[5]*EsSt[5]);
YHz1[1] =
(H2[0]*EsSt[0]+H2[1]*EsSt[1]+H2[2]*EsSt[2]+H2[3]*EsSt[3]+H2[4]*EsSt[4]+H2[5]*EsSt[5]);


EsSt[0]=EsSt[0]+(((K1[0])*(IM[0]-YHz1[0])) +  ((K1[1])*(IM[1]-YHz1[1])));
EsSt[1]=EsSt[1]+(((K2[0])*(IM[0]-YHz1[0])) +  ((K2[1])*(IM[1]-YHz1[1])));
EsSt[2]=EsSt[2]+(((K3[0])*(IM[0]-YHz1[0])) +  ((K3[1])*(IM[1]-YHz1[1])));
EsSt[3]=EsSt[3]+(((K4[0])*(IM[0]-YHz1[0])) +  ((K4[1])*(IM[1]-YHz1[1])));
EsSt[4]=EsSt[4]+(((K5[0])*(IM[0]-YHz1[0])) +  ((K5[1])*(IM[1]-YHz1[1])));
EsSt[5]=EsSt[5]+(((K6[0])*(IM[0]-YHz1[0])) +  ((K6[1])*(IM[1]-YHz1[1])));


// KH=K*H which is 6*6 matrix
    //first row
    for (L=0; L<6; ++L)
     KH1[L]=K1[0]*H1[L]+K1[1]*H2[L];

    //secound row:
    for (L=0; L<6; ++L)
```

```
 KH2[L]=K2[0]*H1[L]+K2[1]*H2[L];

//third row:
for (L=0; L<6; ++L)
 KH3[L]=K3[0]*H1[L]+K3[1]*H2[L];

//fourth row:
for (L=0; L<6; ++L)
  KH4[L]=K4[0]*H1[L]+K4[1]*H2[L];

//fifth row:
for (L=0; L<6; ++L)
KH5[L]=K5[0]*H1[L]+K5[1]*H2[L];

//sixth row:
for (L=0; L<6; ++L)
KH6[L]=K6[0]*H1[L]+K6[1]*H2[L];

// State error covarience correction matrix:
//first row
for (L=0; L<6; ++L)
KHP1[L]=(KH1[0]*P1[L]+KH1[1]*P2[L]+KH1[2]*P3[L]+KH1[3]*P4[L]+KH1[4]*P5[L]+KH1[5]*P6[L]);
for (L=0; L<6; ++L)
KHP2[L]=(KH2[0]*P1[L]+KH2[1]*P2[L]+KH2[2]*P3[L]+KH2[3]*P4[L]+KH2[4]*P5[L]+KH2[5]*P6[L]);
for (L=0; L<6; ++L)
KHP3[L]=(KH3[0]*P1[L]+KH3[1]*P2[L]+KH3[2]*P3[L]+KH3[3]*P4[L]+KH3[4]*P5[L]+KH3[5]*P6[L]);

for (L=0; L<6; ++L)
KHP4[L]=(KH4[0]*P1[L]+KH4[1]*P2[L]+KH4[2]*P3[L]+KH4[3]*P4[L]+KH4[4]*P5[L]+KH4[5]*P6[L]);
```

```
            for (L=0; L<6; ++L)

KHP5[L]=(KH5[0]*P1[L]+KH5[1]*P2[L]+KH5[2]*P3[L]+KH5[3]*P4[L]+KH5[4]*P5[L]+KH5[5]*P6[L]);


            for (L=0; L<6; ++L)

KHP6[L]=(KH6[0]*P1[L]+KH6[1]*P2[L]+KH6[2]*P3[L]+KH6[3]*P4[L]+KH6[4]*P5[L]+KH6[5]*P6[L]);


           for (L=0; L<6; ++L)
           //secound row
           for (L=0; L<6; ++L)
           P2[L]=P2[L]-KHP2[L];
           //third row
           for (L=0; L<6; ++L)
           P3[L]=P3[L]-KHP3[L];
           //fourth row
           for (L=0; L<6; ++L)
           P4[L]=P4[L]-KHP4[L];
           //fifth row
           for (L=0; L<6; ++L)
           P5[L]=P5[L]-KHP5[L];
           //sixth row
           for (L=0; L<6; ++L)
           P6[L]=P6[L]-KHP6[L];
}
#endif
//----------------------------------------------------------------------
__interrupt void cla1Isr1()
{
  PieCtrlRegs.PIEACK.all = M_INT11;
//  asm(" ESTOP0");
}
//---------------------------------------------------------------------------------------
```

```
__interrupt void cla1Isr2()
{
   PieCtrlRegs.PIEACK.all = M_INT11;
//  asm(" ESTOP0");
}
//-----------------------------------------------------------------------------------------
__interrupt void cla1Isr3()
{
   PieCtrlRegs.PIEACK.all = M_INT11;
//  asm(" ESTOP0");
}
//-----------------------------------------------------------------------------------------
__interrupt void cla1Isr4()
{
   PieCtrlRegs.PIEACK.all = M_INT11;
//  asm(" ESTOP0");
}
//-----------------------------------------------------------------------------------------
__interrupt void cla1Isr5()
{
   asm(" ESTOP0");
}
//-----------------------------------------------------------------------------------------
__interrupt void cla1Isr6()
{
   asm(" ESTOP0");
}
//-----------------------------------------------------------------------------------------
__interrupt void cla1Isr7()
{
   asm(" ESTOP0");
}
```

```
//-----------------------------------------------------------------------------------------
__interrupt void cla1Isr8()
{
   PieCtrlRegs.PIEACK.all = M_INT11;
   //asm(" ESTOP0");
}
//-----------------------------------------------------------------------------------------
// end of file
```

# References


[1] W. Leonhard, *Control of electrical drives*: Springer Science & Business Media, 2001.

[2] S.-K. Sul, *Control of electric machine drive systems* vol. 88: John Wiley & Sons, 2011.

[3] J. M. Miller, "Hybrid electric vehicle propulsion system architectures of the e-CVT type," *IEEE Transactions on power Electronics,* vol. 21, pp. 756-767, 2006.

[4] K. T. Chau and Y. S. Wong, "Overview of power management in hybrid electric vehicles," *Energy conversion and management,* vol. 43, pp. 1953-1968, 2002.

[5] L. Harnefors, K. Pietilainen, and L. Gertmar, "Torque-maximizing field-weakening control: design, analysis, and parameter selection," *IEEE Transactions on Industrial Electronics,* vol. 48, pp. 161-168, 2001.

[6] K. H. Nam, *AC Motor Control and Electrical Vehicle Applications*: Taylor & Francis, 2010.

[7] J. Holtz, "Pulsewidth modulation for electronic power conversion," *Proceedings of the IEEE,* vol. 82, pp. 1194-1214, 1994.

[8] J. Holtz, "Pulsewidth modulation-a survey," in *PESC'92 Record. 23rd Annual IEEE Power Electronics Specialists Conference*, 1992, pp. 11-18.

[9] A. M. Hava, R. J. Kerkman, and T. A. Lipo, "Carrier-based PWM-VSI overmodulation strategies: analysis, comparison, and design," *IEEE Transactions on Power Electronics,* vol. 13, pp. 674-689, 1998.

[10] N. Mohan, T. M. Undeland, and W. P. Robbins, *Power electronics: converters, applications, and design*: John wiley & sons, 2003.

[11] D. G. Holmes and T. A. Lipo, *Pulse width modulation for power converters: principles and practice* vol. 18: John Wiley & Sons, 2003.

[12] S. Bolognani and M. Zigliotto, "Novel digital continuous control of SVM inverters in the overmodulation range," *IEEE Transactions on Industry Applications,* vol. 33, pp. 525-530, 1997.

[13] J. Holtz, W. Lotzkat, and A. M. Khambadkone, "On continuous control of PWM inverters in the overmodulation range including the six-step mode," *IEEE transactions on power electronics,* vol. 8, pp. 546-553, 1993.

[14] S. K. Sahoo and T. Bhattacharya, "Field Weakening Strategy for a Vector-Controlled Induction Motor Drive Near the Six-Step Mode of Operation," *IEEE Transactions on Power Electronics,* vol. 31, pp. 3043-3051, 2016.

[15] D.-C. Lee and G. M. Lee, "A novel overmodulation technique for space-vector PWM inverters," *IEEE Transactions on Power Electronics,* vol. 13, pp. 1144-1151, 1998.

[16] H.-Y. O. Yang and R. D. Lorenz, "Torque Ripple Minimization in Six-Step PMSM Drives via Variable and Fast DC Bus Dynamics," *IEEE Transactions on Industry Applications*, 2019.

[17] S. T. Hung, D. C. Hopkins, and C. R. Mosling, "Extension of battery life via charge equalization control," *IEEE Transactions on Industrial Electronics,* vol. 40, pp. 96-104, 1993.

[18] H. Gashtil, M. Kimabeigi, J. Goss, and S. Roggia, "Modelling an Interior Permanent Magnet Traction Motor Based on Current Signals Produced in a Space Vector Modulation," in *2018 XIII International Conference on Electrical Machines (ICEM)*, 2018, pp. 833-839.

[19] H. Gashtil, V. Pickert, D. Atkinson, D. Giaouris, and M. Dahidah, "A Case Study of Real Time Implementation of Extended Kalman Filter in Dual Core DSP for The On-line Estimation of Induction Machine Parameters," in *2019 IEEE 13th International Conference on Compatibility, Power Electronics and Power Engineering (CPE-POWERENG)*, 2019, pp. 1-7.

[20] H. Gashtil, V. Pickert, D. Atkinson, D. Giaouris, and M. Dahidah, "Comparative Evaluation of Field Oriented Control and Direct Torque Control Methodologies in Field Weakening Regions for Interior Permanent Magnet Machines," in *2019 IEEE 13th International Conference on Compatibility, Power Electronics and Power Engineering (CPE-POWERENG)*, 2019, pp. 1-6.

[21] H. Gashtil, V. Pickert, D. J. Atkinson, D. Giaouris, and M. Dahidah, "On-Line Estimation of Magnetizing Inductance and Rotor Resistance in Extended Kalman-Filter for Induction Machines," in *2018 2nd European Conference on Electrical Engineering and Computer Science (EECS)*, 2018, pp. 582-588.

[22] H. Grotstollen and J. Wiesing, "Torque capability and control of a saturated induction motor over a wide range of flux weakening," *IEEE Transactions on Industrial Electronics,* vol. 42, pp. 374-381, 1995.

[23] X. Xu and D. W. Novotny, "Selection of the flux reference for induction machine drives in the field weakening region," *IEEE transactions on industry applications,* vol. 28, pp. 1353-1358, 1992.

[24] M.-H. Shin, D.-S. Hyun, and S.-B. Cho, "Maximum torque control of stator-flux-oriented induction machine drive in the field-weakening region," *IEEE Transactions on Industry Applications,* vol. 38, pp. 117-122, 2002.

[25] K. Sang-Hoon and S. Seung-Ki, "Maximum torque control of an induction machine in the field weakening region," *IEEE Transactions on Industry Applications,* vol. 31, pp. 787-794, 1995.

[26] X. Xu, R. De Doncker, and D. W. Novotny, "A stator flux oriented induction machine drive," in *Power Electronics Specialists Conference, 1988. PESC'88 Record., 19th Annual IEEE*, 1988, pp. 870-876.

[27] T. S. Kwon and S. K. Sul, "Novel antiwindup of a current regulator of a surface-mounted permanent-magnet motor for flux-weakening control," *IEEE Transactions on industry applications,* vol. 42, pp. 1293-1300, 2006.

[28] B. J. Seibel, T. M. Rowan, and R. J. Kerkman, "Field-oriented control of an induction machine in the field-weakening region with DC-link and load disturbance rejection," *IEEE Transactions on Industry Applications,* vol. 33, pp. 1578-1584, 1997.

[29] Y.-C. Kwon, S. Kim, and S.-K. Sul, "Voltage feedback current control scheme for improved transient performance of permanent magnet synchronous machine drives," *IEEE Transactions on Industrial Electronics,* vol. 59, pp. 3373-3382, 2012.

[30] P.-Y. Lin and Y.-S. Lai, "Voltage control technique for the extension of DC-link voltage utilization of finite-speed SPMSM drives," *IEEE Transactions on Industrial Electronics,* vol. 59, pp. 3392-3402, 2012.

[31] P.-Y. Lin and Y.-S. Lai, "Novel voltage trajectory control for field-weakening operation of induction motor drives," *IEEE Transactions on Industry Applications,* vol. 47, pp. 122-127, 2011.

[32] Z. Dong, Y. Yu, W. Li, B. Wang, and D. Xu, "Flux-Weakening Control for Induction Motor in Voltage Extension Region: Torque Analysis and Dynamic Performance Improvement," *IEEE Transactions on Industrial Electronics,* vol. 65, pp. 3740-3751, 2018.

[33] S.-Y. Jung, C. C. Mi, and K. Nam, "Torque control of IPMSM in the field-weakening region with improved DC-link voltage utilization," *IEEE Transactions on Industrial Electronics,* vol. 62, pp. 3380-3387, 2015.

[34] A. Bunte, H. Grotstollen, and P. Krafka, "Field weakening of induction motors in a very wide region with regard to parameter uncertainties," in *PESC Record. 27th Annual IEEE Power Electronics Specialists Conference*, 1996, pp. 944-950.

[35] O. Wasynczuk, S. D. Sudhoff, K. A. Corzine, J. L. Tichenor, P. C. Krause, I. G. Hansen*, et al.*, "A maximum torque per ampere control strategy for induction motor drives," *IEEE Transactions on Energy Conversion,* vol. 13, pp. 163-169, 1998.

[36] S. Bozhko, S. Dymko, S. Kovbasa, and S. M. Peresada, "Maximum torque-per-amp control for traction IM drives: Theory and experimental results," *IEEE Transactions on Industry Applications,* vol. 53, pp. 181-193, 2016.

[37] M. Ahmad, *High Performance AC Drives: Modelling Analysis and Control*: Springer Science & Business Media, 2010.

[38] S.-H. Song, J.-W. Choi, and S.-K. Sul, "Transient torque maximizing strategy of induction machine in field weakening region," in *Power Electronics Specialists Conference, 1998. PESC 98 Record. 29th Annual IEEE*, 1998, pp. 1569-1574.

[39] J.-K. Seok and S. Kim, "Hexagon Voltage Manipulating Control (HVMC) for AC Motor Drives Operating at Voltage Limit," *IEEE Transactions on Industry Applications,* vol. 51, pp. 3829-3837, 2015.

[40] S. Morimoto, M. Sanada, and Y. Takeda, "Effects and compensation of magnetic saturation in flux-weakening controlled permanent magnet synchronous motor drives," *IEEE Transactions on Industry Applications,* vol. 30, p. 1632, 1994.

[41] H. A. Toliyat, E. Levi, and M. Raina, "A review of RFO induction motor parameter estimation techniques," *IEEE transactions on Energy conversion,* vol. 18, pp. 271-283, 2003.

[42] I. Boldea and S. A. Nasar, *Electric drives*: CRC press, 2016.

[43] !!! INVALID CITATION !!! [23, 41].

[44] Y. Liu, J. Zhao, R. Wang, and C. Huang, "Performance improvement of induction motor current controllers in field-weakening region for electric vehicles," *IEEE Transactions on Power Electronics,* vol. 28, pp. 2468-2482, 2013.

[45] V. S. S. P. K. Hari and G. Narayanan, "Space-vector-based hybrid PWM technique to reduce peak-to-peak torque ripple in induction motor drives," *IEEE Transactions on Industry Applications,* vol. 52, pp. 1489-1499, 2015.

[46] L. J. Garces, "Parameter adaption for the speed-controlled static ac drive with a squirrel-cage induction motor," *IEEE Transactions on Industry Applications*, pp. 173-178, 1980.

[47] I. Takahashi and T. Noguchi, "A new quick-response and high-efficiency control strategy of an induction motor," *IEEE Transactions on Industry applications,* pp. 820-827, 1986.

[48] X. Zhang, "Sensorless induction motor drive using indirect vector controller and sliding-mode observer for electric vehicles," *IEEE Transactions on Vehicular Technology,* vol. 62, pp. 3010-3018, 2013.

[49] I. Boldea, L. N. Tutelea, L. Parsa, and D. Dorrell, "Automotive electric propulsion systems with reduced or no permanent magnets: An overview," *IEEE Transactions on Industrial Electronics,* vol. 61, pp. 5696-5711, 2014.

[50] C. Wang, D. W. Novotny, and T. A. Lipo, "An automated rotor time-constant measurement system for indirect field-oriented drives," *IEEE Transactions on Industry Applications,* vol. 24, pp. 151-159, 1988.

[51] K. C. Agrawal, *Industrial power engineering handbook*: Elsevier, 2001.

[52] H. A. Toliyat and G. B. Kliman, *Handbook of electric motors* vol. 120: CRC press, 2018.

[53] R. Krishnan and A. S. Bharadwaj, "A review of parameter sensitivity and adaptation in indirect vector controlled induction motor drive systems," *IEEE Transactions on Power Electronics,* vol. 6, pp. 695-703, 1991.

[54] K. Wang, R. D. Lorenz, and N. A. Baloch, "Enhanced Methodology for Injection-Based Real-Time Parameter Estimation to Improve Back EMF Self-Sensing in Induction Machine Deadbeat-Direct Torque and Flux Control Drives," *IEEE Transactions on Industry Applications*, vol. 54, pp. 6071-6080, 2018.

[55] Y. Wang, N. Niimura, and R. D. Lorenz, "Real-time parameter identification and integration on deadbeat-direct torque and flux control (DB-DTFC) without inducing additional torque ripple," *IEEE Transactions on Industry Applications,* vol. 52, pp. 3104-3114, 2016.

[56] J. Kan, K. Zhang, and Z. Wang, "Indirect vector control with simplified rotor resistance adaptation for induction machines," *IET Power Electronics,* vol. 8, pp. 1284-1294, 2015.

[57] S. Yang, D. Ding, X. Li, Z. Xie, X. Zhang, and L. Chang, "A novel online parameter estimation method for indirect field oriented induction motor drives," *IEEE Transactions on Energy Conversion,* vol. 32, pp. 1562-1573, 2017.

[58] T. Noguchi, S. Kondo, and I. Takahashi, "Field-oriented control of an induction motor with robust on-line tuning of its parameters," *IEEE Transactions on Industry Applications,* vol. 33, pp. 35-42, 1997.

[59] D. J. Atkinson, P. P. Acarnley, and J. W. Finch, "Observers for induction motor state and parameter estimation," *IEEE Transactions on industry applications,* vol. 27, pp. 1119-1127, 1991.

[60] M. Pacas, "Sensorless drives in industrial applications," *IEEE Industrial Electronics Magazine,* vol. 5, pp. 16-23, 2011.

[61] J. Laowanitwattana and S. Uatrongjit, "Estimation of induction motor states and parameters based on Extended Kalman Filter considering parameter constraints," in *Power Electronics, Electrical Drives, Automation and Motion (SPEEDAM), 2016 International Symposium on,* 2016, pp. 755-760.

[62] L.-C. Zai, C. L. DeMarco, and T. A. Lipo, "An extended Kalman filter approach to rotor time constant measurement in PWM induction motor drives," *IEEE Transactions on Industry Applications,* vol. 28, pp. 96-104, 1992.

[63] V. Digalakis, J. R. Rohlicek, and M. Ostendorf, "ML estimation of a stochastic linear system with the EM algorithm and its application to speech recognition," *IEEE Transactions on speech and audio processing,* vol. 1, pp. 431-442, 1993.

[64] M. T. Angulo and R. V. Carrillo-Serrano, "Estimating rotor parameters in induction motors using high-order sliding mode algorithms," *IET Control Theory & Applications,* vol. 9, pp. 573-578, 2014.

[65] F. Jadot, F. Malrait, J. Moreno-Valenzuela, and R. Sepulchre, "Adaptive regulation of vector-controlled induction motors," *IEEE Transactions on control systems technology,* vol. 17, pp. 646-657, 2009.

[66] T. Wildi, "Electrical machines, drives, and power systems," *New Jersey: Upper Saddle River,* 2002.

[67] A. E. Fitzgerald, C. Kingsley, S. D. Umans, and B. James, *Electric machinery* vol. 5: McGraw-Hill New York, 2003.

[68] B. K. Bose, *Modern power electronics and AC drives* vol. 123: Prentice hall Upper Saddle River, NJ, 2002.

[69] D. W. Novotny and T. A. Lipo, *Vector control and dynamics of AC drives* vol. 1: Oxford university press, 1996.

[70] J. M. D. Murphy, *Thyristor control of AC motors* vol. 99: Pergamon Press Oxford, 1973.

[71] A. M. Trzynadlowski, *The field orientation principle in control of induction motors*: Springer Science & Business Media, 2013.

[72] T. G. Habetler, F. Profumo, M. Pastorelli, and L. M. Tolbert, "Direct torque control of induction machines using space vector modulation," *IEEE Transactions on Industry Applications,* vol. 28, pp. 1045-1053, 1992.

[73] P. Vas, *Sensorless Vector and Direct Torque Control*: Oxford University Press, 1998.

[74] G. S. Buja and M. P. Kazmierkowski, "Direct torque control of PWM inverter-fed AC motors-a survey," *IEEE Transactions on industrial electronics,* vol. 51, pp. 744-757, 2004.

[75] D. Casadei, F. Profumo, G. Serra, and A. Tani, "FOC and DTC: two viable schemes for induction motors torque control," *IEEE transactions on Power Electronics*, vol. 17, pp. 779-787, 2002.

[76] R. D. Lorenz, "A simplified approach to continuous on-line tuning of field-oriented induction machine drives," *IEEE Transactions on Industry Applications,* vol. 26, pp. 420-424, 1990.

[77] E. Levi and V. Vučković, "Field-oriented control of induction machines in the presence of magnetic saturation," *Electric Machines and Power Systems,* vol. 16, pp. 133-147, 1989.

[78] R. J. Meinhold and N. D. Singpurwalla, "Understanding the Kalman filter," *The American Statistician,* vol. 37, pp. 123-127, 1983.

[79] P. S. Maybeck, *Stochastic models, estimation, and control* vol. 3: Academic press, 1982.

[80] P. J. Hargrave, "A tutorial introduction to Kalman filtering," in *IEE colloquium on Kalman filters: introduction, applications and future developments*, 1989, pp. 1/1-1/6.

[81] R. Kumar, S. Das, P. Syam, and A. K. Chattopadhyay, "Review on model reference adaptive system for sensorless vector control of induction motor drives," *IET Electric Power Applications,* vol. 9, pp. 496-511, 2015.

[82] J. Holtz, "Sensorless control of induction machines—With or without signal injection?," *IEEE Transactions on Industrial Electronics,* vol. 53, pp. 7-30, 2006.

[83] C. Schauder, "Adaptive speed identification for vector control of induction motors without rotational transducers," in *Conference Record of the IEEE Industry Applications Society Annual Meeting*, 1989, pp. 493-499.

[84] S. Maiti, C. Chakraborty, Y. Hori, and M. C. Ta, "Model reference adaptive controller-based rotor resistance and speed estimation techniques for vector controlled induction motor drive utilizing reactive power," *IEEE Transactions on Industrial electronics,* vol. 55, pp. 594-601, 2008.

[85] Y. D. Landau, "Adaptive control: The model reference approach," *IEEE Transactions on Systems, Man, and Cybernetics*, pp. 169-170, 1984.

[86] G. A. Putrus, P. Suwanapingkarl, D. Johnston, E. C. Bentley, and M. Narayana, "Impact of electric vehicles on power distribution networks," in *2009 IEEE Vehicle Power and Propulsion Conference*, 2009, pp. 827-831.

[87] J. Simanek, J. Novak, R. Dolecek, and O. Cerny, "Control algorithms for permanent magnet synchronous traction motor," in *EUROCON 2007-The International Conference on" Computer as a Tool"*, 2007, pp. 1839-1844.

[88] B. Wang, X. Zhang, Y. Yu, J. Zhang, and D. Xu, "Maximum Torque Analysis and Extension in Six-Step Mode-Combined Field-Weakening Control for Induction Motor Drives," *IEEE Transactions on Industrial Electronics,* 2019.

[89] L. Zarri, M. Mengoni, A. Tani, G. Serra, D. Casadei, and J. O. Ojo, "Control schemes for field weakening of induction machines: A review," in *2015 IEEE Workshop on Electrical Machines Design, Control and Diagnosis (WEMDCD)*, 2015, pp. 146-155.

[90] I. Ralev, T. Lange, and R. W. De Doncker, "Wide speed range six-step mode operation of IPMSM drives with adjustable dc-link voltage," in *2014 17th International Conference on Electrical Machines and Systems (ICEMS)*, 2014, pp. 2987-2993.

[91] D. Casadei, M. Mengoni, G. Serra, A. Tani, and L. Zarri, "A control scheme with energy saving and DC-link overvoltage rejection for induction motor drives of electric vehicles," *IEEE Transactions on Industry Applications,* vol. 46, pp. 1436-1446, 2010.

[92] S.-M. Sue and C.-T. Pan, "Voltage-constraint-tracking-based field-weakening control of IPM synchronous motor drives," *IEEE Transactions on Industrial Electronics*, vol. 55, pp. 340-347, 2008.

[93] T. Kataoka, S. Toda, and Y. Sato, "On-line estimation of induction motor parameters by extended Kalman filter," in *Power Electronics and Applications, 1993., Fifth European Conference on*, 1993, pp. 325-329.

[94] D. C. Hanselman, *Brushless permanent magnet motor design*: The Writers' Collective, 2003.

[95] P. C. Krause, O. Wasynczuk, and S. D. Sudhoff, *Analysis of electric machinery* vol. 564: McGraw-Hill New York, 1986.

[96] S. R. Macminn and T. M. Jahns, "Control techniques for improved high-speed performance of interior PM synchronous motor drives," in *Conference Record of the 1988 IEEE Industry Applications Society Annual Meeting*, 1988, pp. 272-280.

[97] J. Jahn, *Vector optimization*: Springer, 2009.